

TRACER WATER TRANSPORT AND SUBGRID PRECIPITATION VARIATION WITHIN ATMOSPHERIC GENERAL CIRCULATION MODELS

(NASA-CR-182897) TRACER WATER TRANSPORT AND
SUBGRID PRECIPITATION VARIATION WITHIN
ATMOSPHERIC GENERAL CIRCULATION MODELS
Interim Technical Report (Massachusetts
Inst. of Tech.) 366 p

N88-26745

Unclas
0142948

CSCL 08G G3/46

by
RANDAL D. KOSTER
PETER S. EAGLESON
and
WALLACE S. BROECKER

DEPARTMENT
OF
CIVIL
ENGINEERING

RALPH M. PARSONS LABORATORY
HYDROLOGY AND WATER RESOURCE SYSTEMS

SCHOOL OF ENGINEERING
MASSACHUSETTS INSTITUTE OF TECHNOLOGY
Cambridge, Massachusetts 02139

*IN-46
142948*

Report Number 317

P-366

Prepared with the support of the
National Aeronautics and Space Administration
Grant No. NAG 5-743

R88-06

TRACER WATER TRANSPORT AND SUBGRID PRECIPITATION VARIATION
WITHIN ATMOSPHERIC GENERAL CIRCULATION MODELS

by

Randal D. Koster
Peter S. Eagleson
and
Wallace S. Broecker

RALPH M. PARSONS LABORATORY
HYDROLOGY AND WATER RESOURCE SYSTEMS

Department of Civil Engineering
Massachusetts Institute of Technology

Report No. 317

Prepared with the support of
The National Aeronautics and Space Administration
Grant No. NAG 5-743

March, 1988

Abstract

A capability is developed for monitoring tracer water movement in the three-dimensional GISS Atmospheric GCM. A typical experiment with the "tracer water model" follows water evaporating from selected grid squares and determines where this water first returns to the earth's surface as precipitation or condensate, thereby providing information on the lateral scales of hydrological transport in the GCM. Through a comparison of model results with observations in nature, inferences can be drawn concerning real world water transport. Tests of the tracer water model include a comparison of simulated and observed vertically-integrated vapor flux fields and simulations of atomic tritium transport from the stratosphere to the oceans. The inter-annual variability of the tracer water model results is also examined.

The tracer water model is applied to determine the evaporative sources of precipitation falling on representative regions in the Northern Hemisphere for the GCM climate. The results indicate a larger degree of water recycling over mid-latitude continental regions than is generally estimated in the literature. A variation of this experiment determines that the concentration of stable isotopes in Antarctic precipitation is related in part to evaporative source temperature. Model results are compared to those of a different tracer water model developed concurrently by another research group using a different GCM.

A completely separate study addresses the unrealistic uniform wetting assumption common in GCMs, under which precipitation formed over a grid

square falls uniformly across the square. The effects of incorporating a fractional grid square wetting parameterization into a GCM is examined. For computational efficiency, tests are performed with a one-dimensional model designed to simulate the workings of the three-dimensional GISS GCM. The analysis indicates that dividing a grid square area into only two sections, with boundaries that change at the start of every storm, may be sufficient to capture some of the important effects of a more realistic subgrid wetting procedure. The one-dimensional model is found to have potential use for other GCM hydrology studies as well.

Acknowledgments

This project was sponsored by the National Aeronautics and Space Administration under grant NAG-5-743. The work was performed by Randal D. Koster and as presented here fulfills the thesis requirement for the degree of Doctor of Science in Civil Engineering at MIT. The work was supervised by Dr. Peter S. Eagleson, Edmund K. Turner Professor of Civil Engineering at MIT. Professor Wallace S. Broecker of Columbia University acted as Mr. Koster's supervisor during his stay at the NASA/Goddard Institute for Space Studies (GISS) in New York City.

Dr. Jean Jouzel, of the Laboratoire de Geochimie Isotopique-LODYC (CEA-DPC, France), developed the precursor to the tracer water model described in this report and was extremely helpful during all phases of the tracer water research. Robert Suozzo of GISS provided invaluable assistance in running the GISS GCM and in interpreting the tracer water data. Dr. Gary Russell of GISS worked closely with Jouzel on the precursor to the tracer water model and also assisted with the present research. The authors thank Dr. James Hansen for the opportunity to work with the GISS GCM.

The authors thank Dr. David Rind of GISS and Professor Peter Stone of MIT for extremely useful technical discussions. The authors are also grateful to Dr. Anthony Del Genio of GISS, Professor Rafael Bras of MIT, Dr. Inez Fung of GISS, Dr. Max Suarez of NASA/Goddard Space Flight Center, Dr. James White of Lamont-Doherty Geological Observatory, and Dara Entekhabi of MIT for their technical assistance.

TABLE OF CONTENTS

Title Page	1
Abstract	2
Acknowledgments	4
Table of Contents	5
List of Figures	9
List of Tables	16
Notation	18
Chapter 1 Introduction	25
1.1 The Basic Nature of GCMs	25
1.2 Emphasis of the Present Report	27
1.3 Lateral Scales of Water Vapor Transport	28
1.3.1 Definition of Problem	28
1.3.2 Indirect Studies in the Literature	29
1.3.3 Proposed Study with a GCM	33
1.4 Fractional Wetting of Grid Square Areas	35
1.4.1 Definition of Problem	35
1.4.2 Proposed Analysis	38
Chapter 2 Description of the Tracer Water Model	42
2.1 General Background	42
2.2 Isotopic Forms of Water	47
2.2.1 Isotopic Fractionation	47
2.2.2 Units	51
2.3 The Structure of the Tracer Water Model	52
2.3.1 Advection	54
2.3.2 Moist Convective Precipitation	60
2.3.3 Large-Scale Condensation	67
2.3.4 Dry Convection	68
2.3.5 Surface Evaporation and Condensation	69
2.4 Upward Flux of Tracer from the Earth's Surface	72
2.4.1 Surface-Conserved Tracers	73
2.4.2 Aboveground Tracers	75
2.5 Simultaneous Integration of GCM Prognostic Variables and Tracer Transport	77

Chapter 3	Indirect Evaluations of Model Performance	79
3.1	Comparison Between Observed and Modeled Water Vapor Fluxes	79
3.1.1	The Zonal Vapor Flux	81
3.1.2	The Meridional Vapor Flux	120
3.1.3	The Total Vapor Flux Divergence	122
3.1.4	Specific and Relative Humidities	124
3.1.5	Discussion	129
3.2	Interannual Variability	130
3.3	Simulation of Tritium Transport from the Stratosphere to the Oceans	136
3.3.1	The Weiss and Roether Tritium Input Scenario	137
3.3.2	Description of the Tracer Water Model Model Simulations	140
3.3.3	Discussion	158
3.3.4	Summary of Tritium Transport Simulation Results	174
3.4	Stable Isotopes Simulations	175
3.4.1	Description of the Three year Stable Isotope Simulation	176
3.4.2	Results of the Three Year Stable Isotopes Simulation	176
3.4.3	Sensitivity of Model Results to Tracer Advection Scheme	183
Chapter 4	Examples of Model Applications and Comparisons with Other Models	186
4.1	Return of Evaporated Water to the Earth's Surface	187
4.2	Origins of Local Precipitation	195
4.2.1	Description of Experiment	195
4.2.2	Results	198
4.2.3	Comparison with Results from the LMD Tracer Water Model	207
4.3	Precipitation of Deuterium in Antarctica	212
4.3.1	Background	212
4.3.2	Description of Experiment	214
4.3.3	Results	217
4.3.4	Comparison of Results with a Simple Isotope Model	223

4.4	Comparison with Simple Models of Local Water Recycling	227
Chapter 5	Fractional Wetting of GCM Grid Squares: Studies with a One-Dimensional Soil-Atmosphere Model	232
5.1	Fractional Wetting of GCM Grid Squares and Storm Statistics	232
5.2	A One-Dimensional Soil-Atmosphere Model	236
5.2.1	Structure of the 1-D Model	237
5.2.2	Model Deficiencies	247
5.3	A Test of the 1-D Model	249
5.3.1	The GISS GCM Runoff Sensitivity Experiment	249
5.3.2	The 1-D Model Runoff Sensitivity Experiment	250
5.3.3	Comparison of Sensitivities	254
5.4	Fractional Wetting: Investigation with the 1-D Model	262
5.4.1	Parameterization of Fractional Wetting	262
5.4.2	Sensitivity of 1-D Model to Fractional Wetting	264
5.4.3	A Simple Approximation to the Fractional Wetting Parameterization	274
5.5	Interpretation of Model Results	281
Chapter 6	Summary, Conclusions, and Outlook	284
6.1	The GISS GCM Tracer Water Model	284
6.1.1	Validity of the Tracer Water Model	284
6.1.2	Hydrological Implications of Model Results	286
6.1.3	Future Research with the Tracer Water Model	288
6.2	Fractional Wetting of GCM Grid Squares	290
6.2.1	The 1-D Model Fractional Wetting Simulations	290
6.2.2	Other Potential Uses of the 1-D Model	293
References		296
Appendix A	Processing the GISS GCM and GFDL Vapor Flux Data	303
A.1.	The GISS GCM Data	303
A.2	The GFDL Data	305

Appendix B	Supplemental Flux Data from Tritium Simulations	310
Appendix C	Approximations Applied in the 1-D Model Radiation Algorithms	313
	C.1 Form of the Vertical Temperature Profile	313
	C.2 Solar Radiation	314
	C.3 Longwave Radiation	315
	C.4 Adjustment of Eddy Temperatures	316
Appendix D	Computer Code for 1-D Model	318

List of Figures

		<u>Page</u>
Figure 2-1	8° × 10° horizontal grid used in the GISS GCM.	43
Figure 2-2	Schematic of processes occurring above and below a single GISS GCM grid square (From Hansen et al, 1983).	46
Figure 2-3	Slopes scheme calculation of tracer advection. a) Spatial distribution of water vapor in grid box. b) Distribution (with respect to water vapor) of tracer concentration in adjacent grid boxes A and B before advection. c) Distribution of tracer concentration in Grid Box B after advection. d) Newly defined distribution of tracer concentration in Grid Box B.	56
Figure 2-4	Effective phase diagram for water assumed in tracer calculations during moist convection.	64
Figure 3-1	Global distributions of Q_λ for winter (DJF). a) GCM b) Observations c) Absolute differences	83
Figure 3-2	Global distributions of Q_λ for spring (MAM). a) GCM b) observations c) absolute differences	85
Figure 3-3	Global distributions of Q_λ for summer (JJA). a) GCM b) Observations c) Absolute differences	87
Figure 3-4	Global distributions of Q_λ for fall (SON). a) GCM b) Observations c) Absolute differences	89
Figure 3-5	Global distributions of $[Q_\lambda]$. a) Winter (DJF) b) Spring (MAM) c) Summer (JJA) d) Fall (SON)	91
Figure 3-6	Global distributions of Q_ϕ for winter (DJF). A) GCM b) Observations c) Absolute differences	95
Figure 3-7	Global distributions of Q_ϕ for spring (MAM). a. GCM b. observations c. absolute differences	97

Figure 3-8	Global distributions of Q_{ϕ} for summer (JJA). a) GCM b) Observations c) Absolute differences	99
Figure 3-9	Global distributions of Q_{ϕ} for fall (SON). a) GCM b) Observations c) Absolute differences.	101
Figure 3-10	Latitudinal distributions of $[Q_{\phi}]$. a) Winter (DJF) b) Spring (MAM) c) Summer (JJA) d) Fall (SON)	103
Figure 3-11	Global distributions of $Div(Q)$ for winter (DJF). a) GCM b) Observations c) Absolute differences	107
Figure 3-12	Global distributions of $Div(Q)$ for spring (MAM). a) GCM b) Observations c) Absolute differences	109
Figure 3-13	Global distributions of $Div(Q)$ for summer (JJA). a) GCM b) Observations c) Absolute differences	111
Figure 3-14	Global distributions of $Div(Q)$ for fall (SON). a) GCM b) Observations c) Absolute differences	113
Figure 3-15	Latitudinal distributions of $[Div(Q)]$. a) Winter (DJF) b) Spring (MAM) c) summer (JJA) d) fall (SON)	115
Figure 3-16	Global distributions of specific humidity. a) GCM (July) b) Observations (summer, JJA)	126
Figure 3-17	Global distributions of relative humidity. a) GCM (July) b) Observations (summer, JJA)	127
Figure 3-18	Interannual variability study. July precipitation contours for tracer evaporating from Southeast Asia source (shaded box). Initial conditions taken from a) year 1, b) year 2, c) year 3, d) year 4, and (e) year 5 of the 5-year simulation described by Hansen et al (1983).	133

- Figure 3-19 Observed and model-generated vertical profiles of the T/H ratio. Observations were taken above Nebraska and span the period February 10 - June 21, 1966 (Ehhalt, 1971). One of the model-generated profiles lies over the grid square containing Nebraska and the other lies over the North Atlantic (30°W, 43°N). For comparison purposes, all T/H ratios in a given profile were divided by the profile value at 6.1 km. (From Koster et al, in preparation). 160
- Figure 3-20 Map showing the locations of the areas in which Weiss and Roether obtained vapor-precipitation pairs for tritium analysis. The number of pairs collected in each area is indicated. (From Koster et al, in preparation.) 166
- Figure 3-21 Seasonal trend in the T/H ratio in rains at five localities before, during and after the peak fallout year (1963). The measurements at Reykjavik, Azores, Goose Bay and Vienna have been normalized to yield the same mean as Valencia. The normalization factors are listed in the figure (i.e., the Reykjavik results were all divided by 1.6...). The annual means selected by Weiss and Roether for Valencia are shown for comparison. (From Koster et al, in preparation.) 167
- Figure 3-22 Map showing the locations (circles) of the 18 sites used by Weiss and Roether to assess the T/H ratio distribution for oceanic rain. Shown by each point is the ratio of the T/H ratio to that for Valencia, Ireland rain. Also shown is the value for the Midway station (square) not used by Weiss and Roether. Shown on the right are the averages for 10° latitude belts estimated by Weiss and Roether based on the results for these ocean stations. These values are also referenced to Valencia, Ireland. (From Koster et al, in preparation.) 171
- Figure 3-23 Map showing the geographic distribution of T/H ratios for precipitation in the Northern Hemisphere. The average T/H ratios are referenced to that for Valencia, Ireland. (From Koster et al, in preparation.) 173
- Figure 3-24 $\delta^{18}\text{O}$ in precipitation (a) for the model simulation and (b) from observations. (From Jouzel et al, in press.) 178

1987

Figure 3-25	Mean annual $\delta^{18}\text{O}$ in precipitation versus mean annual surface temperature at the precipitation site (a) for the model simulation and (b) from observations. (From Jouzel et al, in press. ¹⁹⁸⁷)	180
Figure 3-26	Mean annual $\delta^{18}\text{O}$ in precipitation versus mean annual precipitation (a) for the model simulation and (b) from observations. (From Jouzel et al, in press. ¹⁹⁸⁷)	182
Figure 3-27	$\delta^{18}\text{O}$ in Antarctic precipitation. (a) Upstream weighting scheme. (b) Slopes scheme. (c) Observations.	185
Figure 4-1	Thirty-day steady-state July tracer precipitation (mm). The tracer source region lies in the Mississippi Valley. During 30 July days, tracer precipitation = 2.7×10^{13} kg and tracer evaporation = 1.9×10^{13} kg.	188
Figure 4-2	Thirty-day steady-state July tracer precipitation (mm). The tracer source region lies in the Amazon Basin. During 30 July days, tracer precipitation = 4.1×10^{13} kg and tracer evaporation = 8.9×10^{13} kg.	189
Figure 4-3	Thirty-day steady-state July tracer precipitation (mm). The tracer source region lies in the African Sahel. During 30 July days, tracer precipitation = 6.4×10^{13} kg and tracer evaporation = 9.3×10^{13} kg.	190
Figure 4-4	Thirty-day steady-state July tracer precipitation (mm). The tracer source region lies in the Sudd area of Sudan. During 30 July days, tracer precipitation = 1.1×10^{14} kg and tracer evaporation = 1.8×10^{14} kg.	191
Figure 4-5	Thirty-day steady-state July tracer precipitation (mm). The tracer source region lies in Western Europe. During 30 July days, tracer precipitation = 6.8×10^{13} kg and tracer evaporation = 9.8×10^{13} kg.	192
Figure 4-6	Thirty-day steady-state July tracer precipitation (mm). The tracer source region lies in the European U.S.S.R. During 30 July days, tracer precipitation = 2.4×10^{14} kg and tracer evaporation = 3.2×10^{14} kg.	193

Figure 4-7	Thirty-day steady-state tracer vapor impact onto ocean surface in July (mm). The tracer source region lies in Southeast Asia.	196
Figure 4-8	Source regions chosen for "origins of precipitation" experiment. Heavy lines separate the tracer source regions. The local precipitations analyzed occur in the small numbered or lettered squares.	197
Figure 4-9	Contours showing percentage of local precipitation derived from combined North Atlantic and Tropical Atlantic source regions. (a) Summer. (b) Winter.	203
Figure 4-10	Contours showing percentage of local precipitation derived from combined North Pacific and Tropical Pacific source regions. (a) Summer. (b) Winter.	204
Figure 4-11	Contours showing percentage of local precipitation derived from Indian Ocean source region. (a) Summer. (b) Winter.	205
Figure 4-12	Contours showing percentage of local precipitation derived from North Africa/Southern Asia source region. (a) Summer. (b) Winter.	206
Figure 4-13	Source regions used in LMD GCM "origins of precipitation" experiment. (From Joussaume et al, 1986.)	209
Figure 4-14	Contours showing percentage of local July precipitation derived from Atlantic source region in LMD GCM experiment. Isolines are drawn every 10%. Light shading: 10 to 30%; medium shading: 30 to 50%; heavy shading: 50 to 70%; black: more than 70%. (From Joussaume et al, 1986.)	210
Figure 4-15	Contours showing percentage of local July precipitation derived from Pacific source region in LMD GCM experiment. Isolines are drawn every 10%. Light shading: 10 to 30%; medium shading: 30 to 50%; heavy shading: 50 to 70%; black, more than 70%. (From Joussaume et al, 1986.)	211
Figure 4-16	Mean annual δD in precipitation versus mean annual surface temperature at the precipitation site, from observations. Two lines are fitted to the data, one for temperatures below 15°C and the other for temperatures above 15°C.	213

Figure 4-17	Definition of tracer source regions by ocean surface temperature. Grid squares marked with "A", for example, belong to Source Region A and are pure open ocean grid squares with a surface temperature $T_G < 5^\circ\text{C}$. The temperature ranges defining the other source regions are listed in the text.	216
Figure 4-18	δD in Antarctic precipitation (in permil) for three different tracers. (a) Tracer from Source Region A. (b) Tracer from Source Region C. (c) Tracer from Source Region F.	219
Figure 4-19	Time-averaged δD in precipitation versus time averaged surface temperature, as determined by the tracer water model. Only Antarctic sites with an average surface temperature below -20°C are considered.	222
Figure 4-20	Time-averaged δD in precipitation versus time-averaged surface temperature for the HDO tracer evaporating from the $10^\circ\text{C} < T_G < 15^\circ\text{C}$ ocean grid squares. Only Antarctic sites with an average surface temperature below -20°C are considered.	224
Figure 5-1	Probability density function of storm duration derived from precipitation data at New England grid square in GISS GCM. Dashed line represents an exponential fit to the observed distribution at Boston. (Mean observed storm duration = 7.7 hours.)	234
Figure 5-2	Probability density function of time between storms derived from precipitation data at New England grid square in GISS GCM. Dashed line represents an exponential fit to the observed distribution at Boston. (Mean observed time between storms = 3 days.)	235
Figure 5-3	Sensitivity of upper soil layer moisture content to a change in the runoff coefficient. a) GISS GCM. b) 1-D model. Moisture contents are expressed in mm for the GISS GCM and as soil saturations for the 1-D model.	255
Figure 5-4	Sensitivity of evaporation (in mm/day) to a change in the runoff coefficient. a) GISS GCM. b) 1-D model.	257
Figure 5-5	Sensitivity of precipitation (in mm/day) to a change in the runoff coefficient. a) GISS GCM. b) 1-D model.	259
Figure 5-6	Sensitivity of surface temperature (in $^\circ\text{C}$) to a change in the runoff coefficient. a) GISS GCM. b) 1-D model.	260

Figure 5-7	Sensitivity of surface runoff (in mm/day) to a change in the runoff coefficient. (a) GISS GCM. (b) 1-D model.	261
Figure 5-8	Seasonal cycle of average saturation in upper soil layer of the 1-D model for varying sizes of the wetted fraction.	266
Figure 5-9	Seasonal cycle of surface runoff in the 1-D model for varying sizes of the wetted fraction. (Units: mm/day)	267
Figure 5-10	Seasonal cycle of precipitation in the 1-D model for varying sizes of the wetted fraction. (Units: mm/day)	269
Figure 5-11	Seasonal cycle of evaporation in the 1-D model for varying sizes of the wetted fraction. (Units: mm/day).	271
Figure 5-12	Seasonal cycle of surface temperature in the 1-D model for varying sizes of the wetted fraction. (Units: °C)	272
Figure 5-13	Seasonal cycle of average saturation in upper soil layer of the 1-D model for varying sizes of the wetted fraction, under simplified parameterization.	276
Figure 5-14	Seasonal cycle of average saturation in upper soil layer of 1-D model. Solid line shows cycle under uniform precipitation wetting, dashed line shows cycle derived in Section 5.4.2 for a wetted fraction of 1/20, and dotted line shows cycle derived under simpler parameterization for a wetted fraction of 1/20.	277
Figure 5-15	Seasonal cycle of precipitation in the 1-D model for varying sizes of the wetted fraction, under simplified parameterization. (Units: mm/day)	279
Figure 5-16	Seasonal cycle of precipitation in 1-D model. (In mm/day). Solid line shows cycle under uniform precipitation wetting, dashed line shows cycle derived in Section 5.4.2 for a wetted fraction of 1/20, and dotted line shows cycle derived under simpler parameterization for a wetted fraction of 1/20.	280
Figure A-1	GCM variables used in calculations of vertically-integrated horizontal water vapor transports.	304
Figure A-2	Area weighting used in processing GFDL data.	307

LIST OF TABLES

Table 2-1	Vertical resolution used in the GISS GCM.	45
Table 3-1	Summary of flux compilations of Weiss and Roether (1980). For each 5° latitudinal band in each ocean, the first three columns show the average evaporation and precipitation rates used and the estimates of combined precipitation and surface vapor exchange tritium input. The fourth and fifth data columns divide the tritium input for each band into the two components, and the sixth data column provides the ratio of the vapor exchange input to the precipitation input. The final column indicates the percent of total tritium deposited into each band. (From Koster et al, in preparation.)	138
Table 3-2	Tritium fluxes as a function of latitude for selected tritium simulations (From Koster et al, in preparation.)	143
Table 3-3	Description of simulations and ratios of vapor impact delivery of tritium to precipitation delivery. Simulations T2-T25 are equivalent to Simulation T1 except for the changes noted in the simulation description. Keep in mind that Weiss and Roether's (1980) analysis suggests a tritium input ratio of 2.3. (From Koster et al, in preparation).	146
Table 3-4	Tritium input ratios as a function of source height. In each simulation below, tritium contents were kept constant in those grid boxes of the indicated atmospheric level lying directly above pure ocean grid squares north of 30°N. (From Koster et al, in preparation).	151
Table 3-5	Tritium input ratios as a function of time for Simulation T26, in which an impulse of tritium was released in the stratosphere at the beginning of the first week. The tritium input ratios are determined from precipitation and vapor exchange inputs into the ocean averaged over each listed week. (From Koster et al, in preparation.)	159

Table 3-6	Summary of the T/H data obtained by Weiss and Roether (1980) from measurements on rain/vapor pairs. The data are grouped below according to the areas in which they were measured. (See Figure 3-20.) (From Koster et al, in preparation; the data were kindly provided for use in this paper by Wolfgang Weiss of Freiburg, West Germany.)	164
Table 3-7	Comparisons of runoff and precipitation inputs of tritium into the North Atlantic and North Pacific, as estimated by Weiss and Roether (1980). The ocean tritium inventories listed were obtained during the GEOSECS program (see Broecker et al, 1986, for summary). The entries are decay-corrected to the year 1981. (From Koster et al, in preparation.)	169
Table 4-1	Percent contributions of the source regions to the local precipitations. Each numbered section corresponds to a like-numbered local area in Figure 4-8. The Southern Hemisphere is the tenth source region.	199
Table 4-2	Percent contributions of the source regions to the January and July precipitations in the lettered squares of Figure 4-8.	201
Table 4-3	Zonal mean of δD in precipitation versus latitude for each tracer. All numbers are in units of permil.	220
Table 4-4	Correlation coefficients obtained when fitting a linear relationship between time-averaged surface temperature and time-averaged δD .	225
Table 5-1	Values used for 1-D model parameters.	251
Table 5-2	Annual water balance quantities for the wetted fractions simulations.	273

NOTATION

		Units
A	area of land surface	L^2
A_k	area of intersection of square k with larger square	L^2
a_0	radius of earth	L
$C(\ell)$	heat capacity of layer ℓ	$ML^2T^{-2}deg^{-1}$
C_H	sensible heat transfer coefficient	
C_p	tritium concentration in precipitation	
C_q	water vapor transfer coefficient	
C_s	correction factor for isotope concentration in near-surface waters	
C_v	tritium concentration in ocean vapor	
C_o	average weight ratio of water isotope to H_2O in seawater	
c_p	specific heat of air	$L^2T^{-2}deg^{-1}$
$D_{isotope}$	molecular diffusivity of water isotope in air	L^2T^{-1}
D_{water}	molecular diffusivity of water vapor in air	L^2T^{-1}
Div	divergence operator	L^{-1}
d_ℓ	fraction of day receiving solar radiation	
$d_{\ell amp}$	seasonal amplitude of fraction of day receiving solar radiation	
E	evaporation of water	$ML^{-2}T^{-1}$
E_{ave}	average evaporation rate along length of land surface	$ML^{-2}T^{-1}$
E_{down}	downward flux of water vapor at ocean surface	$ML^{-2}T^{-1}$
E_T	evaporation of tracer	$ML^{-2}T^{-1}$

$E_{T,down}$	downward flux of tracer vapor at ocean surface	$ML^{-2}T^{-1}$
$E_{T,HDO}$	evaporation of deuterium water tracer	$ML^{-2}T^{-1}$
E_{T,H_2O}	evaporation of non-isotopic water tracer	$ML^{-2}T^{-1}$
$E_{T,up}$	upward flux of tracer vapor at ocean surface	$ML^{-2}T^{-1}$
E_{up}	upward flux of water vapor at ocean surface	$ML^{-2}T^{-1}$
f	fraction of land surface wetted by storm	
f_{local}	local recycling ratio	
g	gravitational acceleration	LT^{-2}
H	sensible heat flux at earth's surface	MT^{-3}
H_{conv}	vertically-integrated convergence of heat flux in atmospheric column	ML^2T^{-3}
H_{conva}	seasonal amplitude of vertically-integrated convergence of heat flux	ML^2T^{-3}
H_{convo}	annual mean vertically-integrated convergence of heat flux	ML^2T^{-3}
$H_{\ell\omega-bot}(\ell)$	net upward longwave radiation flux at bottom boundary of layer ℓ	ML^2T^{-3}
$H_{\ell\omega-top}(\ell)$	net upward longwave radiation flux at top boundary of layer ℓ	ML^2T^{-3}
h	average relative humidity of water vapor in air	
h_i	relative humidity at beginning of process	
I_{EP}	total deposition of tritium into ocean via precipitation and vapor exchange	MT^{-1}
i	meridional index for GCM grid	
j	latitudinal index for GCM grid	
K	empirical eddy diffusion coefficient	L^2T^{-1}
k	isotope evaporation parameter	

l	length of land surface	L
l	vertical index for GCM grid	
m_{tb}	mean time between storms	T
m_{tr}	mean storm duration	T
n_o	number of time steps in a GCM integration	
P	precipitation rate	$ML^{-2}T^{-1}$
P	pressure	$ML^{-1}T^{-2}$
P_S	surface pressure	$ML^{-1}T^{-2}$
P_{SL}	sea level pressure	$ML^{-1}T^{-2}$
Q	vertically-integrated water vapor flux	$ML^{-1}T^{-1}$
Q(x)	mass of water passed when traveling a distance x from the side of a grid box	M
Q_A	mass of water vapor in grid box A	M
Q_{conv}	vertically-integrated convergence of moisture flux in atmospheric column	MT^{-1}
Q_{conva}	seasonal amplitude of vertically-integrated convergence of moisture flux	MT^{-1}
Q_{convo}	annual mean vertically-integrated convergence of moisture flux	MT^{-1}
Q_l	amount of liquid water present	M
Q_s	amount of solid water present	M
Q_v	amount of water vapor present	M
Q_{vo}	original water vapor content	M
Q_λ	zonal component of vertically-integrated water vapor flux	$ML^{-1}T^{-1}$
Q_ϕ	meridional component of vertically-integrated water vapor flux	$ML^{-1}T^{-1}$
q	specific humidity	
\bar{q}	seasonal mean specific humidity	

q_G	saturation specific humidity at surface temperature	
q_{GT}	specific humidity of tracer at surface	
q_S	specific humidity at top of the parameterized surface layer	
q_{ST}	specific humidity of tracer at top of the parameterized surface layer	
q_1	average specific humidity in first layer grid box	
q_{1T}	average specific humidity of tracer in first layer grid box	
$\overline{q'u'}$	seasonal mean of zonal component of transient eddy vapor flux	LT^{-1}
$\overline{q'v'}$	seasonal mean of meridional component of transient eddy vapor flux	LT^{-1}
R	gas constant	$L^2T^{-2}deg^{-1}$
R	tracer water content	M
R	surface runoff	MT^{-1}
R_A	mass of tracer in grid box A	M
R_l	amount of tracer or water isotope in liquid form	M
$R_{lw-surf}$	upward longwave radiation flux at the earth's surface	MT^{-3}
R_s	amount of tracer or water isotope in solid form	M
R_{sw}	shortwave radiation flux at top of atmosphere	MT^{-3}
R_{swa}	seasonal amplitude of shortwave radiation flux at top of atmosphere	MT^{-3}
R_{swo}	mean annual shortwave radiation flux at top of atmosphere	MT^{-3}

R_v	amount of tracer or water isotope in vapor form	M
R_{v0}	original tracer vapor content	M
R_{xA}	"slope" of tracer content in grid box A, for use in slopes scheme formulation	M
S	supersaturation of water vapor in air	
T	temperature	(deg)
T_E	average surface temperature of tracer source region	(deg)
$T_{eddy}(\ell)$	difference between actual temperature and approximate profile temperature at layer ℓ	(deg)
T_G	surface temperature	(deg)
T_p	temperature of moist convective plume	(deg)
$T_{prof}(\ell)$	estimated temperature at layer ℓ from approximate profile	(deg)
T_S	temperature at top of parameterized surface layer	(deg)
T_1	average temperature of first layer grid box	(deg)
T/H	ratio of tritium to normal hydrogen in a sample	
TU	tritium unit, equal to one tritium atom per 10^{18} hydrogen atoms	
t	time	T
t_{day}	time elapsed since the most recent midnight	T
u	zonal component of wind velocity	LT^{-1}
u	velocity of uniform incoming wind	LT^{-1}
\bar{u}	seasonal mean of zonal component of wind velocity	LT^{-1}
v	meridional component of wind velocity	LT^{-1}

\bar{v}	seasonal mean of meridional component of wind velocity	LT^{-1}
W_{fc1}	maximum water content of upper soil layer	ML^{-2}
W_{fc2}	maximum water content of lower soil layer	ML^{-2}
W_s	surface wind speed	LT^{-1}
W_1	water content of upper soil layer	ML^{-2}
$W_{1-local}$	water content in upper soil layer of land section being wetted	ML^{-2}
W_2	water content of lower soil layer	ML^{-2}
w	average water vapor content of incoming air	ML^{-2}
$X_{k\ell}$	value of given quantity at level ℓ over square k	
X_ℓ	average value of given quantity at level ℓ	
x	distance from side of box	L
x_D	mole fraction of deuterium atoms in sample	
x_{DA}	mole fraction of deuterium atoms from source region A in sample	
x_H	mole fraction of hydrogen atoms in sample	
x_{HA}	mole fraction of hydrogen atoms from source region A in sample	
x_{16O}	mole fraction of ^{16}O atoms in sample	
x_{18O}	mole fraction of ^{18}O atoms in sample	
z	topographic height	L
z_s	height of the parameterized surface layer	L
z_1	height of the first atmospheric layer in the GCM	L
α_{eff}	effective fractionation factor	

$\alpha_{l/v}$	liquid/vapor equilibrium fractionation factor	
$\alpha_{s/v}$	solid/vapor equilibrium fractionation factor	
β	efficiency factor in calculation of evaporation from soil	
β	uniform vertical temperature gradient	deg L ⁻¹
δD	relative deviation of deuterium concentration from that of Standard Mean Ocean Water	
$\delta^{18}O$	relative deviation of oxygen-18 concentration from that of Standard Mean Ocean Water	
ϵ	surface emissivity	
λ	longitude on earth's surface	
ρ	density of air	ML ⁻³
σ	Stefan-Boltzmann constant	MT ⁻³ deg ⁻⁴
τ_D	soil moisture diffusion time constant	T
τ_{eddy}	radiative decay time for eddy temperatures	T
ϕ	latitude on earth's surface	

Chapter 1

Introduction

Atmospheric general circulation models (GCMs) are designed for numerical simulation of global climate. An adequately developed GCM could provide important information on climate sensitivity to human-induced environmental change. An adequate GCM, however, requires a realistic intrinsic hydrological cycle, and many aspects of this cycle in GCMs are still not understood. The present report investigates some of the yet unexplored aspects of this cycle.

1.1 The Basic Nature of GCMs

A brief description of the nature of GCMs is now provided. For a more complete description of GCMs and their characteristics, the reader is referred to Chang (1977) and to the descriptions of individual GCMs, such as those provided by Hansen et al (1983), Randall (1982), Sadourny and Laval (1984), Washington et al (1977), and Arakawa and Lamb (1977).

Imagine the earth's atmosphere divided in the following way. The earth's surface is divided latitudinally and meridionally into a two-dimensional gridded array, and the atmospheric column above each surface division is itself divided into a number of vertically stacked boxes. Atmospheric conditions at a given time, as represented by pressure, temperature, specific humidity, and wind speed, vary spatially within any given grid box of this imaginary three-dimensional grid.

An average value of each variable can, however, be assigned to the box. Similarly, although the fluxes of moisture and energy vary spatially along any given face of the grid box, average fluxes can be assigned to the face. The GCM models the earth's atmosphere with such a three-dimensional grid. In the course of a model simulation, it computes and monitors the average atmospheric conditions existing in each model grid box.

The GCM attempts to generate climate patterns and features resembling those found in nature. The climate is defined by the long-term average of weather patterns determined at every simulation time step; the weather patterns themselves are generated by sub-models of the important mass and energy transport processes existing in the real world. At each simulation time step, for example, fluxes of air mass, moisture, and energy between each pair of adjacent grid boxes are determined by solving discretized forms of the fundamental conservation and state equations.

Parameterizations of precipitation processes produce, under appropriate thermodynamic conditions, rainfall onto the surface grid squares. Models of soil and surface ice store portions of the rainwater for future evaporation. A seasonally varying solar radiation flux at the top of the atmosphere can drive the GCM.

It is important to realize that although the GCM generates a series of weather states, it is not designed to predict weather events in the real world. An instantaneous temperature or precipitation value at a single surface grid square, for example, has no meaning. Only GCM quantities that have been averaged temporally over, say, a month and spatially over several grid squares deserve attention. Again,

monthly-averaged spatial distributions of climatic variables such as temperature and precipitation can define the inherent GCM climate. The modeler's goal is to have this model climate match the observed climate as well as possible.

The GCM concentrates only on the average quantities in each grid box. The effects of subgrid variations in temperature or specific humidity, for example, are either crudely parameterized or are ignored. Some subgrid variations, however, such as those defining moist convective precipitation and surface evaporation, have very important climatic effects. The accuracy of a GCM may therefore always be limited by its grid resolution.

Nevertheless, the GCM represents the best effort to date in the modeling of the earth's climate. An effective climate model is highly desirable for climate sensitivity analysis. An adequately developed GCM could determine, for example, the extent of earth warming due to the human-induced increase in atmospheric carbon dioxide. GCMs at the present state of development have a great many flaws but are continually being extended and improved.

1.2 Emphasis of the Present Report

The proper modeling of large-scale water transports is crucial for producing a realistic climate. These transports not only determine global precipitation distributions, but they also affect, for example, large scale energy transports (through fluxes of latent heat) and the radiation budget (through the albedo of clouds). As mentioned above, however, the

intrinsic hydrological cycle within GCMs is not completely understood. The present report investigates certain aspects of this cycle and suggests possible ways of making it more realistic. To the extent that the particular GCM used is valid, the report also provides estimates of certain water balance components which are not measurable in the real world.

The report consists of two completely separate GCM hydrology studies. The first uses a GCM to produce data on water vapor transport in the model atmosphere. The second examines the effect of assigning GCM-generated precipitation masses to more realistic portions of surface grid squares. The nature of these studies will now be discussed.

1.3 Lateral Scales of Water Vapor Transport

1.3.1 Definition of Problem

All water evaporating from the earth's surface will eventually return to the surface as precipitation or condensed vapor. What lateral distance does the water vapor generally travel while in the atmosphere? Stated another way, what fraction of the precipitation in a given region is derived from water evaporating from the region itself? These questions have practical significance. Large-scale engineering projects, such as the irrigation of previously arid lands or the drainage of the swamps in the Sudd region of Sudan, can change the evaporation characteristics of a region and could conceivably cause adverse or beneficial changes in the precipitation rates of neighboring regions.

Unfortunately, information of this type cannot be directly obtained from measurements in nature. The precipitation onto a given land region is derived from locally evaporated water and from advected vapor from outside the region, and the individual water vapor molecules from the two sources are indistinguishable. Since they are not mixed homogeneously in the vertical, and since complete information concerning atmospheric mixing and the levels at which precipitation forms over a region is not available, their relative contributions to the precipitation cannot be determined. Alternative, indirect methods of determining the relative contributions must therefore be applied.

1.3.2 Indirect Studies in the Literature

Many researchers have attempted to determine the relative contributions of advected and local moisture to local precipitation. The results of the studies, however, are hardly conclusive or necessarily applicable to regions outside the study areas.

The importance of locally evaporated water has been the subject of a long-standing controversy. Holzmann (1937) contends that most of the precipitation over continents is derived from evaporated ocean water. Benton et al (1950) analyze a time series of weather maps for the Ohio Valley and estimate that evaporated ocean water accounts for over 85% of the precipitation in the region. (See Section 4.4 below.) Based on this result, Benton et al state that Holzmann's scenario is more realistic than that of Horton (1943) or the National Resources Board (1934), who stress the importance of continental water vapor sources.

The simple moisture budget model of Budyko (1974) allows one to calculate the relative contribution of local evaporation to precipitation from mean values of evaporation and water vapor influx. (See Section 4.4.) Budyko determines that in July, 86% of the water precipitating onto the European U.S.S.R. is derived from outside sources. McDonald (1962) strongly asserts that increased local evaporation would have little effect on local precipitation and supports his statements with a simple water budget study over Arizona.

The analyses of Benton et al (1950), Budyko (1974), and McDonald (1962) therefore discount the importance of locally evaporated moisture to precipitation. Each of these analyses, however, is based on the assumption that water evaporating from the ground is immediately and homogeneously mixed into the advected water vapor above. The analyses do not account for the fact that evaporated moisture in the real world might remain relatively close to the ground and that perhaps precipitation (especially by moist convection) is mostly derived from near-surface moisture. Stidd (1968, 1975) comments on the problems with the assumption and implies further that moisture introduced at ground level can enhance rainfall by increasing convective instability.

Stidd (1968, 1975) uses a Student's t test to analyze precipitation in the Columbia Basin of Washington. The analysis suggests that irrigation development in the basin has caused a noticeable increase in local rainfall. Stidd's results are challenged by Fowler and Helvey (1974, 1975), who perform a different statistical test (double-mass plotting) on Stidd's data set. Fowler and Helvey conclude that the increased

irrigation does not have a statistically significant effect on local rainfall.

Other statistical studies that provide qualitative estimates of evaporative contributions to precipitation include those of Schickedanz and Ackermann (1977) and Eagleson and Lariviere (1970). Using Empirical Orthogonal Function analysis, Schickedanz and Ackermann find significant increases in precipitation following irrigation development in the Great Plains of North America. Eagleson and Lariviere determine the lag one serial correlation coefficient of monthly point precipitation for various measurement stations across North America. The lateral scale of the Pacific Ocean influence on North American precipitation is inferred from the decay of the coefficient with distance from the West Coast.

The recycling of water in the Amazon Basin has been the subject of many studies. Lettau et al (1979) used "climatology" techniques to quantify each component of the basin's water balance. They determine that in the westernmost section of the basin, 47% of the precipitation is derived from water evaporating from the basin itself. Their analysis, however, is based on parameters that are difficult to quantify, such as "the fraction of regional evaporation returned to the regional air-soil interface". They do not mention the method used to estimate these parameters. Stallard and Edmund (1981) note that chlorine concentrations in precipitation decrease toward the interior of the Amazon Basin. Salati and Vose (1984), in their extensive review of Amazon Basin hydrology, infer from these chlorine data that evaporated Pacific Ocean water

contributes little to Amazon precipitation. Benton et al (1950), however, warn against inferring oceanic vapor contributions from chlorine concentrations; they note, for example, that chlorine concentration in coastal precipitation is enhanced by the scavenging of large salt particles that cannot travel very far inland. Salati and Vose (1984) only briefly outline a model that suggests that roughly half the precipitation falling on a 3° meridional section in the Amazon Basin consists of water evaporated from the section itself.

Salati et al (1979) use stable water isotope distributions to determine important centers of water recycling in the Amazon Basin. They admit, however, that the isotope distributions cannot be used to quantify recycling rates. Libby's (1959) isotopic analysis, on the other hand, does produce quantitative results. From tritium concentrations in Chicago precipitation, he deduces that two-thirds of the precipitation is composed of evaporated ocean water. Some of his assumptions, however, are subject to question (see Section 4.4 below).

Finally, the contribution of one region's evaporated water to another region's precipitation has been inferred from large-scale atmospheric vapor flux measurements. Peixoto and Oort (1983), for example, study such measurements and note the strong contribution of evaporated ocean water to continental precipitation. Rasmussen (1971) finds a correlation in winter between increased vapor flux across the Gulf Coast of the United States and increased precipitation in Eastern North America. Neither study, however, provides quantitative information on relative contributions.

1.3.3 Proposed Study with a GCM

Again, the analyses discussed above are somewhat inconclusive, largely because water vapor molecules released from one evaporative source in the real world are indistinguishable from those released from another source. Consider, on the other hand, the motion of water vapor in a GCM. A suitably modified GCM could "tag" the water evaporating from a specified set of surface grid squares and follow this water as it moves through the atmosphere. The GCM would need only to determine, for any given atmospheric process in any given grid box at any given time step, the proper portion of the tagged water mass leaving the box to enter another. In the process of following the tagged water mass, the GCM would record the locations at which it precipitates to the surface, thereby providing the desired information on the lateral scales of horizontal water vapor transport.

A model of this type would have certain important advantages. The evaporative source for the tagged water molecules could be specified anywhere on the globe. Also, a model simulation could, in principle, be run as long as necessary to produce sufficient data for a proper statistical analysis.

The main disadvantage of such a model is, however, obvious. The accuracy of the model results are necessarily constrained by the accuracy of the GCM climate itself. At present, GCM modelers have achieved only limited success in reproducing the earth's observed climate. Current GCMs perform quite poorly, in fact, in reproducing some climatic features,

especially at smaller spatial scales. Thus, any water transport information obtained from the model would be inconclusive. Still, creating a model for following specific water masses is justifiable, since the model would provide in many cases a "best estimate" of evaporative source contributions to precipitation. Again, this type of information cannot be directly measured in nature. When estimating the effect, for example, of the current drainage of the Sudd swamps on future precipitation in neighboring African regions, consideration, at least in part, of crude and flawed model results is certainly better than relying on guessing or conjecture alone.

With this in mind, a water transport monitoring capability was incorporated into the GCM of the NASA/Goddard Institute for Space Studies (NASA/GISS, or simply GISS). The GCM itself is described in detail by Hansen et al (1983). Much of the present report describes the structure and performance of the extended model. Since the extended model determines the atmospheric pathways traveled by a water mass between its evaporation from a specified site and its return to the earth's surface, the model effectively follows a water tracer. Thus, for the remainder of this report, the extended version of the GISS GCM will be referred to as "the tracer water model".

Crucial to the development of the tracer water model was the development of a water isotopes model by Dr. Jean Jouzel of the Centre de Études Nucléaires in Paris, France. Jouzel spent a year at GISS working with Dr. Gary Russell and other GISS personnel on the global modeling of the stable water isotopes HDO and H₂¹⁸O. They extended the GCM to

monitor water isotope transport, accounting for all physical differences between the water isotopes and normal water. Their simulated global distributions of isotope concentration in precipitation roughly agree with observed distributions (Jouzel et al, 1987; see also Section 3.4 below). The tracer water model described in the present report is essentially an extension of the Jouzel water isotopes model. The water isotopes model provided the basic formulations used in the tracer water model for transporting the tagged water mass, or tracer water, between GCM grid boxes.

Chapter 2 will describe the structure of the tracer water model, and Chapter 3 will evaluate its performance indirectly by comparing model output with certain observable water transport features in nature. Chapter 4 will present further applications of the tracer water model. As will be seen, these applications are not limited to following evaporated water masses through the atmosphere. The extensions to the water isotopes model that produced the tracer water model also allow the analysis of certain important problems in isotope geochemistry.

1.4 Fractional Wetting of Grid Square Areas

1.4.1 Definition of Problem

Some very important water transport processes occur at subgrid scale, inhibiting the proper formulation of a GCM's hydrological cycle. For example, evaporation from the earth's surface in the real world is partly controlled by conditions in the atmosphere's laminar sublayer, and the

height of this surface layer is well below the standard vertical resolution of GCMs. Since an adequate increase in model resolution is usually computationally prohibitive, it is necessary to parameterize the various subgrid-scale processes. That is, it is necessary to develop simplified formulations based on the known average conditions within a grid box that produce within the box the desired average effects of the subgrid processes.

An important, perhaps crucial subgrid variability that is largely ignored in GCMs involves the wetting of soil surfaces during precipitation events. A moist convective storm in nature might span 10^4 km² or less, (e.g., Houze and Betts, 1981), an area much smaller than that of even a fine ($2^\circ \times 2.5^\circ$) GCM grid square. The soil area wetted by such a storm should therefore be only a fraction of a grid square's area. Even large-scale storms could cause fractional wetting; Eagleson and Wang (1985) employ geometric arguments to show that the expected value of the area of intersection of a circular storm and a circular region of the same size is approximately 1/4 the area of the region.

Most GCMs, however, assume that when a precipitation event occurs over a grid square, the rainwater is distributed uniformly over the entire square. Thus, for example, a rainfall event that would realistically cover 1/10 of a grid square with a storm depth of 5 cm would, in such a GCM, cover the entire grid square with a storm depth of 0.5 cm. Not accounting for the fractional wetting of grid squares might adversely affect the GCM's ability to produce a realistic hydrological cycle. As noted by Sellers et al (1986), the difference in precipitation depth

can have an important effect on computed values of surface runoff; the 5 cm storm depth might produce a greater amount of runoff than the 0.5 cm storm depth, since the former can more easily saturate a local surface moisture reservoir. Also, variations in soil moisture within the grid square, not possible with the assumed uniform wetting, can have a significant effect on the average evaporation rate for the square, especially when the evaporation is nonlinearly related to the local soil saturation.

If the fractional wetting of grid squares was suddenly imposed in a GCM, the following changes might occur. Runoff might initially increase, especially if precipitation generated in consecutive time steps was assumed to be part of the same storm system and thus was assigned to fall on the same land fraction. An increase in runoff would lead to a decrease in soil water infiltration and thus to a decrease in average soil moisture content. This could in turn lead to a decrease in evaporation and possibly to a decrease in subsequent precipitation.

It is well documented that changes in soil moisture and surface evaporation characteristics have important effects on GCM climate. Studies include those of Walker and Rowntree (1977) with a tropical model from the United Kingdom meteorological office, Shukla and Mintz (1982) with the GLAS GCM, Sud and Fennessy (1984) with the GLAS GCM, Rind (1982) with the NASA/GISS GCM, and Yeh et al (1984) with the GFDL GCM. Most of the studies indicate that a local reduction in soil moisture or surface evaporation in a GCM can lead to a locally drier GCM climate, i.e., a climate with reduced precipitation. Sud and Fennessy's analysis

indicates the opposite trend; they note, however, that their soil moisture anomalies were small enough to allow changes in moisture convergence to play an important role. Yeh et al (1984) explain that an increased evaporation rate in a given area can affect the entire general circulation by modifying the thermal state of the atmosphere. The increased evaporation rate can both cool the atmosphere near the surface, through a decrease in surface sensible heat flux and longwave radiation, and heat the middle troposphere, through an increase in latent heat release from enhanced precipitation.

The extent to which the absence of a realistic fractional wetting parameterization in a GCM affects the inherent GCM climate is largely unexplored. If the effect is large, realism dictates that fractional wetting be incorporated into future versions of GCMs. Unfortunately, the best way to achieve this is also not clear.

1.4.2 Proposed Analysis

The present report will attempt to quantify the changes induced in a GCM's climate when fractional wetting is imposed. It will also seek a reasonable fractional wetting parameterization.

In principle, the effects of wetting only a portion of a GCM grid square could be examined by directly incorporating fractional wetting into the GCM's surface and subsurface hydrology parameterizations. Precipitation forming above a land grid square, for example, could be assigned to fall onto only one of several divisions of the square, each division having its own computed moisture and temperature state. Thus, with this

change, the GCM's horizontal resolution would be increased for the ground hydrology but not for the atmospheric processes.

Unfortunately, computer computation constraints greatly restrict the number of such sensitivity tests that could be performed. Any GCM sensitivity run testing a new ground hydrology parameterization requires at least a full simulation year, due to the interdependence of seasonal climates; summer precipitation and surface temperatures in a given land region, for example, are strongly dependent on the moisture state of the soil in the previous spring, and this moisture state must also be consistent with the new hydrology. Furthermore, increasing the number of surface soil reservoirs would lead to a corresponding increase in the number of ground hydrology computations performed at every time step.

The effects of fractional wetting could also be studied (albeit approximately) with an offline model of the GCM soil hydrology. Hourly precipitation and potential evaporation fluxes over some land surface could be stored during a GCM simulation, and the time series of fluxes could be applied later in the offline model to force hourly values of runoff, evaporation, and soil moisture storage. Running the offline model with and without fractional surface wetting might indicate the importance of incorporating this feature into the GCM. In the GCM, however, a change in the formulation of surface hydrology could also affect future precipitation and potential evaporation fluxes. An offline soil hydrology model cannot account for these feedbacks.

A one-dimensional soil-atmosphere model is chosen for the present study. This model lies somewhere between a modified GCM and an offline

soil hydrology model. The one-dimensional model is constructed to simulate the workings of the three-dimensional GISS GCM; it uses, however, far less computer storage and time. Feedbacks between the soil hydrology and the state of the overlying atmosphere can be determined with the one-dimensional model. The model can serve not only to examine the effects of fractional wetting, but also as the basis for an unlimited number of other sensitivity studies.

One-dimensional radiative-convective models have, in fact, been used in other climate modeling studies. Ramanathan (1981), for example, studied energy transfers at the ocean surface with a one-dimensional model designed to mimic a GCM.

Chapter 5 describes in detail the structure of the present report's one-dimensional model. The model is then tested to evaluate its applicability to GCM climate sensitivity studies. The climates inherent in the one-dimensional model and in the GISS GCM are found to experience roughly the same changes when a particular change is made in their surface runoff parameterizations.

Simulations are then performed in which the one-dimensional model's ground surface area is partitioned into a number of sections. Precipitation formed during a time step falls onto only one surface section, chosen randomly. All surface processes, including evaporation, sensible heat flux, and soil water diffusion, are calculated separately for each section, and thus the model's ground surface maintains spatially inhomogeneous distributions of moisture and temperature.

The number of surface divisions varies among the simulations in order to demonstrate how wetted fraction size affects the average model climate. Simulated climates are compared by comparing the generated annual means and seasonal variations of average precipitation, evaporation, surface runoff, surface temperature, and soil saturation. Since the water vapor convergence above the surface is assigned, annual mean runoffs do not vary.

Dividing the land surface into sections effectively increases the horizontal resolution for hydrological computation and thus avoids any subgrid parameterization problems. This method, however, is too computationally demanding for general use in GCMs. Chapter 5 therefore also presents a simple subgrid parameterization for fractional wetting. The parameterization is examined with the one-dimensional model; the sensitivity of the model's climate to storm size under the simple parameterization, for example, is compared to the sensitivity observed when the land surface is divided into sections.

Chapter 5 concludes with a discussion of the proper interpretation of the one-dimensional model results. Again, Chapter 5 contains the wetted fraction analysis presented in this report in its entirety. It is thus quite distinct from Chapters 2, 3, and 4, which discuss the tracer water model.

Chapter 2

Description of the Tracer Water Model

2.1 General Background

The framework for the tracer water model is the Model II version of the NASA/GISS GCM. A report by Hansen et al (1983) describes in detail the structure of this GCM and includes a critical comparison of model-generated climate patterns with observations.

A GCM's individuality is inherent in its discretization of the fundamental conservation and state equations, its application of initial and boundary conditions, and its parameterizations of the various atmospheric and surface processes affecting the general circulation. The individuality of the GISS GCM is in turn reflected in its grid resolution requirements. While most GCMs require a fine horizontal grid resolution (e.g., $4^\circ \times 5^\circ$), the GISS GCM was specifically (and successfully) designed to simulate the major global climate patterns observed in nature with a coarser grid, such as the $8^\circ \times 10^\circ$ horizontal grid shown in Figure 2-1. Researchers using the GISS GCM will often use this grid for preliminary simulations and a finer grid for their final simulations. Since adding tracers to Model II greatly increased the computational and storage requirements for a simulation, the simulations in the present work generally use the $8^\circ \times 10^\circ$ grid.

As for the prescribed vertical resolution in the simulations, the atmospheric column above each grid square is separated into nine vertically stacked boxes using a sigma coordinate system, meaning that each box

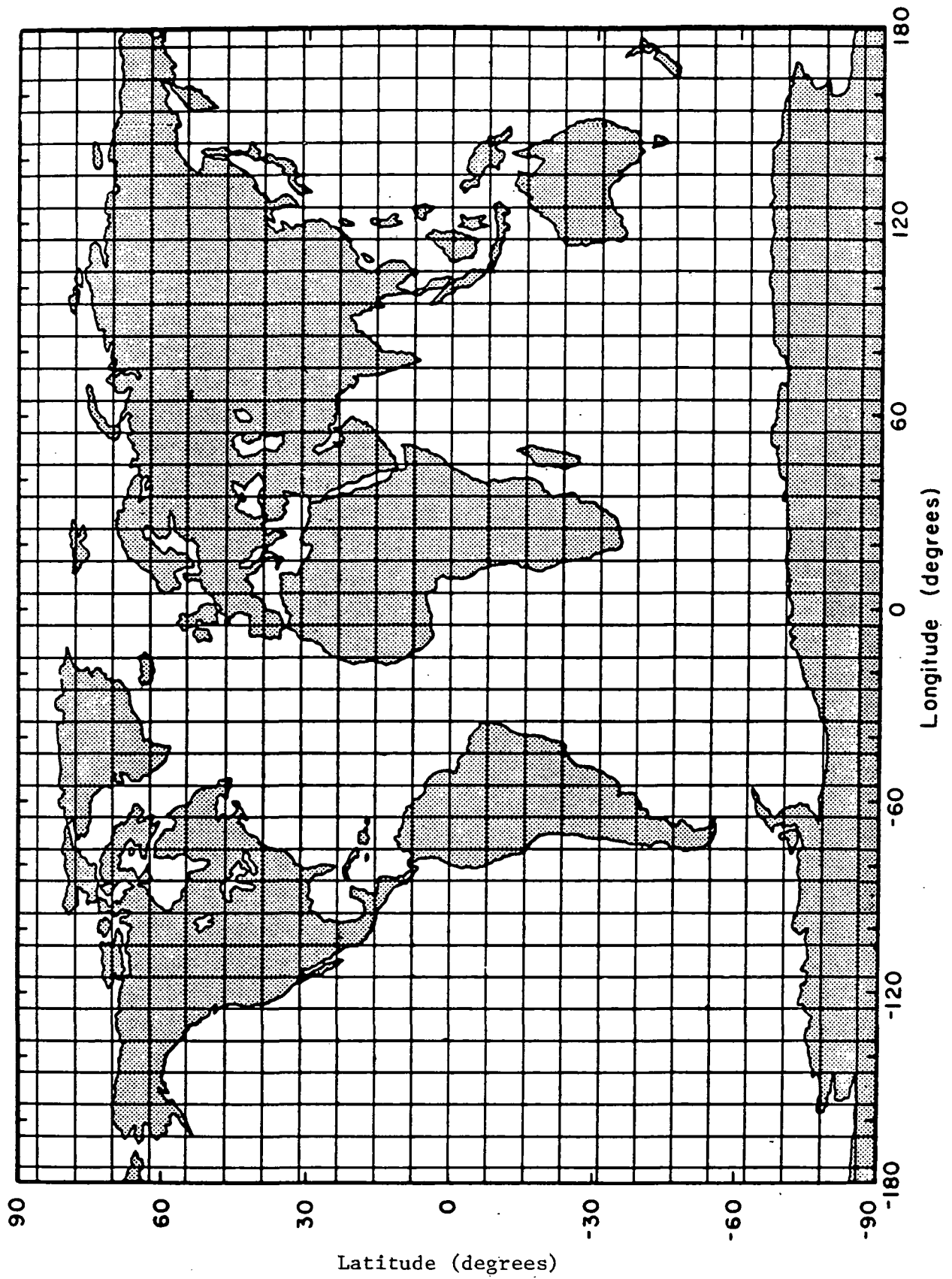


Figure 2-1 8° x 10° horizontal grid used in the GISS GCM.

ORIGINAL PAGE IS
OF POOR QUALITY

in the column contains a pre-assigned fraction of the column air mass below 10 mb. Since the column air mass varies with time, so does the air mass in each box. The vertical grid box spacing for a surface pressure of 984 mb is described in Table 2-1. The top two layers represent the stratosphere, the bottom two represent the boundary layer, and the levels between represent the troposphere.

A very brief sketch of the types of processes modeled in the GISS GCM is provided in Figure 2-2. Moist convection or large-scale condensation events condense water vapor at various atmospheric levels and thereby produce precipitation at the earth's surface. Convection also mixes the heat and momentum in the atmospheric column. Up to four different surface types can exist in a grid square, namely ocean, ocean ice, permanent land ice, and land. Runoff is calculated and surface water storage, including snow cover, is updated when precipitation falls on the three latter types. On land, the surface water can diffuse into a second soil layer, and the second soil layer contributes to evaporation during the growing season. Evaporation and sensible heat fluxes at the earth's surface are calculated over each surface type, and an energy balance computes the new surface temperature on ocean ice, land ice, and land. The ocean surface temperature and the fraction of ocean covered by ice remain at assigned climatic mean values that are revised daily. The entire model is driven by the incoming diurnal radiation, with time-varying surface and cloud albedos, modeled water vapor, and prescribed trace gases affecting the distributions of radiative heating and cooling in the atmosphere.

Table 2-1. Vertical resolution used in the GISS GCM,
given a surface pressure of 984 mb.

<u>Atmospheric layer</u>	<u>Mean pressure (mb)</u>	<u>Pressure difference between top and bottom of layer (mb)</u>
9	27	60
8	103	80
7	201	105
6	321	135
5	468	160
4	634	170
3	786	134
2	894	80
1	959	50

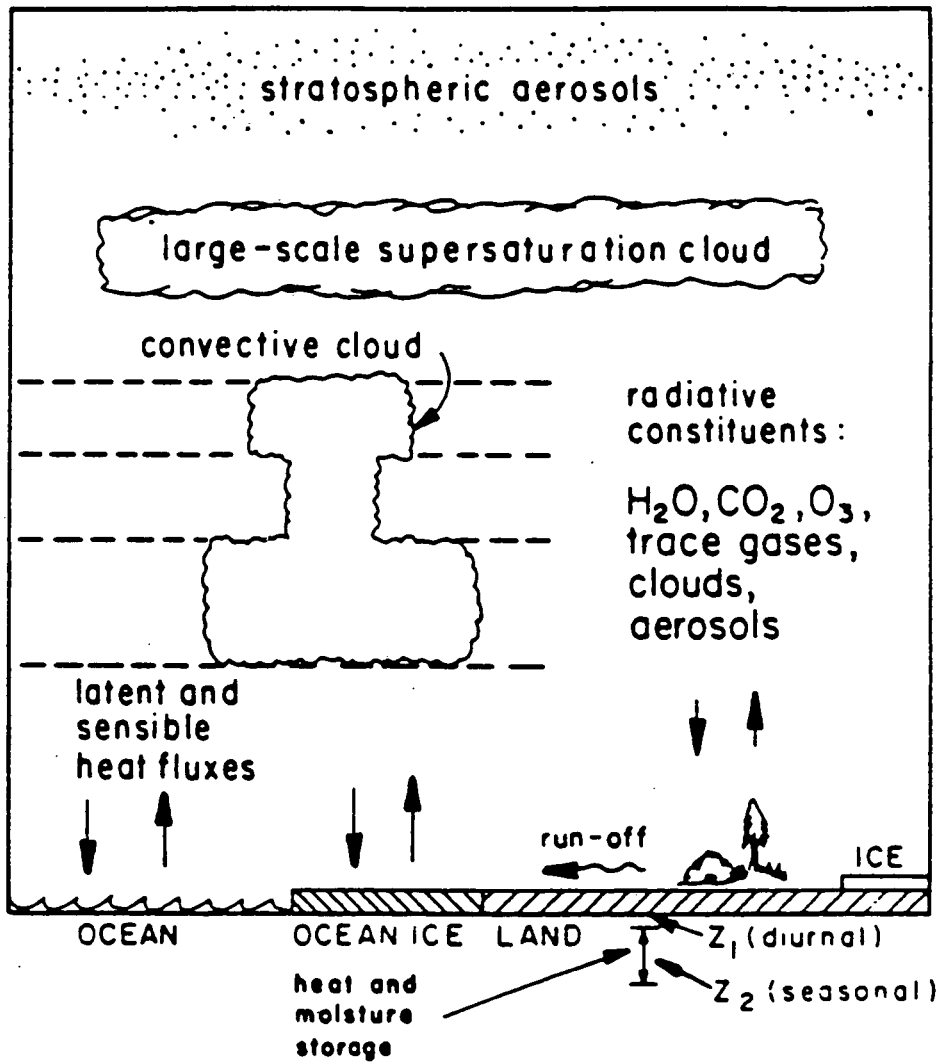


Figure 2-2 Schematic of processes occurring above and below a single GISS GCM grid square (From Hansen et al, 1983).

Again, the reader is referred to the report of Hansen et al (1983) for a complete treatment of the GISS GCM's structure. The model's structure and behavior is described further by Hansen et al (1984) and Rind (1984). Two minor changes in the GCM were implemented before creating the tracer water model; first, a limitation on the outward advection of water vapor from a grid box was imposed to insure a positive vapor content in the box at all times (see Section 2.3.1), and second, the snow albedo over land ice surfaces was assumed to remain constant at 0.85 to produce more accurate summer polar temperatures (Jouzel et al, 1987).

2.2 Isotopic Forms of Water

Since the tracers followed can represent water isotopes, a brief discussion of the special transport properties of water isotopes is provided first.

2.2.1 Isotopic Fractionation

The three major isotopic forms of water found in nature are HDO, $H_2^{18}O$, and HTO, the chemical symbols D and T representing the hydrogen isotopes deuterium and tritium, respectively. The water isotopes have the same chemical properties as normal water but have slightly different physical properties, due to their higher mass. The two physical properties affecting water isotope transport are vapor pressure and molecular diffusivity.

Consider a closed system, with a liquid water quantity Q_l in equilibrium with a water vapor quantity Q_v . If a trace amount of water

isotope enters the system, it eventually partitions itself between the liquid and vapor compartments. The water isotope has a lower vapor pressure than normal water, and thus the equilibrium partitioning of the water isotope relatively favors the condensed state. More quantitatively, if R_l is the final amount of water isotope in liquid form and R_v is the final amount in vapor form, then the following relationship holds:

$$\frac{R_l}{Q_l} = \alpha_{l/v} \cdot \frac{R_v}{Q_v} \quad (2-1)$$

where $\alpha_{l/v}$ is slightly larger than 1. The favoring of the condensed state is known as isotopic fractionation, and $\alpha_{l/v}$ is called an equilibrium fractionation factor.

In the tracer water model, the value of $\alpha_{l/v}$ is computed as a function of the temperature (Majoube, 1971a; Craig and Lal, unpublished manuscript):

$$\begin{aligned} \text{HDO: } \alpha_{l/v} &= \exp(24844/T^2 - 76.248/T + 0.052612) \\ \text{H}_2^{18}\text{O: } \alpha_{l/v} &= \exp(1137/T^2 - 0.4156/T - 0.0020667) \\ \text{HTO: } \alpha_{l/v} &= \exp(46480/T^2 - 103.87/T) \end{aligned} \quad (2-2)$$

For example, $\alpha_{l/v}$ at $T=283^\circ\text{K}$ (10°C) is 1.10 for HDO. In the temperature range of interest, $\alpha_{l/v}$ decreases with increasing temperature and, for HDO and H_2^{18}O , remains between 1.0 and 1.2. The fractionation factor

for the solid/vapor phase change is defined similarly and is also computed as a function of the temperature (Merlivat and Nief, 1967; Majoube, 1971b; Craig and Lal, unpublished manuscript):

$$\begin{aligned} \text{HDO: } \alpha_{S/V} &= \exp(16288/T^2 - 0.0934) \\ \text{H}_2^{18}\text{O: } \alpha_{S/V} &= \exp(11.839/T - 0.028224) \\ \text{HTO: } \alpha_{S/V} &= \exp(46480/T^2 - 103.87/T) \end{aligned} \quad (2-3)$$

These fractionation factors are used in the determination of water isotope condensate during precipitation events.

The molecular diffusivities of water isotopes are smaller than that of normal water, by the following factors:

$$\begin{aligned} \text{HDO: } D_{\text{isotope}}/D_{\text{water}} &= 0.9755 \\ \text{H}_2^{18}\text{O: } D_{\text{isotope}}/D_{\text{water}} &= 0.9723 \\ \text{HTO: } D_{\text{isotope}}/D_{\text{water}} &= 0.968 \end{aligned}$$

Merlivat (1978) provided the diffusivities for HDO and H_2^{18}O ; the value for HTO was inferred from the same data set. The differences in the diffusivities are important when modeling kinetic fractionation, under which the water isotope partitions itself between phases in a non-equilibrium manner due to kinetic effects. (Equilibrium fractionation assumes that the isotope has sufficient time to arrive at the equilibrium partitioning; for some processes, this is not a good assumption.) For example, supersaturated vapor over ice induces kinetic fractionation during the

formation of solid condensate in precipitation events. The effective fractionation factor α_{eff} is calculated as a function of the equilibrium fractionation factor, the supersaturation S , and the diffusivity ratio (Jouzel and Merlivat, 1984):

$$\alpha_{\text{eff}} = \alpha_{\text{s/v}} \cdot \left\{ \frac{S}{1 + \alpha_{\text{s/v}}(S-1) \frac{D_{\text{isotope}}}{D_{\text{water}}}} \right\} \quad (2-4)$$

Kinetic effects produce a different α_{eff} when raindrops re-evaporate below the cloud base during moist convection (Stewart, 1975):

$$\alpha_{\text{eff}} = \frac{h}{\frac{h-1}{\left(\frac{D_{\text{isotope}}}{D_{\text{water}}}\right)^{0.58}} + \frac{1}{\alpha_{\text{l/v}}}} \quad (2-5)$$

where h , the average relative humidity during re-evaporation, must lie between the initial relative humidity h_1 and 1. Preliminary sensitivity runs found an appropriate estimator for h :

$$h = 0.75 + 0.25h_1 \quad (2-6)$$

The effective fractionation factors will be referred to later.

The molecular diffusivities of the water isotopes also affect their relative rates of evaporation from the ocean surface. Upward and downward

movements of water isotope molecules at the ocean surface are slowed down by a factor $1-k$, where

$$\begin{aligned}
 \text{HDO:} \quad k &= \begin{cases} .00528 & W_s < 7 \\ .0002508 W_s + .0007216 & W_s \geq 7 \end{cases} \\
 \text{H}_2^{18}\text{O:} \quad k &= \begin{cases} .006 & W_s < 7 \\ .000285 W_s + .00082 & W_s \geq 7 \end{cases} \quad (2-7) \\
 \text{HTO:} \quad k &= \begin{cases} .01056 & W_s < 7 \\ .0005016 W_s + .0014432 & W_s \geq 7 \end{cases}
 \end{aligned}$$

The derivations of the HDO and H_2^{18}O formulas for k were described by Jouzel et al (1987); the HTO formula for k is essentially an extrapolation of the HDO formula. W_s represents the wind speed in m/sec.

A non-isotopic water tracer always partitions itself between phases at the same ratio as does the model water. That is, the diffusivity ratio and all fractionation factors are set to unity for a non-isotopic water tracer. The transport properties of isotopic and non-isotopic tracers are identical for all processes not involving a change in water phase.

2.2.2 Units

An HDO or H_2^{18}O concentration in water is usually expressed in the literature as a deviation δ of the isotope/water ratio from the

reference ratio in SMOW, or Standard Mean Ocean Water (Craig, 1961, as cited by Dansgaard, 1964). Thus,

$$\delta D = \frac{\frac{x_D}{x_H} - 155.76 \times 10^{-6}}{155.76 \times 10^{-6}} \times 1000\%.$$

(2-8)

$$\delta^{18}O = \frac{\frac{x_{18}O}{x_{16}O} - 2005.2 \times 10^{-6}}{2005.2 \times 10^{-6}} \times 1000\%.$$

where x_H , x_D , $x_{16}O$ and $x_{18}O$ are the mole fractions of H, D, ^{16}O and ^{18}O atoms, respectively, present in a sample. The relative deviations δD and $\delta^{18}O$ are expressed in permil (‰) units; the permil is analogous to a percent, being based on a scale of 1000 rather than 100.

HTO amounts are generally expressed in terms of tritium units, or TU. One TU is equivalent to a concentration of one tritium atom per 10^{18} hydrogen atoms.

2.3 The Structure of the Tracer Water Model

The tracer water model is initialized with any atmospheric and surface reservoir tracer distribution, and during the course of a GCM simulation, the transport processes discussed below act on this distribu-

tion and modify it. A simulation of sufficient duration will determine the average tracer transport characteristics for the model climate.

To create the tracer water model, every process that moves model water in the GCM was extended to move tracer water as well. Suppose R represents the tracer content of a given atmospheric grid box. An equation for the change in R during some time interval can be written as

$$\Delta R = \Delta R_{adv} + \Delta R_{mc} + \Delta R_{lsc} + \Delta R_{dc} + \Delta R_{ev} \quad (2-9)$$

where ΔR_{adv} represents the change due to advective transport, ΔR_{mc} is the tracer added to the box during moist convection, ΔR_{lsc} is the tracer added during a large-scale non-convective storm, ΔR_{dc} is the change due to a dry convective overturning of air, and ΔR_{ev} is the change due to evaporation or condensation of tracer at the earth's surface. (ΔR_{ev} is thus nonzero only for first layer boxes.) Advective tracer transports and tracer evaporation are calculated every half hour, moist and dry convective transports of tracer are calculated every hour, and tracer transports by large-scale storms are calculated every five hours.

Regardless of its abundance, a tracer does not influence the thermodynamics, the water motion or any other aspect of a model simulation. All of the tracer transport formulations are completely linear; for example, a twofold increase in the initial tracer distribution would lead to the same increase in all future tracer diagnostics.

The discussion of each transport process below is divided into two parts, the first pertaining to model water transport only and the second describing the formulations added for tracer water transport.

2.3.1 Advection

a. Water Advection. Water is advected between grid boxes via the model winds. The model first determines the air mass flux between two adjacent grid boxes and then multiplies it by a specific humidity to determine the water vapor flux. This specific humidity is the arithmetic mean specific humidity of the two boxes when they are horizontally adjacent, and because of the exponential falloff of water vapor content with height, it is the harmonic mean specific humidity when the boxes are vertically adjacent. A positive final water vapor content is insured for each box by constraining the fraction of water that can exit through a given side of the box. The greatest vapor divergence allowed in a time step would still leave 0.1% of the original vapor behind.

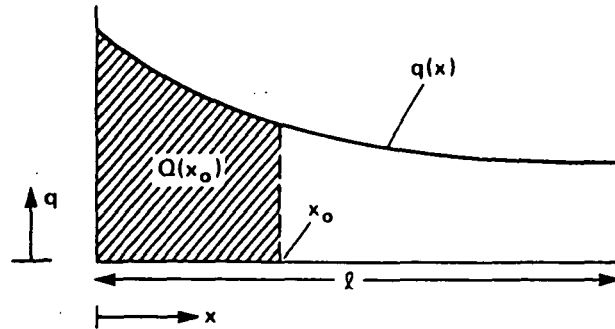
b. Tracer Advection. Tracer advection between adjacent grid boxes is determined directly from the calculated water vapor flux and an estimate of the amount of tracer in that water. A "slopes scheme" (Russell and Lerner, 1981) is applied to the tracer concentration in water to produce the desired estimate. With the slopes scheme, the average gradient of tracer concentration inside every grid box is updated and stored after every atmospheric process. The slopes scheme therefore provides valuable information on the subgrid distribution of the tracer.

The tracer concentration gradients stored with the slopes scheme are defined with respect to water vapor content and not to a distance; when moving in a given direction inside a single grid box, the assumed tracer/water ratio increases by a constant amount as a unit amount of water vapor is passed. The idea is to relate the tracer flux out the side of a box directly to the water vapor flux rather than to the air mass flux, thereby producing smoother global distributions of tracer/water ratios (Jouzel et al, 1987).

Figure 2-3 illustrates this and the tracer transport calculation in one dimension. First, Figure 2-3a shows the distribution of water vapor specific humidity along the length of the box. Although a non-uniform distribution is never computed during a GCM simulation, it is nevertheless implicitly assumed in the water vapor advection calculation, which employs an assigned mean specific humidity between grid boxes (see above). In moving a distance x_0 from the left side of the box, a certain mass of water vapor $Q(x_0)$ is passed, equal to the area of the shaded region in Figure 2-3a.

$Q(x)$ is naturally a monotonically increasing function of x , and it is used as the horizontal coordinate in Figure 2-3b. Note that points on the left side of the axis represent the water vapor residing on the left side of the box and that any two segments of equal length on the axis represent the same water vapor mass. The tracer/water ratio is plotted in the vertical as a function of this transformed distance coordinate, effectively a one-dimensional water vapor coordinate. The ratio varies linearly with the water vapor.

a.



b.

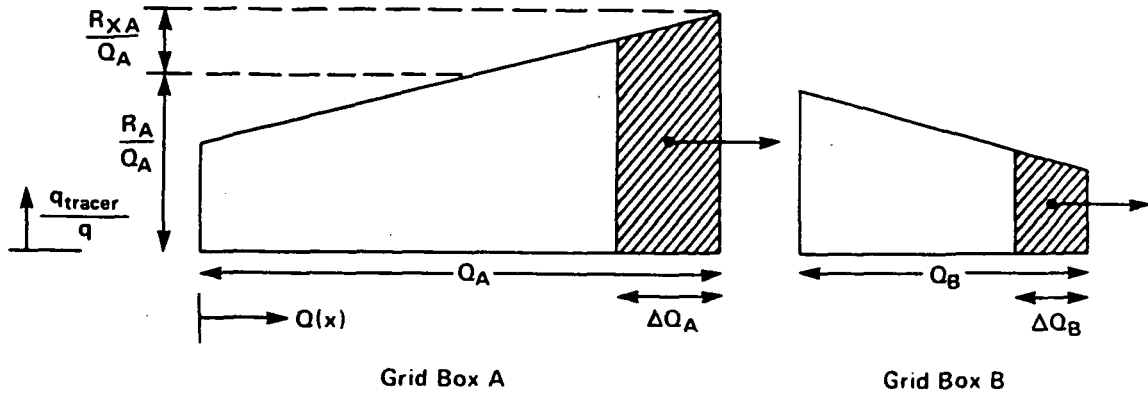
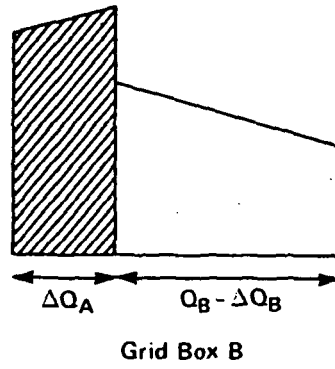


Figure 2-3

Slopes scheme calculation of tracer advection.
 a) Spatial distribution of water vapor in grid box. b) Distribution (with respect to water vapor) of tracer concentration in adjacent grid boxes A and B before advection. c) Distribution of tracer concentration in Grid Box B after advection. d) Newly defined distribution of tracer concentration in Grid Box B.

c.



d.

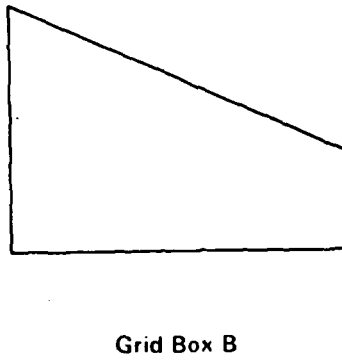


Figure 2-3 (cont.)

Grid Box A contains a total water content Q_A and a tracer content R_A , so the tracer/water ratio at the midpoint of the horizontal axis in Figure 2-3b is R_A/Q_A . Suppose the tracer/water ratio at the far right of the box is $(R_A+R_{XA})/Q_A$. If a water amount ΔQ_A leaves through the right side of the box, the area of the shaded region indicates the amount of tracer ΔR_A that also leaves:

$$\Delta R_A = \frac{\Delta Q_A}{Q_A} \left(R_A + \left(1 - \frac{\Delta Q_A}{Q_A} \right) R_{XA} \right) \quad (2-10)$$

Figure 2-3c shows the results of the transfer. Grid Box B obtained some water vapor and tracer from Grid Box A but also lost some through the other side. The resulting distribution of tracer concentration within Grid Box B is redefined to be that shown in Figure 2-3d. In going to this new distribution, the tracer in Grid Box B retains its total mass but is given a new slope, calculated so that the resulting linear distribution is a least-squares approximation to the discontinuous distribution in Figure 2-3c.

There is one major problem with the slopes scheme formulation for tracer advection. Under conditions of large internal tracer gradients, the scheme can advect a tracer out of a grid box so as to leave behind a negative tracer content in the box. Subsequent tracer precipitation and vapor exchange calculations can conceivably deposit negative tracer amounts onto the earth's surface.

Negative tracer quantities are certainly not realistic and would be quite disturbing if not viewed in the proper perspective. A field of tracer concentrations in nature must consist entirely of non-negative concentrations; the tracer water model merely approximates it with a field that is unconstrained by the non-negativity requirement. Individual values, such as any negative values, in the approximate field are far less important than the field quantities integrated over time and space.

The forced prevention of negative tracer contents would also lead to problems. Simply zeroing the negative values would violate conservation of tracer mass in the atmosphere. Limiting the gradients in the slopes scheme formulation would artificially increase tracer diffusion. Eventually a tracer advection formulation without these problems will be developed; until then, negative tracer contents are allowed to occur:

The negative tracer contents produced by the model are never very large under steady-state conditions, and steady-state tracer distributions are of the greatest interest. The negative contents are most pronounced at the beginning of a simulation, due to the large gradients of tracer concentration between grid boxes near a tracer source. Further advection, precipitation, surface condensation, and oceanic vapor exchange act to reduce the magnitude of negative tracer concentrations as the atmospheric tracer distribution moves toward steady state. In a spatial distribution of monthly steady-state tracer precipitations, negative tracer precipitation will typically account for less than 2% of the total tracer precipitation mass.

Isotopic fractionation effects need not be considered in computing tracer advection, since the process involves no changes in phase. Tracer concentration slopes are modified during the moist convection, large-scale condensation, and dry convection processes described below.

2.3.2 Moist Convective Precipitation

a. Moist Convective Precipitation of Water. A moist convective event in the model is characterized by an air mass rising moist-adiabatically through an unstable region of the model's atmosphere, condensing moisture along the way. The condensed moisture can partially or completely re-evaporate in lower levels before reaching the surface.

Moist convection is a subgrid-scale process; events in nature might cover 10^4 km² or less (e.g., Houze and Betts, 1981), whereas a typical coarse grid square spans on the order of 10^6 km². Since a GCM provides only mean values of prognostic quantities for each grid box, and since a subgrid-scale process by definition must reflect subgrid variations in these quantities, moist convection cannot be modeled directly in a GCM. Modelers are forced instead to parameterize moist convection. A brief description of the moist convection algorithm used in the GISS GCM demonstrates the oversimplification and arbitrariness inherent in all such parameterizations:

- 1) A fraction of a Level 1 (near surface) grid box is defined as the moist convective plume and its moist static energy is compared to that of the box immediately above it. If the plume's moist static

energy is higher, the column of grid boxes is considered moist convectively unstable, and convection proceeds.

- ii) As the plume rises into the Level 2 box, it cools moist adiabatically. The moisture that condenses is temporarily set aside.
- iii) The plume's moist static energy is then tested against that of the next higher box. If buoyant, the plume continues rising, condensing moisture as it goes. The plume stops below the first box with a higher moist static energy. Note that the plume's vapor content always decreases as it rises.
- iv) Suppose the plume is finally deposited in Level L. Subsidence then replaces the air mass that was removed from Level 1 in creating the plume. First, an air mass equal to the plume mass sinks adiabatically from Level 2 into Level 1. The same amount is then moved from Level 3 into Level 2, and so on. The box in Level L thus retains its original air mass.
- v) The condensate, which can be solid or liquid, now begins to fall. The moisture that condensed when the plume rose from Level L-1 to Level L enters the grid box at Layer L-1 and re-evaporates into a specified fraction of the box. If the fraction becomes saturated, the leftover condensate is assumed to fall through the box and is added to the moisture that condensed when the plume rose from Level L-2 to Level L-1.
- vi) This new supply of condensed moisture then re-evaporates into a fraction of the Level L-2 grid box. The process continues down through Level 1. Any condensate remaining after the Level 1 box fraction is saturated is assumed to precipitate onto the ground.

vii) The entire process is repeated, this time with a plume originating in Level 2. The determination of moist convective precipitation is complete when a plume starting from each atmospheric level is given the opportunity to convect.

The grid box fractions mentioned above are chosen arbitrarily. The plume normally consists of half the air mass in the originating grid box. The top of this grid box is defined as the cloud base; one-fourth of each grid box above the cloud base and one-half of each box below the cloud base is saturated during the re-evaporation of condensate. The smaller fraction above the cloud base reflects the fact that some of the droplets fall through the saturated environment of the plume itself.

When the lateral extent of a typical convective cloud in nature is compared to the area represented by a grid square, these fractions seem rather large. The plume as defined, however, can be thought to represent all of the plumes forming over the area during the one-hour time step. Some sensitivity studies indicate that changing the plume size in the model results in only a small change in the time-averaged precipitation, apparently because of an inverse change in the precipitation frequency. The precipitation frequency should increase as the plume size decreases because moist convective instabilities are removed less efficiently.

b. Moist Convective Precipitation of Tracer. The effective phase diagrams used in the model for water and tracer condensation are different. During moist convective events in the GISS GCM, water condenses as solid below 0°C and as liquid above, with the phase affecting only the assigned latent heat of vaporization. The tracer behaves, however, as if the water

condenses according to the phase diagram in Figure 2-4. That is, it behaves as though the water condenses as solid below -25°C , as liquid above -25°C , or as both if the moist adiabatic lifting lowers the plume's temperature through this cutoff. The supersaturation assumed over the solid phase, for use only in Equation 2-4, is calculated as

$$S = 1. - 0.003T_p \quad (2-11)$$

where T_p is the plume temperature in $^{\circ}\text{C}$. This supersaturation function produces proper isotopic behavior in Antarctic precipitation (Jouzel et al, 1987). The decision to use different effective phase diagrams for water and tracer condensation stemmed from the desire to remain consistent with the published Model II version of the GISS GCM while also providing a more realistic separation of the phases for the tracer condensation and equilibration formulations discussed below (see, e.g., Mason, 1971; Prupaccher and Klett, 1978).

If the plume contains tracer as it starts its journey up the grid box column, the tracer condenses with the model water. For non-isotopic tracers, the final tracer/water ratio in liquid droplets is forced to equal that in the remaining plume vapor. For isotopic tracers, the equality imposed during the formation of water and tracer liquid is a form of Equation 2-1:

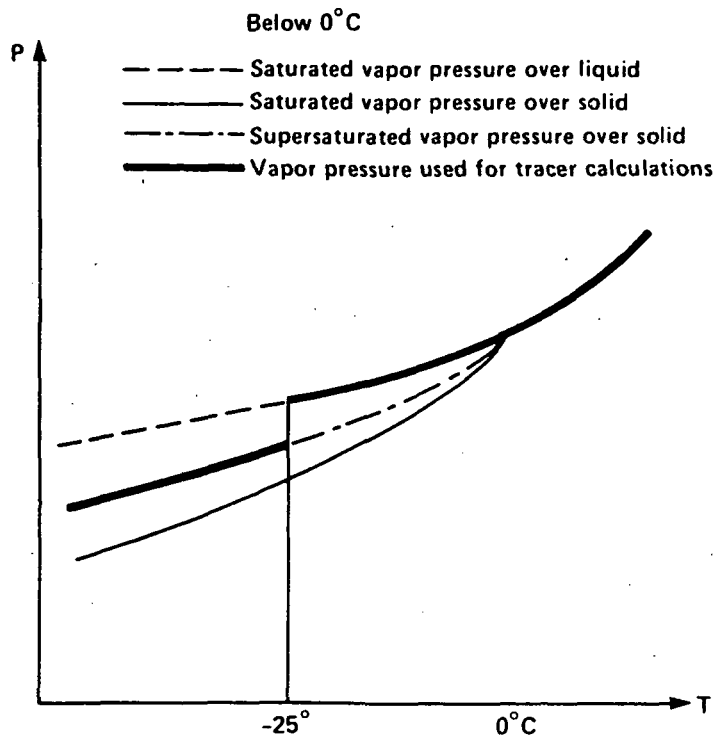


Figure 2-4 Effective phase diagram for water assumed in tracer calculations during moist convection.

$$\alpha_{\ell/v} \frac{R_{vo} - R_{\ell}}{Q_{vo} - Q_{\ell}} = \frac{R_{\ell}}{Q_{\ell}} \quad (2-12)$$

where R_{vo} is the original tracer vapor content of the plume, Q_{vo} is the original water vapor content of the plume, R_{ℓ} is the tracer liquid formed, Q_{ℓ} is the liquid water formed, and $\alpha_{\ell/v}$ is the fractionation factor defined in Section 2.2. Equation 2-12 can be rearranged to produce the equation for R_{ℓ} :

$$R_{\ell} = \frac{Q_{\ell} R_{vo}}{Q_{\ell} + \frac{Q_{vo} - Q_{\ell}}{\alpha_{\ell/v}}} \quad (2-13)$$

As liquid droplets fall into lower levels, the tracer in the droplets equilibrates with the tracer in the new surrounding vapor. Physically, equilibration corresponds to tracer vapor exchange at the droplet surface. The tracer redistributes itself between the liquid and the surrounding vapor compartments so that the tracer/water ratio in both phases is the same, or different by a factor α for isotopic tracers. (For isotopic tracers, the fractionation factor used is $\alpha_{\ell/v}$ from Equation 2-2 above the cloud base and α_{eff} from Equation 2-5 below the cloud base.) Thus, a net flux of tracer out of the droplet is possible even when there is no net re-evaporation of water condensate. Similarly, tracer-free droplets falling through grid boxes laden with tracer vapor will absorb tracer before falling further.

Equilibration should probably be incomplete for the characteristically large droplets associated with moist convective events, due to the limited time the droplets could spend in a grid box. Federer et al (1982), for example, demonstrated with a convective cloud model the large isotopic relaxation times of raindrops in moist convective events. The assigned extent of equilibration in the tracer water model is chosen arbitrarily. Normally, as water droplets containing tracer fall into a new grid box, half of the water remaining after re-evaporation, along with the tracer it contains, does not participate in the equilibration process. The other half equilibrates completely. Fortunately, the results of a sensitivity study, not presented here, indicate that the model results are quite insensitive to the chosen extent of equilibration.

Due to the negligible diffusivity of tracer in the solid phase, equilibration of existing solid tracer condensate with surrounding vapor is not allowed in the model. The negligible diffusivity also affects, for isotopic tracers, the initial formation of solid tracer condensate; due to isotopic fractionation, the tracer/water ratio in the vapor forming the condensate is larger at the beginning of the condensation process than at the end. The model uses an integrated expression for Rayleigh condensation to account for this, using the effective fractionation factor defined in Equation 2-4:

$$R_s = R_{vo} \left(1 - \left(1 - \frac{Q_s}{Q_{vo}} \right)^{\alpha_{eff}} \right) \quad (2-14)$$

where R_s and Q_s are the solid tracer and water quantities formed, respectively. Equilibration may proceed if the solid condensate melts.

2.3.3 Large-scale Condensation

a. Large-scale Condensation of Water. The other precipitation process modeled in the GCM is large-scale condensation, corresponding to the large, non-convective storm fronts found in nature. Essentially, the process simply condenses grid box water so as to keep all relative humidities in the model atmosphere at or below 100%. Large-scale condensation in the model produces a relatively small fraction of the total global precipitation.

A straightforward algorithm determines the non-convective precipitation from a given column of grid boxes. First, the water vapor content in the topmost (Level 9) box is compared to the saturation content at the grid box temperature. If the box is supersaturated, condensate forms until the box reaches saturation, and the condensate falls into Level 8. If the Level 8 box is saturated or supersaturated, the condensate falls through it into Level 7. If the box is subsaturated, the condensate re-evaporates, and if the re-evaporation saturates the box, any leftover condensate falls into Level 7. Also, new condensate forms and falls into Level 7 if the Level 8 box is supersaturated. The process continues downward through each box of the column. Any condensate leaving the Level 1 box is added to the earth's surface as precipitation.

b. Large-scale Condensation of Tracer. During non-convective precipitation events, the tracer behaves as if water vapor condenses as solid below -10°C and as liquid above -10°C (Mason, 1971; Prupaccher and Klett, 1978). The tracer condenses so that the tracer/water ratio in the condensate is the same as that in the remaining grid box vapor (or different by a factor α , for isotopic tracers). As in moist convective events, falling liquid condensate equilibrates with surrounding vapor; in contrast to moist convective events, however, this equilibration is complete, due to the characteristically smaller droplet sizes. Solid condensate may not equilibrate with surrounding vapor until it melts.

2.3.4 Dry Convection

a. Dry Convection of Water. A set of vertically adjacent grid boxes will experience dry convection, or a complete overturning of air mass, if the boxes are thermally unstable with respect to each other. Dry convection thoroughly mixes the heat, momentum and moisture of the boxes without producing precipitation. As a result, each box involved in the dry convection process will obtain the same specific humidity of water.

b. Dry Convection of Tracer. Tracer is also thoroughly mixed among the boxes involved in dry convection. The tracer is redistributed so as to produce the same tracer/water ratio in each box while conserving tracer mass. Isotopic fractionation plays no role, since the process involves no changes in phase.

2.3.5 Surface Evaporation and Condensation

a. Evaporation/Condensation of Water. On the average, for every drop of water the atmosphere loses through precipitation, an equivalent amount of water must evaporate from the earth's surface. The GCM, however, must determine the proper spatial and temporal distributions for the evaporation rates. This is difficult; determining the proper evaporation rate from a grid square requires knowledge of near-surface humidity conditions and therefore of the vertical humidity distribution within the overlying Level 1 grid box, and this information is simply not available. The model therefore uses a parameterization of the surface boundary layer to produce an approximate evaporation rate, the surface boundary layer being a portion of the Level 1 grid box lying just above the earth's surface.

The model computes the evaporation E from a grid square as

$$E = \beta \cdot \rho \cdot W_S \cdot C_q \cdot (q_G - q_S) \quad (2-15)$$

where q_G is the saturation specific humidity at the surface temperature, q_S is the specific humidity at the top of the surface boundary layer, β is an efficiency factor, ρ is the air density, W_S is the surface wind speed, and C_q is a humidity transfer coefficient whose value is a function of the roughness length and the Richardson number in the surface layer. As will be shown in a later chapter, changing the value of C_q has little effect on the time-averaged evaporation, since the change

induces an inverse change in the specific humidity deficit. The parameter β acts to reduce the actual evaporation rate from subsaturated soils to below the potential rate; β therefore reflects soil resistance to water movement. For subsaturated soils, β is set to the soil saturation (i.e., the water content divided by the water holding capacity) of the first soil layer. Since ocean, ocean ice, land ice, and snow surfaces are assumed to evaporate at the potential rate, β is set to 1 over these surfaces.

The subgrid parameterization of the surface boundary layer produces the value of q_s . By assuming that the net vapor flux from the ground into the surface layer is exactly equal to the net flux from the surface layer into the remainder of the Level 1 grid box, a value of q_s is determined that is effectively a weighted average of q_G and q_1 , the average specific humidity in the Level 1 grid box:

$$q_s = \frac{C_w q_s \cdot q_G + \frac{K}{z_1 - z_s} \cdot q_1}{C_w q_s + \frac{K}{z_1 - z_s}} \quad (2-16)$$

where K is an empirical eddy diffusion coefficient, z_1 is the height of the first layer, and z_s is the height of the parameterized surface layer. Notice that if q_s is greater than q_G , Equation 2-15 predicts a negative evaporation, or condensation, onto the earth's surface.

b. Evaporation/Condensation of Tracer. For time steps when water condenses onto an ocean ice, land ice, or land surface, the tracer condenses

with the water so that the tracer/water ratio in the condensate is the same as that in the Level 1 grid box (or is greater by a factor α , for isotopic tracers.) When water evaporates from these non-ocean surfaces, tracer may or may not evaporate, depending on whether the tracer is defined as "surface-conserved" or "aboveground". These definitions and the tracer evaporation formulation are discussed in Section 2.4.

Tracer evaporation or condensation over the ocean is more accurately termed tracer vapor exchange. Water vapor molecules in the surface layer can strike the ocean surface and remain in the ocean as liquid water, and liquid water molecules at the ocean surface can break away and enter the surface layer as water vapor. The difference in these downward and upward fluxes constitutes the net water evaporation. If tracer vapor lies over tracer-free ocean waters, the tracer diffuses down and strikes the surface with the downward water vapor flux. The upward water vapor flux, however, will be free of tracer, since any tracer deposited with the downward flux is well mixed into the surface waters and cannot be retrieved. This results in a net downward flux of tracer into the ocean, even when the net water evaporation is positive. This behavior is unique to ocean surfaces. Over land or ice surfaces, the tracer flux must be in the same direction as the net water vapor flux.

The transfer of tracer across the ocean surface, E_T , is calculated in the model as

$$E_T = \rho \cdot W_s \cdot C_q \cdot (1 - k) \cdot (q_{GT} - q_{ST}) \quad (2-17)$$

where $1-k$, defined in Equation 2-7, is a factor dependent on isotope molecular diffusivity. The value of k is 0 for non-isotopic tracers. The determination of q_{GT} , the specific humidity of tracer just above the ocean surface, depends on whether the tracer is defined as "surface-conserved" or "aboveground"; again, this will be explained in Section 2.4.

To determine q_{ST} , the specific humidity of tracer at the top of the surface layer, the flux of tracer into the surface layer from below is assumed to equal exactly the flux of tracer out of the surface layer into higher levels. This assumption leads to an expression analogous to Equation 2-16:

$$q_{ST} = \frac{C W_s \cdot (1 - k) \cdot q_{GT} + \frac{K}{z_1 - z_s} \cdot q_{1T}}{C W_s \cdot (1 - k) + \frac{K}{z_1 - z_s}} \quad (2-18)$$

where q_{1T} is the average Level 1 specific humidity of tracer.

2.4. Upward Flux of Tracer from the Earth's Surface

The formulation of the upward evaporative flux of tracer from the earth's surface, which is the net upward evaporative flux over non-ocean surfaces and which is controlled by the value of Q_{GT} in Equation 2-17 over ocean surfaces, must still be described. Two different formulations are employed in the present report, and they define two very different types of tracers, hereafter referred to as surface-conserved tracers and aboveground tracers. Surface-conserved tracers are particularly suitable

for studies of steady-state isotope geochemistry, and aboveground tracers are useful for addressing the problems in global hydrology outlined in Chapter 1.

2.4.1 Surface-Conserved Tracers

Surface-conserved tracers are so named because they are conserved in surface reservoirs after precipitating or condensing onto the earth's surface. For example, after a precipitation event delivers tracer to a soil surface, some of the tracer is carried away with the water runoff, and the remainder enters the first soil layer and is given the chance to diffuse into the second soil layer. The model always keeps track of the amount of tracer in each reservoir. The tracer is similarly stored in ocean ice, land ice, and snow reservoirs, but it is lost if it enters the ocean during precipitation or vapor exchange.

Most importantly, though, the surface-conserved tracer in the surface reservoir is allowed to re-evaporate into the atmosphere. The amount of tracer that evaporates from a non-ocean surface is found by multiplying the water evaporation from the surface by the tracer/water ratio in the topmost surface reservoir. (Due to an assumed negligible mixing below the surface, isotopic fractionation does not influence the tracer/water ratio in the evaporating water.) For ocean surfaces, the tracer evaporation is calculated with Equation 2-17, using Henry's law to determine the values of Q_{GT} from observed mean isotope concentrations in ocean water:

$$\begin{array}{ll}
 \text{H}_2\text{O}: & q_{\text{GT}} = q_{\text{G}} \\
 \text{HDO, H}_2^{18}\text{O, and HTO}: & q_{\text{GT}} = q_{\text{G}} \cdot C_{\text{O}} \cdot C_{\text{S}}/\alpha_{\text{L/V}}
 \end{array}
 \tag{2-19}$$

where C_{O} is the average weight ratio of the water isotope to H_2O in seawater (3.2873×10^{-4} for HDO, 2.2275×10^{-3} for H_2^{18}O , and 2.2222×10^{-8} for HTO) and C_{S} is a correction factor for isotope concentration in near surface waters (1.004 for HDO, 1.0005 for H_2^{18}O , and 1.00 for HTO).

A surface-conserved tracer will eventually spread into every atmospheric grid box and every surface reservoir. The global distribution of a surface-conserved non-isotopic tracer would necessarily be smoothed by the atmospheric and soil moisture transport processes discussed above until the tracer/water ratio was everywhere the same. Surface-conserved tracers are thus far more interesting when they represent water isotopes; the global steady-state distribution of a water isotope's concentration is non-uniform due to the fractionation properties peculiar to the isotope. Jouzel et al (1987) provide an excellent example of a simulation experiment that uses surface-conserved isotopic tracers; they use the tracer water model to determine the global distributions of HDO and H_2^{18}O as a function of season. Some of their comparisons of model results with observations are discussed in Chapter 3.

2.4.2 Aboveground Tracers

When an aboveground tracer reaches the earth's surface through precipitation, surface condensation, or oceanic vapor exchange, the model stores the tracer flux value for the appropriate grid square, and the deposited tracer effectively disappears from existence. In other words, the surface reservoirs effectively remain tracer-free. The idea is to prevent the tracer from re-evaporating; studies using aboveground tracers are of interest for determining where and how a tracer in the atmosphere first reaches the earth's surface. Thus, given sufficient time, the model would remove from the atmosphere any nonzero aboveground tracer distribution placed there at the beginning of a simulation. The model would simultaneously compute the two-dimensional distributions of cumulative tracer precipitation flux and downward tracer vapor flux at the earth's surface.

Specific weather events, however, can move the initial tracer in ways not consistent with time-averaged transport, and it is therefore desirable to complement the tracer sink at the earth's surface with a tracer source. At steady-state, the source injects the tracer into the atmosphere and the surface sink removes the tracer from the atmosphere at the same rate. A simulation of sufficient duration will determine the characteristic pathways followed by the tracer between source and sink.

The most common type of tracer source is called a "tracer source region" and consists of a set of surface grid squares. At each time step in the simulation, a non-isotopic tracer evaporates from a source region

grid square at the water evaporation rate from that square, without regard to any surface reservoir tracer content. Put another way, tracer is simply injected into the Level 1 grid box above the square at the same rate as the evaporated water.

For a non-ocean section of a source region grid square, the tracer evaporation rate is set equal to the net water evaporation rate. For an ocean surface, it is necessary to separate the equations for net water evaporation (Equation 2-15) and net tracer evaporation (Equation 2-17) into their upward and downward components:

$$E_{\text{down}} = \rho \cdot W_s \cdot C_q \cdot q_s \quad (2-20)$$

$$E_{\text{up}} = \rho \cdot W_s \cdot C_q \cdot q_G \quad (2-21)$$

$$E_{T,\text{down}} = \rho \cdot W_s \cdot C_q \cdot q_{ST} \quad (2-22)$$

$$E_{T,\text{up}} = \rho \cdot W_s \cdot C_q \cdot q_{GT} \quad (2-23)$$

Over an ocean section of a source region grid square, the upward tracer vapor flux into the Level 1 grid box proceeds at the same rate as the upward water vapor flux into the box. Outside the source region, no tracer is injected into the Level 1 box. A downward flux of tracer vapor can occur onto any ocean surface, inside or outside the source region. Thus, Equation 2-17 is used for the vapor exchange of aboveground tracer over the ocean, with q_{GT} defined as:

$$q_{GT} = q_G \quad \text{inside the tracer source region}$$

$$q_{GT} = 0 \quad \text{outside the tracer source region} \quad (2-24)$$

An aboveground, non-isotopic tracer evaporating from a tracer source region has a simple interpretation. Water that evaporates from the source region is effectively tagged, and the tag is removed once the water returns to the earth's surface during precipitation, surface condensation, or oceanic vapor exchange events. By studying the surface distributions of downward tracer flux, the modeler can determine the characteristic directions and horizontal distances traveled by the source region's evaporated water and thereby determine the regions on the globe that are directly influenced by it, at least for the model climate.

2.5 Simultaneous Integration of GCM Prognostic Variables and Tracer Transport.

It is conceivably possible to store the model winds and precipitation data at every time step during a single GCM simulation and to use this data later as input to a completely isolated tracer model to determine tracer transport. Such a strategy would avoid the inefficient re-calculation of GCM wind and precipitation fields during every tracer water model simulation and thus might save on computational costs. Jacob et al (1987), for example, used stored fluxes from a GISS GCM simulation to study the atmospheric distribution of ^{85}Kr .

The tracer water model described in this report employs a different strategy. The model water and tracer fluxes are determined simultaneously; i.e., a complete GISS GCM simulation is a part of every tracer water model simulation. The reasons for this are threefold. First, the amount of stored data required by a completely isolated tracer water model would be tremendous. For example, the calculation of tracer transport in moist convection would require, for every moist convective event at every time step, data describing the bottom and top grid boxes involved in the convection, the condensation of water at each level as the moist convective plume rises, the re-evaporation of water at each level as the droplets fall, and all water fluxes occurring during subsidence. This information is far more detailed than that used in standard isolated tracer models (e.g., Jacob et al., 1987). Second, a simultaneous integration of water and tracer fluxes is especially suitable for studying the sensitivity of tracer transport to changes in GCM structure; many such sensitivity studies were performed and are discussed in Chapter 3. For an isolated model to determine the effect of some model parameterization change, a new complete GCM simulation would have to be performed to obtain a new set of wind and precipitation data, thereby removing the sole advantage of computational savings. Finally, the tracer water model described in this report is designed to follow more than one tracer during a single GCM simulation anyway, the number allowed being limited only by available computer storage.

Chapter 3

Indirect Evaluations of Model Performance

The tracer water model can determine the characteristic distances and directions traveled by water evaporating from a specified source region, at least for the model climate. As discussed in Chapter 1, this type of information cannot be inferred from measurements in the real world. The lack of such observational data is both a motivation for developing the tracer water model and a barrier to accepting the model results as representative of nature.

Fortunately, some indirect tests of the tracer water model are available. These tests are utilized in the present chapter. The chapter is divided into four sections, the first presenting a comparison of model-generated and observed vapor flux fields, the second discussing the inter-annual variability of the model results, the third describing a set of model runs that simulate atomic tritium transport from the stratosphere to the oceans, and the last describing a model run that simulates the global distributions of stable water isotopes. While none of the sections conclusively prove or disprove the accuracy of the tracer water model, they do illustrate well the character of the model and indicate problems that must be considered when assessing model results.

3.1 Comparison Between Observed and Modeled Water Vapor Fluxes

For the GCM to transport a tracer water mass correctly, it must transport the global model water correctly. That is, an adequate

performance of the tracer water model requires that GCM-generated fields of time-averaged, vertically-integrated atmospheric vapor flux agree with observed fields. The present section provides a comparison between GCM vapor flux data and the observations compiled by the Geophysical Fluid Dynamics Laboratory (GFDL) of NOAA at Princeton University (Oort, 1983).

In addition to simulating the total vapor flux correctly, the GCM must also reproduce observed fields of specific and relative humidity, temperature, surface pressure, and so forth. A comparison between observed and modeled humidity distributions is provided below. For an evaluation of the model's performance in reproducing other important climate features, the reader is again referred to the GISS GCM analysis of Hansen et al (1983).

For the vapor flux comparisons, the model-generated data and the observed data were processed to produce global distributions of Q_λ and Q_ϕ , where

$$Q_\lambda = \int_0^{P_S} q u \, (dp/g) \quad (3-1)$$

is the zonal component of vertically-integrated water vapor transport in kg/m-sec averaged over a season, and

$$Q_\phi = \int_0^{P_S} q v \, (dp/g) \quad (3-2)$$

is the meridional component. In the equations, u and v are zonal and meridional components of wind velocity, q is specific humidity, P_s is surface pressure, and g is gravitational acceleration. The global distributions took the form of estimated mean values at each of the $8^\circ \times 10^\circ$ grid boxes shown in Figure 2-1.

The GCM values for Q_λ and Q_ϕ were determined during a two-year model simulation. Thus, the winter value of Q_λ , for example, is the mean value over two Decembers, two Januarys, and two Februarys. (Note: For this discussion, the December-January-February season is referred to as winter, the March-April-May season as spring, and so on, even though the seasons are reversed in the Southern Hemisphere.) The seasonal GFDL data was determined from observations taken between 1963 and 1973. Putting the GCM and GFDL data sets into the same form required a substantial amount of data processing; the procedure used is described in detail in Appendix A.

3.1.1 The Zonal Vapor Flux

The global distributions of the zonal vapor flux Q_λ for each season have been plotted from both the model-generated and observed data sets, and a brief discussion of the differences between the model results and observations is included below. A greatly detailed discussion is not necessary here, since the maps serve mainly as a reference for evaluating later tracer water model runs. A quick look at the maps, for example, would show if the vapor fluxes in a given region are modeled properly and

thus if computed tracer transport in the region can be believed. Plots of zonally-averaged Q_λ are also provided.

a) Global Distributions. Figure 3-1a displays the model-determined curves of constant Q_λ for the winter (DJF) season, and Figure 3-1b shows the corresponding GFDL results. For ease in comparison, contours of negative Q_λ , or westward-moving vapor, are shown as dashed curves.

The basic structures of the two Q_λ distributions are roughly the same. In both the "real world" (as understood through the observations, which may be faulty) and the GCM, water vapor moves toward the west in the tropics and toward the east in midlatitudes and high latitudes. The band of westward movement, however, is thinner in the GCM. Also, the GCM-generated Q_λ distribution seems to have more variation than that produced from the observations; for example, notice that while both data sets show a large eastward transport off the east coast of the U. S., only the GCM produces a region of high eastward transport in Central China.

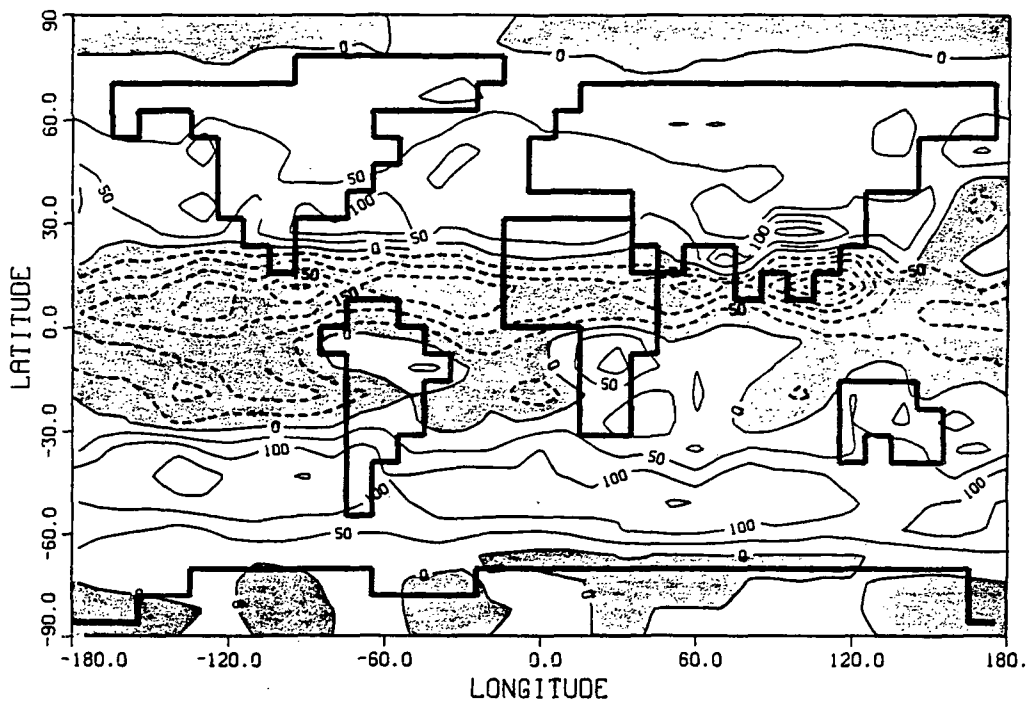
The distributions can also be compared by plotting the absolute difference between the GCM-generated Q_λ values and the observed Q_λ values as a function of position on the earth. This is done in Figure 3-1c. The distributions differ the most in Central America, Equatorial South America, Southern Asia, and the East Pacific; tracer transport determined in these regions should be trusted the least.

Figures 3-2, 3-3, and 3-4 each display the same three sets of contours for the spring (MAM), summer (JJA) and fall (SON) seasons, respectively. The equatorial band of westward-moving vapor is present in both

a. GISS GCM

Q_λ (kg/m-sec)

DJF



b. GFDL data

Q_λ (kg/m-sec)

DJF

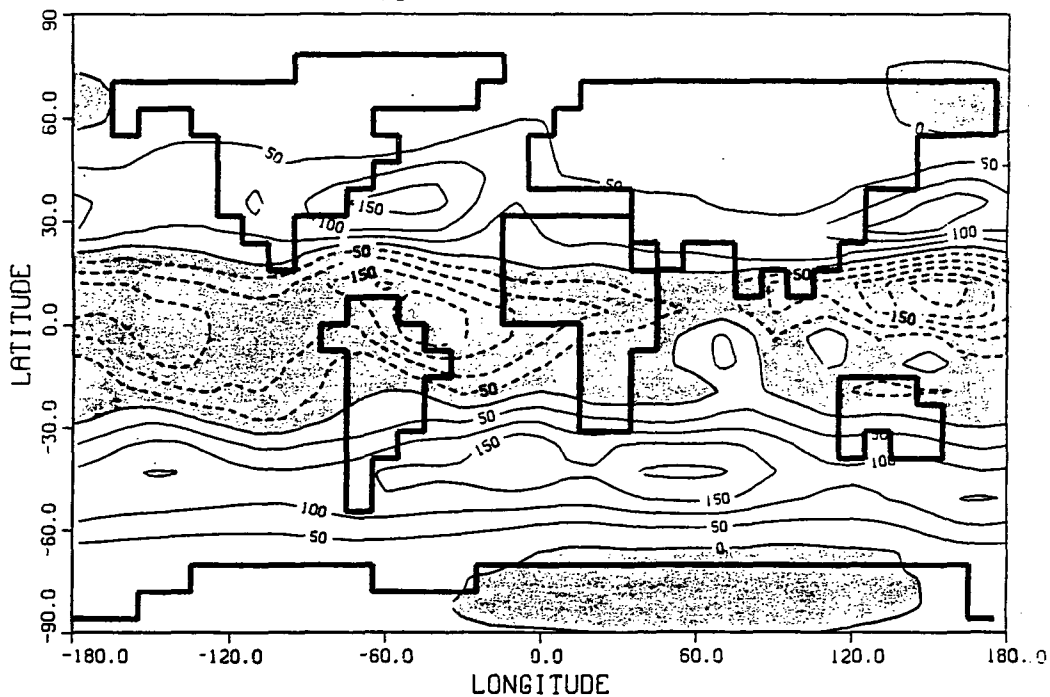
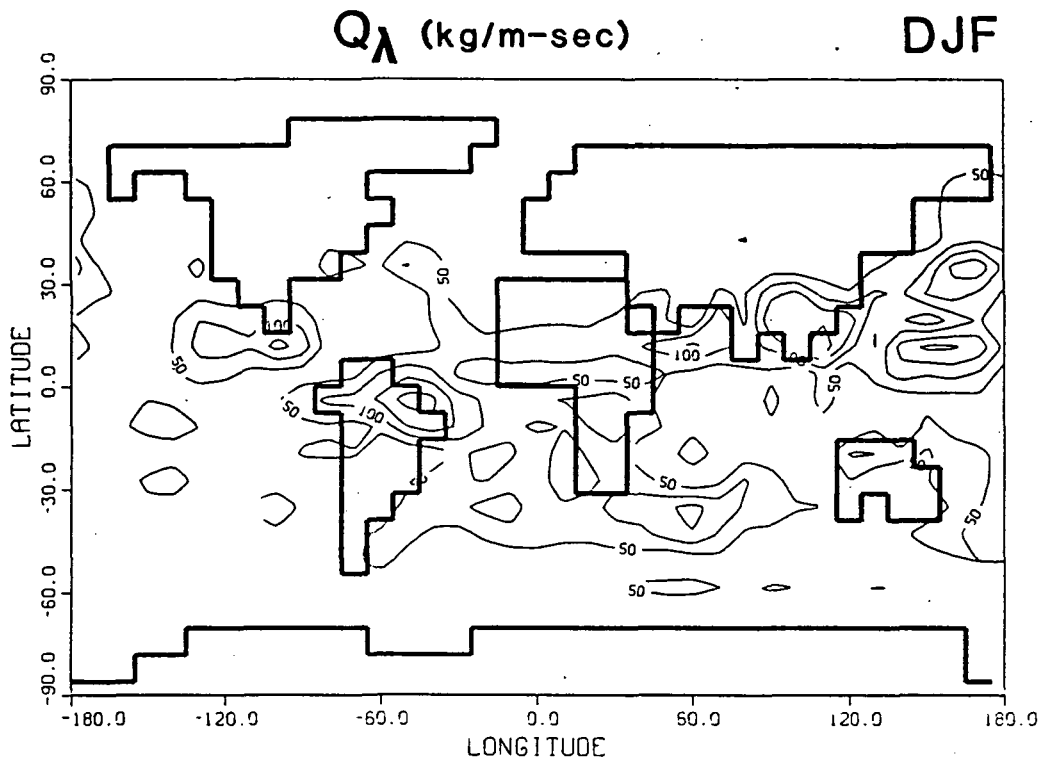


Figure 3-1

Global distributions of Q_λ for winter (DJF).
a) GCM b) Observations c) Absolute differences



c. Absolute differences

Figure 3-1 (cont.)

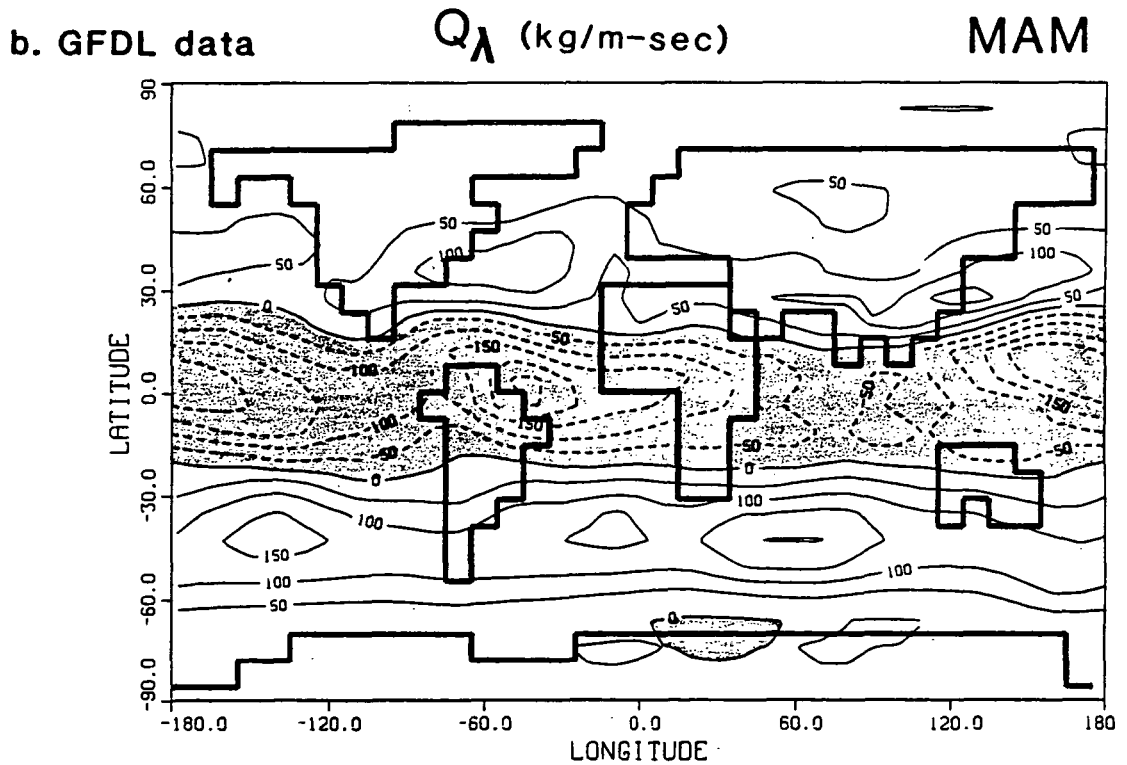
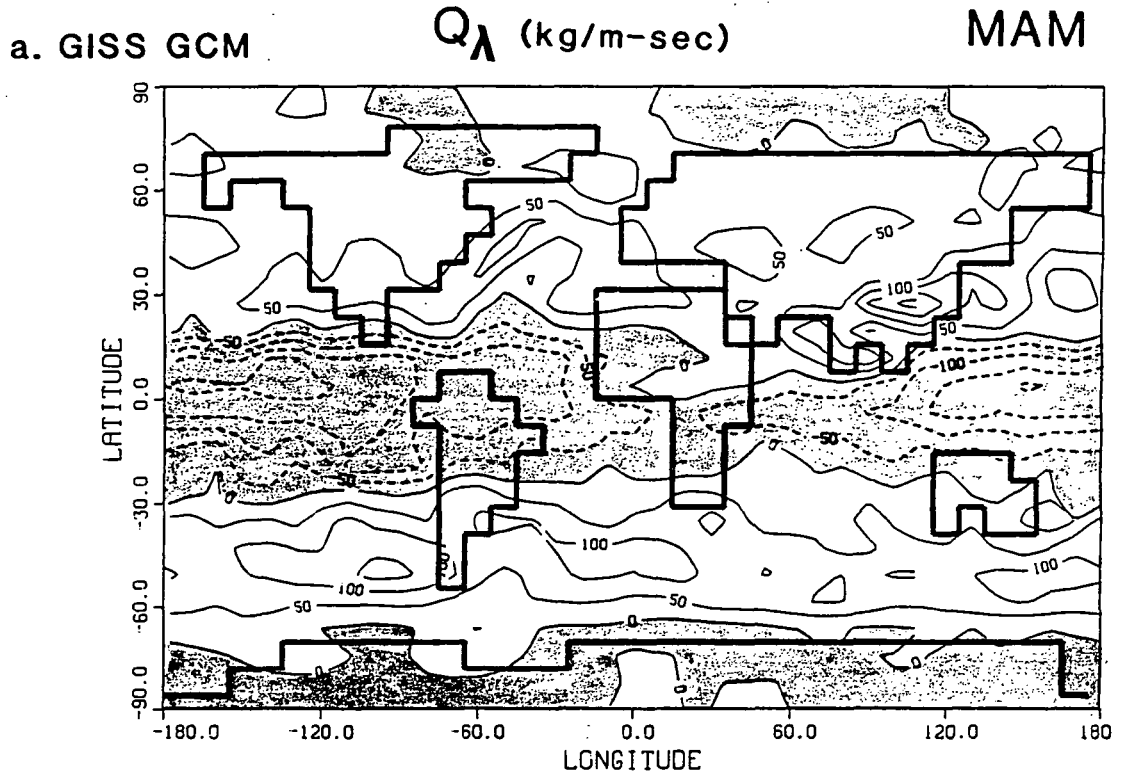
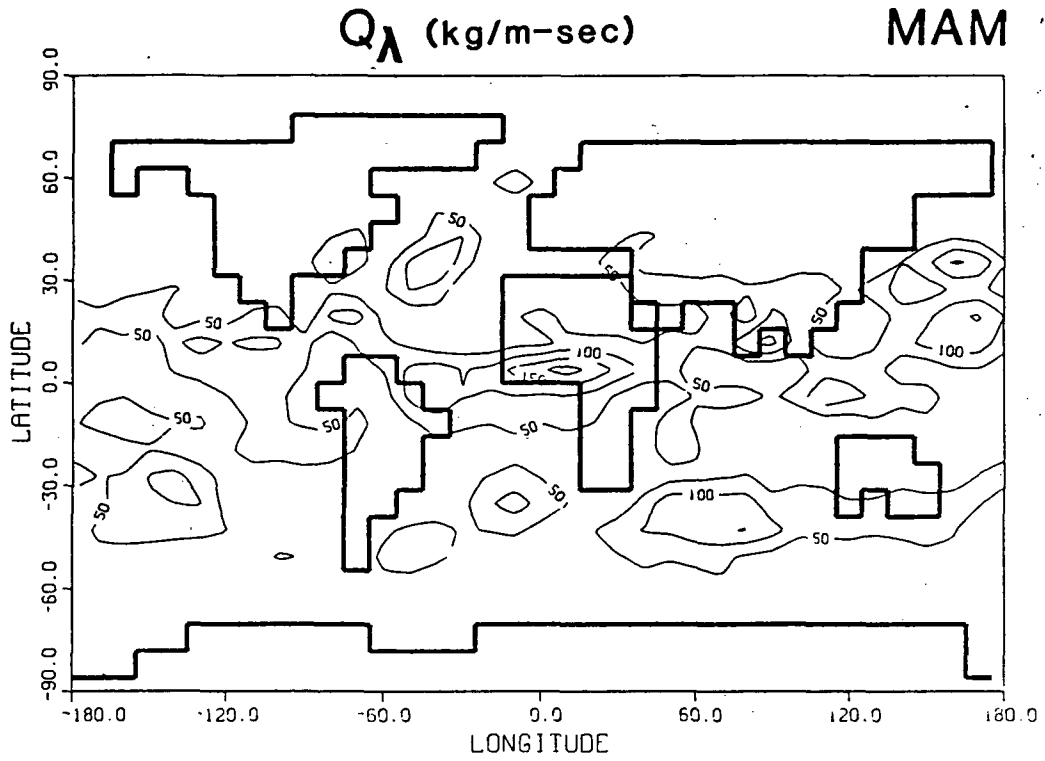


Figure 3-2 Global distributions of Q_{λ} for spring (MAM).
 a) GCM b) observations c) absolute differences



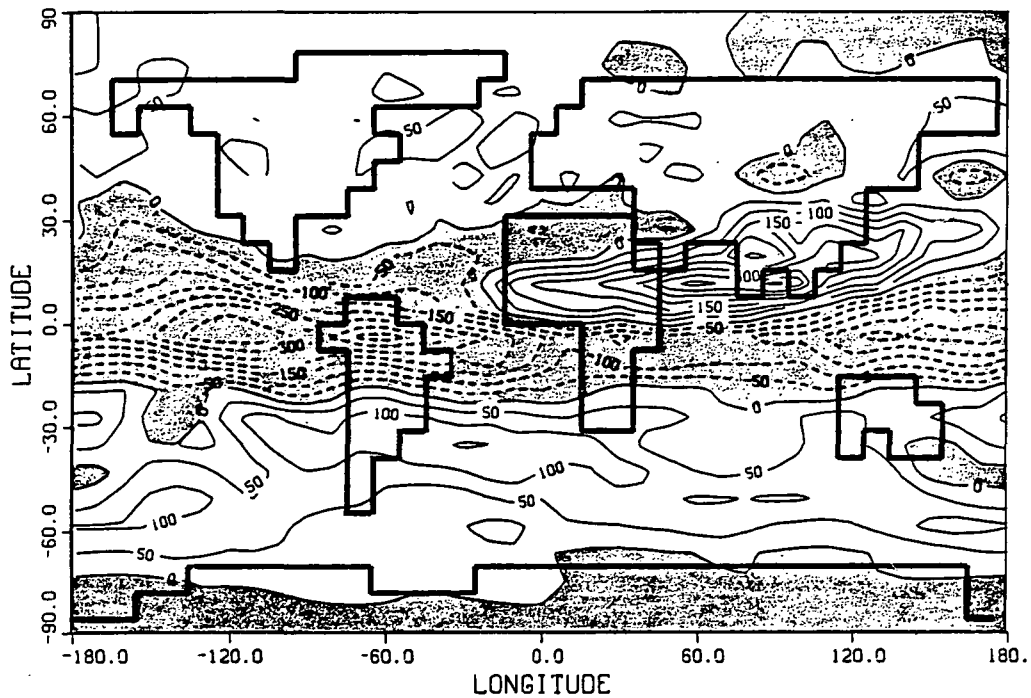
c. Absolute differences

Figure 3-2 (cont.)

a. GISS GCM

Q_{λ} (kg/m-sec)

JJA



b. GFDL data

Q_{λ} (kg/m-sec)

JJA

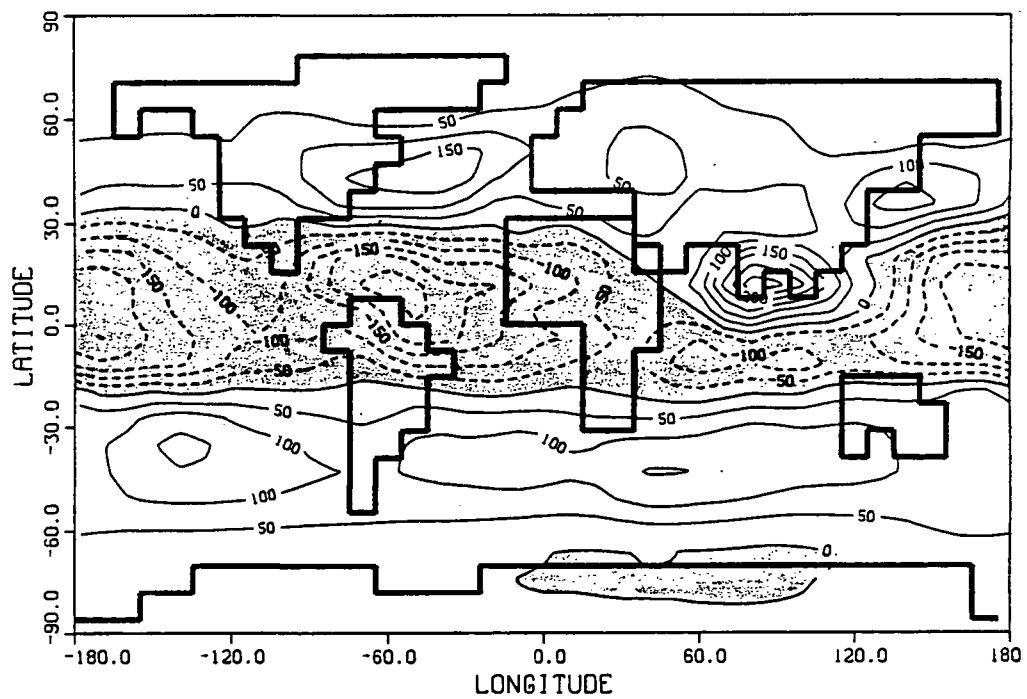
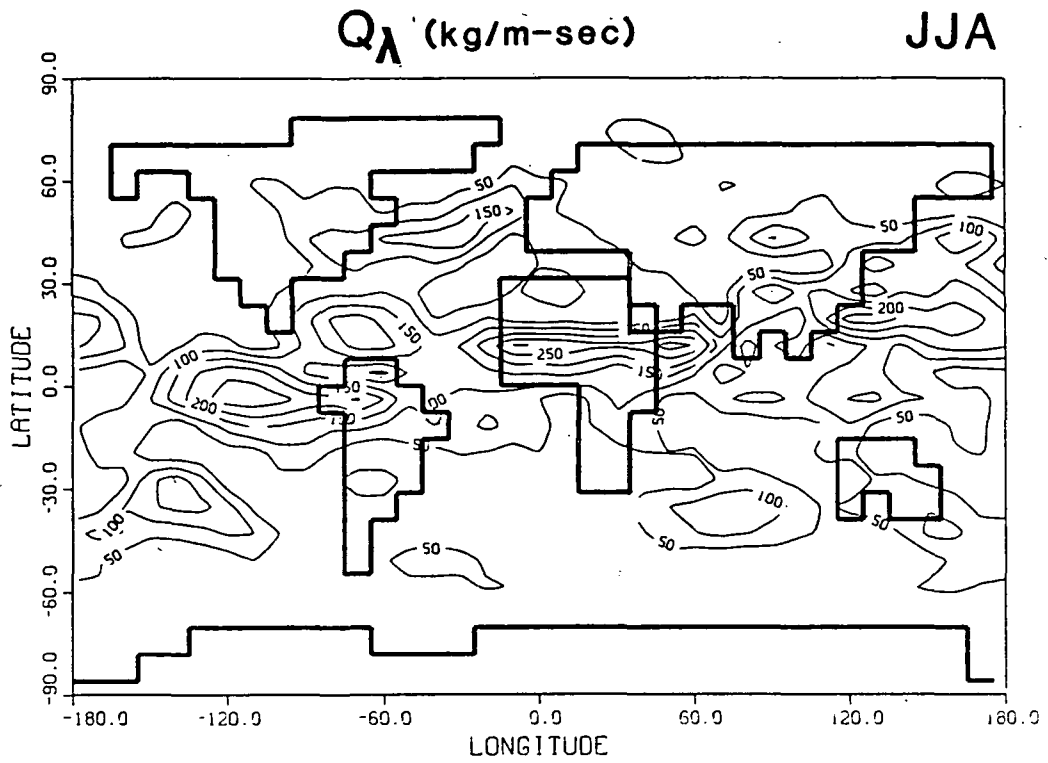


Figure 3-3

Global distributions of Q_{λ} for summer (JJA).
a) GCM b) Observations c) Absolute differences



c. Absolute differences

Figure 3-3 (cont.)

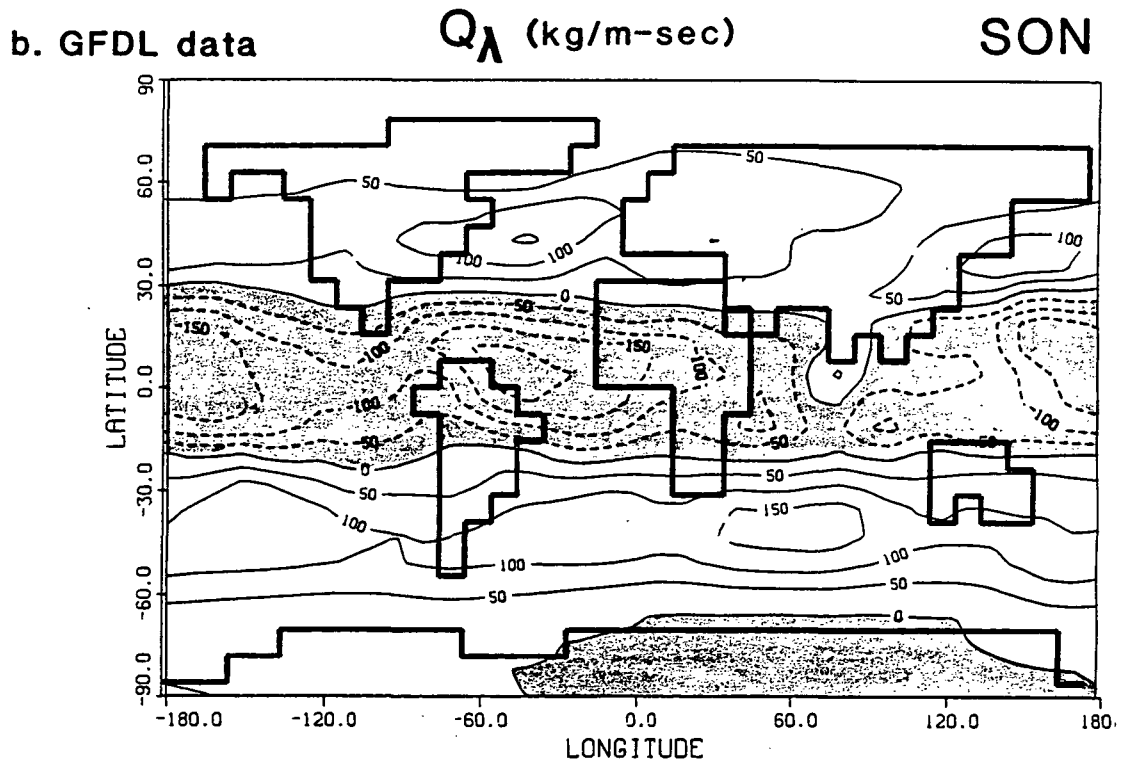
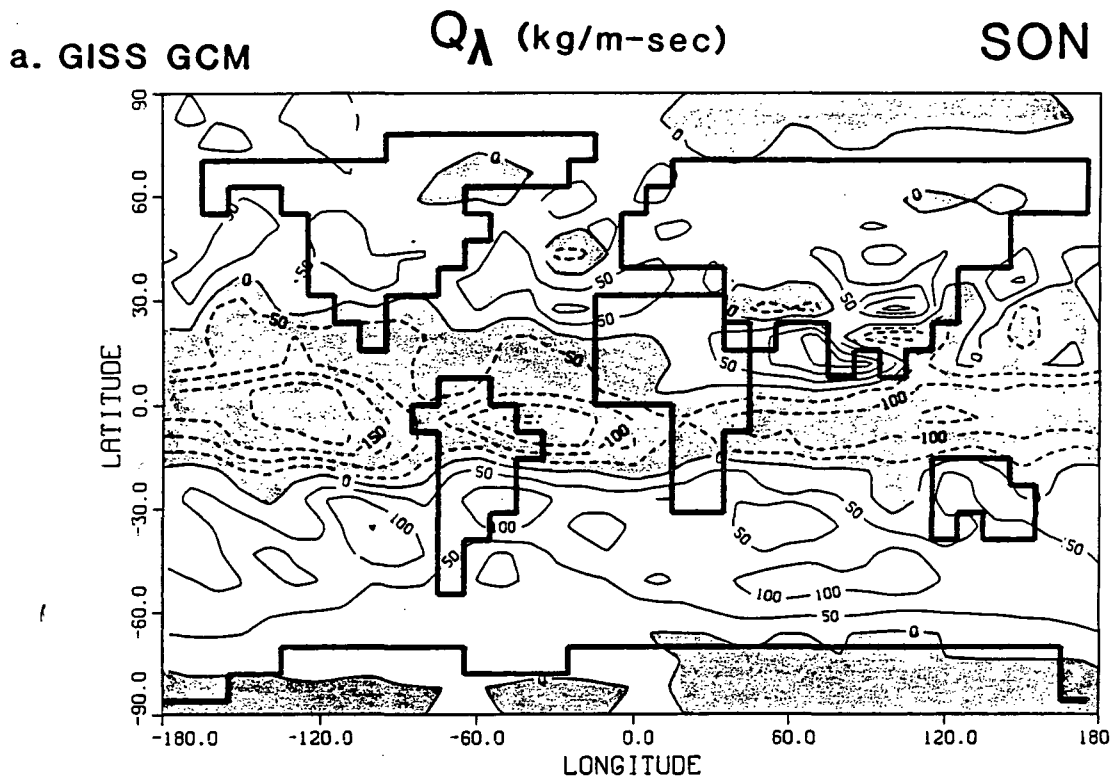
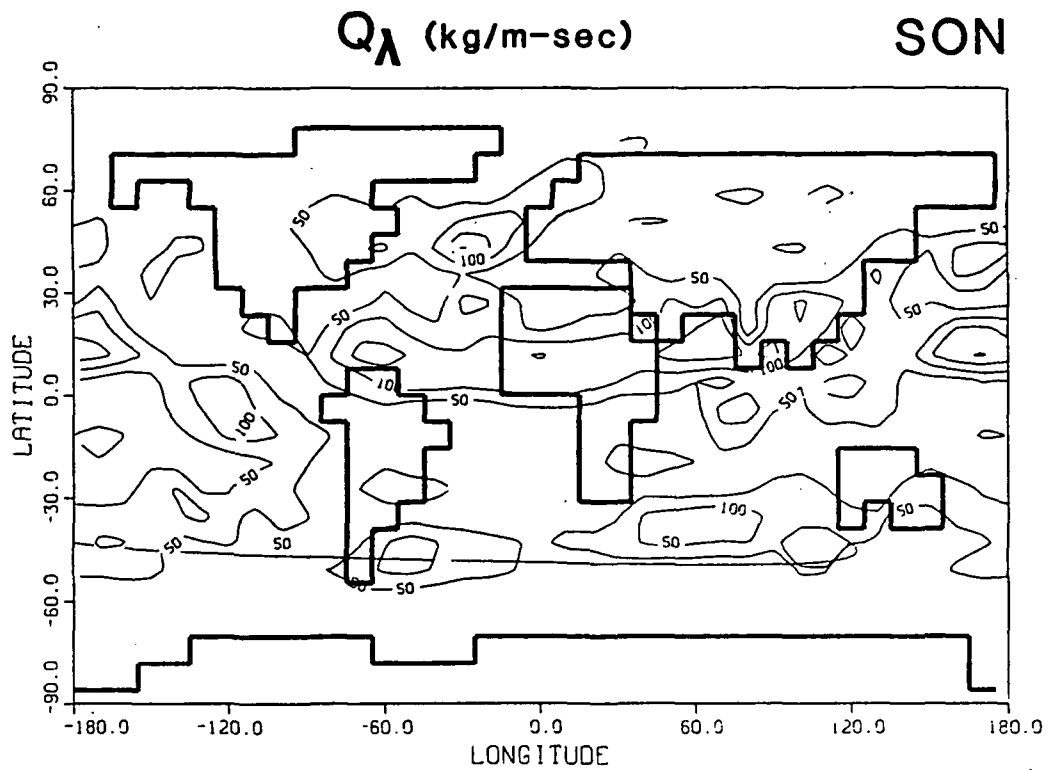
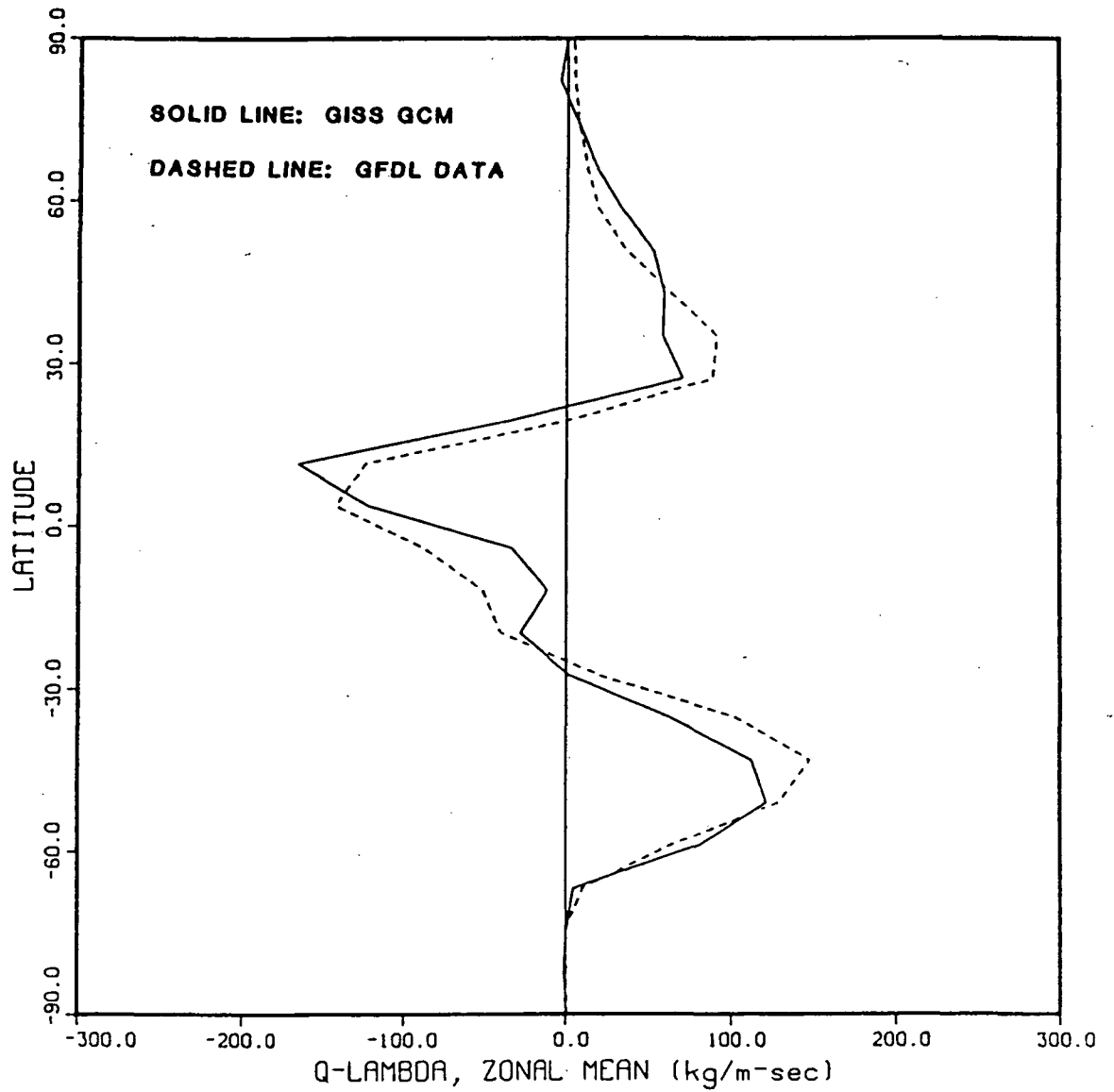


Figure 3-4 Global distributions of Q_A for fall (SON).
 a) GCM b) Observations c) Absolute differences



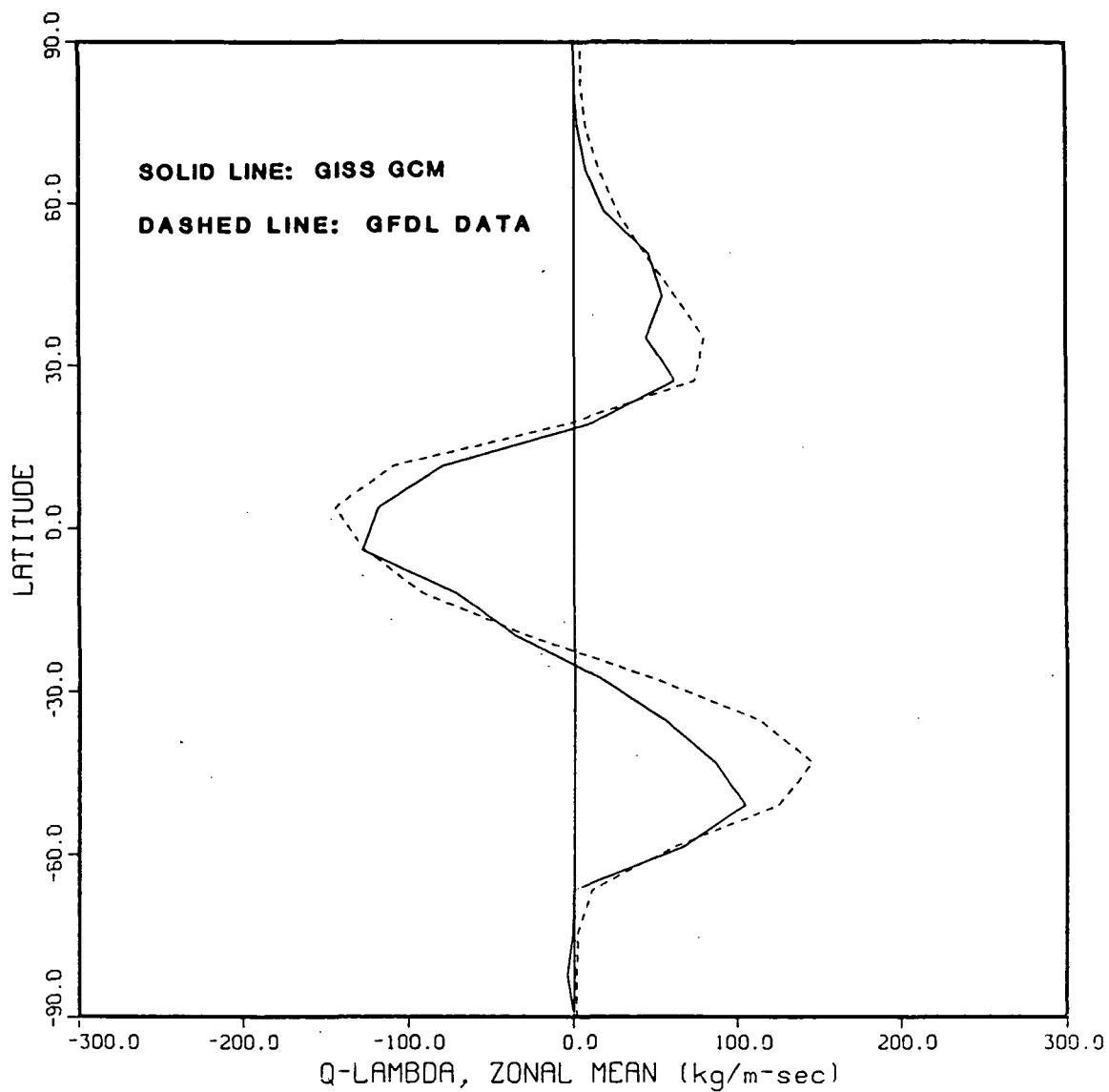
c. Absolute differences

Figure 3-4 (cont.)



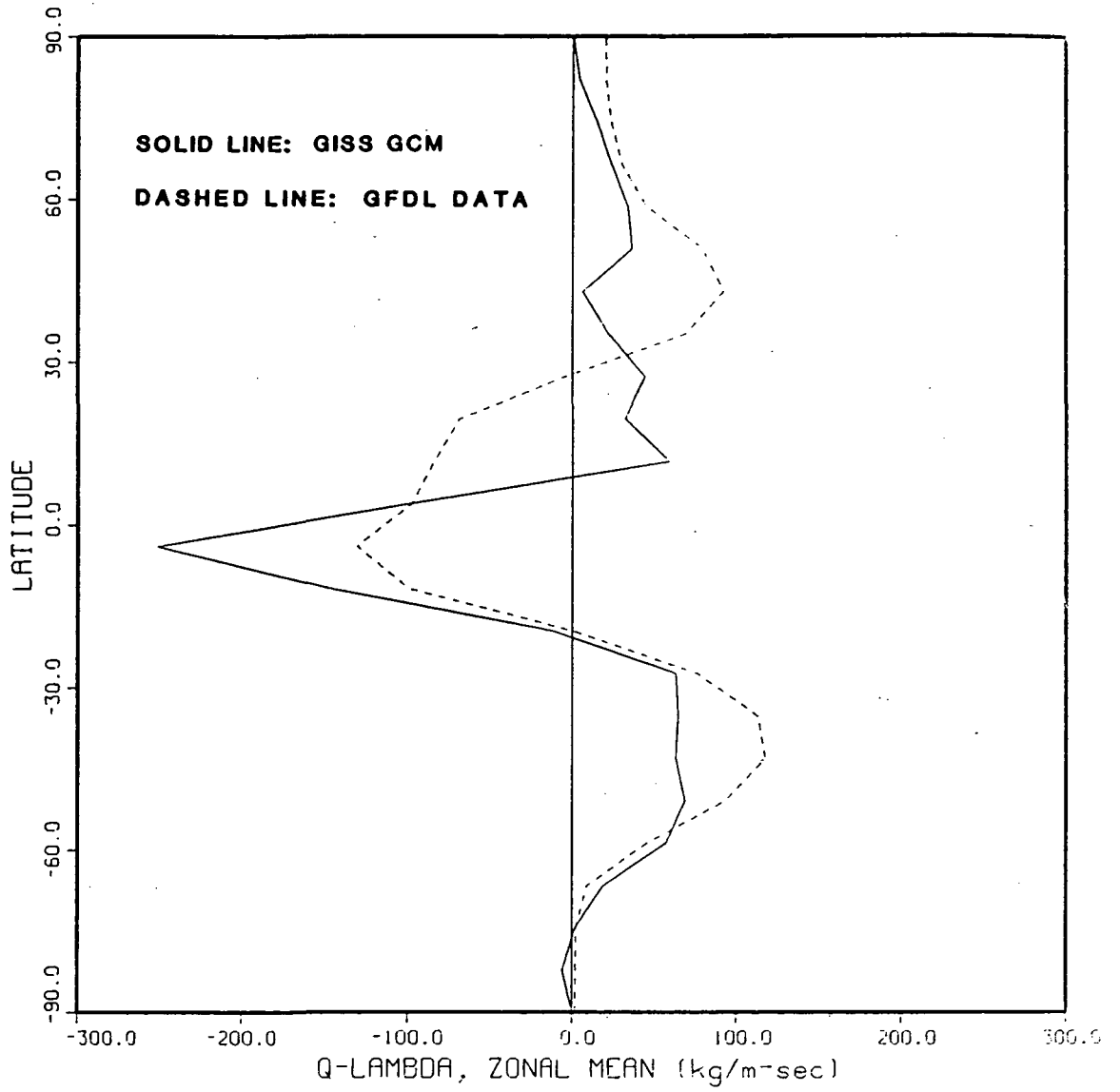
a. Winter (DJF)

Figure 3-5 Latitudinal distributions of $\{Q_\lambda\}$.
 a) Winter (DJF) b) Spring (MAM)
 c) Summer (JJA) d) Fall (SON)



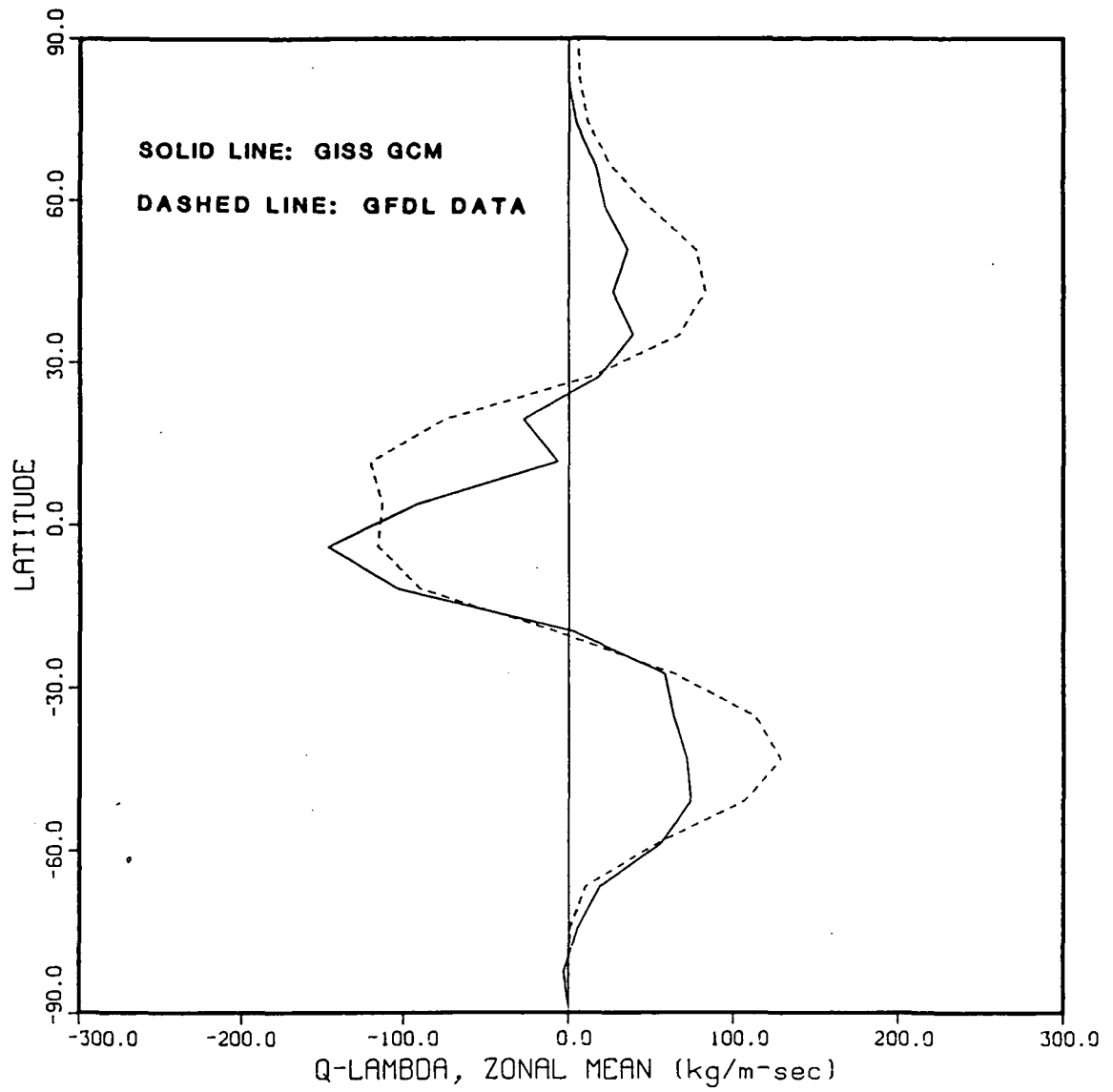
b. Spring (MAM)

Figure 3-5 (cont.)



c. Summer (JJA)

Figure 3-5 (cont.)



d. Fall (SON)

Figure 3-5 (cont.)

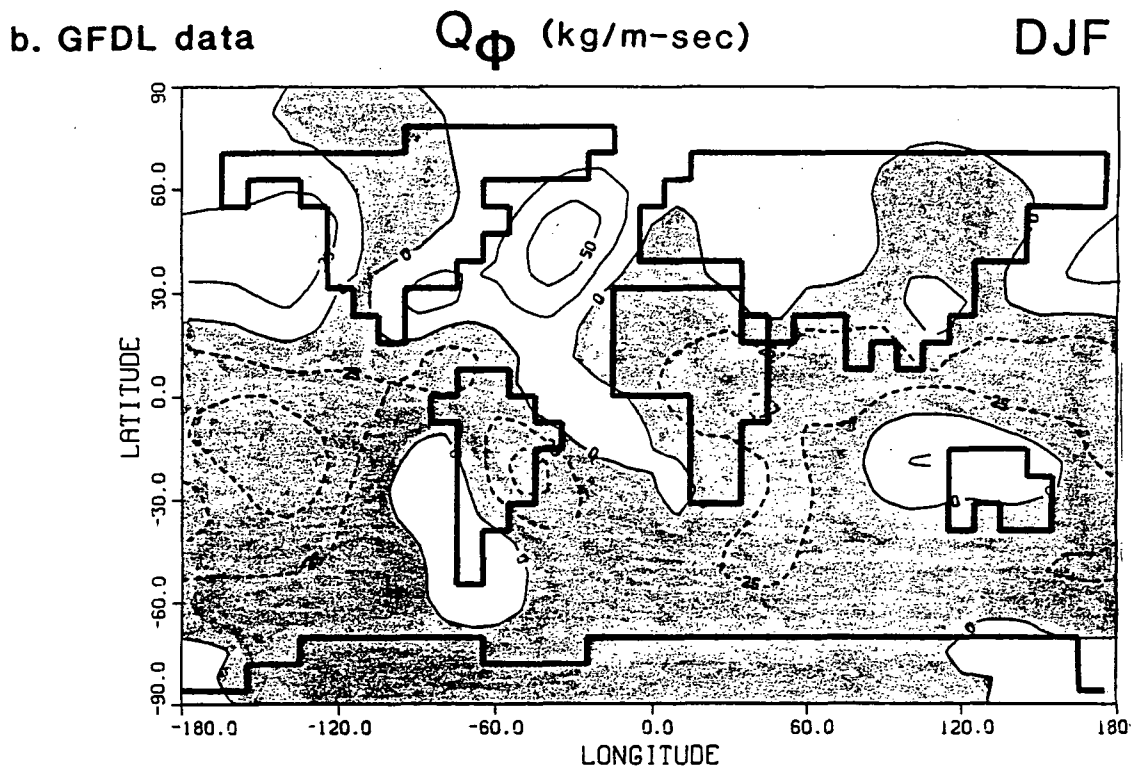
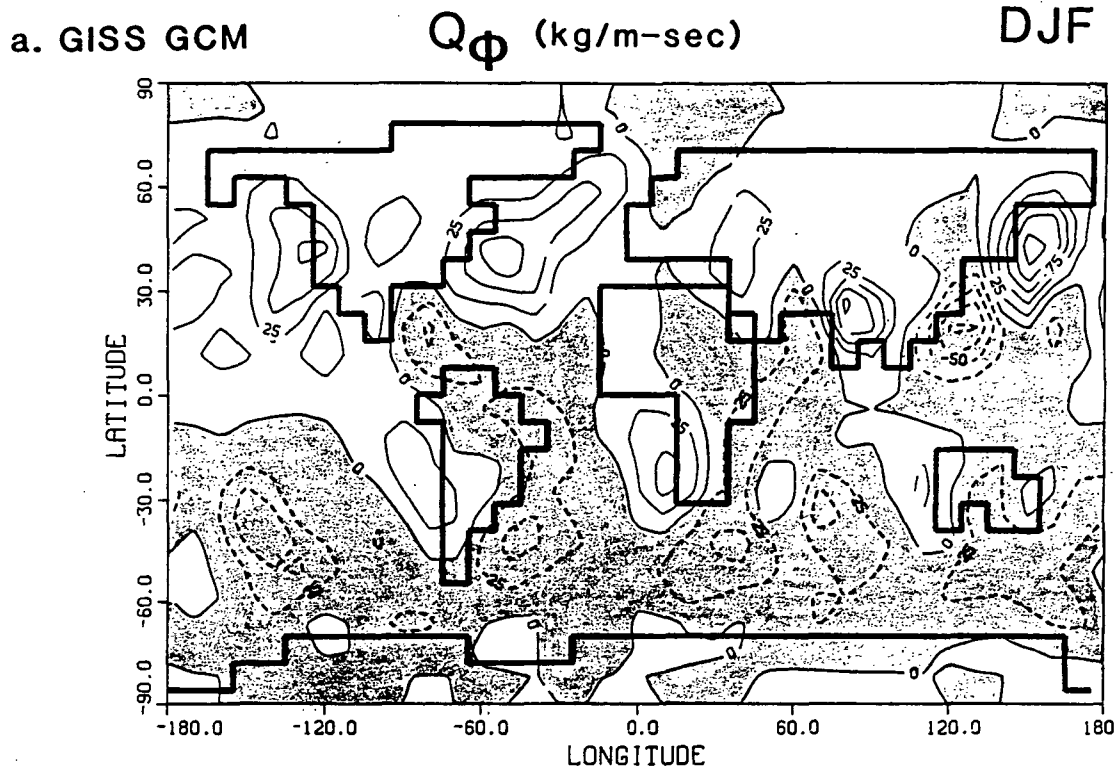
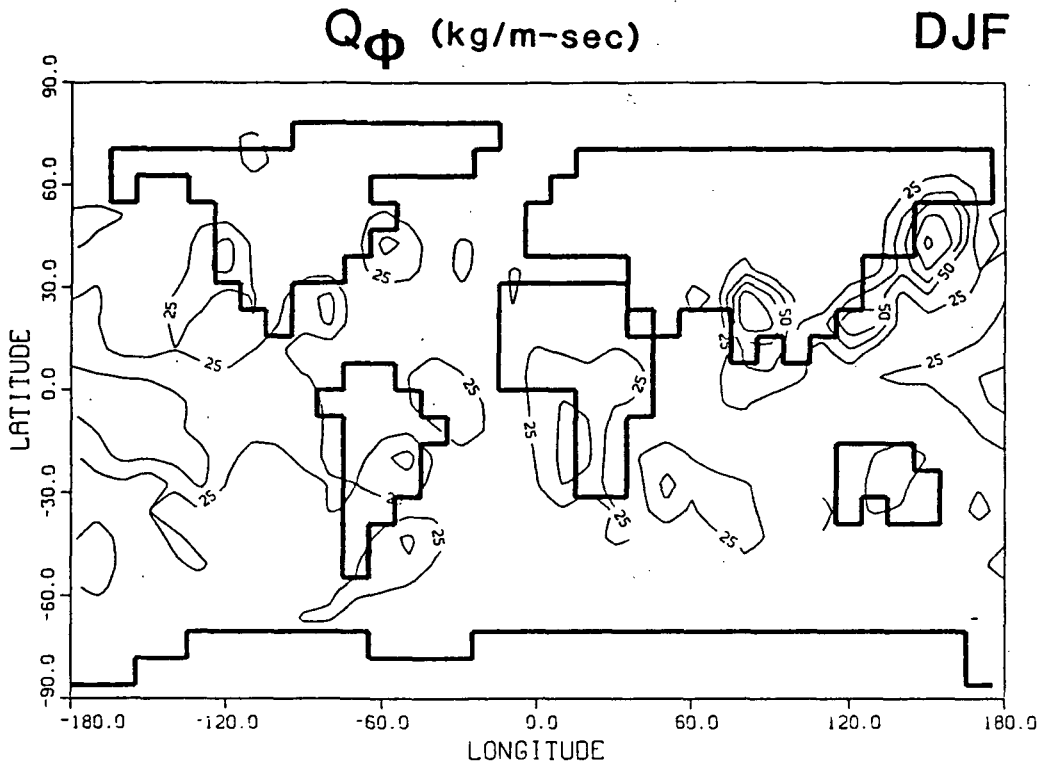


Figure 3-6 Global distributions of Q_{ϕ} for winter (DJF).
A) GCM b) Observations c) Absolute differences



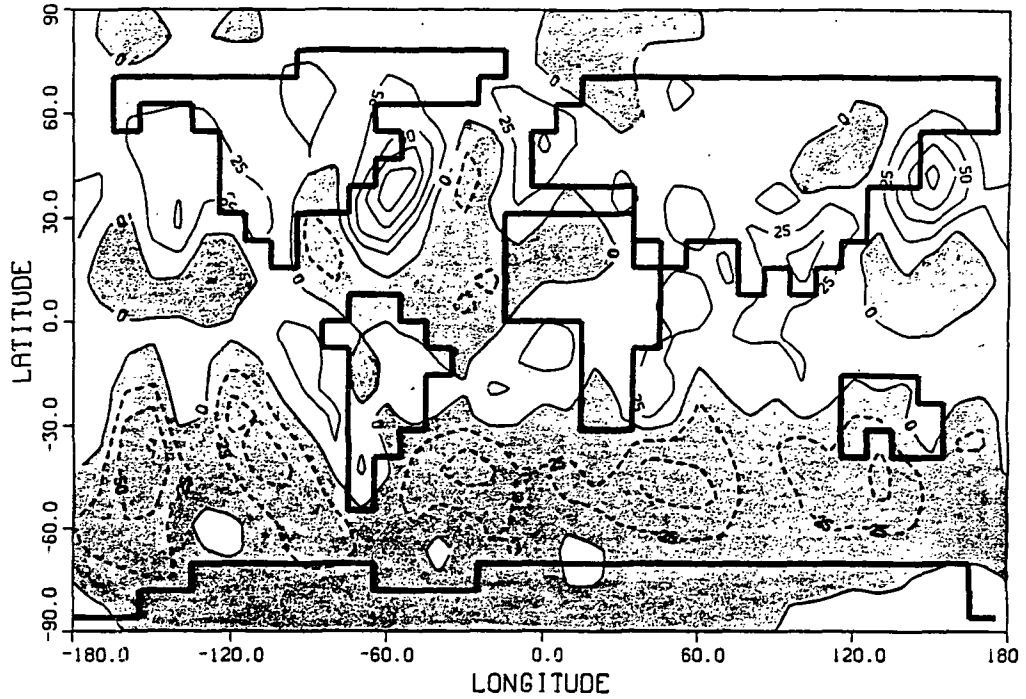
c: Absolute differences

Figure 3-6 (cont.)

a. GISS GCM

Q_{ϕ} (kg/m-sec)

MAM



b. GFDL data

Q_{ϕ} (kg/m-sec)

MAM

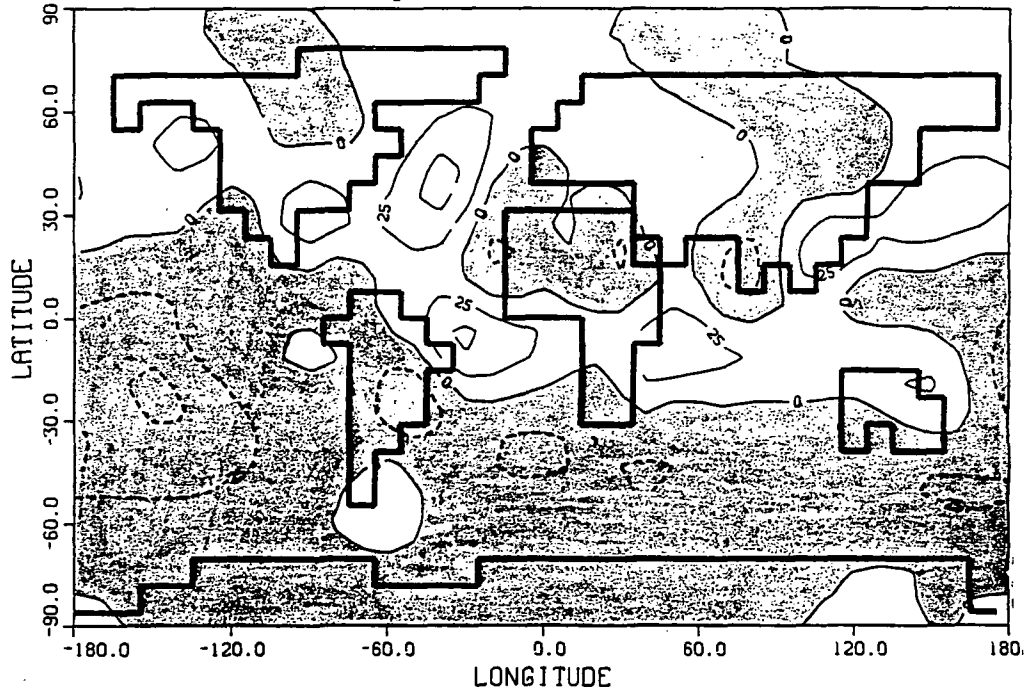
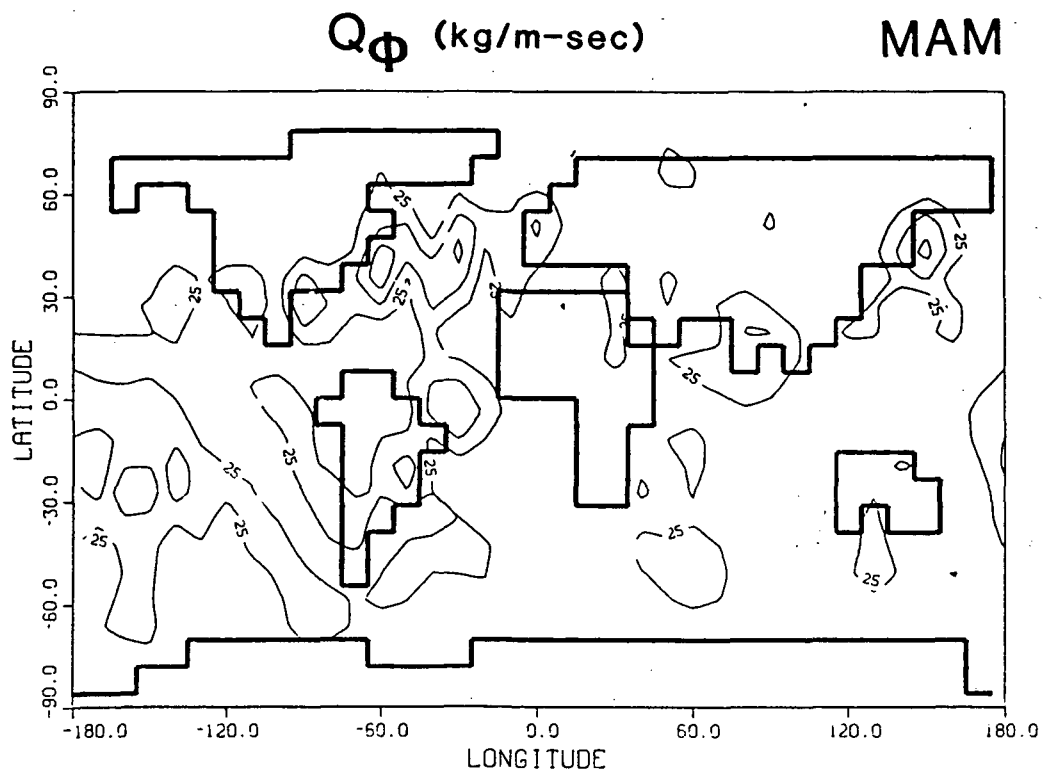


Figure 3-7

Global distributions of Q_{ϕ} for spring (MAM).
a. GCM b. observations c. absolute differences



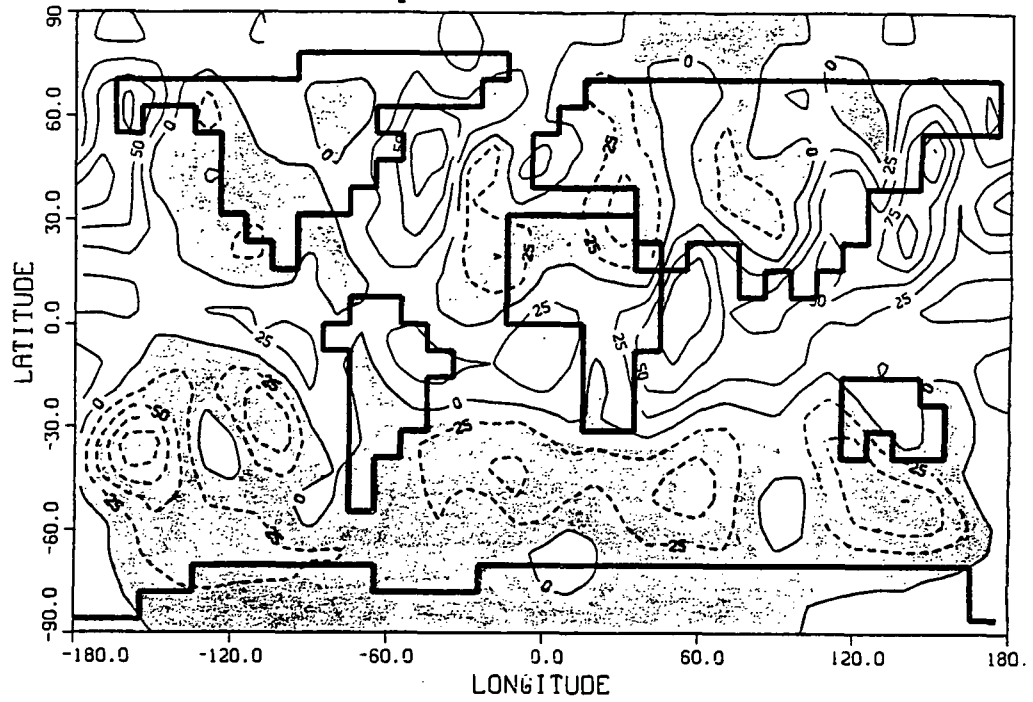
c. Absolute differences

Figure 3-7 (cont.)

a. GISS GCM

Q_{ϕ} (kg/m-sec)

JJA



b. GFDL data

Q_{ϕ} (kg/m-sec)

JJA

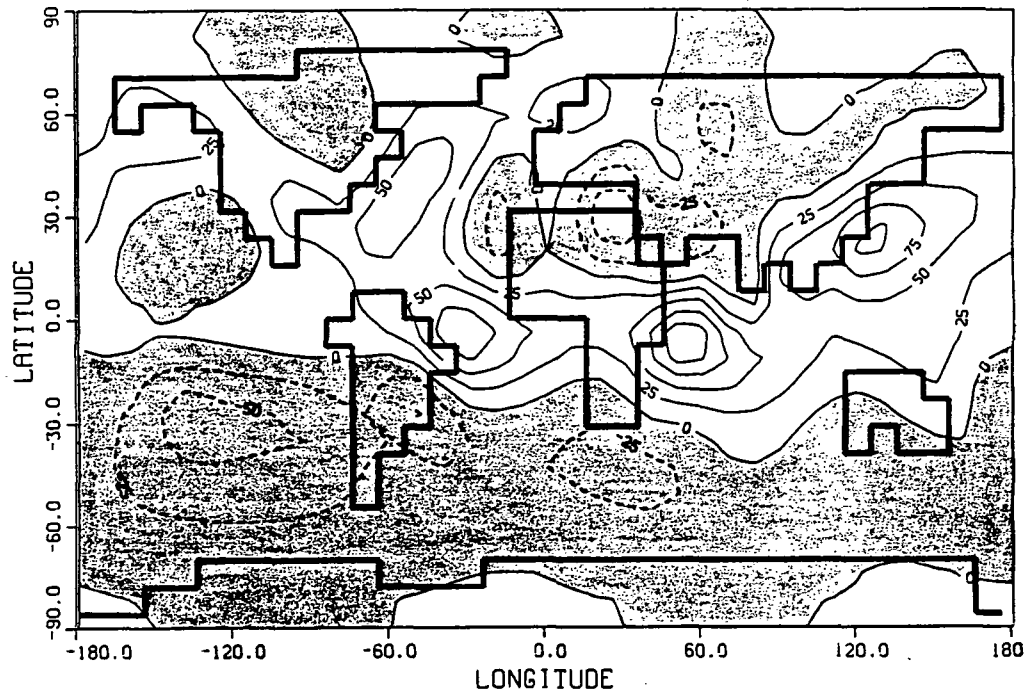
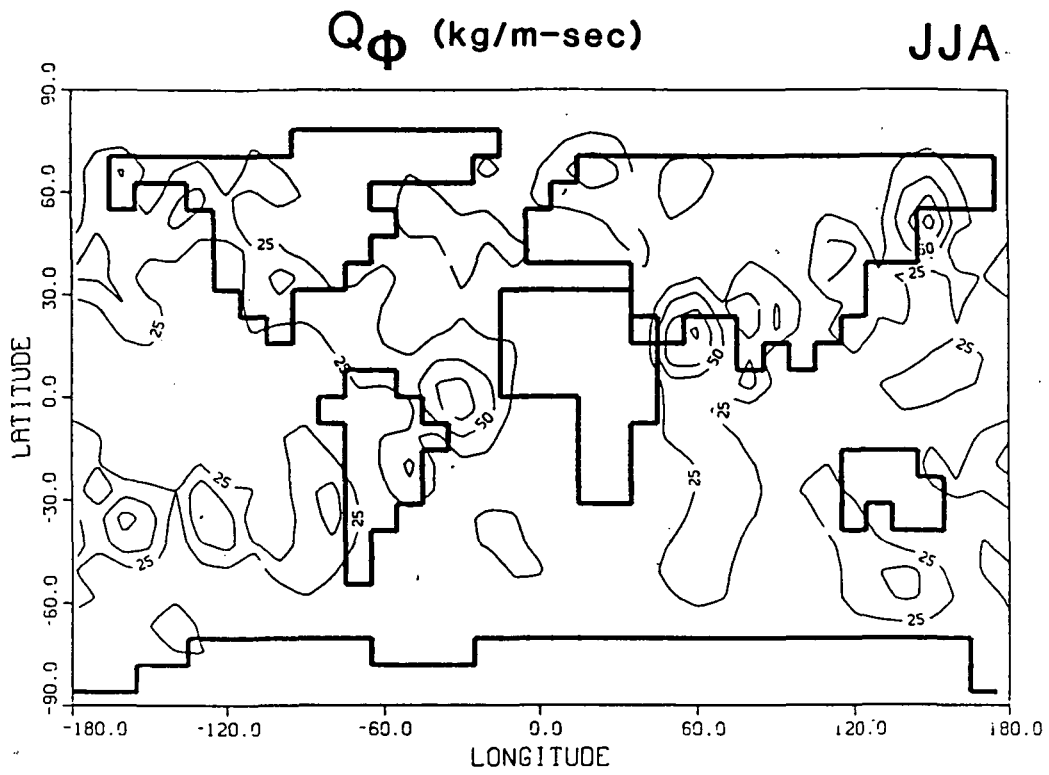


Figure 3-8

Global distributions of Q_{ϕ} for summer (JJA).

a) GCM b) Observations c) Absolute differences

ORIGINAL PAGE IS
OF POOR QUALITY



c. Absolute differences

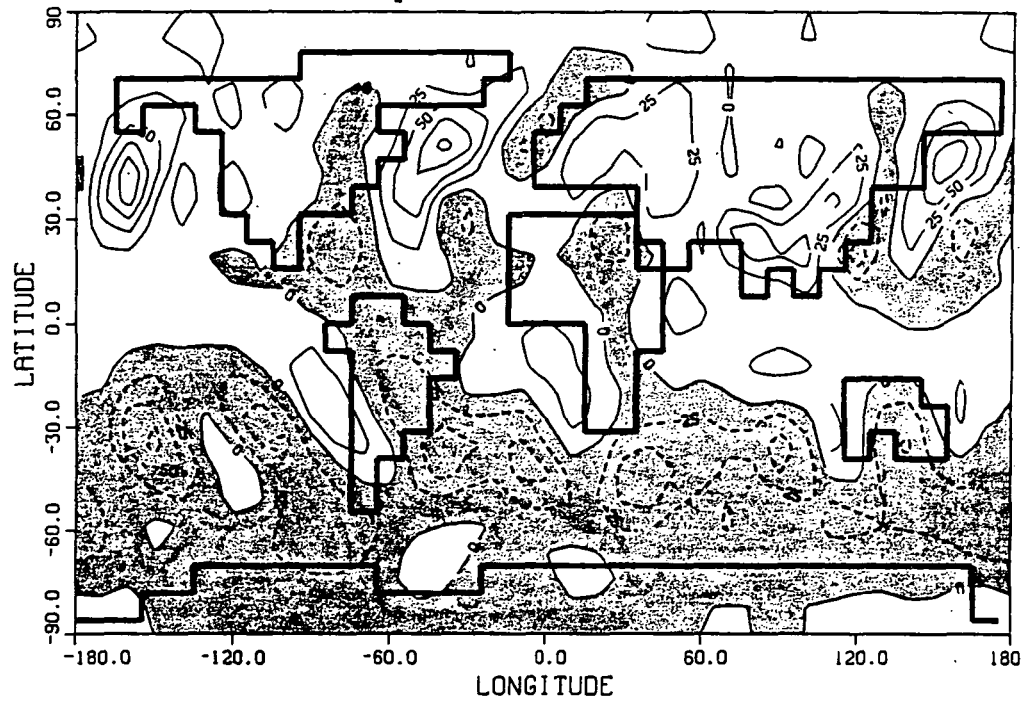
Figure 3-8 (cont.)

ORIGINAL PAGE IS
OF POOR QUALITY

a. GISS GCM

Q_{ϕ} (kg/m-sec)

SON



b. GFDL data

Q_{ϕ} (kg/m-sec)

SON

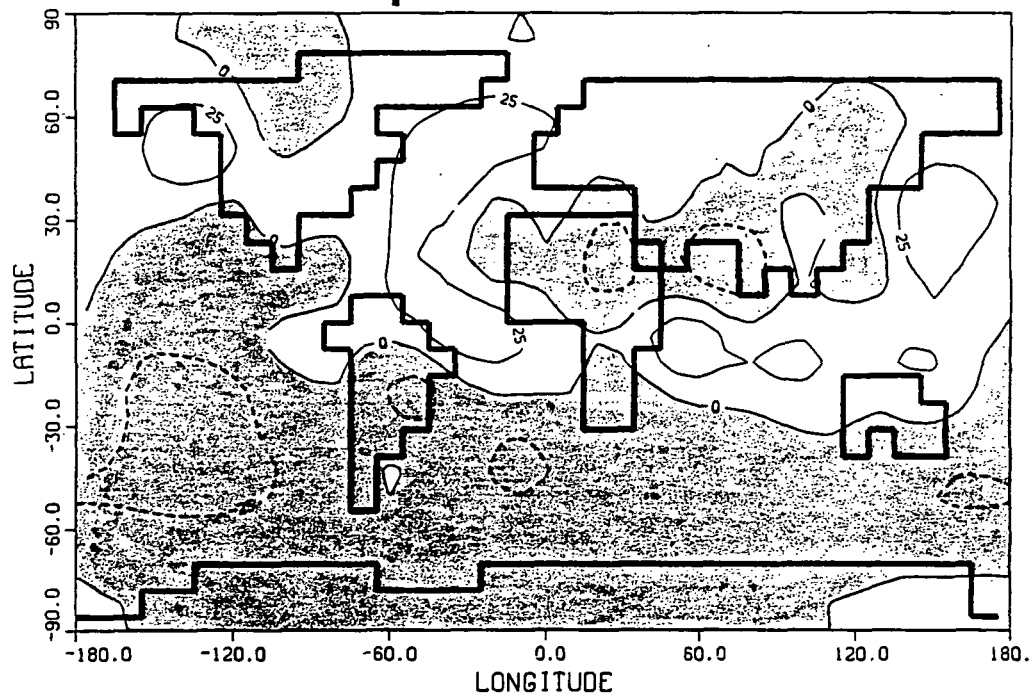
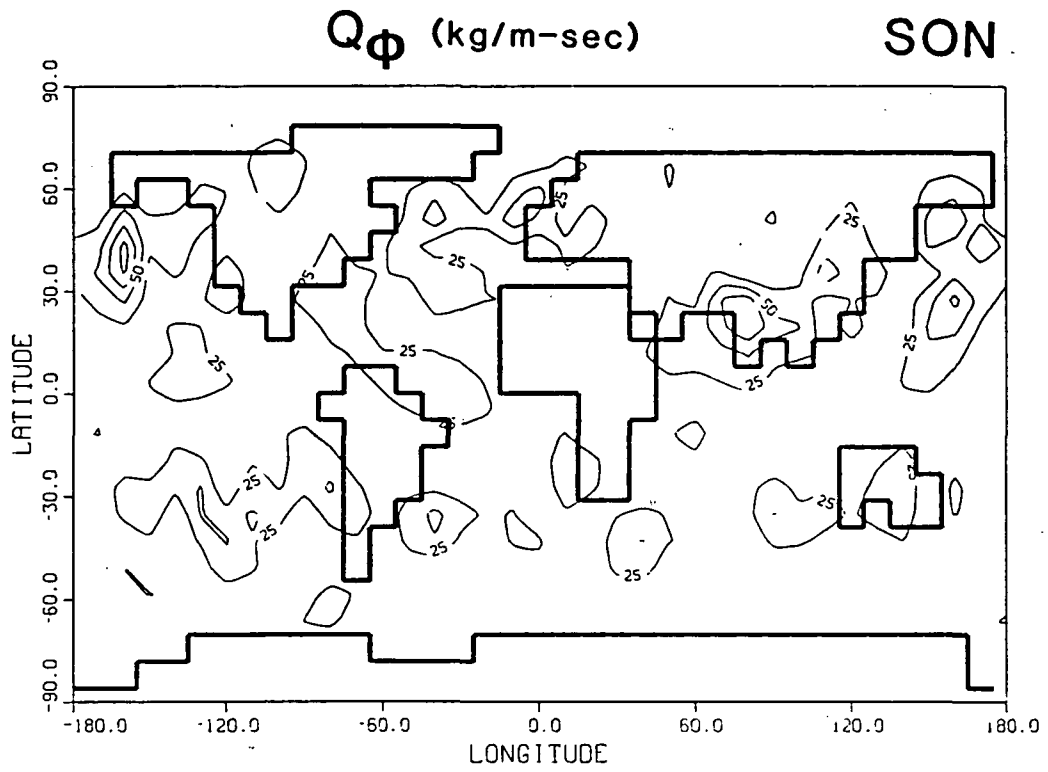


Figure 3-9

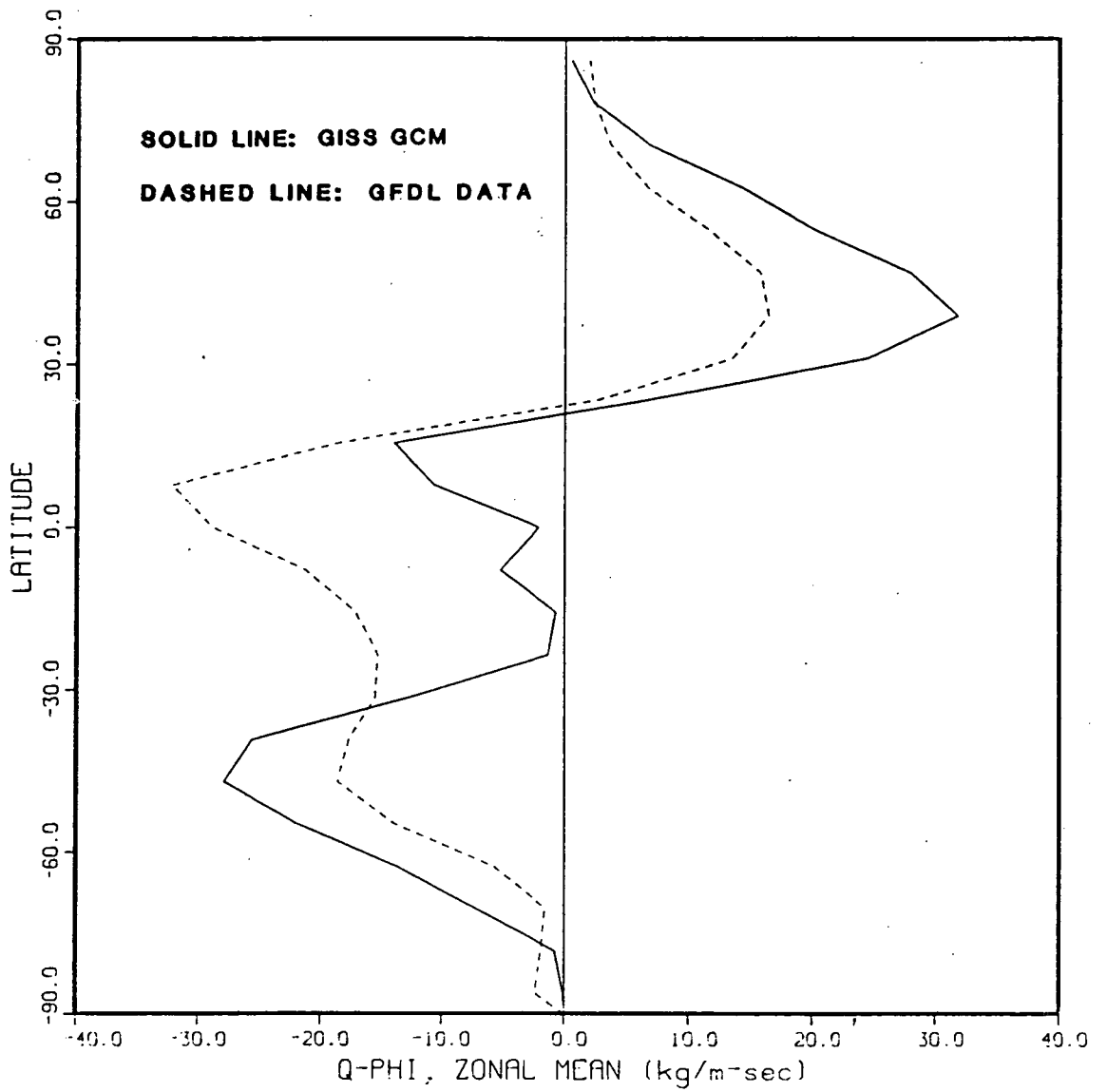
Global distributions of Q_{ϕ} for fall (SON).

a) GCM b) Observations c) Absolute differences.



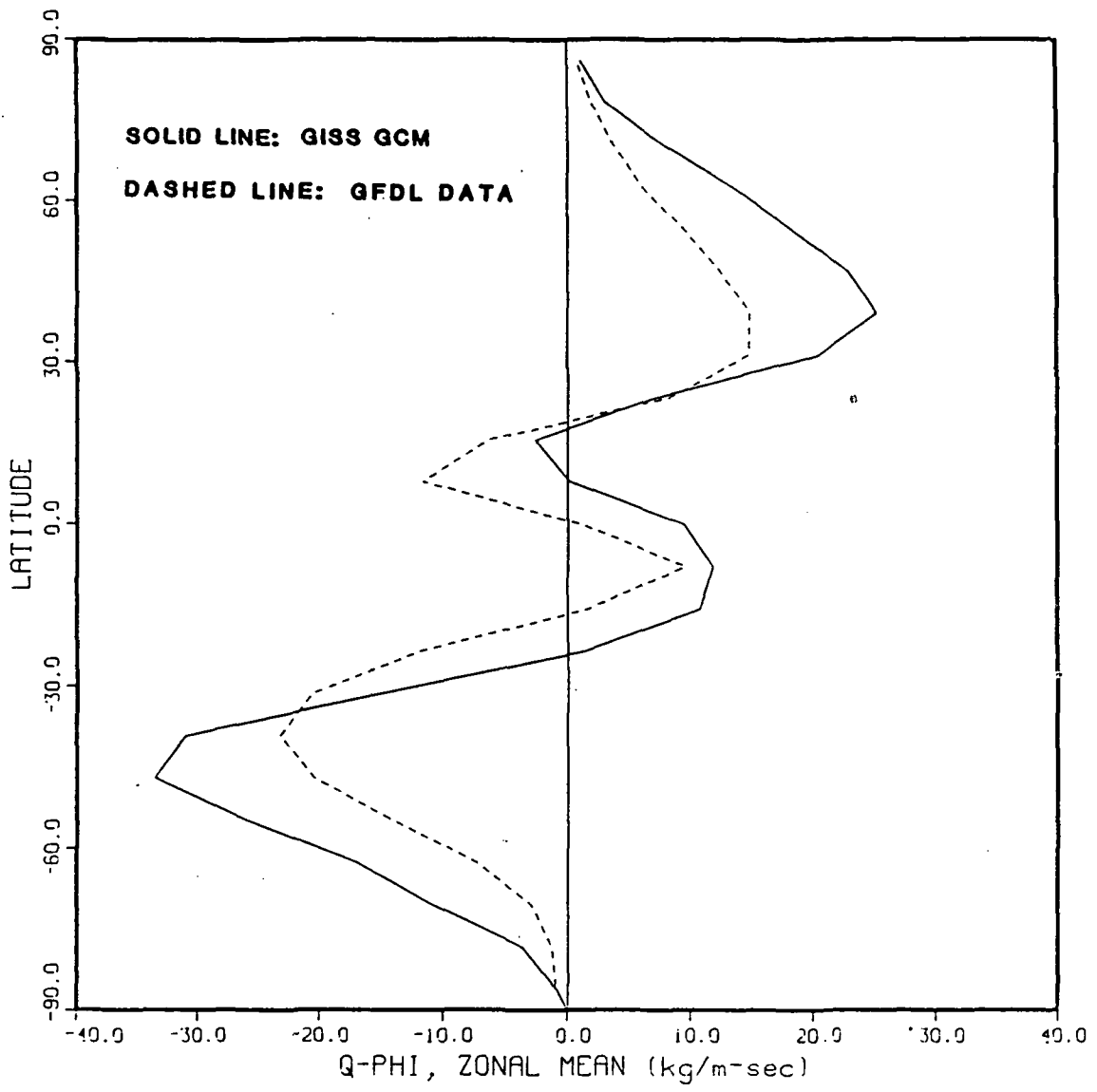
c. Absolute differences

Figure 3-9 (cont.)



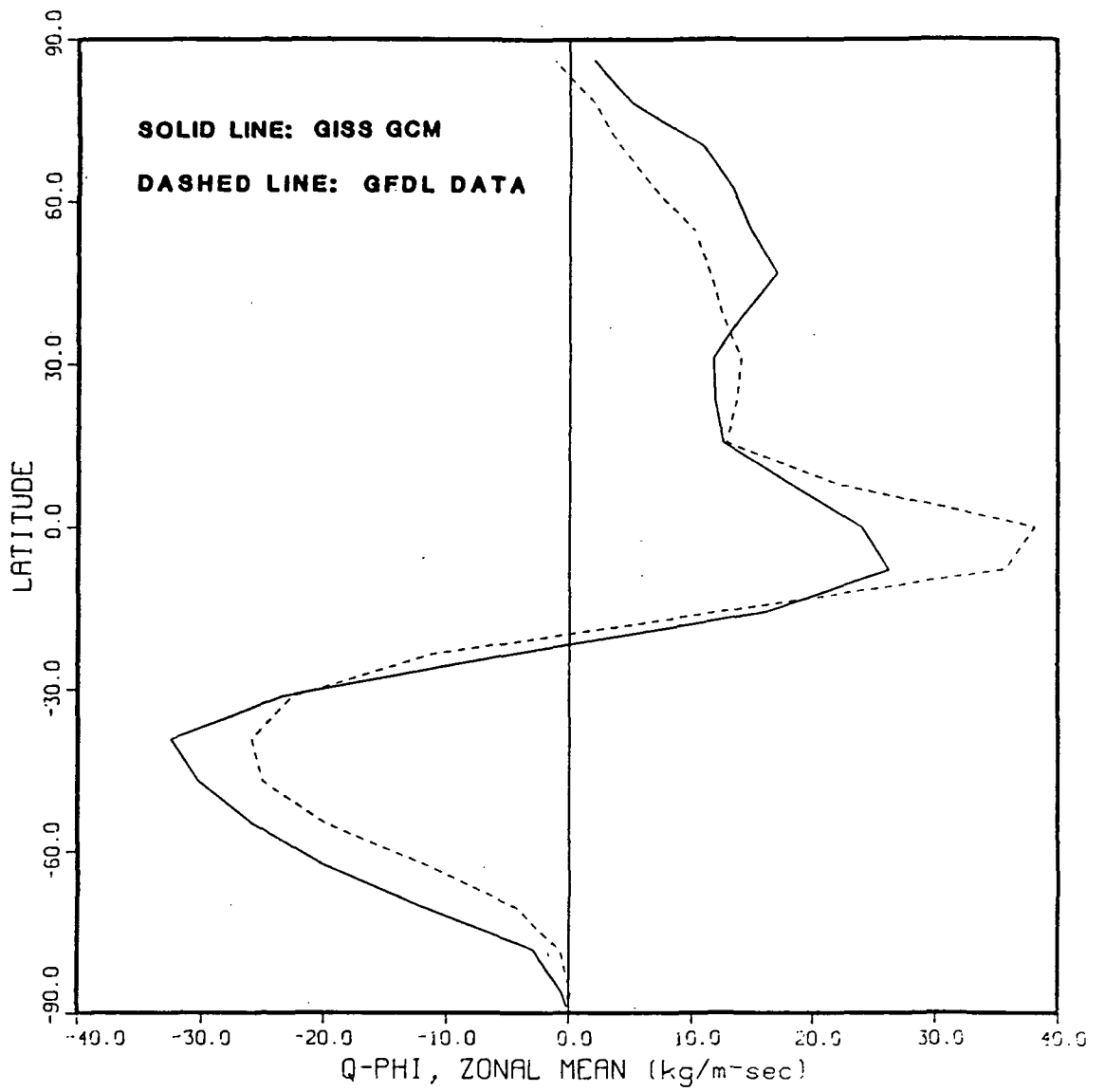
a. Winter (DJF)

Figure 3-10 Latitudinal distributions of $[Q_\phi]$.
 a) Winter (DJF) b) Spring (MAM)
 c) Summer (JJA) d) Fall (SON)



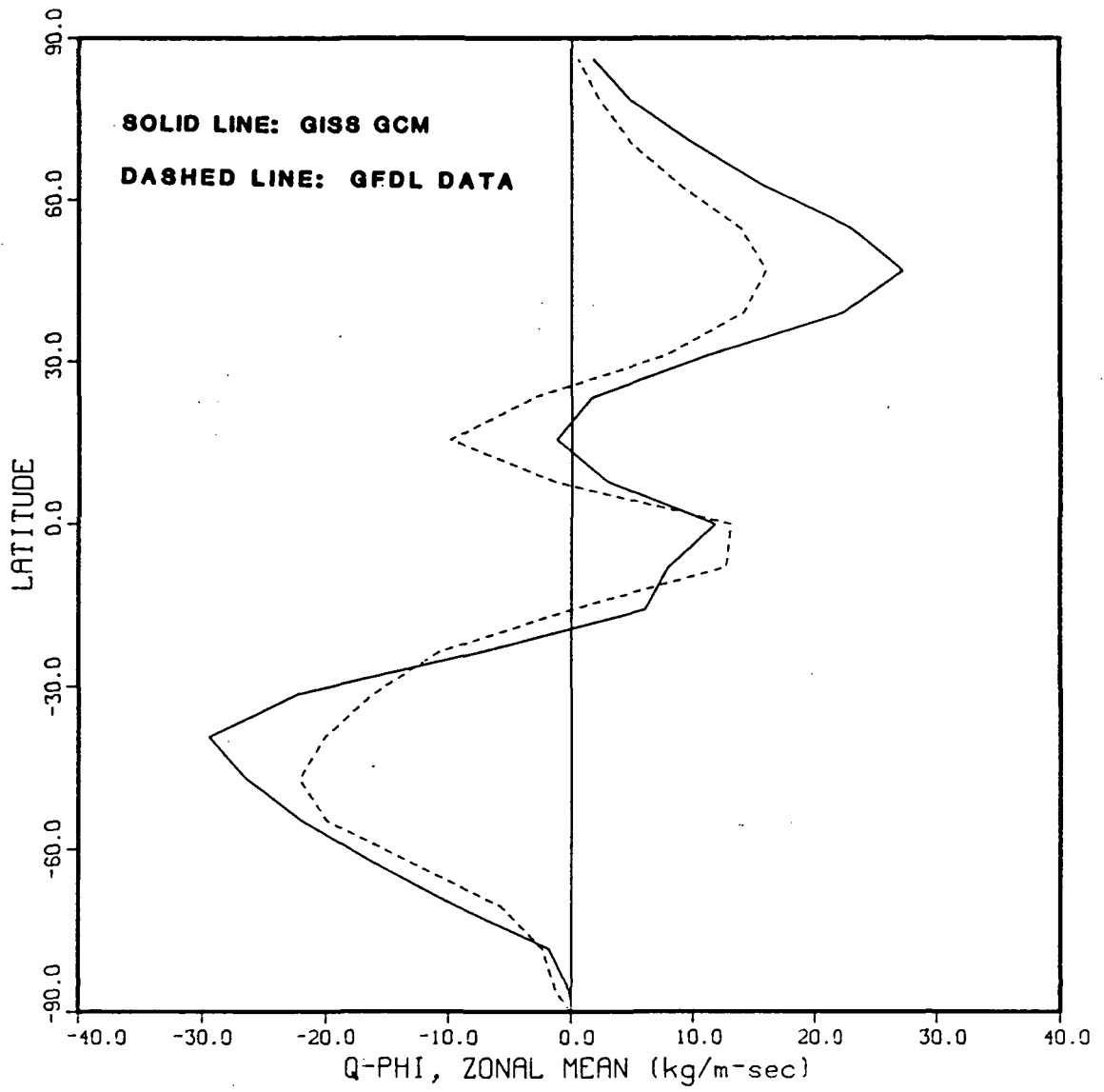
b. Spring (MAM)

Figure 3-10 (cont.)



c. Summer (JJA)

Figure 3-10 (cont.)



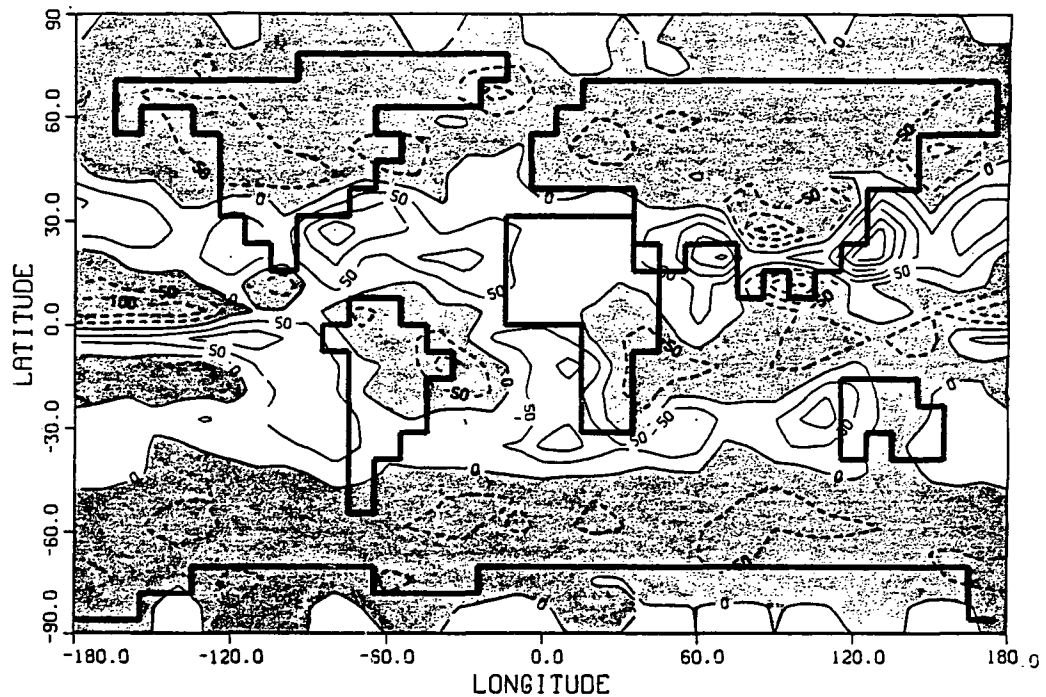
d. Fall (SON)

Figure 3-10 (cont.)

a. GISS GCM

Div(Q) (cm/year)

DJF



b. GFDL data

Div(Q) (cm/year)

DJF

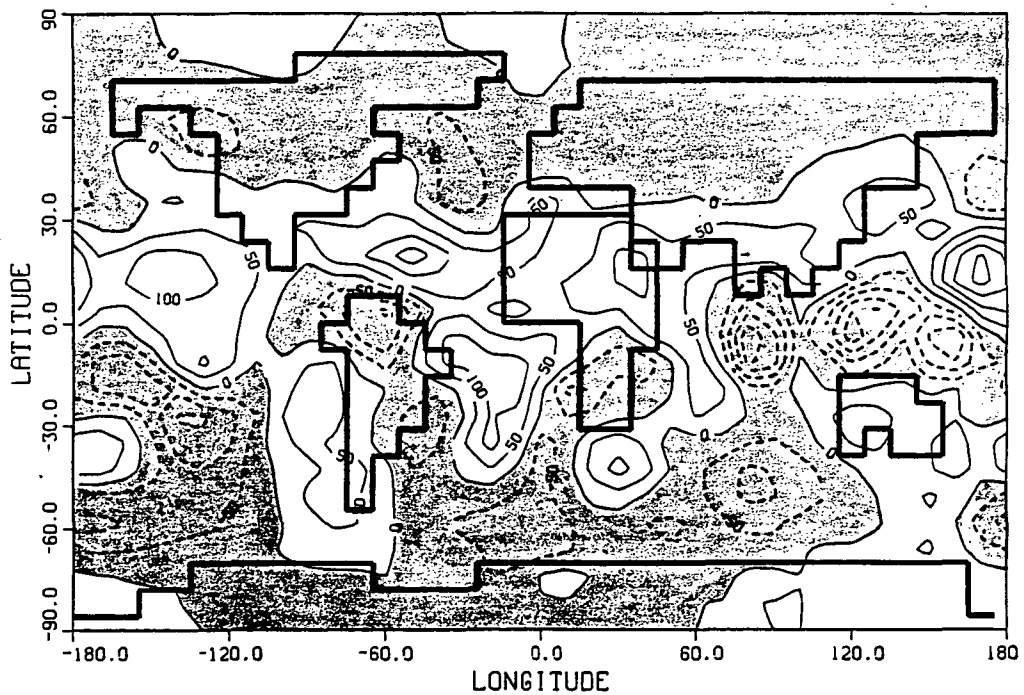
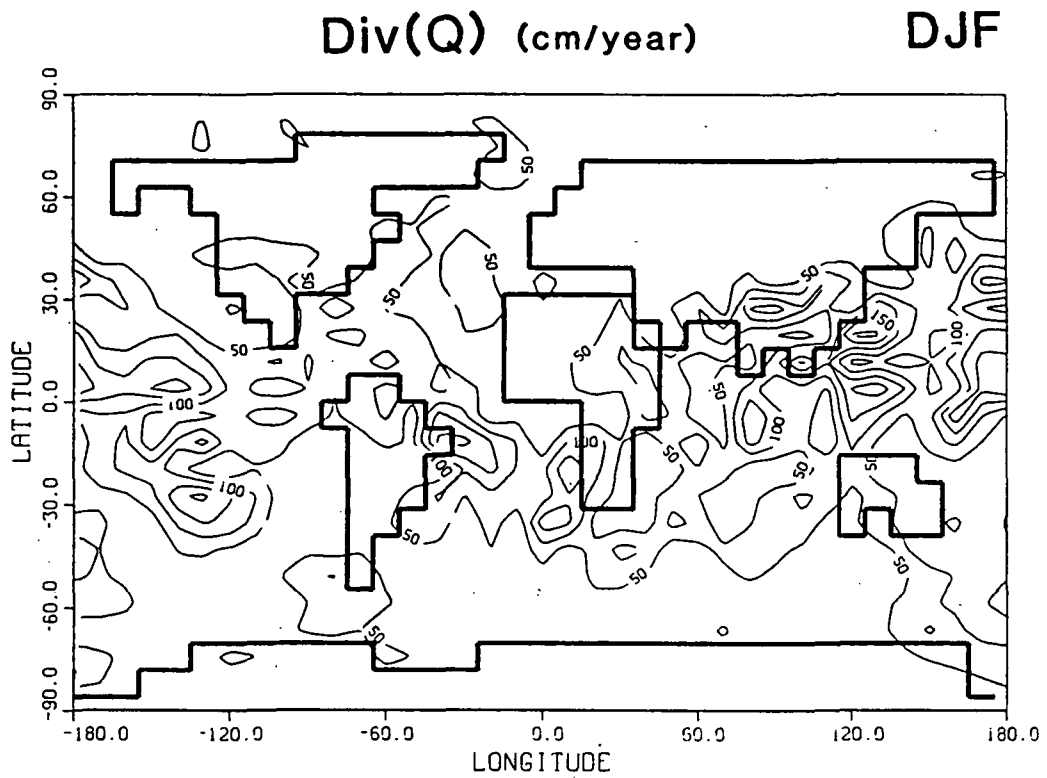


Figure 3-11 Global distributions of Div(Q) for winter (DJF).
a) GCM b) Observations c) Absolute differences



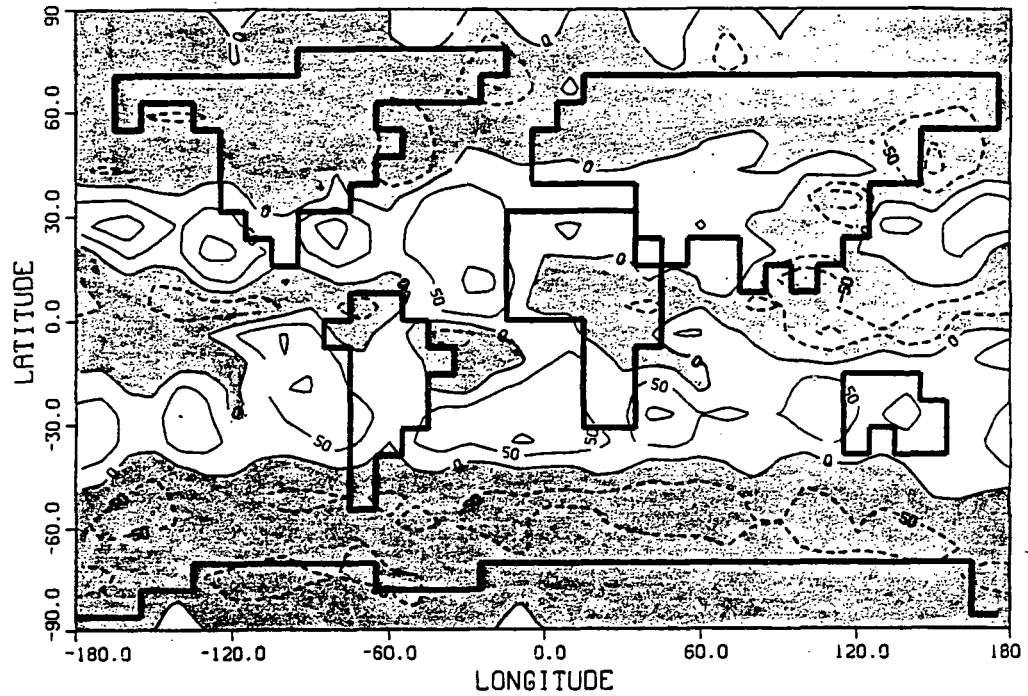
c. Absolute differences

Figure 3-11 (cont.)

a. GISS GCM

Div(Q) (cm/year)

MAM



b. GFDL data

Div(Q) (cm/year)

MAM

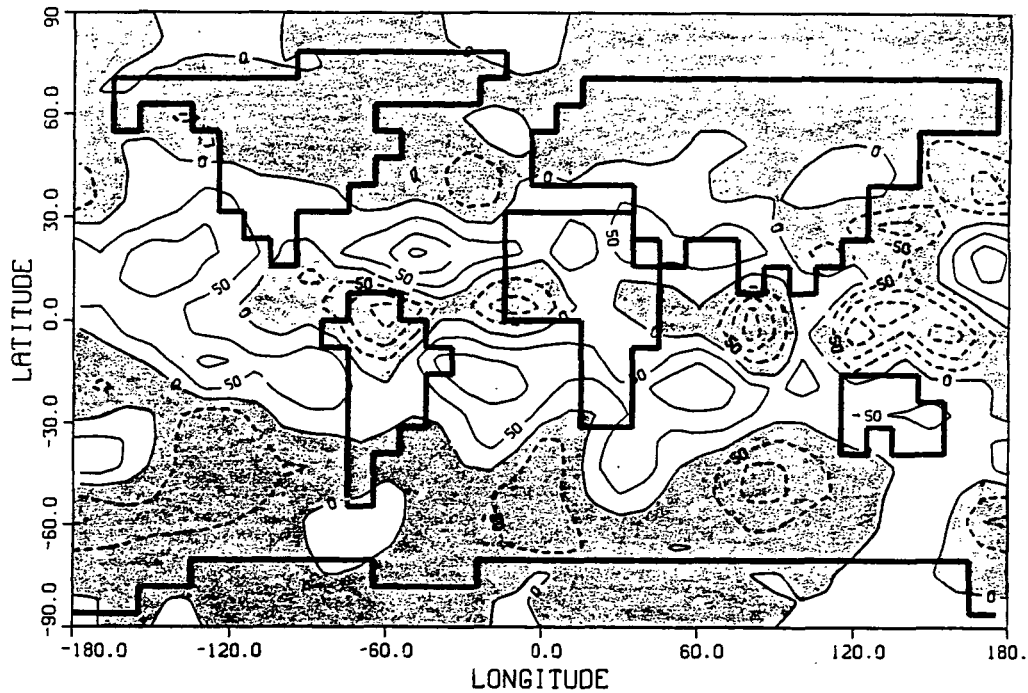
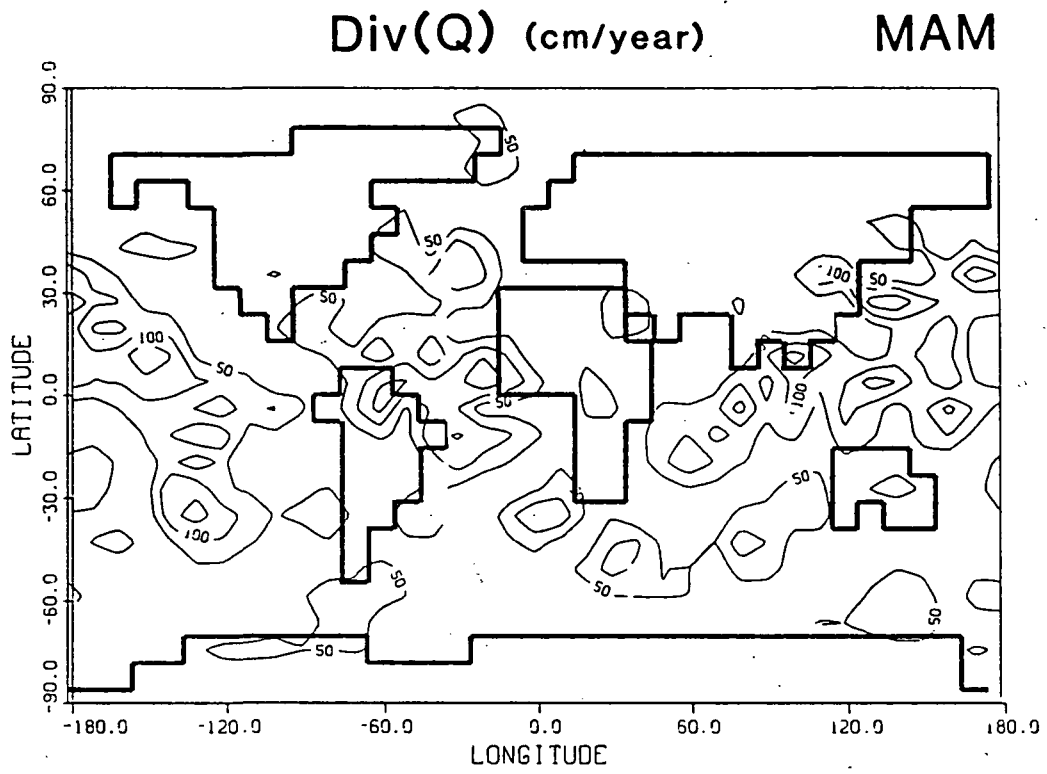


Figure 3-12

Global distributions of Div(Q) for spring (MAM).
a) GCM b) Observations c) Absolute differences



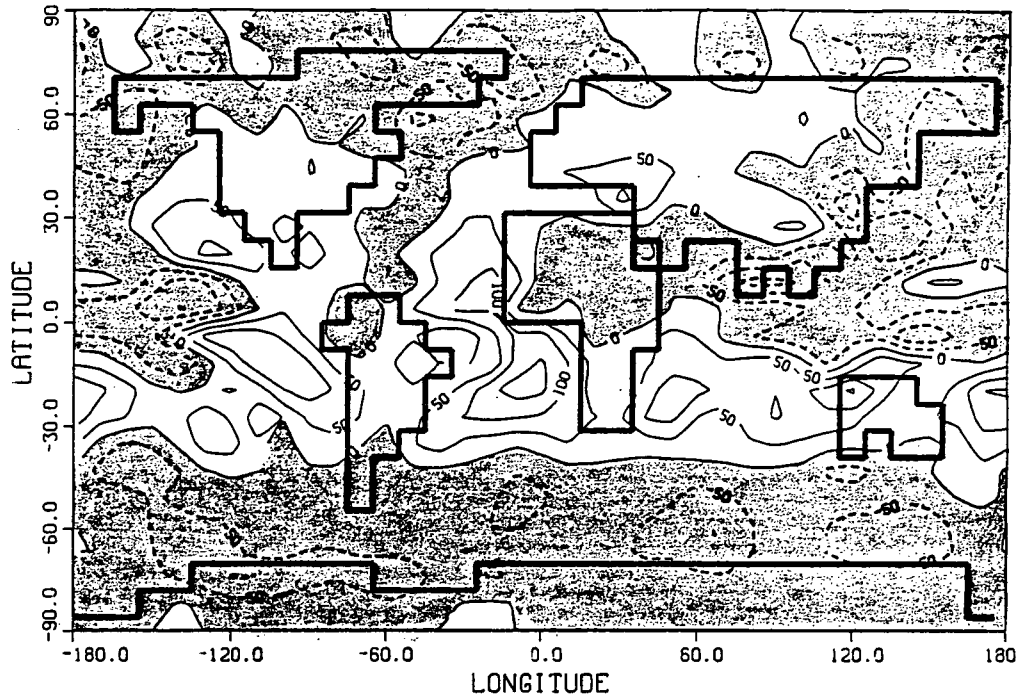
c. Absolute differences

Figure 3-12 (cont.)

a. GISS GCM

Div(Q) (cm/year)

JJA



b. GFDL data

Div(Q) (cm/year)

JJA

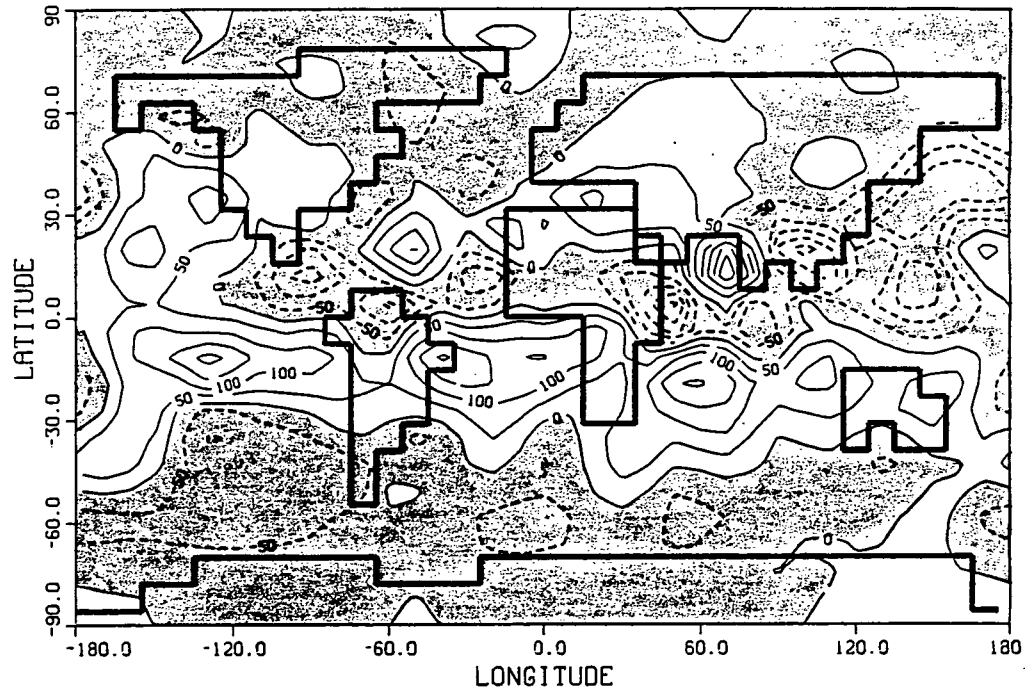
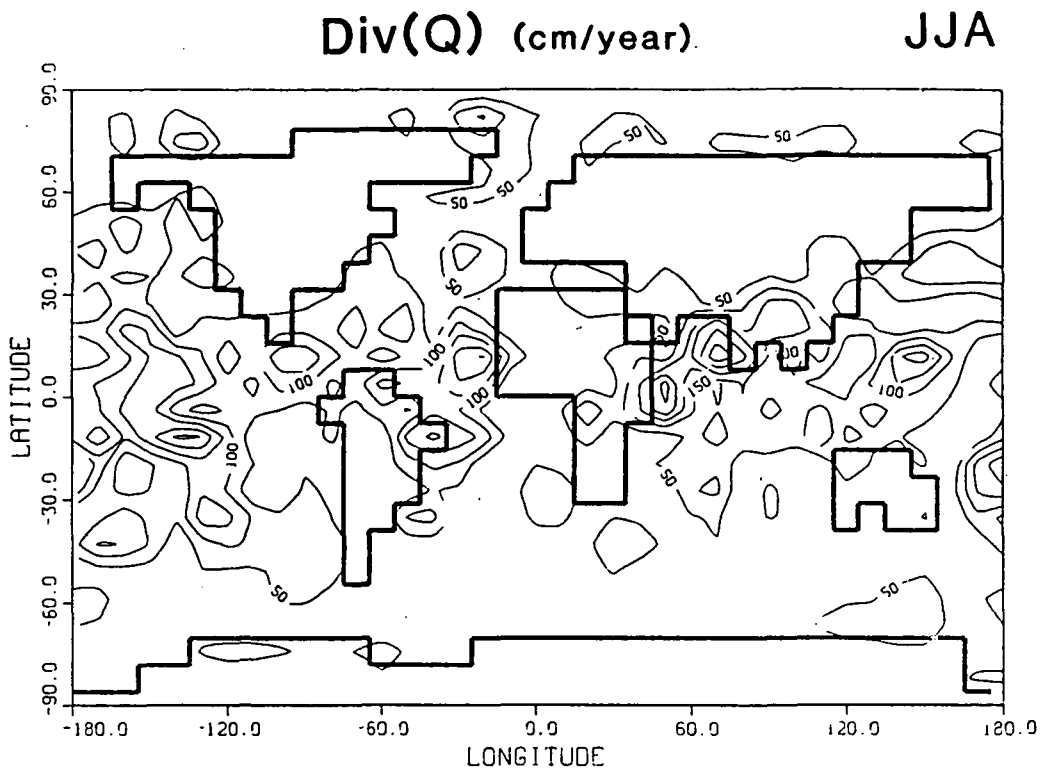


Figure 3-13

Global distributions of Div(Q) for summer (JJA).

a) GCM b) Observations c) Absolute differences

ORIGINAL PAGE IS
OF POOR QUALITY



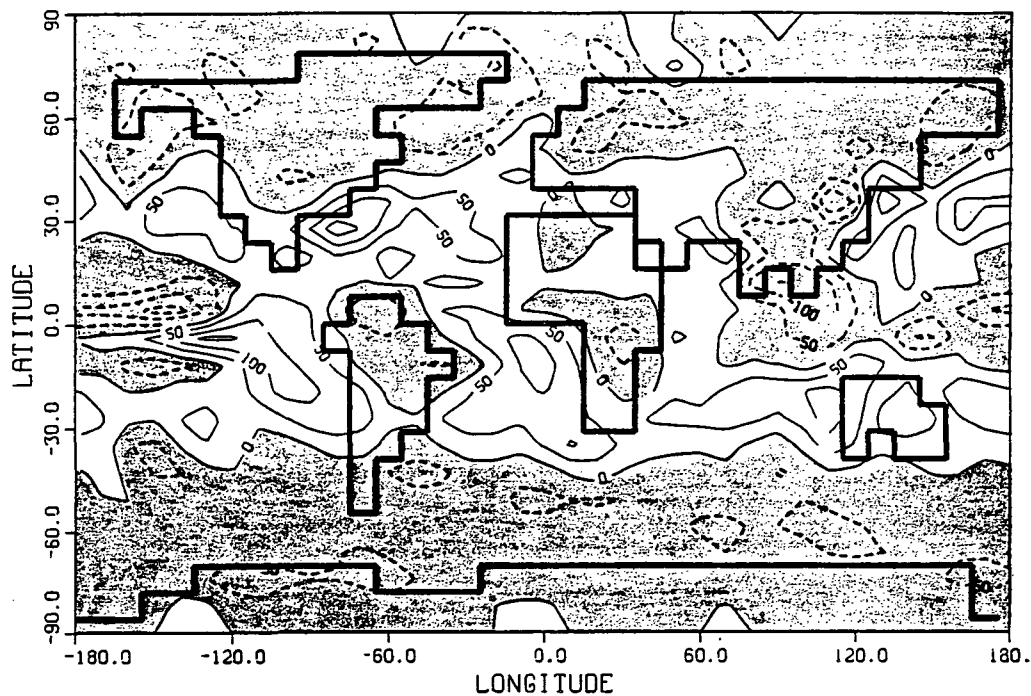
c. Absolute differences

Figure 3-13 (cont.)

a. GISS GCM

Div(Q) (cm/year)

SON



b. GFDL data

Div(Q) (cm/year)

SON

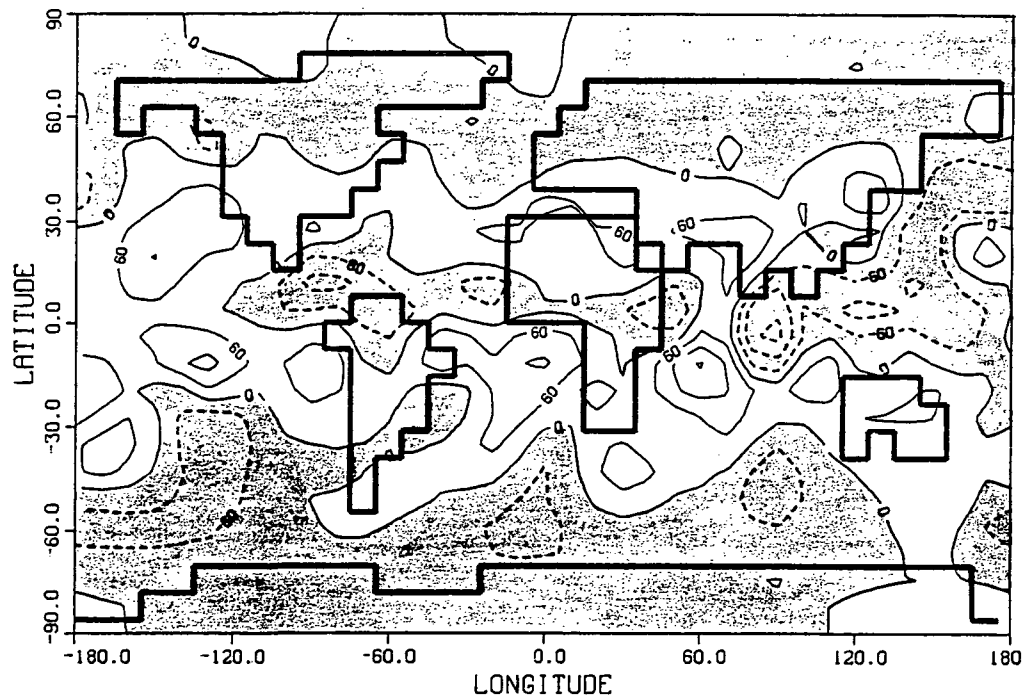
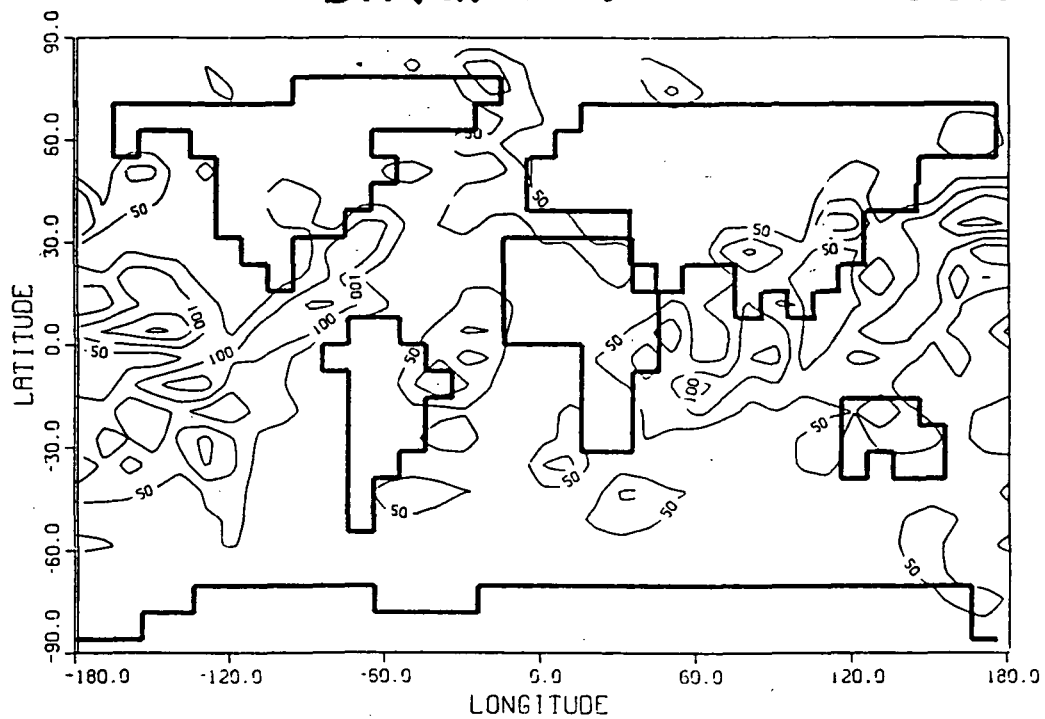


Figure 3-14 Global distributions of Div(Q) for fall (SON).
a) GCM b) Observations c) Absolute differences

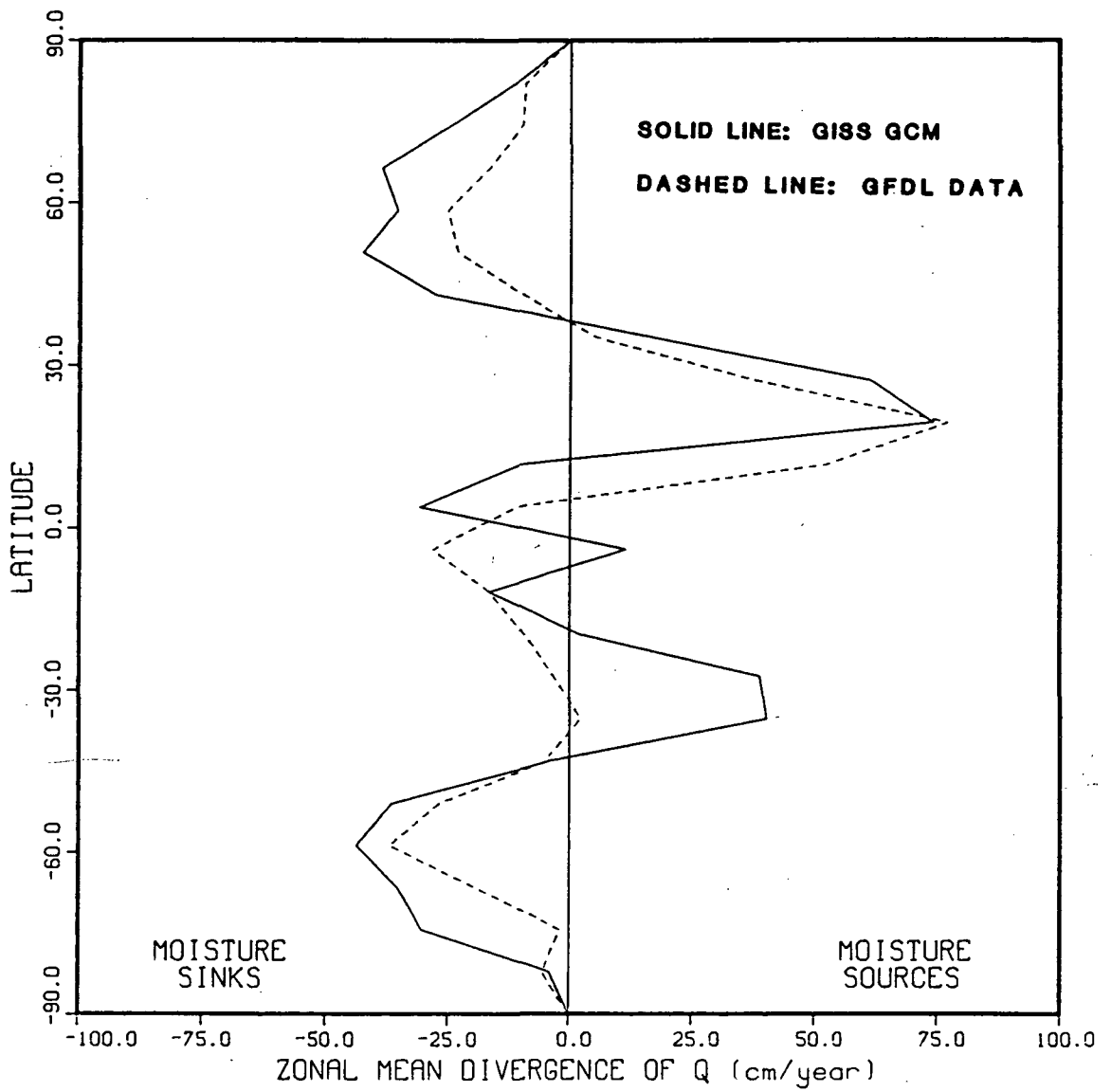
Div(Q) (cm/year)

SON



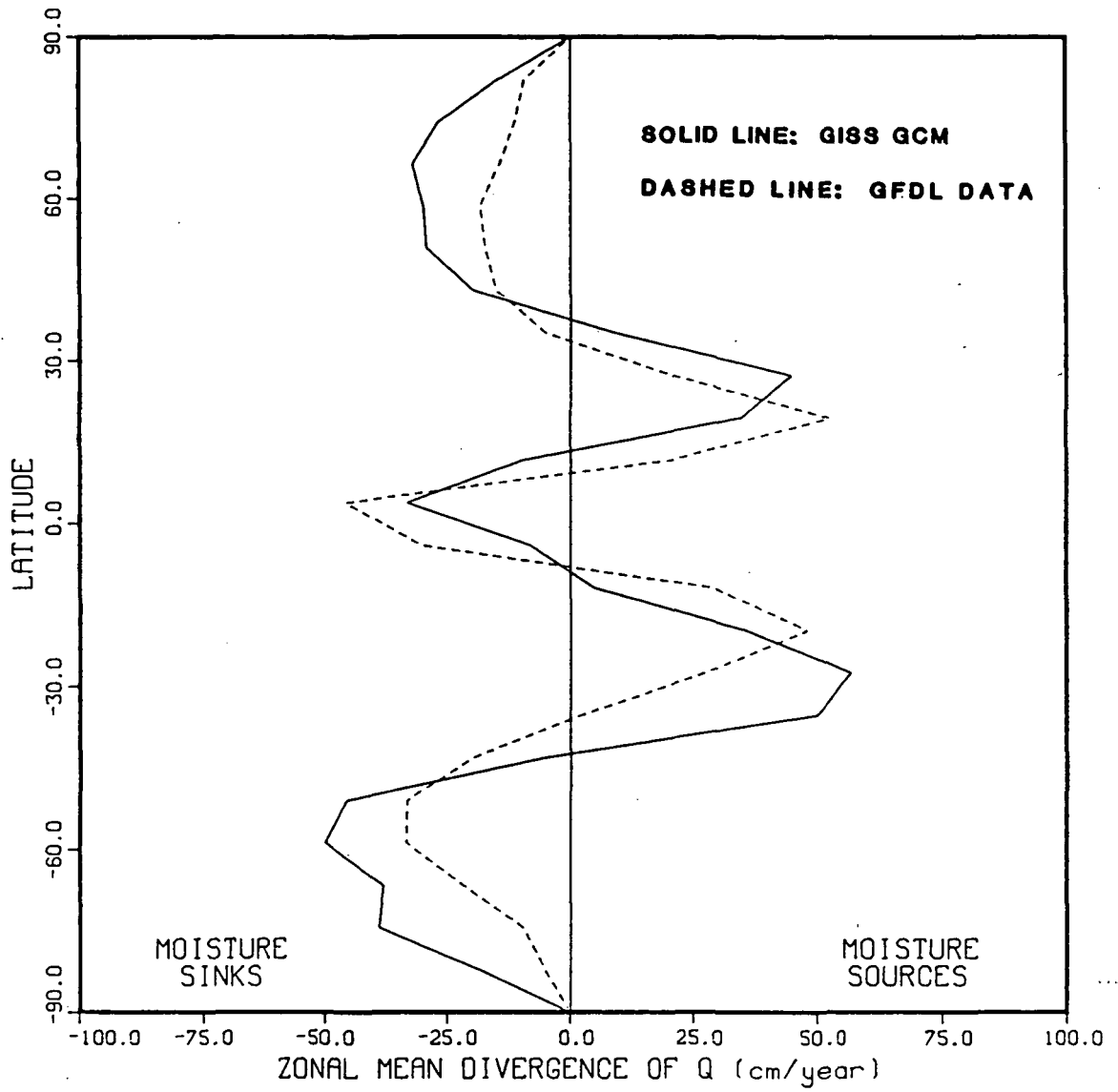
c. Absolute differences

Figure 3-14 (cont.)



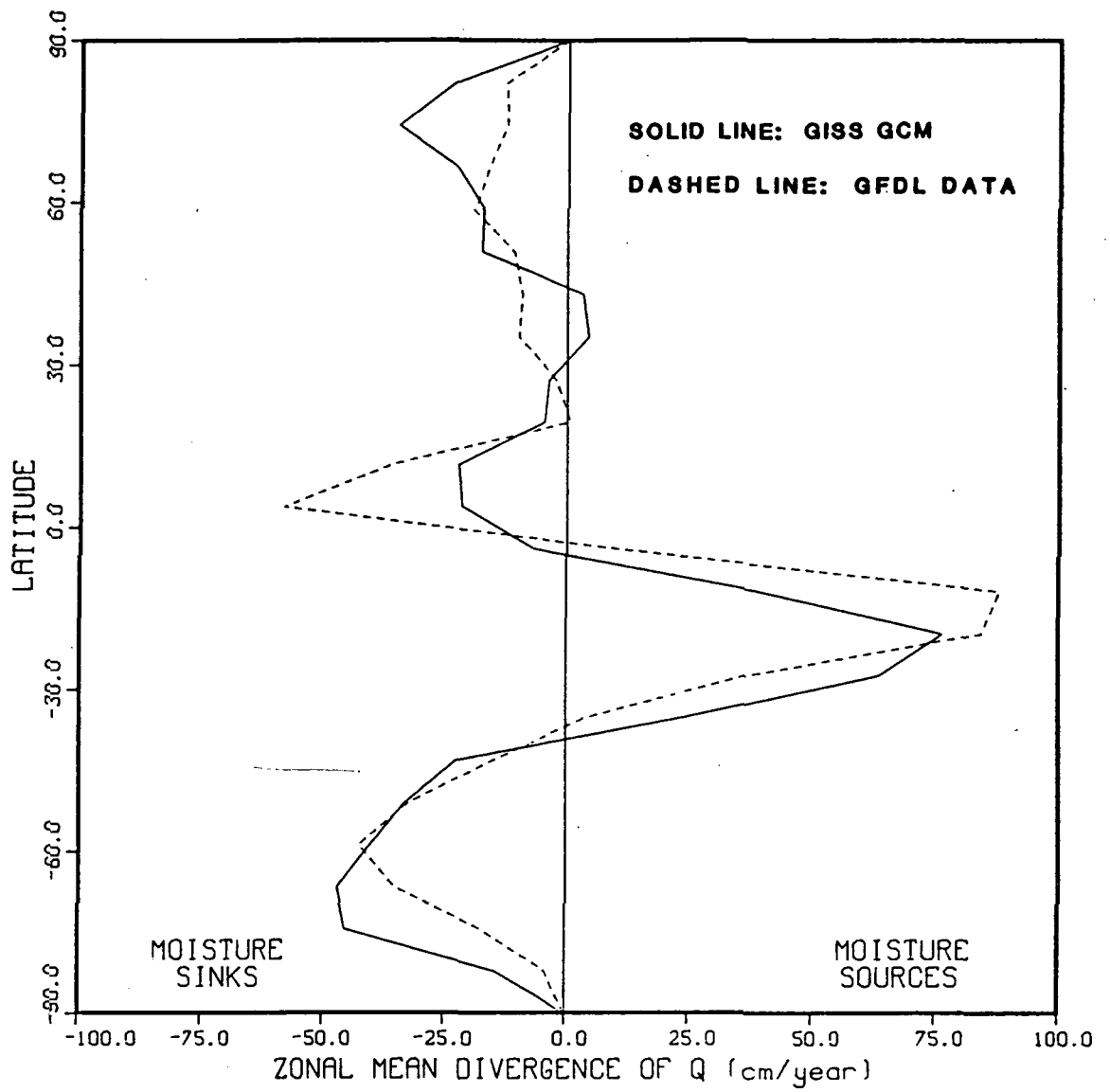
a. Winter (DJF)

Figure 3-15 Latitudinal distributions of $[\text{Div}(Q)]$.
 a) Winter (DJF) b) Spring (MAM)
 c) Summer (JJA) d) Fall (SON)



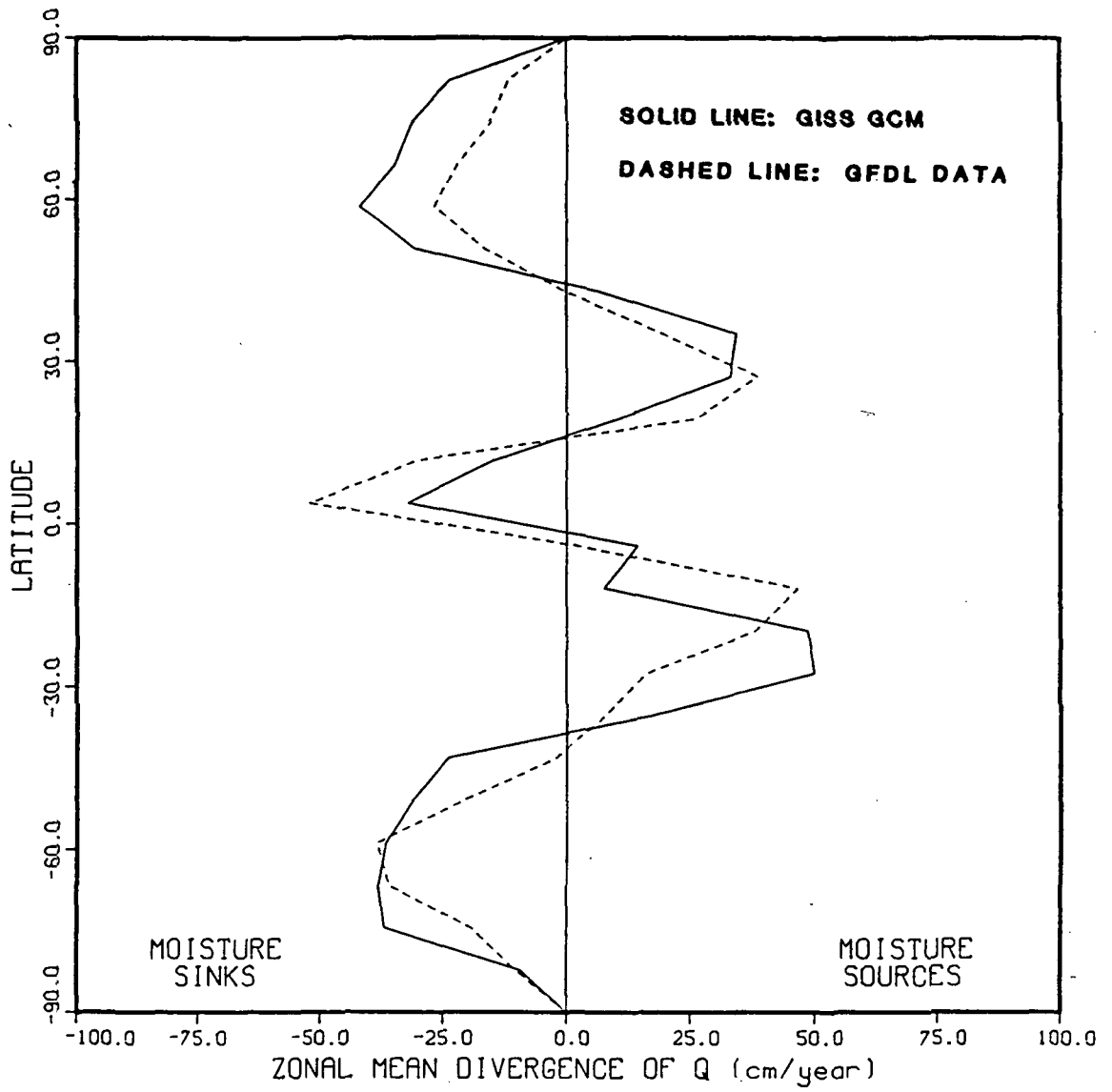
b. Spring (MAM)

Figure 3-15 (cont.)



c. Summer (JJA)

Figure 3-15 (cont.)



d. Fall (SON)

Figure 3-15 (cont.)

the observed and modeled data sets for each season, and each GCM Q_λ distribution is less smooth than the corresponding observed distribution. In the summer, the GCM spatially exaggerates the observed region of high eastward vapor flux centered in India. In the spring and fall, observations show a continuous band of high eastward vapor flux (greater than 100 kg/m-sec) in the Southern Hemisphere; the band is represented only spottily in the GCM.

The processing of the GFDL data has been checked by comparing Figures 3-1b and 3-3b with the maps of observed winter and summer Q_λ distributions provided by Peixoto and Oort (1983). Figures 3-1b and 3-3b are quite consistent with the published maps.

b) Zonal Mean Distributions. Zonal mean values of Q_λ were obtained, naturally, by averaging the Q_λ values on each row of the horizontal grid. Figure 3-5 displays $[Q_\lambda]$ (the brackets denote zonal mean) as a function of latitude for winter, spring, summer, and fall. The solid curves represent the GCM data, and the dashed curves represent the observations.

The zonal mean values of Q_ϕ ($[Q_\phi]$) provided later can indicate latitudinal sources and sinks of atmospheric moisture. No analogous information can be derived from the distribution of $[Q_\lambda]$. All quantitative information concerning meridional sources and sinks is lost in the course of zonal averaging. The distribution of $[Q_\lambda]$ reflects little more than the distribution of $[u]$, where u is the zonal component of surface wind velocity. The GCM produces $[Q_\lambda]$ distributions with the

same basic trends as the observed $[Q_\lambda]$ distributions, doing worse in the Northern Hemisphere in summer and fall. The observed distributions are much smoother than the modeled distributions. Notice that the GCM systematically underestimates the eastward zonal mean transports.

3.1.2 The Meridional Vapor Flux

The analysis of the meridional vapor flux data parallels that of the zonal vapor flux data.

a) Global Distributions. Figure 3-6a provides the GCM's distribution of Q_ϕ for the winter season, and Figure 3-6b provides the corresponding Q_ϕ distribution from the GFDL data. Dashed lines indicate contours of negative, or southward, transport. The absolute differences between the two distributions as a function of position of the globe are plotted in Figure 3-6c.

Both the GCM and observations show largely poleward transport of water vapor, with greater poleward transport off the coasts of North America, and with some equatorward transport off the west coasts of South America, Africa, and Australia. It is difficult, however, to identify any further similarities in the two Q_ϕ distributions. The GCM data exhibit a higher spatial variability and include, for example, some huge transports off the east coast of Asia that do not have observational counterparts.

Figures 3-7, 3-8, and 3-9 provide the same set of plots for spring, summer, and fall, respectively. Each of the model-generated distributions

is more spatially variable than the corresponding observed distribution. In spring, the zone of northward flow in the Pacific extends much farther south in the GCM than it does in observations, and the northward transports off the east coasts of North America and Asia are much larger in the GCM. In the summer, a region of large northward transport off the east and south coasts of Asia is clearly present in both data sets, the GCM positioning it slightly further north. In the fall, the GCM and observations disagree about the general direction of flow in Asia and the West Atlantic, and only the GCM produces very large poleward transports in the North Pacific.

b) Zonal Mean Distributions. Figure 3-10 displays the latitudinal distributions of modeled and observed zonal mean meridional vapor flux, $[Q_\phi]$, for each season. As with the $[Q_\lambda]$ values, the values of $[Q_\phi]$ were obtained by averaging over the rows of the horizontal grid. Again, the GCM data are represented by the solid curves, and the observations are represented by the dashed curves.

The GCM reproduces the basic trends in the observed $[Q_\phi]$ distributions, though it doesn't generate the observed cross-equatorial transport in winter. The GCM systematically overestimates $[Q_\phi]$ in midlatitudes and high latitudes. Thus, on the average, the GCM transports more water vapor poleward than indicated by observations. A possible reason for this is provided in Section 3.1.5.

3.1.3 The Total Vapor Flux Divergence

Regions with positive vapor flux divergence in the steady state evaporate more water into the atmosphere than they receive through precipitation; they therefore act as sources of atmospheric moisture. Conversely, regions with negative vapor flux divergence receive excess precipitation and act as moisture sinks. Since the vapor flux divergence distribution is effectively a distribution of atmospheric moisture sources and sinks, it should serve as a useful diagnostic of the GCM's hydrologic cycle.

The divergence of vapor flux on the spherical earth is defined as

$$\text{Div}(Q) = \frac{1}{a_o \cos \phi} \left[\frac{\partial Q_\lambda}{\partial \lambda} + \frac{\partial}{\partial \phi} (Q_\phi \cos \phi) \right] \quad (3-3)$$

This equation was applied in the finite difference form:

$$\text{Div}(Q) \approx \frac{1}{a_o \cos \phi_j} \left[\frac{Q_{\lambda ij} - Q_{\lambda i-1, j}}{\Delta \lambda} + \frac{Q_{\phi i, j+1} \cos \phi_{j+1/2} - Q_{\phi ij} \cos \phi_{j-1/2}}{\Delta \phi} \right] \quad (3-4)$$

for grid square i, j , with a_o being the earth's radius and $\phi_{j+1/2}$, ϕ_j , and $\phi_{j-1/2}$ being the latitudes at the top, the center, and the bottom of the grid square, respectively. The divergences at the poles were automatically set to zero.

a) Global Distributions. Figures 3-11a and 3-11b present the modeled and observed distributions of total vapor flux divergence for the winter season. Isocontours of negative divergence (i.e. moisture sinks) are shown as dashed curves. The absolute differences between the values of the two data sets are plotted in Figure 3-11c. The corresponding set of plots for spring, summer, and fall are shown in Figures 3-12, 3-13, and 3-14, respectively.

For each season, both the modeled and the observed distributions identify the subtropics and parts of the tropics as the main sources for atmospheric moisture. Midlatitudes and high latitudes generally appear in both distributions as moisture sinks. Notice that in both data sets, some midlatitude continental regions that are moisture sinks in the winter become moisture sources in the summer.

It is difficult, however, to go beyond these generalities and identify specific structures in the GCM data that are also present in the observations. Specific differences, in fact, abound. In the summer, for example, the GCM does not reproduce the observed narrow band of convergence crossing the Atlantic at the equator. Also in the summer, the GCM simulates a large convergence in India, while the observations indicate a strong divergence there.

b) Zonal Mean Distributions. Averaging the values of $\text{Div}(Q)$ over each row of the horizontal grid produced the zonal mean values, $[\text{Div}(Q)]$. The latitudinal distributions of $[\text{Div}(Q)]$ are shown for each season in Figure

3-15, with solid lines representing the model results and dashed lines representing the observations.

Certain seasonal trends are inherent in both the modeled and the observed distributions of zonal mean divergence. In the winter, the Northern Hemisphere subtropics provide the moisture for the other latitudinal bands, though the GCM data also indicate some positive divergence in the Southern Hemisphere. The large subtropical source strength may correspond to the downward branch of the Northern Hemisphere Hadley cell. In the spring, the Northern and Southern Hemisphere subtropics are moisture sources, while the equatorial, midlatitude, and high latitude bands are moisture sinks. The Southern Hemisphere subtropics are the only source of moisture in the summer. Fall has the same moisture sources and sinks as spring.

Some differences between the data sets, however, are also apparent. In both spring and fall, the GCM places the latitudes of maximum $[\text{Div}(Q)]$ further from the equator than the observations do. Also, the GCM systematically overestimates the observed vapor flux convergence at high latitudes, implying an excessive poleward transport of water. This, remember, was also indicated from the plots of the $[Q_\phi]$ distributions.

3.1.4 Specific and Relative Humidities

It is important that the simulated global distributions of specific humidity match reasonably well with the observed distributions. The model cannot be expected to transport water vapor realistically if it holds too much or too little water vapor in the air.

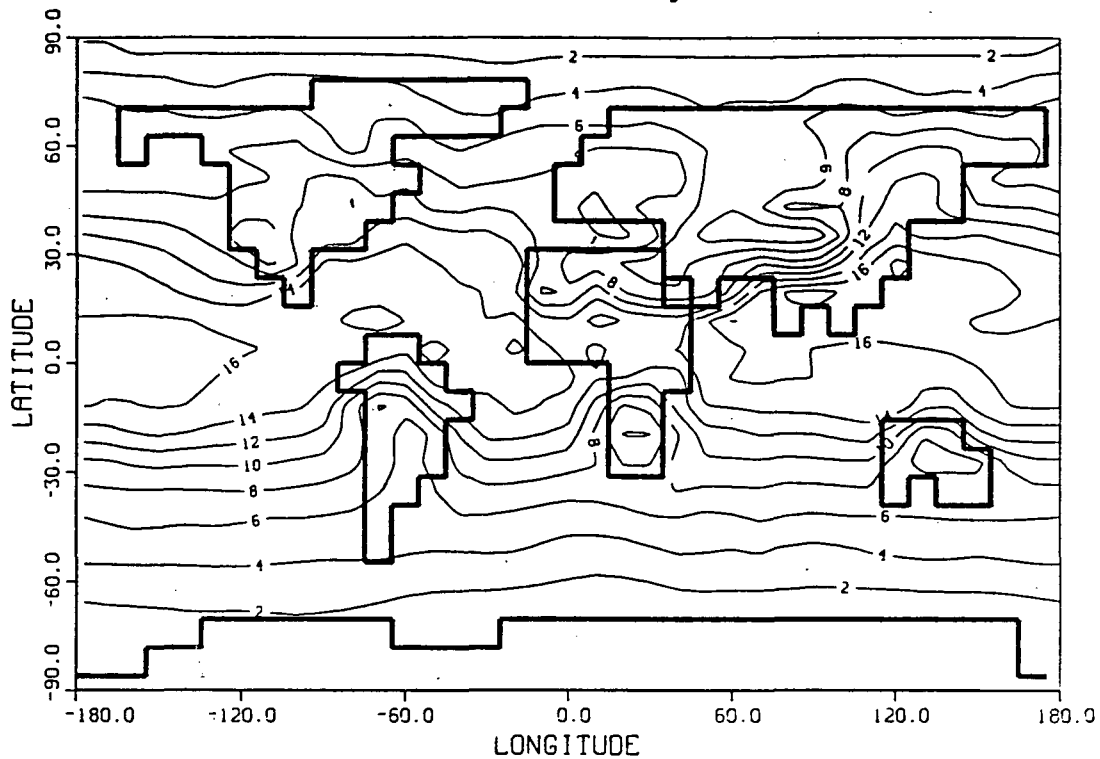
An average global specific humidity distribution for the lowest GCM atmospheric layer was obtained from five July simulations. (These are the same five simulations that will be discussed in Section 3.2.) The GCM specific humidities are approximate; since the model saved only the average total water mass in each grid box for each simulation, an average GCM summer surface pressure field had to be applied to estimate the corresponding grid box air masses. The GCM summer surface pressure field was also used to establish the ground level when processing the GFDL specific humidity data.

Figure 3-16a shows the GCM specific humidity distribution, and Figure 3-16b shows the distribution of ground level specific humidity obtained from summer (JJA) GFDL data. The two distributions have basically the same structure. Notice in both distributions the steady decrease of specific humidity as one moves toward the poles or toward the interiors of continents. Agreement between the two distributions over the oceans is actually not surprising, given that GCM sea surface temperatures are assigned observed climatic mean values. It is encouraging, though, that the magnitudes of modeled and observed specific humidity are generally the same over continents.

The air above climatic regions such as deserts or wetlands, however, is characterized more by its relative humidity than by its specific humidity. Thus, global distributions of relative humidity are compared in Figure 3-17. To produce the distribution for the GISS GCM in Figure 3-17a, the average July specific humidity in each first layer grid box was divided by the saturated specific humidity at the average July grid box

a. GISS GCM specific humidity distribution for July

(Units: g/kg)



b. Observed specific humidity distribution for summer

(Units: g/kg)

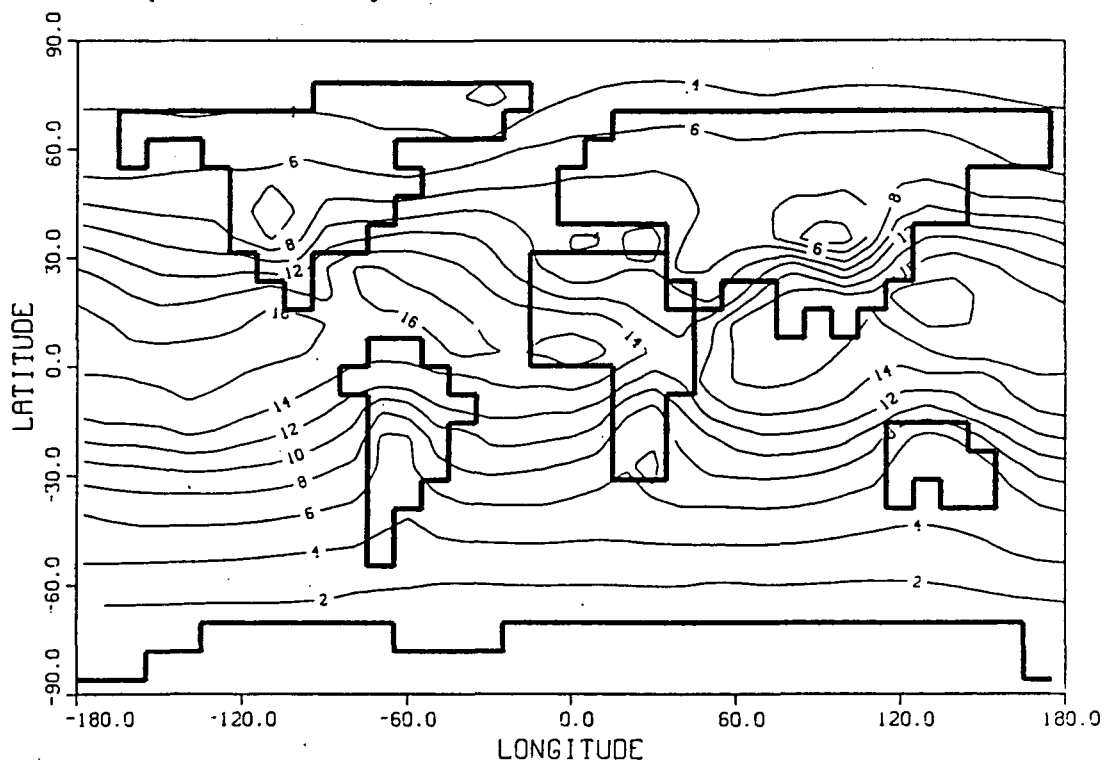
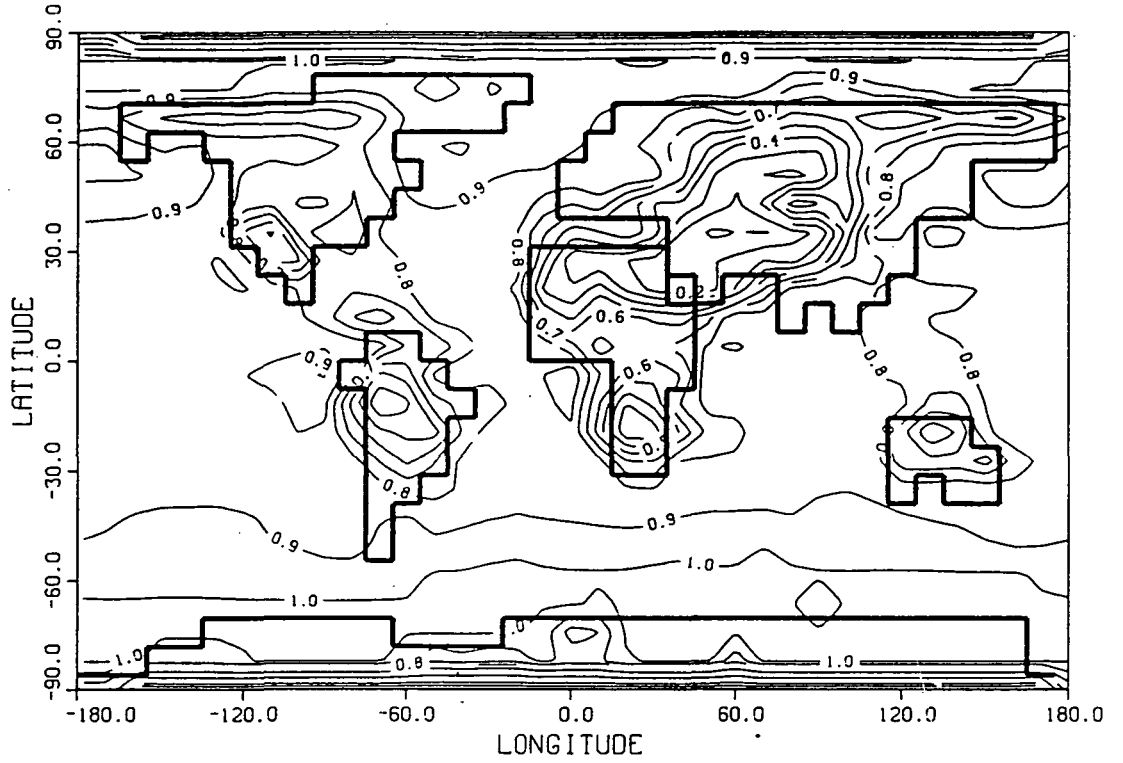


Figure 3-16 Global distributions of specific humidity.
a) GCM (July) b) GFDL Data (summer, JJA)

a. GISS GCM relative humidity distribution for July



b. Observed relative humidity distribution for summer

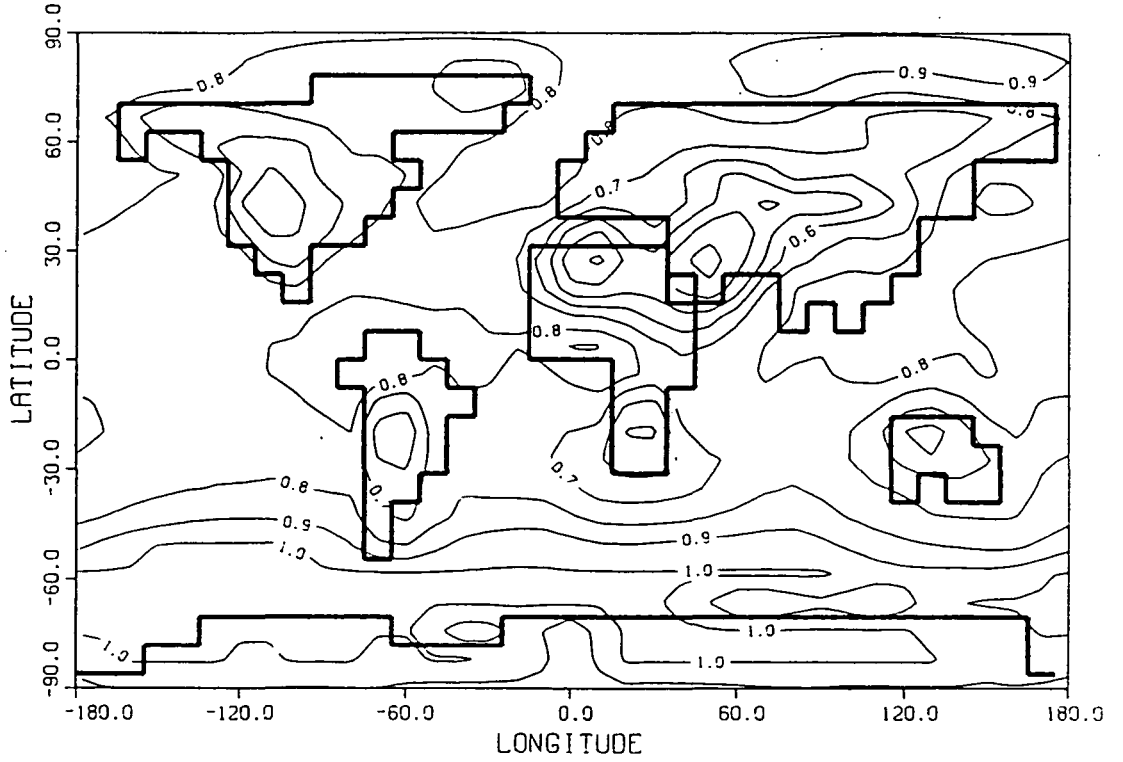


Figure 3-17 Global distributions of relative humidity.
 a) GCM (July) b) GFDL Data (summer, JJA)

temperature. The "observed" distribution in Figure 3-17b was obtained in the same way, using ground-level summer (JJA) specific humidities and temperatures from the GFDL data set. The average GCM summer surface pressure field was used in the processing of both data sets. Due to the various approximations made, relative humidities calculated near the poles tended to be greater than 1; these relative humidities were reset to 1 for purposes of illustration.

Both the modeled and the observed distributions show reduced relative humidities over each continent. The GISS GCM correctly simulates certain desert features; it identifies, for example, North Africa and the Middle East as being particularly dry. The GCM, however, generally overestimates the dryness of continental interiors. For example, the minimum relative humidities generated by the GCM in South America and Southern Africa are two-tenths lower than those obtained from observations. On the other hand, the GCM seems to generate excessively high relative humidities over the oceans. The combined behavior is reflected in the GCM's larger horizontal relative humidity gradients.

It is not surprising that the magnitudes of the relative humidities produced by the GCM differ from those in the real world. Relative humidities in the lowest atmospheric layer of the GCM may be controlled in part by the parameterization of surface evaporation. In certain sensitivity simulations, to be described in Section 3.3, arbitrarily increasing the transfer coefficient C_q in Equation 2-15 apparently induces a corresponding decrease in the average humidity deficit

$q_G - q_S$. The lower deficit effectively reduces the change in the net global evaporation caused by the change in C_q and may be related to an increase in relative humidity. Relative humidities may therefore be influenced by C_q . The best value to use for this parameter has never been known with certainty.

3.1.5 Discussion

The NASA/GISS GCM's generated distributions of zonal vapor flux, meridional vapor flux, and vapor flux divergence, in both global and zonal mean form, have the same basic structures and exhibit the same basic trends as the corresponding observed distributions. It is not surprising that the model-generated and observed vapor flux values have similar magnitudes; the GCM produces reasonable surface wind fields (Hansen et al, 1983), and the specific humidities above the ocean are largely controlled by prescribed ocean surface temperatures. Inconsistencies between the model data and observations abound, however, especially at smaller spatial scales.

Four possible reasons for these inconsistencies come to mind. First, they may be due to the second-order differencing scheme used for vapor transport, which, though stable, is inferior to certain other available schemes. Second, vapor flux divergence has a first-order dependence on evaporation and precipitation, and thus inconsistencies between the modeled and observed divergence distributions might result from inadequate parameterizations of these two subgrid processes. The present simplicity of the GCM's ground hydrology, for example, might easily reduce the accuracy of simulated continental evaporation rates. Third, some features of

the observed data may be too fine to be reproduced by a GCM using a coarse $8^\circ \times 10^\circ$ grid. The narrow band of convergence in the Tropical Atlantic seen in the observed summer $\text{Div}(Q)$ distribution, for example, has a thickness of approximately one or two coarse grid squares; the GCM rarely produces dependable results on that small a scale. Finally, the observations themselves may be faulty. The gradient of $\text{Div}(Q)$ between India and Somalia in the summer observations, for example, looks suspiciously large. Observations are especially sparse in the Southern Hemisphere.

An interesting difference between the model results and observations is the aforementioned excessive poleward transport of water in the GCM. GISS personnel speculate that the problem is one of grid resolution. With the coarse ($8^\circ \times 10^\circ$) resolution, the model stores too much energy in wave numbers 6 through 10, and these wave numbers are associated with transient eddy transports in the lower troposphere, where most of the water vapor is. With a finer grid, more energy is stored in lower wave numbers, which are less concentrated in the lower troposphere and therefore transport less water. A comparison of zonally-averaged latent heat convergence in winter for a coarse grid run, a fine grid ($4^\circ \times 5^\circ$) run, and observations (not provided here) provides evidence that a fine grid run does indeed better reproduce the observed convergences.

3.2 Inter-annual Variability

The tracer water fluxes presented as model output in this report are generally obtained by integrating hourly tracer fluxes over a single simulation month. If, however, in an extended simulation a given month's tracer transport characteristics vary greatly from year to year, the tracer

results from a single one-month simulation would be of little practical use. It is necessary, therefore, to examine the inter-annual variability of the tracer water model results in detail.

Hansen et al (1983) provide a discussion of the interannual variability inherent in the GCM's temperature, precipitation, and pressure fields. Standard deviations of January and July monthly temperatures at 850 mb, for example, were determined from five years of model data and were compared to the corresponding observed standard deviations. The magnitude and geographical distribution of the model's temperature variability was found to agree well with observations over continents but fall short of observations over the oceans, apparently due to the assignment of climatic mean temperatures to the ocean surface. The standard deviation of the model's July temperature over continents is generally between 1° and 4°K, while that of January temperatures is slightly higher, exceeding 5°K in parts of Northern Canada and Western China. Standard deviations of modeled 850 mb temperatures over oceans are generally less than 2°K for both months.

The relative variability of annual precipitation in the model also agrees roughly with observations. The relative variability generally lies between ten and twenty percent, with regions of higher variability being centered over deserts. Hansen et al (1983) further comment on the excessively low variability produced by the model over the Equatorial Pacific. They also note that sea level pressure fields produced by the model exhibit strong interannual variability, of the order observed in nature.

The experiment described now, however, provides the most relevant information concerning the inter-annual variability of tracer transport. During the five year Model II GISS GCM simulation described by Hansen et al (1983), GISS researchers stored on tape the instantaneous state of the atmosphere and surface at the beginning of each simulation month. Each instantaneous state is consistent with the inherent Model II climate and thus provides a suitable set of initial conditions for a tracer water model simulation. A single tracer water experiment was repeated five times with five different sets of June 1 initial conditions, and the average tracer transports in five different summers were then computed and compared.

The experiment followed the motion of an aboveground tracer (see Section 2.4) evaporating from a source region in Southeast Asia. The model atmosphere was completely devoid of tracer at the beginning of the simulation. At each time step, the source region (a single grid square) evaporated tracer into the overlying grid box at the water evaporation rate, as described in Section 2.4.2. The atmospheric residence time of an evaporated tracer was seen in preliminary simulations to be on the order of days; thus, a one-month start-up time was considered sufficient to bring the tracer to its proper steady-state atmospheric distribution. The downward precipitation flux of the tracer onto each grid square was monitored for thirty simulation days, starting on July 1.

The resulting spatial distributions of tracer precipitation for all five simulations are shown in Figure 3-18. The exact location of the source region is indicated by the small shaded square. The results imply

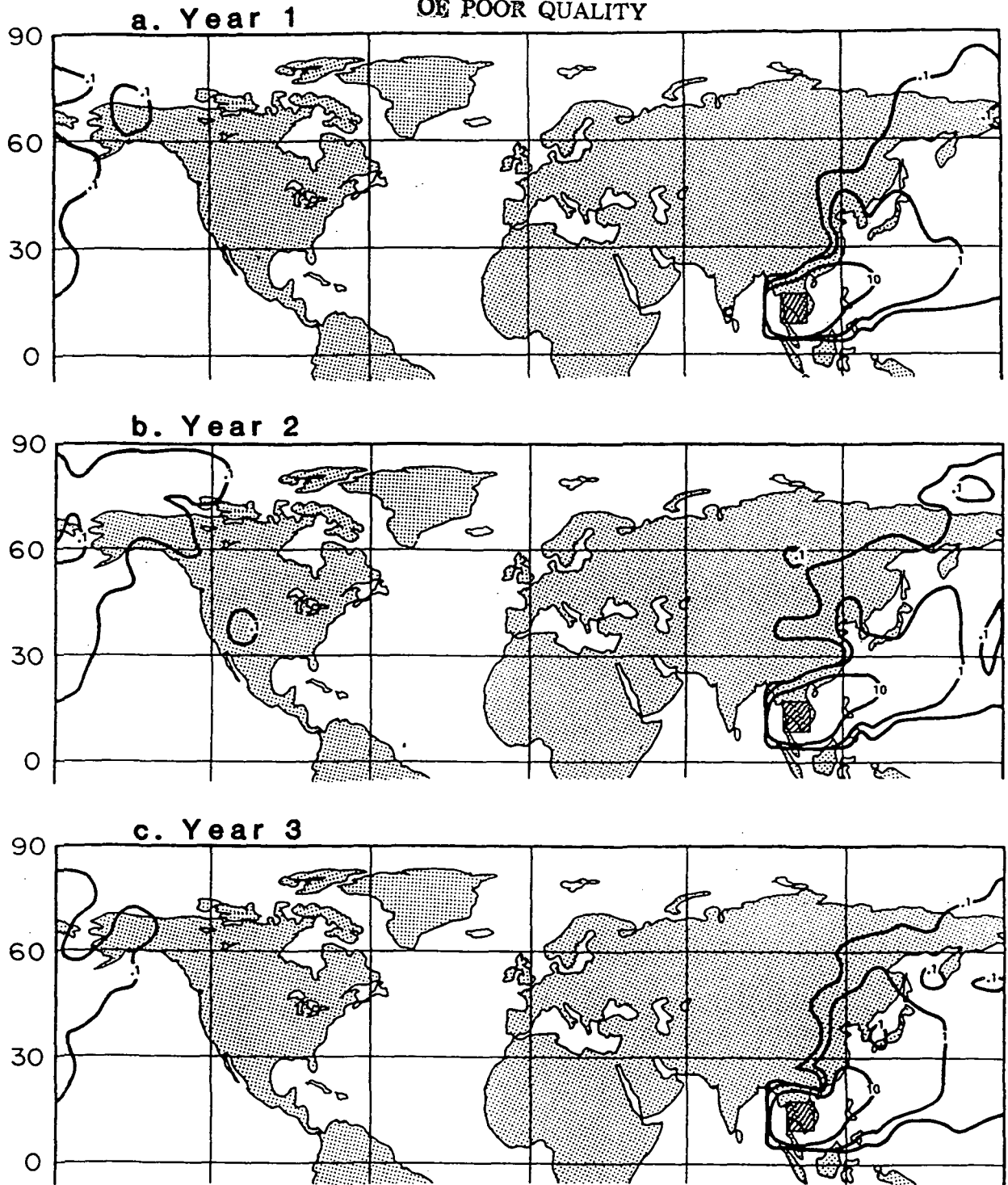
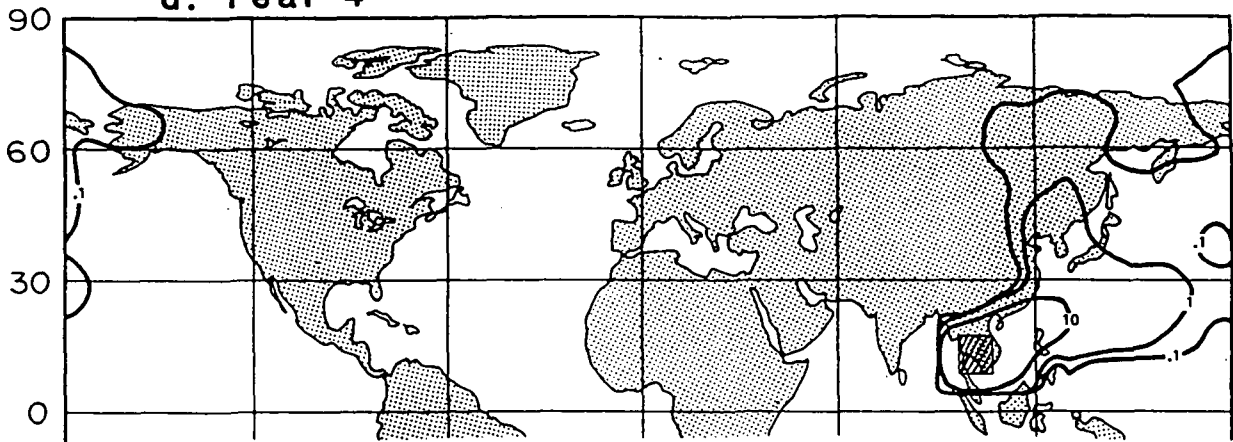


Figure 3-18

Interannual variability study. July precipitation contours for tracer evaporating from Southeast Asia source (shaded box). Initial conditions taken from a) year 1, b) year 2, c) year 3, d) year 4, and (e) year 5 of the 5-year simulation described by Hansen et al (1983).

ORIGINAL PAGE IS
OF POOR QUALITY

d. Year 4



e. Year 5

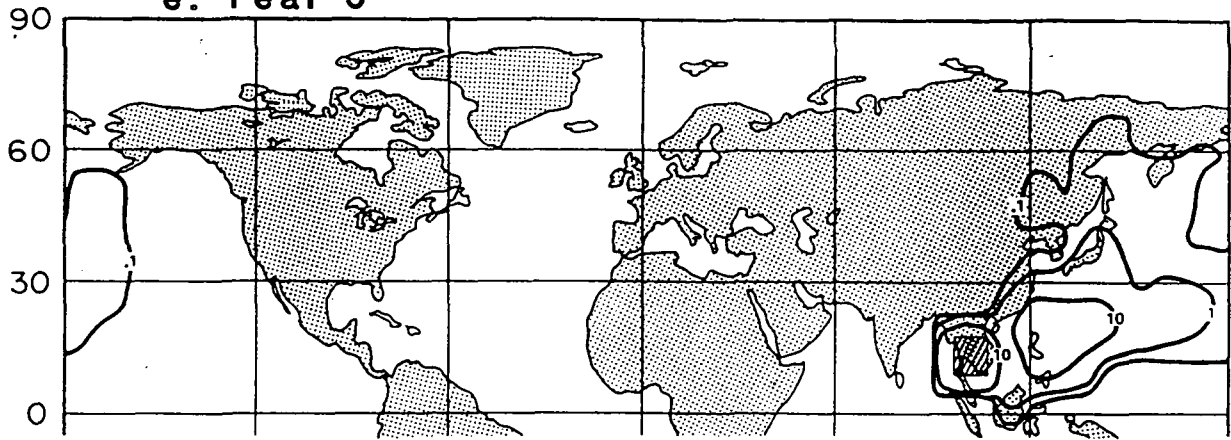


Figure 3-18 (cont.)

a rather low degree of inter-annual variability. Each 10-mm/30-day contour shows roughly the same lateral extent and indicates tracer motion to the east and slightly to the north. The 1-mm/30-days contour varies slightly more between the simulations but again has roughly the same lateral extent and positioning in each.

The .1-mm/30-days contours represent a very small amount of water and therefore have little practical significance. Examining the inter-annual variability of these contours is useful, however, because they span a larger portion of the earth. GCM results are generally more meaningful when averaged over larger spatial scales. The .1-mm/30-day contours in Figure 3-18 span far more GCM grid squares than the 10 or 1-mm/30-day contours and therefore provide for a more effective comparison of interannual variability.

The .1-mm/30-day contours for all five Julys have the same basic form. The contours show that tracer transport to the south and west is sharply limited, as is transport to due north of the source region. The contours extend northeast into Alaska and the Arctic Ocean north of the Bering Strait. Deviations from this basic form do exist; the contour for July of Year 5, for example, only extends northward to below the Aleutian Islands, and the contour for July of Year 2 reaches Northern Canada. The deviations are slight, however. The general agreement speaks well for the use of a one month integration to estimate tracer transport.

3.3 Simulation of Tritium Transport from the Stratosphere to the Oceans

The atomic tests of the early 1960's injected a substantial amount of tritiated water (HTO or, for this discussion, simply tritium) into the earth's stratosphere, and this tritium has since been spreading into each of the earth's water compartments. Eventually, almost all of the atomic tritium must end up in the earth's oceans, since the oceans hold over 97% of the earth's water. Since the atomic tritium was originally placed far from its ultimate sink, and since the amount generated far outweighs all natural background tritium, atomic tritium is a unique real-world water tracer.

The tritium can enter the ocean in three different ways, i.e. through oceanic precipitation, through continental runoff, and through vapor exchange at the ocean surface. Weiss and Roether (1980), using measurements of tritium concentration in precipitation and a model of isotopic vapor exchange proposed by Craig and Gordon (1965), imply that for the Northern Hemisphere Atlantic and Pacific Oceans, 2.3 times as much tritium has reached the ocean surface through surface vapor exchange as through precipitation. Measurements of tritium inventories in the ocean are not inconsistent with the Weiss and Roether scenario.

The experiment described in the present section used the tracer water model to simulate tritium transport from the stratosphere to the oceans. The model determined the relative amounts of tritium entering the ocean via vapor impact and precipitation for comparison with the Weiss and Roether scenario. Many sensitivity studies were performed to determine

how the model's tritium transport is affected by changes in the location of the stratospheric source or by changes in the parameterization of model physics.

3.3.1. The Weiss and Roether Tritium Input Scenario

Weiss and Roether (1980) list the annual evaporation and precipitation depths over the Northern Hemisphere Atlantic and Pacific Oceans averaged over 5° latitudinal bands. The values were taken from Baumgartner and Reichel's (1975) analysis and are reproduced in Table 3-1. Weiss and Roether also list as a function of latitude their estimates of total tritium deposition I_{EP} into these oceans, already weighted by area. These values are also given in Table 3-1.

Weiss and Roether compute tritium deposition through the equation

$$I_{EP} = \text{Area} \cdot \left(P \cdot C_p + E \cdot \frac{h}{1-h} \cdot C_v - \text{upward flux} \right) \quad (3-5)$$

The first addend is the precipitation input; P and C_p are observed latitude-dependent precipitations and tritium concentrations in precipitation, respectively. The second addend is essentially the Craig and Gordon (1965) relationship for downward isotope vapor flux, with E being the evaporation rate, h the relative humidity of the air ten meters above the ocean, and C_v the concentration of tritium in ocean vapor. Weiss and Roether assume h to be uniform over the ocean surface with a value of 0.74. Since very few measurements were available to produce average

Table 3-1 Summary of flux compilations of Weiss and Roether (1980). For each 5-degree latitudinal band in each ocean, the first three columns show the average evaporation and precipitation rates used and the estimates of combined precipitation and surface vapor exchange tritium input. The fourth and fifth data columns divide the tritium input for each band into the two components, and the sixth data column provides the ratio of the vapor exchange input to the precipitation input. The final column indicates the percent of total tritium deposited into each band. (From Koster et al, in preparation.)

TRITIUM IN NORTH ATLANTIC							
LAT BAND	E (m/yr)	P (m/yr)	TOTAL INPUT OF TRITIUM (MCi)	PRECIP INPUT (MCi)	VAPOR INPUT (MCi)	RATIO	% OF TOTAL
75-80	0.18	0.26	9.50	3.44	6.06	1.76	1.83
70-75	0.34	0.34	24.90	7.03	17.87	2.54	4.79
65-70	0.44	0.53	32.00	10.29	21.71	2.11	6.16
60-65	0.59	0.97	44.40	17.45	26.95	1.54	8.55
55-60	0.77	1.02	53.30	18.27	35.03	1.92	10.26
50-55	0.93	1.18	47.90	15.96	31.94	2.00	9.22
45-50	0.98	1.14	46.30	14.54	31.76	2.18	8.91
40-45	1.19	1.00	55.20	13.72	41.48	3.02	10.63
35-40	1.53	0.82	46.40	8.08	38.32	4.74	8.93
30-35	1.62	0.63	42.20	5.60	36.60	6.53	8.12
25-30	1.53	0.64	37.80	5.34	32.46	6.07	7.28
20-25	1.53	0.52	28.00	3.30	24.70	7.47	5.39
15-20	1.53	0.68	20.50	3.05	17.45	5.71	3.95
10-15	1.46	1.01	14.30	3.06	11.24	3.67	2.75
5-10	1.33	1.69	9.30	3.10	6.20	2.00	1.79
0-5	1.20	1.45	7.50	2.42	5.08	2.10	1.44

Totals: 134.68 384.82
TRITIUM INPUT RATIO = 2.86

TRITIUM IN NORTH PACIFIC							
LAT BAND	E (m/yr)	P (m/yr)	TOTAL INPUT OF TRITIUM (MCi)	PRECIP INPUT (MCi)	VAPOR INPUT (MCi)	RATIO	% OF TOTAL
75-80	0.00	0.00	0.00	0.00	0.00	0.00	0.00
70-75	0.00	0.00	0.00	0.00	0.00	0.00	0.00
65-70	0.00	0.00	0.00	0.00	0.00	0.00	0.00
60-65	0.24	0.61	7.69	3.85	3.84	1.00	1.14
55-60	0.34	1.15	37.49	21.41	16.08	0.75	5.56
50-55	0.48	1.41	53.52	28.70	24.82	0.86	7.93
45-50	0.67	1.46	67.03	30.95	36.08	1.17	9.94
40-45	0.93	1.34	70.58	25.55	45.03	1.76	10.46
35-40	1.13	1.17	72.45	20.98	51.47	2.45	10.74
30-35	1.34	1.01	70.92	16.23	54.69	3.37	10.51
25-30	1.51	0.82	61.55	10.84	50.71	4.68	9.13
20-25	1.62	0.83	57.49	9.65	47.84	4.96	8.52
15-20	1.60	1.13	55.21	12.01	43.20	3.60	8.19
10-15	1.46	1.75	49.92	16.00	33.92	2.12	7.40
5-10	1.30	2.57	45.25	19.80	25.45	1.28	6.71
0-5	1.20	1.81	25.42	9.47	15.95	1.68	3.77

Totals: 225.45 449.07
TRITIUM INPUT RATIO = 1.99

Total precipitation input of tritium for North Atlantic+Pacific=360 MCi.
Total vapor input of tritium for North Atlantic+Pacific=834 MCi.
Resulting tritium input ratio for North Atlantic+Pacific=2.32.

values of C_V versus latitude during the period of peak bomb tritium delivery to the ocean (1963 - 1965), Weiss and Roether assumed that the concentrations of tritium in ocean precipitation and ocean vapor were roughly in isotopic equilibrium, i.e. that $C_V = C_P/\alpha_{l/v}$, where $\alpha_{l/v}$ is tritium's liquid/vapor fractionation factor (see Section 2.2.1). They justified this assumption through measurements on vapor/rain pairs collected in the North Atlantic. The value of $\alpha_{l/v}$ was taken to be 1.12 everywhere.

Table 3-1 also separates each value of I_{EP} computed by Weiss and Roether into its precipitation and vapor exchange components. (This separation assumes a negligible upward flux of tritium.) The precipitation and vapor exchange contributions are summed over the latitudes, and the totals for each ocean are provided at the bottom of Table 3-1. In the Northern Hemisphere Atlantic Ocean, 2.9 times as much tritium entered the ocean via vapor exchange than via precipitation. In the Northern Hemisphere Pacific Ocean, 2.0 times as much entered via vapor exchange than via precipitation. When the two oceans are considered together, the vapor exchange input of tritium is seen to be 2.3 times the precipitation input.

The assumptions leading to the ratio of 2.3 bear further scrutiny and will be discussed again in Section 3.3.3. First, though, a description of the tracer water model simulations is provided.

3.3.2 Description of the Tracer Water Model Simulations

The 26 tritium transport simulations performed with the tracer water model will be described by discussing the first in detail and then noting the variations imposed in the other 25. For purposes of discussion, the first simulation will be referred to as Simulation T1, the second as Simulation T2, and so on.

a. Simulation T1: The Standard Case

The initial conditions for the basic atmosphere and surface variables in Simulation T1 were the model conditions on June 1 of Year 3 of the five year GCM run described by Hansen et al (1983). The tritium concentration in atmospheric water vapor (i.e. the T/H ratio) was initially set everywhere to zero except in a single latitudinal band, where a uniform T/H ratio was imposed. The latitudinal band consisted of 36 grid boxes circling the globe at 51°N and at the 200 mb level (the seventh GCM level), high in the troposphere. The band was assumed to represent the site of tritium injection from the stratosphere. Since all of the tracer transport processes are completely linear, and since only the relative tritium inputs into the ocean through precipitation and vapor exchange are studied, the magnitude of the imposed T/H ratio is unimportant.

To avoid the problem of specific weather events in the model simulation transporting the initial tritium in a way not consistent with time-averaged transport, the T/H ratio in each box of the latitudinal band was reset to its original value at every time step. The original T/H ratio therefore acted as a constant boundary condition at the latitudinal band,

and during the first month of simulation, the distribution of tritium in the atmosphere moved toward a "steady-state" distribution. The tritium inputs into the ocean were monitored for 30 days, starting on July 1, the beginning of the second month. The thirty July days were assumed to be an adequate averaging period. As a test of this approach, Simulation T26 followed tritium transport without resetting the T/H ratios in the source boxes.

The tritium tracer used was of the aboveground type (see Section 2.4). That is, tritium was not allowed to re-evaporate from any earth surface reservoir; the model recorded only where and how the atmospheric tritium first hit the surface. This lessened the required preconditioning time for the simulation. The thirty June days used would have been insufficient if continental groundwater reservoirs had to be properly loaded with tritium. Unfortunately, though, the simulation thereby neglected an important pathway for transporting tritium into the surface layer over the ocean. Tritium could conceivably precipitate onto a continent, re-evaporate, and then remain in lower atmospheric levels while advection carries it to sea. The importance of this pathway was investigated in Simulation T6, which employed a continental tritium source.

Most of the model simulations discussed in this report evaporate tracer water from a specific source region on the earth's surface, as described in Section 2.4. Notice how the tritium transport simulations described here use an alternative method of releasing aboveground tracers into the atmosphere.

The tritium amounts entering the ocean as exchanged vapor and in precipitation were determined at every time step of Simulation T1. The precipitation and downward vapor flux of model water were also monitored; the latter flux was calculated with Equation 2-20. The thirty-day grid square totals for each of these four fluxes were summed over latitudinal bands, with the precipitation fluxes divided into continental and oceanic components.

The results are presented in Table 3-2. First, the total model water surface fluxes for each band were divided by their respective areas to produce average, per-unit-area fluxes, which appear in Columns 1 - 3. Each tritium flux for a band was then divided by the corresponding water flux to obtain an average T/H ratio for that flux. These ratios, meaningful only in their relative values, appear in Columns 4 - 6. Finally, the total tritium fluxes are listed in Columns 7 - 9, expressed in percent of the total tritium deposition between 16°N and 80°N. Nearly all of the tritium was deposited in this latitude range.

The last three columns of Table 3-2 were summed to determine the global relative inputs of tritium onto the continents and oceans. In Simulation T1, 28% of the tritium entered the ocean as precipitation, while only 22% entered as exchanged vapor. The rest precipitated onto the continents. Thus, the ratio of the vapor exchange input of tritium into the ocean to the precipitation input was 0.79, quite different from the ratio of 2.3 suggested by Weiss and Roether (1980). This difference, in fact, is an essential point of this section.

Table 3-2

Tritium fluxes as a function of latitude for selected tritium simulations. Ocean water vapor fluxes (but not ocean tritium vapor fluxes) are somewhat approximate. "Continental" precipitation includes precipitation onto ocean ice. (From Koster et al, in preparation.)

Median Lat. °N	Water Fluxes kg/m ²			Tritium/Hydrogen Ref to 51°N Ocean			Tritium Fluxes % of total		
	Cont. Precip.	Ocean Precip.	Ocean Vapor	Cont. Precip.	Ocean Precip.	Ocean Vapor	Cont. Precip.	Ocean Precip.	Ocean Vapor
Simulation T1 Upper Troposphere Injection 51°N									
74	41	38	110	1.51	1.10	0.16	6.25	1.39	0.61
66	69	56	119	1.07	0.95	0.15	11.50	2.35	0.76
59	68	55	138	0.86	1.16	0.21	9.17	6.69	3.02
51	80	59	114	0.67	1.00	0.28	9.79	7.87	4.23
43	87	55	151	0.49	0.57	0.20	7.52	6.00	5.87
35	68	86	273	0.26	0.14	0.09	3.06	2.82	5.60
27	68	115	231	0.15	0.03	0.02	1.89	0.84	1.67
20	106	112	258	0.05	0.00	0.01	0.77	-0.01	0.34
TOTAL							49.94	27.96	22.10
Simulation T2 Lower Stratosphere Injection 51°N									
74	41	38	110	2.34	1.54	0.27	8.21	1.65	0.85
66	69	56	119	1.35	1.15	0.19	12.35	2.40	0.85
59	68	55	138	0.93	1.18	0.22	8.45	5.80	2.67
51	80	59	114	0.70	1.00	0.27	8.74	6.66	3.50
43	87	55	151	0.58	0.61	0.20	7.51	5.46	4.96
35	68	86	273	0.34	0.22	0.11	3.43	3.76	6.03
27	68	115	231	0.14	0.07	0.04	1.51	1.85	2.12
20	106	112	258	0.03	0.01	0.01	0.36	0.39	0.50
TOTAL							50.56	27.97	21.47
Simulation T3 Upper Troposphere Injection 35°N									
74	41	38	110	0.62	0.36	0.06	2.29	0.41	0.19
66	69	56	119	0.51	0.40	0.05	4.96	0.89	0.24
59	68	55	138	0.46	0.69	0.12	4.43	3.57	1.51
51	80	59	114	0.51	1.00	0.20	6.75	7.08	2.69
43	87	55	151	0.65	0.91	0.20	9.01	8.59	5.28
35	68	86	273	0.56	0.44	0.14	5.98	8.11	8.55
27	68	115	231	0.30	0.19	0.10	3.28	5.21	5.22
20	106	112	258	0.12	0.05	0.03	1.76	1.51	2.51
TOTAL							38.46	35.36	26.18
Simulation T6 Evaporation from continents 30°N-60°N*									
74	41	38	110	1.51	1.54	0.34	5.08	1.66	0.59
66	69	56	119	2.02	1.59	0.36	17.88	2.80	0.87
59	68	55	138	4.25	1.92	0.34	1.26	3.98	2.28
51	80	59	114	4.72	1.00	0.40	1.35	3.23	2.80
43	87	55	151	4.45	1.03	0.24	0.14	1.68	3.23
35	68	86	273	2.91	0.32	0.56	1.53	4.66	16.71
27	68	115	231	0.77	0.16	0.25	7.82	4.02	7.23
20	106	112	258	0.27	0.06	0.10	3.57	1.61	4.03
TOTAL							38.62	23.64	37.74

*Note: The tritium and water fluxes used to calculate the numbers in the final four columns for Simulation T6 did not include the fluxes onto the evaporative source itself.

Table 3-2 (cont.)

Median Lat. °N	Water Fluxes kg/m ²			Tritium/Hydrogen Ref to 51°N Ocean			Tritium Fluxes % of total		
	Cont. Precip.	Ocean Precip.	Ocean Vapor	Cont. Precip.	Ocean Precip.	Ocean Vapor	Cont. Precip.	Ocean Precip.	Ocean Vapor
	Simulation T17			Drag coef. increased 3 times					
74	42	65	406	1.89	1.01	0.12	4.98	1.38	0.99
66	83	77	411	1.68	1.60	0.12	13.40	3.34	1.30
59	94	74	180	1.26	1.67	0.33	11.51	7.98	3.77
51	95	65	269	0.77	1.00	0.19	8.31	5.33	4.28
43	90	79	405	0.64	0.47	0.17	6.28	4.36	8.14
35	90	105	590	0.24	0.18	0.09	2.32	2.77	7.24
27	92	122	489	0.10	0.00	0.01	1.07	0.09	0.93
20	186	157	598	0.01	0.00	0.00	0.16	-0.08	0.15
TOTAL							48.03	25.18	26.79
	Simulation T18			Drag coef. divided by 3					
74	45	42	55	1.50	1.19	0.22	7.42	1.83	0.46
66	59	40	85	1.25	1.03	0.14	12.45	1.97	0.56
59	63	54	46	0.93	1.13	0.28	9.92	6.95	1.55
51	68	48	66	0.63	1.00	0.26	8.53	6.89	2.48
43	80	58	70	0.47	0.71	0.21	7.12	8.42	3.10
35	95	64	97	0.24	0.21	0.14	4.39	3.48	3.42
27	42	87	118	0.20	0.06	0.06	1.61	1.57	2.02
20	114	88	86	0.07	0.03	0.05	1.39	0.97	1.51
TOTAL							52.82	32.09	15.09

The ratio of 0.79 for Simulation T1 is listed in Table 3-3 along with the corresponding ratios determined in the other simulations. The flux data for simulations not included in Table 3-2 can be found in Appendix B.

b. Simulations T2 - T14: Variation in the Tritium Source Location. In Simulation T2, the latitudinal band representing the tritium source remained at 51°N but was displaced one grid box level upward, so that it was vertically centered at 100 mb. The simulation was otherwise equivalent to Simulation T1. The resulting ratio of the total tritium input into the ocean via vapor exchange to that via precipitation, hereafter referred to as the tritium input ratio, was 0.77. Apparently, moving the tritium source vertically into the stratosphere has little effect on the relative importance of the tritium delivery mechanisms. As shown in Table 3-2, neither does it significantly effect the geographic distribution of the delivery.

The latitudinal band for tritium injection was displaced southward in Simulation T3, placing the tritium source at 35°N and 200 mb. Although this did displace southward the location of maximum tritium inputs into the ocean (see Table 3-2), the effect on the tritium input ratio was slight, the new value being 0.74.

Simulations T4 and T5 investigated the effects of a more localized release of tritium. The tritium source for Simulation T4 was not a latitudinal band but two single grid boxes lying over North America and Eurasia. The tritium source in Simulation T5 was also two single grid

Table 3-3

Description of simulations and ratios of vapor impact delivery of tritium to precipitation delivery. Simulations T2-T25 are equivalent to Simulation T1 except for the changes noted in the simulation description. Keep in mind that Weiss and Roether's (1980) analysis suggests a tritium input ratio of 2.3. (From Koster et al, in preparation.)

Simulation No.	Description	Trit. Input Ratio
T1	Control: Tritium content kept constant in latitudinal band at 51°N and 200 mb (upper troposphere)	0.79
<u>Variations in the tritium source location</u>		
T2	Tritium source band placed at 100 mb (lower stratosphere)	0.77
T3	Tritium source band placed at 35°N.	0.74
T4	Tritium content kept constant in only 2 boxes, over continents.	0.74
T5	Tritium content kept constant in only 2 boxes, over oceans.	1.05
T6	No atmospheric tritium source; tritium evaporates from continental squares between 30°N and 60°N	1.60
T7	Tritium content kept constant in first layer boxes over pure ocean grid squares north of 30°N.	1.82
<u>Variations in model physics</u>		
T15	Upstream weighting scheme used for dynamical tracer transport	0.84
T16	Tritium in lowest three atmospheric levels vertically mixed	0.85
T17	Drag coefficient in surface flux calculations increased three-fold	1.06
T18	Drag coefficient in surface flux calculations divided by three	0.47
T19	Tritium concentration in surface boundary layer assumed equal to average tritium concentration in first layer grid box	1.25
T20	Total equilibration of falling tritium condensate during moist convection	0.86

Table 3-3 (cont.)

Simulation No.	Description	Trit. Input Ratio
T21	No equilibration of falling tritium condensate during moist convection	0.73
T22	Moist convective downdrafts imposed; no equilibration of falling tritium condensate during moist convection	0.58
T23	Fraction of grid box column forming moist convective plume reduced to 1/10	0.70
T24	Tritium condensate formed above 600 mb set aside and placed in first layer grid box as tritium vapor	0.77
T25	Control simulation run under winter (rather than summer) conditions	0.71

boxes, but these boxes were located over the Atlantic and Pacific Oceans. As in the other simulations, the T/H ratios in the source boxes were initialized to a given value and reset to that value at every time step. The resulting tritium input ratios for Simulations T4 and T5 were 0.74 and 1.05, respectively. While the longitudinal position of the tritium source clearly has an effect on the tritium input ratio, the effect is not large.

As mentioned before, Simulation T6 examined one possible pathway for moving high level tritium into lower levels over the ocean, namely by advection to sea of tritium that initially precipitates onto continents and subsequently re-evaporates. For Simulation T6, the atmosphere was assumed completely free of tritium at the beginning of the simulation, and no tritium sources as utilized above were defined in the atmosphere. Instead, an evaporative source region was defined for the aboveground tritium tracer, of the type described in Section 2.4.2. Tritium evaporated from continental grid squares between 31°N and 63°N at rates proportional to the water evaporation rates. The simulation was otherwise equivalent to the previous simulations. The resulting tritium input ratio was a relatively large 1.60. Thus, tritium evaporated off continental surfaces appears to remain in lower atmospheric layers as it moves out to sea.

If Simulation T1 had accounted for the re-evaporation of tritium from continents, one might expect that the re-evaporated tritium would have entered the oceans as indicated by Simulation T6. Consider that in Simulation T1, as shown in Table 3-2, 50% of the tritium released from the upper troposphere source first precipitated onto non-ocean surfaces, while the rest entered the ocean directly. Consider also that at the time of

the GEOSECS observational survey (see Broecker et al, 1986, for summary), 70% of continental tritium had re-evaporated and had advected out over the oceans, 15% had been incorporated into continental runoff, and 15% had remained on the continents. Thus, for every fifty units of tritium that enter the ocean via precipitation or vapor exchange directly, i.e., without reaching the continental surface first, perhaps 35 units of re-evaporated continental tritium enter the ocean via these same processes. This would lead to an average tritium input ratio of $(0.79) \cdot (50/85) + (1.60) \cdot (35/85)$, or 1.1.

Simulation T7 moved the atmospheric tritium source to just above the ocean surface; the first layer grid box above each pure ocean grid square north of 30°N was defined as a source for tritium and was maintained at a constant T/H ratio. As this is certainly not a realistic representation of a bomb tritium source, the high (1.82) tritium input ratio generated in this simulation does not reflect conditions in the real world. Rather, Simulation T7 tested the importance of moving tritium vapor to surface levels before it precipitates. It suggests that if the GCM transported high level tritium to lower levels more efficiently, its delivery of tritium to the ocean might move closer to the Weiss and Roether scenario.

Studied together, Simulations T7 through T14 describe more completely the response of the tritium input ratio to the source layer height. Simulation T8 used the same horizontal distribution of source boxes as did Simulation T7, but all source boxes were located in the second atmospheric layer (890 mb). In Simulation T9, the same horizontal source box distribution was placed in the third atmospheric layer (790 mb), and so on

through the eighth layer. The results, listed in Table 3-4, show an essentially steady decrease in tritium input ratio with an increase in source height. Each atmospheric level seems to provide some resistance to the transport of tritium downward to the ocean surface.

c. Simulations T15 - T24: Variation in Model Physics. The simulations in this section, each featuring a single change in some model parameterization, used the same tritium source and the same model initial conditions as used in Simulation T1. The resulting tritium input ratios should be compared to the Simulation T1 value of 0.79.

i) Changes in the Dynamical Transport of Tritium Vapor

To increase the model's tritium input ratio, the relative importance of tritium vapor exchange at the ocean surface must increase. Two simulations attempted to move more tritium vapor from the seventh layer source to the ocean surface by modifying the tracer advection scheme.

As discussed in Section 2.3.1, the tracer water model normally uses a form of the slopes scheme of Russell and Lerner (1981) to estimate advective tracer transport between adjacent grid boxes; the scheme combines computed water vapor tracer transports with information on subgrid tracer distributions to produce the estimates. The slopes scheme was replaced by an upstream weighting scheme in Simulation T15. Tritium transport was calculated in this simulation by assuming that the average T/H ratio for a given grid box applied everywhere within the box and thus within any water vapor transported out of the box. That is, no subgrid variation of

Table 3-4

Tritium input ratios as a function of source height. In each simulation below, tritium contents were kept constant in those grid boxes of the indicated atmospheric level lying directly above pure ocean grid squares north of 30 Degrees North. (From Koster et al, in preparation.)

Simulation No.	Description	Trit. Input Ratio
T7	Tritium source in level 1 (960 mb)	1.82
T8	Tritium source in level 2 (890 mb)	1.49
T9	Tritium source in level 3 (790 mb)	1.06
T10	Tritium source in level 4 (630 mb)	0.93
T11	Tritium source in level 5 (470 mb)	0.98
T12	Tritium source in level 6 (320 mb)	0.98
T13	Tritium source in level 7 (200 mb)	0.89
T14	Tritium source in level 8 (100 mb)	0.80

tritium concentration was assumed. The upstream weighting scheme is inherently more diffusive and was therefore expected to ease the vertical transport of tritium vapor to the ocean surface. Simulation T15, however, produced a tritium input ratio of only 0.84.

Simulation T16 attempted to ease the downward transport of tritium vapor by maximizing vertical mixing in the lowest three atmospheric layers. At every time step in this simulation, the tritium (but not the water vapor) in the lowest three boxes of every vertical column was redistributed so as to produce the same T/H ratio in each box while conserving tritium mass. This seemingly arbitrary mixing was suggested by certain vertical profile measurements that show the T/H ratio in vapor to be roughly uniform in the first two kilometers above the earth's surface (Ehhalt, 1971; Taylor, 1972). The added mixing did not, however, substantially increase the tritium input ratio; it raised it only slightly to 0.85.

ii) Changes in the Parameterization of Surface Vapor Exchange

The sensitivity of the tritium input ratio to the surface vapor exchange parameterization was tested first by varying the transfer coefficient C_q in Equations 2-15 and 2-17; the best values to use for this parameter have never been known with certainty. The values of C_q were increased threefold in Simulation T17 and were divided by three in Simulation T18. The resulting global evaporation of water was increased only 20% in Simulation T17 and was decreased 20% in Simulation T18; apparently each change in the transfer coefficient was counterbalanced by an opposing

change in the average vapor deficit ($q_G - q_S$) in Equation 2-15. The resulting tritium input ratios were 1.06 for Simulation T17 and 0.47 for Simulation T18. The Simulation T17 ratio is still far from the Weiss and Roether ratio of 2.3. The increase in C_Q must have eased tritium transport across the ocean surface, but depleted first layer tritium apparently was not replenished rapidly enough by tritium from higher layers.

The parameterization of downward tritium vapor flux across the ocean surface is quite crude. Equation 2-15 was developed to estimate net water evaporation only; interpreting the two terms in the expanded equation as an upward and downward flux, and thereby producing Equation 2-22 by analogy for the downward flux of tracer, is arguably inappropriate. It is reasonable to assume, however, that the downward flux of tritium vapor into the ocean is proportional to the tritium content of the first layer grid box. The sensitivity of the results to a change in the proportionality constant is effectively examined in Simulations T17 and T18.

Simulation T19 attempted to increase the surface vapor exchange of tritium by calculating q_{ST} in Equation 2-22 as:

$$q_{ST} = q_S \cdot \frac{q_{1T}}{q_1} \quad (3-6)$$

where q_{1T}/q_1 represents the average T/H ratio in the first layer grid box. Simulation T19 thus assumed the average T/H ratio for the grid box to apply at the top of the model's parameterized surface boundary layer. Normally the T/H ratio at the top of the boundary layer would be

relatively less, due to dilution by tritium-free water evaporating from the ocean surface. (See Equations 2-16 and 2-18; q_{GT} is zero, but q_G is nonzero.) Although the modifications in tritium transport introduced in Simulations T17 and T19 can be shown to be qualitatively equivalent, Simulation T19 is considered separately because it left the transport of water vapor unchanged. The tritium input ratio for Simulation T19 was 1.25, again suggesting some difficulty in moving tritium from higher to lower atmospheric levels in the GCM.

iii) Changes in the Parameterization of Precipitation

If the vapor exchange input of tritium into the ocean is not too small in the model, then perhaps the precipitation input of tritium is too large. Also, perhaps the precipitation processes can be made more efficient at loading the lower atmospheric levels with tritium vapor. The following sensitivity studies address these hypotheses.

One mechanism for moving tritium vapor into lower atmospheric levels involves the equilibration of falling liquid condensate. Precipitation droplets forming from the tritium-rich vapor in upper levels become enriched with tritium themselves. As they fall into lower levels, they equilibrate with vapor relatively deficient in tritium, resulting in a net transfer of tritium out of the droplets. Ehhalt (1971) suggests this mechanism to explain certain features of observed vertical profiles of T/H ratio.

The efficiency of this lower-level tritium loading naturally depends on the extent of equilibration. Recall from Section 2.3.2 that normally

in the tracer water model, falling droplets in moist convective events are allowed to equilibrate only halfway with surrounding vapor. In Simulation T20, however, all of the falling moist convective precipitation was allowed to equilibrate with surrounding vapor, and in Simulation T21, none of it was. The resulting tritium input ratios for Simulations T20 and T21 were 0.86 and 0.73, respectively, to be compared with the ratio 0.79 from Simulation T1. An increase in the extent of equilibration produces a clear, though probably insignificant, increase in the tritium input ratio.

Moist convective downdrafts, which are not currently modeled in the GCM, constitute another mechanism for moving high level tritium into layers nearer the surface. Normally, when a moist convective plume forms and lifts an air mass from Level A into a higher Level B, the air mass deficit in Level A is filled by letting the air outside the plume gently subside. Simulation T22 tested the importance of the downdraft mechanism by replacing subsidence with a more direct downward transport of air. After a plume rose from Level A to Level B in Simulation T22, an equivalent air mass was removed from Level B and directly inserted into Level A without affecting the layers in between. If tritium existed in Level B, an appropriate portion was also transported downward. The structure of the moist convection algorithm made it necessary in this simulation to allow no equilibration of tritium in falling raindrops, as in Simulation T21. The complete replacement of subsidence by downdrafts is by all means an extreme, and the resulting tritium input ratio of 0.58 indicates that downdrafts as modeled do not increase the relative importance of tritium vapor exchange at the ocean surface.

In Simulation T23, the fraction of an unstable grid box that becomes a moist convective plume, arbitrarily chosen to be one-half in the standard simulation, was changed to one-tenth. The grid box fractions used in the condensate re-evaporation and equilibration calculations were correspondingly reduced. The resulting monthly precipitation for Simulation T23 differed only slightly from that of Simulation T1; apparently the reductions in hourly moist convective precipitation over a grid square were counterbalanced by an increased precipitation frequency, since instabilities in the air column were removed less efficiently. The modified parameterization and any associated changes in precipitation frequency also had little effect on the tritium input ratio, producing a value of 0.70.

It was then suggested that the model-produced tritium input ratio is lower than the ratio suggested by Weiss and Roether due to the formation of spurious precipitation in the model's upper troposphere. The moisture holding capacity of air is much greater in the lower atmospheric levels, where temperatures are higher; thus most of the GCM's atmospheric water resides in these levels, and these levels naturally produce most of the GCM's precipitation. Precipitation amounts formed in the colder higher levels are necessarily small and thus can be quite inaccurate without greatly affecting the GCM's surface precipitation fields. When coupled, however, with the relatively large T/H ratios in higher levels (these will be illustrated in Section 3.3.3), spurious precipitation formed in higher levels could contain significant amounts of tritium. This tritium precipitation would also be spurious.

Simulation T24 investigated this possibility. In the simulation, tritium contained in droplets falling into the fourth vertical level (centered at 630 mb) was removed from the droplets and set aside. Once the droplets reached the earth's surface, this tritium was inserted into the first atmospheric level as tritium vapor. Therefore, spurious tritium condensate formed above Level 4 was given ample opportunity to enter the ocean as exchanged vapor. The tritium input ratio for this run was 0.77, slightly less than that for the standard run. Spurious precipitation from higher levels, if it exists, does not seem to enhance much the precipitation of tritium at the ocean surface.

c. Simulation T25: Test of Seasonality

If the importance of a tritium transport mechanism varies with season, so might the value of the tritium input ratio. To test this, Simulation T1 was repeated under winter conditions as Simulation T25. The model's prognostic variables were initialized using the model conditions on Dec. 1 of Year 2 of the five year simulation described by Hansen et al (1983). Tritium fluxes across the ocean surface were monitored over a thirty day period, starting on Jan. 1. The resulting tritium input ratio of 0.71 is actually less than the value of 0.79 found for summer.

d. Simulation T26: Transient case

The above simulations maintained the tritium source boxes at a constant T/H ratio and allowed the atmospheric distribution of tritium to approach steady-state before monitoring the tritium fluxes at the ocean

surface. Again, this was to produce a tritium input ratio based on monthly averaged weather conditions and not on a few specific and possibly singular weather events. Simulation T26 checked the validity of this approach by monitoring the transient behavior of a single impulse of tritium released at the beginning of the simulation. One unit of tritium was placed in one grid box in the lower stratosphere (100 mb), directly above an important Soviet nuclear testing site in Northern Siberia (at 75°N, 55°E). Tritium leaving the box was never restored; thus the sum of the total tritium contained in the atmosphere and the cumulative total downward tritium flux at the earth's surface remained constant. Simulation T26 followed the tritium transport for thirteen weeks, starting on June 1. The tritium input ratio and the total amount of tritium removed from the atmosphere (in %) for each week is tabulated in Table 3-5; notice that in the transient regime, as in the steady-state regime, the ratio is never close to the ratio of 2.3 suggested by Weiss and Roether. The weighted average tritium input ratio over the first 13 weeks was 0.68.

3.3.3. Discussion

a. Vertical T/H Profiles. With the tritium source in the upper troposphere and a tritium sink and water source at the earth's surface, an equilibrium vertical profile for tritium might be characterized by an increase in T/H ratio with height. Ehhalt (1971) observed this profile structure over Scottsbluff, Nebraska. The average profile (derived from 12 measured profiles) over Scottsbluff for the period between February 10 and June 21, 1966, is reproduced in Figure 3-19. Ehhalt suggests some

Table 3-5

Tritium input ratios as a function of time for Simulation T26, in which an impluse of tritium was released in the stratosphere at the beginning of the first week. The tritium input ratios are determined from precipitation and vapor exchange inputs into the ocean averaged over each listed week. (From Koster et al, in preparation.)

Week	Tritium input ratio	Amount of initial tritium removed during week (%)
1	0.39*	3.7
2	0.17*	4.3
3	0.75*	7.8
4	0.74	8.7
5	0.71	8.4
6	0.58	7.9
7	0.61	6.6
8	0.76	6.4
9	0.74	5.8
10	0.78	5.2
11	0.90	3.6
12	0.80	3.6
13	0.77	3.1
Total removed:		75.0%

*The tracer model is designed to run under steady-state conditions. During the first few weeks of this transient simulation, the model produced spatial distributions of surface tritium fluxes that were physically unrealistic. Thus, the first three tritium input ratios listed may be considered spurious.

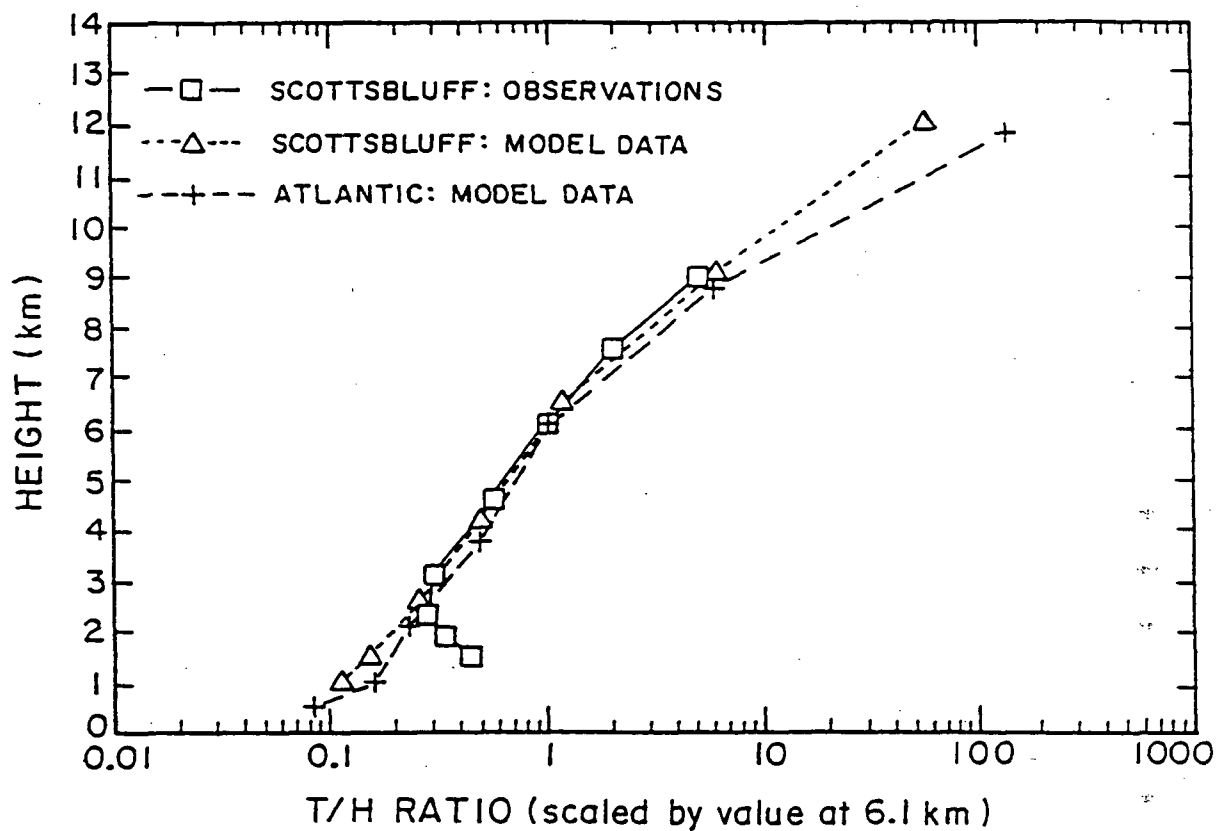


Figure 3-19 Observed and model-generated vertical profiles of the T/H ratio. Observations were taken above Nebraska and span the period February 10 - June 21, 1966 (Ehhalt, 1971). One of the model-generated profiles lies over the grid square containing Nebraska and the other lies over the North Atlantic (30°W, 43°N). For comparison purposes, all T/H ratios in a given profile were divided by the profile value at 6.1 km. (From Koster et al, in preparation).

possible reasons for the small increase in T/H ratio at ground level, including local re-evaporation of tritium and the short-term presence of two different air masses; the lower one consisting of polar air loaded with tritium due to an extended residence time over the continent. Note that since re-evaporation of tritium from the ground surface is prevented in the tracer model, these processes cannot similarly affect the model's vertical T/H profiles.

The model-generated vertical profiles of T/H ratio over the grid square containing Scottsbluff and over a grid square in the Atlantic Ocean are also shown in Figure 3-19. These profiles were constructed from Simulation T1 data as follows. The average monthly tritium content for each grid box in a column was divided by the average monthly water content for the box. Then, the profiles were scaled so that they matched the observed profile exactly at a height of 6 km. (Due to the arbitrary source box concentration, only relative tritium quantities in the model atmosphere have meaning.) Therefore, only the vertical gradients of relative tritium concentration are being compared in Figure 3-19. The observed and modeled gradients agree quite well.

The form of the profiles implies an upper limit to the tritium input ratio generated by the model. The water flux values for Simulation T1 in Table 3-2 indicate that in the 20°N - 74°N latitude range, the ratio of the monthly downward vapor flux of water to the monthly water precipitation flux at the ocean surface is generally less than 3. If tritium was constantly vertically mixed so that T/H ratios were always uniform with height, and if the tritium did not experience any isotopic

fractionation, the tritium would enter the ocean at the same ratio as the water. Isotopic fractionation favoring tritium precipitation does occur, however, and as indicated in Figure 3-19, the stratospheric source and ocean sink induce a non-uniform T/H profile favoring tritium precipitation. In fact, although not indicated in the figure, the non-uniformity of the T/H profile continues into the model's parameterized surface boundary layer, due to the dilution of near-surface tritium vapor by evaporating tritium-free water vapor. As a result, the tritium input ratio in the model must be less than the corresponding ratio of water fluxes. It should be noted that the ratio of water fluxes is itself strongly sensitive to the choice of the drag coefficient. (See Table 3-2, Simulations T17 and T18.)

b. Comparison with the Weiss and Roether Ratio. The model results indicate a strong insensitivity of the tritium input ratio to the location of the tritium source and to the parameterizations of the model physics. Perhaps the best estimate of the model-generated tritium input ratio is 1.1, based (as mentioned above) on the ratio of 0.79 for the standard simulation (Simulation T1), the ratio of 1.6 for the continental tritium source simulation (Simulation T6), and the fact that half of the tritium in Simulation T1 reached the earth's surface in continental precipitation, of which 70% might be expected to re-evaporate. This ratio lies below the ratio of 2.3 implied in Weiss and Roether's analysis.

Weiss and Roether's analysis, however, bears closer inspection. First consider the assumed isotopic equilibrium between vapor and

precipitation over the ocean, perhaps the weakest link in their argument. The observational data they used to support the assumption is provided in Table 3-6. The data takes the form of tritium concentrations in paired vapor/precipitation samples collected in the North Atlantic between 1966 and 1968. The vapor samples were collected continuously over fixed time intervals and were paired with samples of rain which fell during these intervals. At complete isotopic equilibrium, and with their assumed value of 1.12 for $\alpha_{l/v}$, the value of (T/H vapor)/(T/H rain) would be 0.89; Weiss and Roether considered the observed ratios in Table 3-6 to roughly approximate this value. For the 37 measurements listed, however, the average ratio of tritium concentration in vapor to that in rain is 0.81. Thus, by assuming isotopic equilibrium, Weiss and Roether overestimate the vapor exchange input of tritium by a factor 0.89/0.81, or 1.10. Their implied tritium input ratio is therefore reduced from 2.3 to 2.1.

Since the tritium concentrations in vapor tend to be more stable than those in precipitation in Table 3-6, it might be argued that the average ratio of tritium concentration in precipitation to that in oceanic vapor should be found instead. The reciprocal of the result would then be compared to the equilibrium value of 0.89. When processed in this fashion, the data in Table 3-6 suggest that Weiss and Roether overestimate the vapor influx of tritium by a factor (0.89)/(0.68), or 1.31. The tritium input ratio implied by the observations would then be reduced to 1.8.

In truth, the proper way to process the observational data is not obvious. It seems clear, though, that the observations suggest an average (T/H vapor)/(T/H rain) ratio less than 0.89.

Table 3-6

Summary of the T/H data obtained by Weiss and Roether (1980) from measurements on rain/vapor pairs. The data is grouped below according to the areas in which they were measured. (See Figure 3-20.) (From Koster et al, in preparation; the data were kindly provided for use in this paper by Wolfgang Weiss of Freiburg, West Germany.)

Date	Latitude	Longitude	T/H rain T.U.	T/H vapor T.U.	<u>T/H vapor</u> <u>T/H rain</u>	<u>T/H rain</u> <u>T/H vapor</u>
8/1-3/66	51 to 59°N	8 to 3°E	442	242	0.55	1.82
8/4-6/66	59 to 63°N	3 to 23°W	598	286	0.48	2.08
8/10-14/66	63°N	24 to 40°W	188	248	1.32	0.76
8/15-19/66	63 to 62°N	18 to 40°W	205	204	1.00	1.00
8/20-24/66	62 to 61°N	40 to 41°W	197	158	0.80	1.25
8/25-29/66	61 to 59°N	41 to 43°W	142	129	0.91	1.10
8/30-9/3/66	59 to 61°N	43 to 28°W	48	124	2.58	0.39
9/4-8/66	61 to 62°N	28 to 8°W	222	155	0.70	1.43
9/11-13/66	62 to 54°N	7°W to 8°E	190	95	0.50	2.00
				Mean	0.98	1.31
9/27-10/2/66	51 to 37°N	1°E to 8°W	98	76	0.77	1.30
10/2-7/66	37 to 41°N	8°W to 8°E	98	79	0.81	1.23
10/10-15/66	43°N	8 to 7°E	137	79	0.58	1.72
10/17-22/66	44°N	8°E	46	67	1.46	0.68
10/24-29/66	44 to 43°N	8 to 7°E	89	58	0.65	1.54
10/31-11/4/66	44 to 36°N	7 to 8°E	40	70	1.75	0.57
11/9-11/66	36 to 50°N	8 to 3°E	66	74	1.13	0.88
				Mean	1.02	1.13
1/18-22/67	38 to 35°N	11 to 7°W	44	30	0.69	1.45
1/30-2/4/67	34 to 37°N	9°W	124	61	0.50	2.00
2/5-9/67	37°N	9°W	92	58	0.63	1.59
2/12-17/67	37°N	10°W	74	58	0.78	1.28
2/18-22/67	37°N	10°W	29	20	0.69	1.45
2/23-27/67	37 to 36°N	10 to 6°W	62	34	0.55	1.82
				Mean	0.64	1.60
4/15-20/67	30°N	28 to 29°W	87	40	0.46	2.17
4/20-5/4/67	30 to 29°N	29 to 25°W	69	52	0.74	1.35
5/22-26/67	28°N	18 to 16°W	96	41	0.42	2.38
6/1-5/67	30 to 29°N	28 to 29°W	44	40	0.91	1.10
				Mean	0.63	1.75
7/13-18/67	62 to 63°N	9°W	157	95	0.60	1.67
7/19-23/67	63 to 62°N	9 to 12°W	96	53	0.55	1.82
7/26-31/67	62 to 64°N	12 to 9°W	119	38	0.32	3.13
				Mean	0.49	2.20
4/16-21/68	52 to 42°N	5 to 10°W	89	71	0.79	1.27
				Mean	0.79	1.27
9/10-14/68	39 to 42°N	25 to 14°W	27.3	23.5	0.86	1.16
9/15-19/68	42 to 40°N	14 to 12°W	29.5	33.2	1.13	0.88
10/5-9/68	40°N	12 to 10°W	45.2	20.5	0.45	2.22
10/21-26/68	39 to 42°N	10 to 13°W	28.1	20.8	0.74	1.35
10/27-31/68	42 to 43°N	13 to 15°W	34.9	20.9	0.60	1.67
11/1-5/68	43°N	15 to 14°W	33.6	20.9	0.62	1.61
11/6-7/68	43 to 42°N	14 to 11°W	25.5	24.1	0.95	1.05
				Mean	0.76	1.42
				Overall Mean	0.81	1.46

Reciprocal of 1.46 = 0.68

One might also argue that the data presented in Table 3-6 are not representative of all Northern Hemisphere ocean points. Figure 3-20 displays the geographical locations of the measurement sites; many of the measurements were collected off the coast of Europe and perhaps were influenced by tritium from the European continent.

Other important aspects of Weiss and Roether's analysis to consider are the latitude-dependent precipitation (P), evaporation (E), and tritium concentration in precipitation (C_p) values and the assumed uniform relative humidity and isotopic fractionation factor. Although these quantities are known to vary strongly with season, Weiss and Roether employ annual averages and therefore might miss important seasonal correlations. For example, as shown in Figure 3-21, summer is by far the most important season for tritium input. In Northern Hemisphere midlatitudes, estimates of summer evaporation rates over the oceans (Peixoto and Oort, 1983), which, by the way, roughly match the July evaporation rates produced in Simulation T1, are about half the observed mean annual evaporation rates. The use of annual rates in Equation 3-5 could therefore lead to an overestimate of the vapor exchange input of tritium into the ocean.

The overestimation, however, might be counteracted by the use of an annual mean relative humidity h (with respect to sea surface temperature) of 0.74 in Equation 3-5, which is significantly lower than observed summer values (von Loon, 1984). It is difficult to predict the net effect of using annual evaporation rates and relative humidities on the computed vapor exchange input of tritium. Other seasonalities may also be important; oceanic precipitation rates in summer (Peixoto and Oort, 1983, citing Jaeger, 1976) are reduced from their annual mean values, though not by as much as the evaporation rates, and values for the fractionation factor should decrease in summer. In a previous publication focussing on the North Atlantic (Weiss et al, 1979), Weiss and Roether mention that seasonal effects effectively cancel out, allowing for the use of annual means. They do not mention the extent to which this cancellation is fortuitous and whether or not it also applies to the Pacific Ocean. In a more complete analysis, monthly tritium inputs would be calculated.

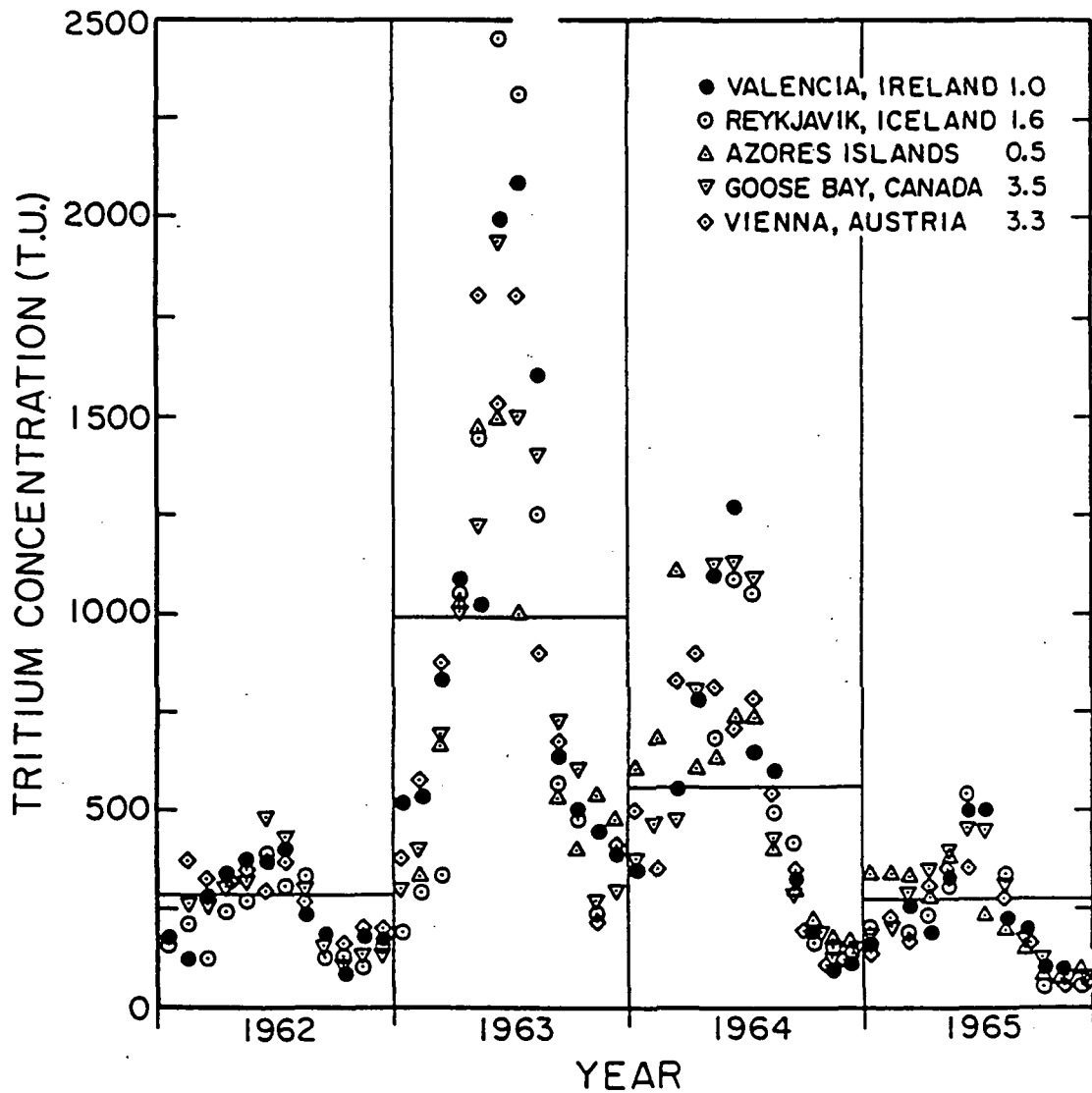


Figure 3-21 Seasonal trend in the T/H ratio in rains at five localities before, during and after the peak fallout year (1963). The measurements at Reykjavik, Azores, Goose Bay and Vienna have been normalized to yield the same mean as Valencia. The normalization factors are listed in the figure. (i.e., the Reykjavik results were all divided by 1.6...). The annual means selected by Weiss and Roether for Valencia are shown for comparison. (From Koster et al, in preparation.)

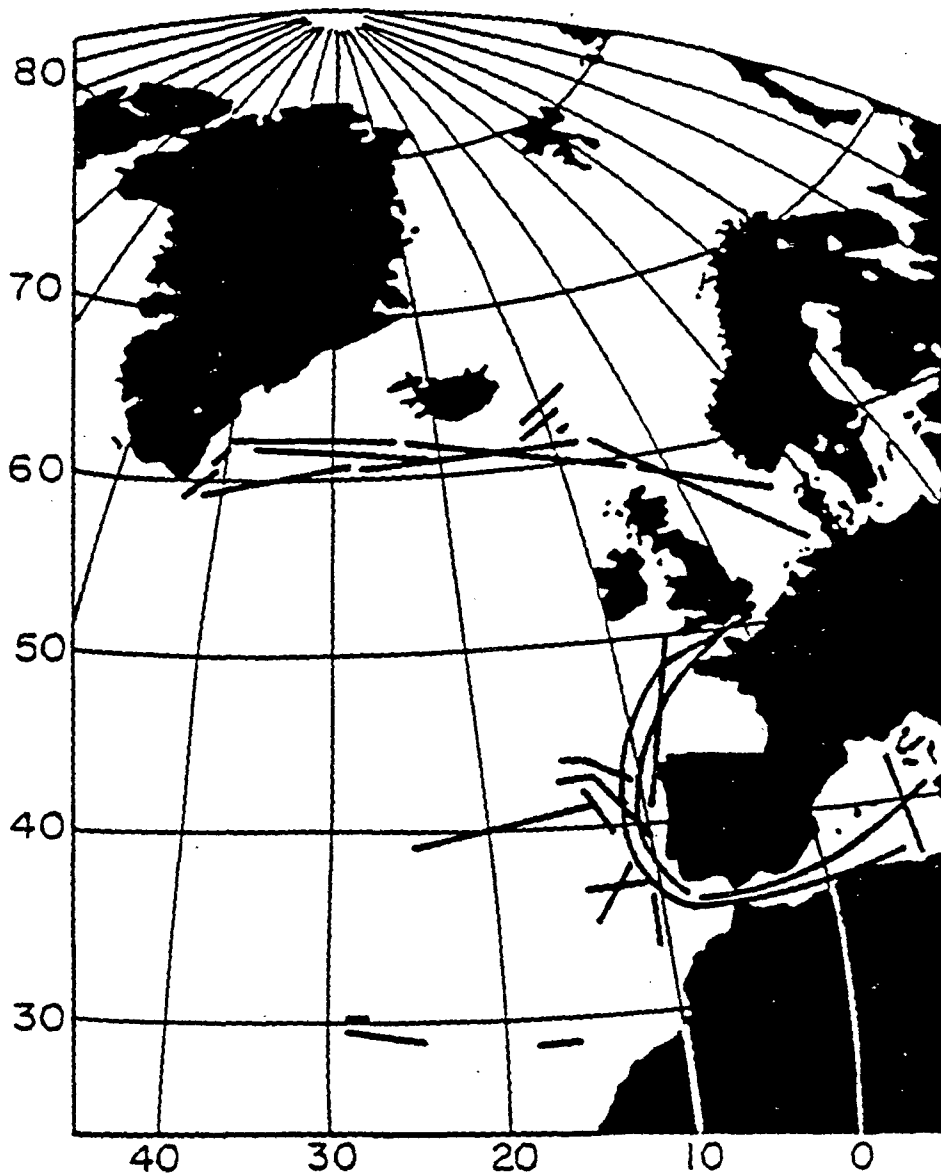


Figure 3-20 Map showing the locations of the areas in which Weiss and Roether obtained vapor-precipitation pairs for tritium analysis. (From Koster et al, in preparation).

ORIGINAL PAGE IS
OF POOR QUALITY

The sparseness of evaporation and precipitation measurements over the oceans must also be considered, as should the small number of ocean stations used to estimate values of C_p (see Figure 3-22). Furthermore, as shown in Figure 3-23, strong continent-to-ocean gradients are inherent in the global field of T/H ratio in precipitation; this complicates the task of determining the effective average ratio over the ocean for a latitudinal band. Consider also the use of the Craig and Gordon (1965) relationship for computing the downward flux of tritium vapor. The relationship, embodied in the second addend on the right-hand-side of Equation 3-5, is built around the assumption that a water vapor molecule has the same probability of moving from the ocean surface to the ten-meter measurement height as it has of moving from the ten-meter height to the ocean surface. This assumption may oversimplify the dynamical structure of near-surface ocean air. A relatively easier upward motion would reduce the vapor exchange input of tritium suggested by observations.

c. Oceanic Tritium Inventory Measurements. Tritium inventories measured as part of the GEOSECS survey (see Broecker et al, 1986, for summary) seem to support the Weiss and Roether scenario of tritium delivery. Weiss and Roether include in their work estimates of cumulative tritium delivery into the Northern Hemisphere Atlantic and Pacific Oceans via precipitation and continental runoff. These inputs and the total amounts of tritium measured in each ocean are listed in Table 3-7. The precipitation and runoff inputs into an ocean are subtracted from that ocean's total tritium content, and the remaining ocean tritium is assumed to have entered the ocean via-surface vapor exchange. Vapor exchange inputs of tritium estimated in this fashion are actually larger than the values obtained using Equation 3-5. Using this inventory method, the tritium input ratio for the Northern Hemisphere Pacific Ocean becomes 2.2. When the two oceans are considered together, the tritium input ratio is 2.8.

It is necessary, however, to examine the tritium inventory method in detail, particularly the way in which the precipitation inputs in Table 3-7 are estimated. Neither of the factors that determine this input,

Table 3-7

Comparisons of runoff and precipitation inputs of tritium into the North Atlantic and North Pacific, as estimated by Weiss and Roether (1980). The ocean tritium inventories listed were obtained during the GEOSECS program (see Broecker et al, 1986, for summary). The entries are decay-corrected to the year 1981. (From Koster et al, in preparation.)

	North Atlantic 10^{27} atoms	North Pacific 10^{27} atoms	Total Northern Ocean 10^{27} atoms
Observed ocean inventory	10.9	11.5	22.4
Precipitation	2.0	3.2	5.2
Runoff	<u>1.3</u>	<u>1.1</u>	<u>2.4</u>
Runoff + Precip.	3.3	4.3	7.7
Apparent vapor input i.e. Inventory - (Runoff + Precip.)	7.6	7.1	14.7
<u>App. vap. input</u> <u>Precip. input</u>	3.8	2.2	2.8

namely the average yearly precipitations (P) and average tritium concentrations in precipitation (C_p), are known with certainty. The values used for C_p are based only on measurements at the few sites indicated in Figure 3-22. It is conceivable that storms with tritium-rich water deposited large quantities of tritium into the ocean far from the few remote measuring stations. Suppose now that the estimated precipitation input of tritium for the combined oceans in Table 3-7 was increased by, say, 30%. The tritium input ratio obtained with the inventory method would not be 2.8 then but rather 2.0. In other words, the computed tritium input ratio using the inventory method is quite sensitive to the estimated precipitation input.

Furthermore, an input of tritium into the ocean not accounted for by the inventory method is the local fallout of tritium directly after the atomic tests. Perhaps significant quantities of tritium entered the ocean with explosion-generated particulates and aerosols, or perhaps local rainfall immediately after the explosions contained much higher tritium concentrations than those indicated in Figure 3-22, these higher concentrations never being measured. The Soviet tests in Northern Siberia may have added large unmeasured quantities of tritium to the Arctic Ocean, and some of this tritium may have later found its way into the Atlantic. All of this, of course, is pure speculation. Still, any such local fallout would tend to reduce the tritium vapor exchange input calculated with the inventory method.

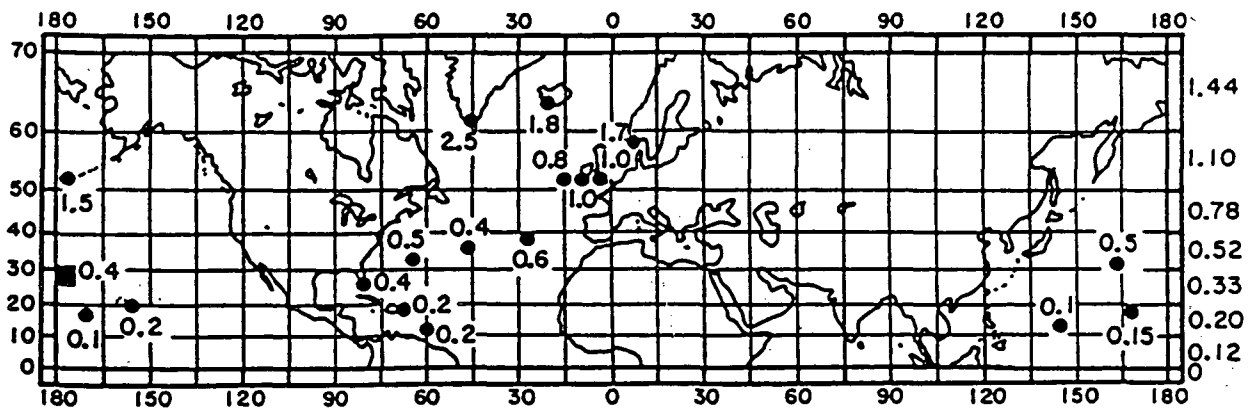


Figure 3-22 Map showing the locations (circles) of the 18 sites used by Weiss and Roether to assess the T/H ratio distribution for oceanic rain. Shown by each point is the ratio of the T/H ratio to that for Valencia, Ireland rain. Also shown is the value for the Midway station (square) not used by Weiss and Roether. Shown on the right are the averages for 10° latitude belts estimated by Weiss and Roether based on the results for these ocean stations. These values are also referenced to Valencia, Ireland. (From Koster et al, in preparation.)

d. Continental Versus Oceanic T/H Ratios in Precipitation. Figure 3-23 provides a geographical contour map of average tritium concentration in precipitation based on measurements at various Northern Hemisphere sites. Continental precipitation is clearly characterized by higher T/H ratios than those found in oceanic precipitation.

The fourth and fifth columns of Table 3-2 for Simulation T1 show that for the standard simulation, with the tritium source in the upper troposphere, there is no such distinction between oceanic and continental rains. This may be due to the prevention in the model of tritium re-evaporation from the ground surface. In the real world, tritium-laden precipitation water reaching a land or ice surface can re-evaporate and thereby increase the T/H ratio in lower atmospheric layers. This would explain the shape of the observed vertical T/H profile in Figure 3-19. The higher T/H ratio in lower layers would in turn increase the T/H ratio in subsequent precipitation events, e.g. by reducing the transfer of tritium out of falling raindrops during isotopic equilibration.

Columns 4 and 5 of Table 3-2 show that for Simulation T6, the simulation using the continental tritium source, the variations between the T/H ratios in oceanic and continental precipitations are similar to the observed variations. Although this is at least partly due to the source location, it may also reflect the effects of maintaining large lower level T/H ratios through re-evaporation.

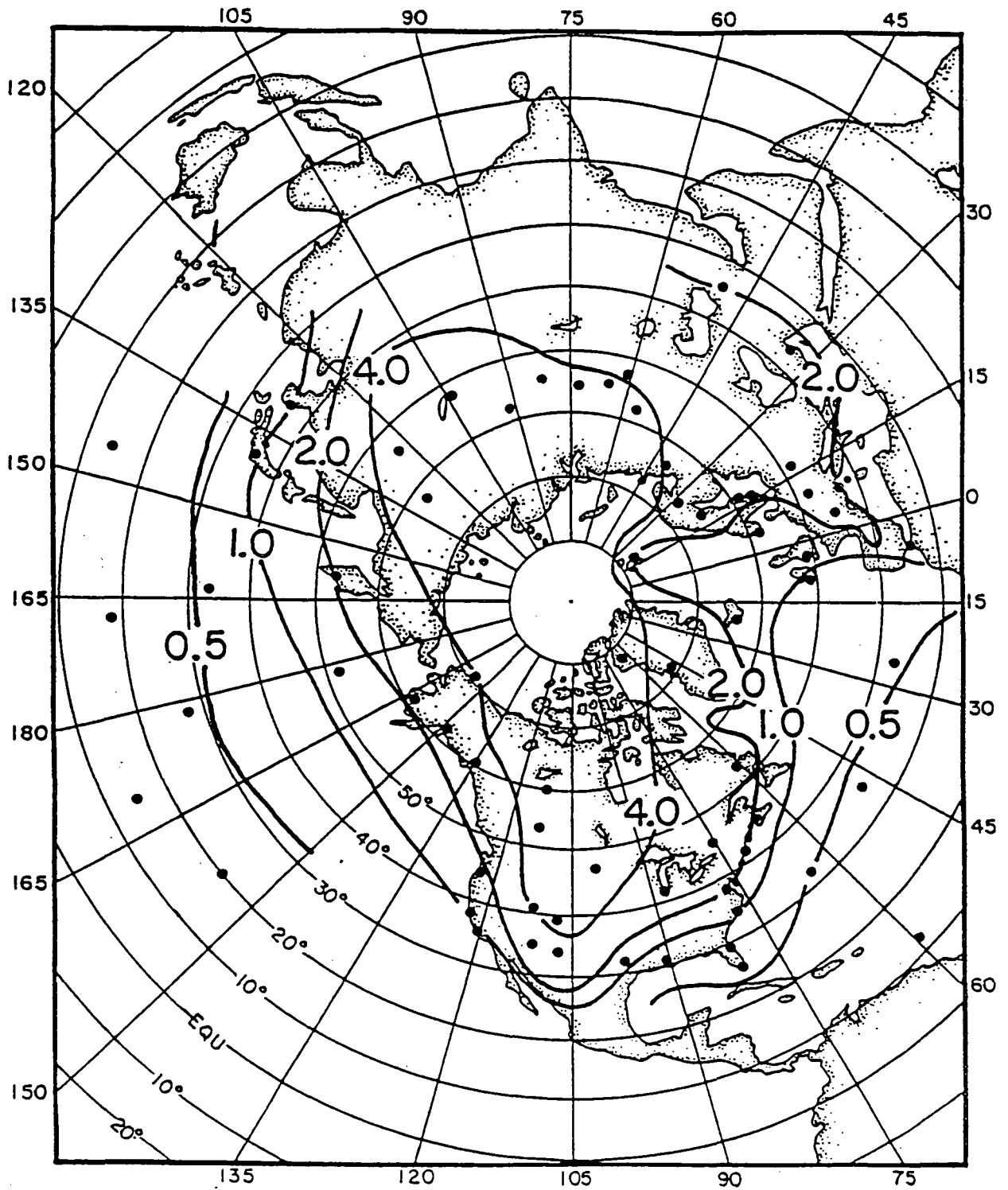


Figure 3-23 Map showing the geographic distribution of T/H ratios for precipitation in the Northern Hemisphere. The average T/H ratios are referenced to that for Valencia, Ireland. (From Koster et al, in preparation.)

3.3.4 Summary of Tritium Transport Simulation Results

Several GCM simulations of tritium transport from the upper troposphere to the ocean have been performed, and the results, characterized by the ratio of the tritium input into the ocean via vapor exchange to that via precipitation, are quite insensitive to the tritium source location and to changes in the parameterizations of model physics. Many of the prescribed changes were designed specifically to ease the transport of tritium vapor to the ocean surface. The steady-state atmospheric distributions of tritium vapor apparently adjusted themselves to mitigate the effects of the changes. The insensitivity to changes in model physics is encouraging, for although the insensitivity does not imply that the model parameterizations are correct, a strong sensitivity could raise difficult questions about the choice of the best model parameters.

Combining the results of Simulations T1 and T6, the standard and continental source simulations, produces the GCM-generated tritium input ratio of 1.1. The analysis of Weiss and Roether (1980), on the other hand, suggests that a tritium input ratio of 2.3 is consistent with observations. The discrepancy is due in part to Weiss and Roether's assumption of complete isotopic equilibrium between ocean vapor and rain. The observed tritium concentrations in rain/vapor pairs are, in fact, far enough from equilibrium to reduce the tritium input ratio suggested by observations to perhaps as low as 1.8. Given the uncertainties in the observational data, such as the observed precipitation rates in the Northern Hemisphere oceans and their associated tritium concentrations,

the model's simulation of tritium delivery into the ocean is not necessarily inconsistent with nature.

The model results also suggest, in three different ways, the importance of continental re-evaporation as an intermediate step in the transfer of tritium from the upper troposphere to the oceans. First, as indicated in Table 3-2, half of the tritium released from the upper troposphere in Simulation T1 first reached the earth's surface in continental precipitation. Second, the simulations with the upper tropospheric tritium source did not produce tritium input ratios close to that suggested by Weiss and Roether's analysis, while the simulation with the continental source did. Finally, the observed variation in T/H ratio between continental and oceanic precipitation is matched in the GCM only when the tritium is evaporated from the continents.

3.4 Stable Isotope Simulations

The ability of the tracer water model to reproduce the observed global distributions of the stable water isotopes HDO and H₂¹⁸O was tested in a three year simulation using surface-conserved isotopic tracers. Recall from Chapter 1 that the model forming the basis of the tracer water model was developed at GISS by Dr. Jean Jouzel of the Centre de Etudes Nucleaires in Paris, France. The experiment and analysis described in Sections 3.4.1 and 3.4.2 are Jouzel's work, discussed in detail in a separate publication (Jouzel et al, 1987). A brief description of the experiment is included in this report because it further illustrates the character of the GISS tracer water model and provides another means of comparing model output with observations.

A short-term stable isotopes simulation is also described in Section 3.4.3. The two simulations are the only ones discussed in this report that use surface-conserved tracers. As explained in Section 2.4, surface-conserved tracers are monitored not only in the atmosphere but also in ocean ice, land ice, and land surface reservoirs. Long-term spatial and temporal distributions of the surface-conserved tracer are made non-uniform by its assigned isotopic fractionation properties.

3.4.1 Description of the Three Year Stable Isotopes Simulation

The initial conditions for the GCM's prognostic variables were the model conditions on Nov. 1 of Year 1 of the five year simulation described by Hansen et al (1980). The initial concentrations of the stable isotopes in each atmospheric grid box and each ground surface reservoir were assigned reasonable values; after two simulation months, the spatial distributions of isotope concentration in the atmosphere and in the surface reservoirs were assumed effectively independent of the initial distributions. The model was then run for three more years, storing various tracer diagnostic quantities every month.

3.4.2 Results of the Three Year Stable Isotope Simulation

A small sample of the simulation results presented by Jouzel et al (1987) is provided below. Jouzel also analyzed model-generated vertical profiles of stable isotope concentration and the relative δD and $\delta^{18}O$ values in model precipitation.

a. $\delta^{18}\text{O}$ in Precipitation.

Figure 3-24 compares the model's mean annual spatial distribution of $\delta^{18}\text{O}$ (see Section 2.2.2) in precipitation with that observed in the real world. In both data sets, the $\delta^{18}\text{O}$ values vary with latitude in higher latitudes and are largely controlled by the positions of the continents in lower latitudes. These trends reflect a well established relationship between surface temperature and $\delta^{18}\text{O}$ in precipitation (e.g., Dansgaard, 1964). At low temperatures, these two quantities are highly correlated, as discussed further below. The quantities are not correlated at higher temperatures. In fact, in equatorial regions, the $\delta^{18}\text{O}$ values are affected more by precipitation depth.

Not surprisingly, specific differences between the observed and modeled results do exist, possibly due to differences in the observed and modeled temperature and precipitation fields. Jouzel et al (1987) note in particular the differences in Central Greenland, South America, and Southern Africa. Modeled $\delta^{18}\text{O}$ values in precipitation tend to be too low in midlatitudes and too high at the poles. In general, though, the modeled and observed distributions are found to match fairly well.

Jouzel also compared model results with observations on a seasonal basis. Again, the basic trends in the $\delta^{18}\text{O}$ distributions matched well, but specific differences abounded. The model, for example, failed to reproduce the observed seasonal cycle of $\delta^{18}\text{O}$ in Greenland precipitation. The deficiency might be related to an established GISS GCM deficiency, that of excessive model rainfall in Greenland.

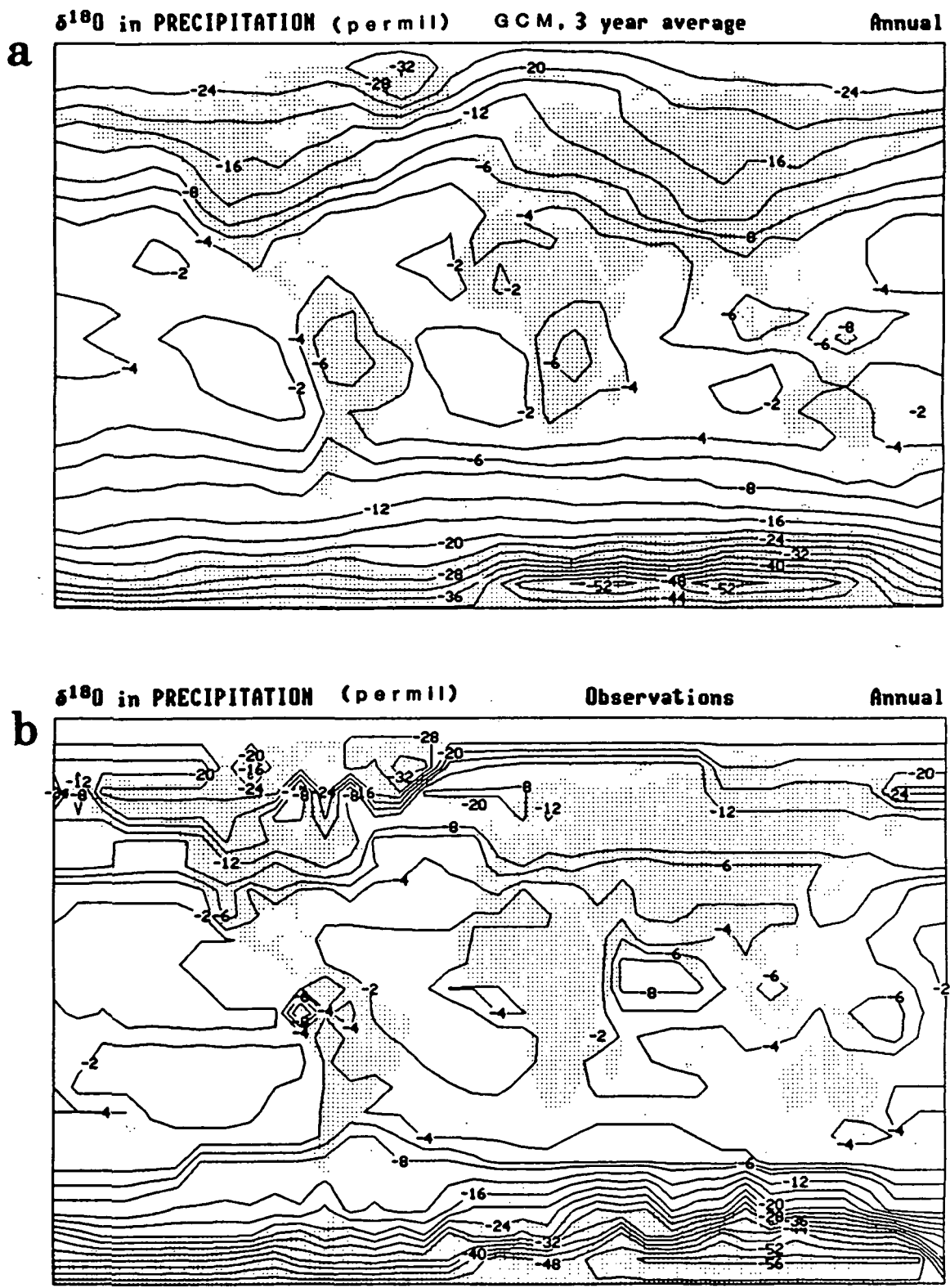


Figure 3-24 $\delta^{18}O$ in precipitation (a) for the model simulation and (b) from observations. (From Jouzel et al, in press.)

b. $\delta^{18}\text{O}$ versus Temperature

In nature, surface temperatures T_G below 15°C are linearly related to $\delta^{18}\text{O}$ contents in precipitation. This is illustrated in Figure 3-25a. Each point in the plot represents a single site and is located in the plot according to the site's mean annual surface temperature and mean annual $\delta^{18}\text{O}$ in precipitation, as measured through the IAEA/WMO precipitation network (IAEA, 1981) and other sources (see Jouzel et al, 1987, for summary).

The standard explanation for this relationship (e.g. Dansgaard, 1964) involves Rayleigh condensation, under which droplets fall out of a parcel as soon as they are formed. Due to isotopic fractionation, the isotope/water ratio in the vapor of an air parcel is reduced after every condensation event. As the air parcel moves into colder and colder regions, more and more condensation events occur and the parcel becomes more and more depleted in the isotope. The isotope content of condensate formed in the parcel is therefore dependent on the amount of previous condensation having occurred in the parcel and is thus related to the surface temperature at the precipitation site. The relationship has been used to infer average polar surface temperatures during glacial and interglacial periods from the isotope contents observed along Antarctic ice cores (e.g., Lorius et al, 1985).

Figure 3-25b shows the corresponding plot Jouzel constructed from model data (Jouzel et al, 1987). The same linear trend is apparent below 15°C , although the slope of the fitted line is slightly smaller than

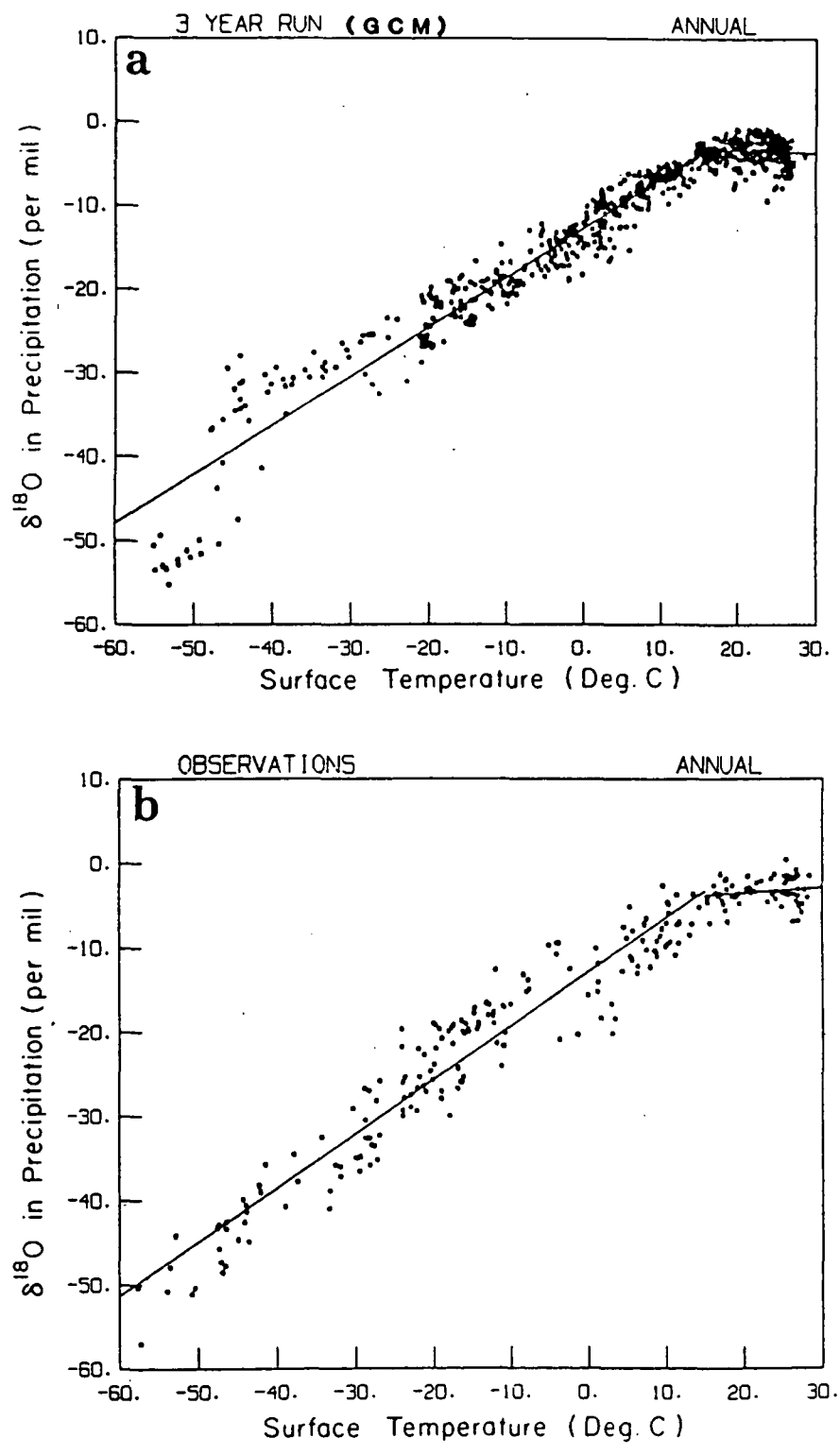


Figure 3-25 Mean annual $\delta^{18}\text{O}$ in precipitation versus mean annual surface temperature at the precipitation site (a) for the model simulation and (b) from observations. (From Jouzel et al, 1987.)

that for the observed data. The linear relationship is also present when the observed and modeled data sets are examined by season.

Again, the differences in the spatial distributions of $\delta^{18}\text{O}$ shown in Figure 3-24 may be due in part to differences between observed and modeled distributions of surface temperature. By comparing $\delta^{18}\text{O}$ values directly with surface temperature in Figure 3-25, this potential source of disagreement is avoided.

c. Precipitation versus $\delta^{18}\text{O}$

The greater a tropical region's precipitation is, the lower the average $\delta^{18}\text{O}$ in that precipitation is likely to be. Dansgaard (1964) provides three possible explanations for this "amount effect". First, due to Rayleigh condensation, the $\delta^{18}\text{O}$ in rainwater decreases as a given precipitation event proceeds. Thus, the greater a storm's precipitation depth is, the lower the rainwater's $\delta^{18}\text{O}$ is in the final stages of the storm, and the lower the overall average $\delta^{18}\text{O}$ is for the complete storm. Second, Dansgaard suggests that light rains allow for greater isotopic exchange above the cloud base, enhancing the $\delta^{18}\text{O}$ values in such precipitation. Finally, re-evaporation of precipitation below the cloud base increases isotopic concentrations in the remaining condensate, and this effect is most pronounced for lighter rains.

Figure 3-26b illustrates how the amount effect is reflected in observations. Each point in the figure represents a single measurement site and is located in the plot according to the site's mean annual pre-

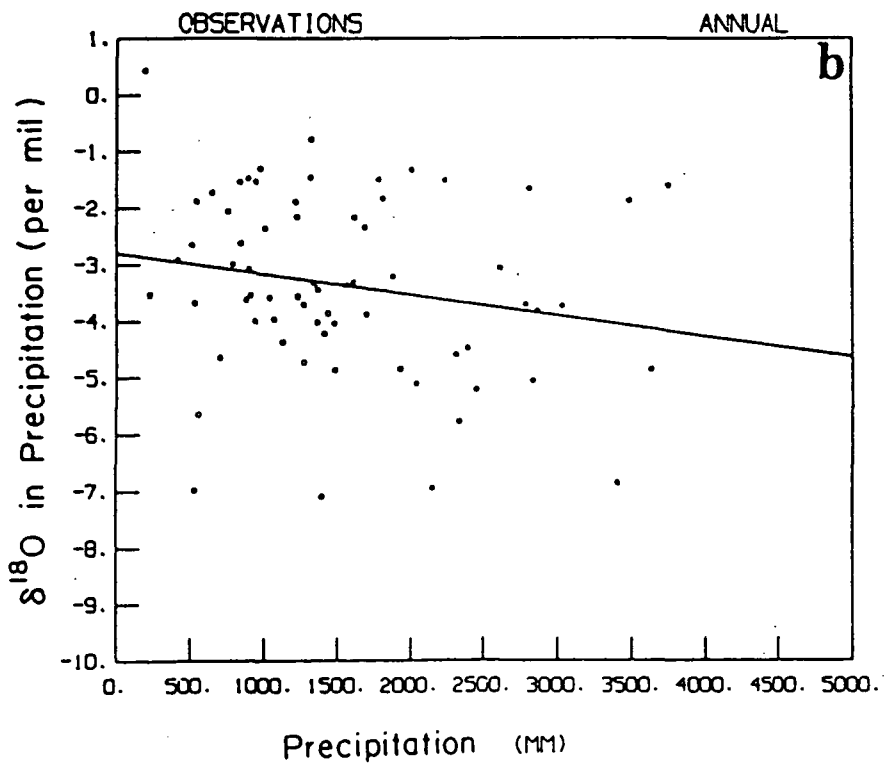
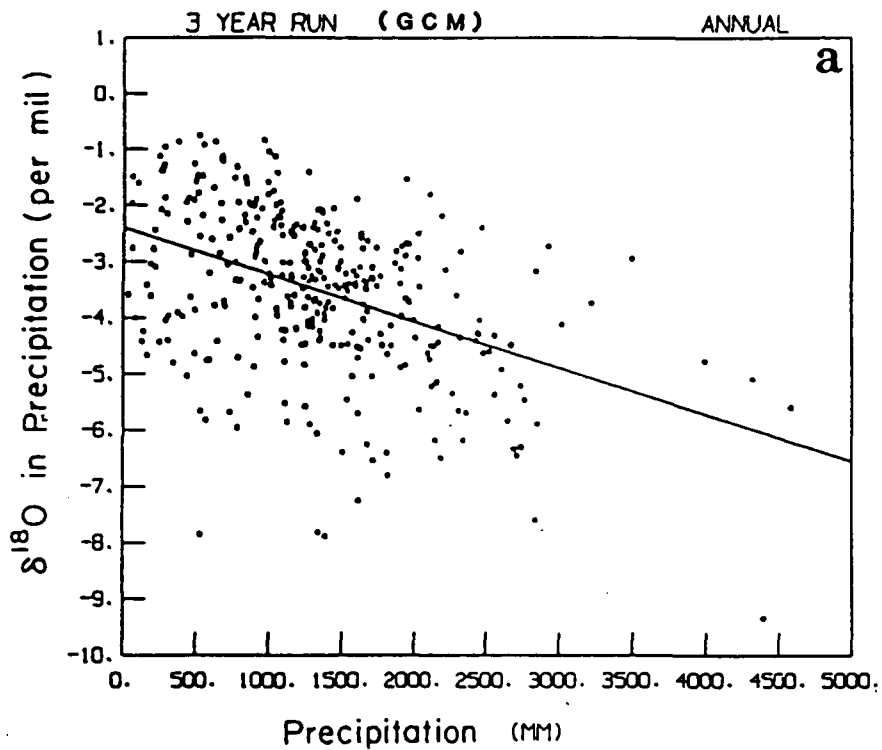


Figure 3-26 Mean annual $\delta^{18}\text{O}$ in precipitation versus mean annual precipitation (a) for the model simulation and (b) from observations. (From Jouzel et al, 1987.)

precipitation and mean $\delta^{18}\text{O}$ in that precipitation. The sites considered have mean annual surface temperatures greater than 15°C , outside the regime where temperature controls the $\delta^{18}\text{O}$ values. A decrease in $\delta^{18}\text{O}$ with precipitation is apparent, although the correlation is not as great as the $\delta^{18}\text{O}$ - temperature correlation discussed above. Figure 3-26b indicates that the model reproduces the amount effect. It shows the corresponding plot constructed with data from the model (Jouzel et al, in press); notice the similar trend. The slope of the fitted line, however, is twice that of the fitted line for the observed data.

3.4.3 Sensitivity of Model Results to the Tracer Advection Scheme

Jouzel et al (1987) concluded that although many specific discrepancies between the model-generated and observed distributions of δD and $\delta^{18}\text{O}$ were found, the model on the whole was successful in reproducing the observed distributions. Due to the nature of the simulation, however, the success may result largely from the formulations of isotopic fractionation. The extent to which the success applies to the transport of non-isotopic tracers is not readily apparent.

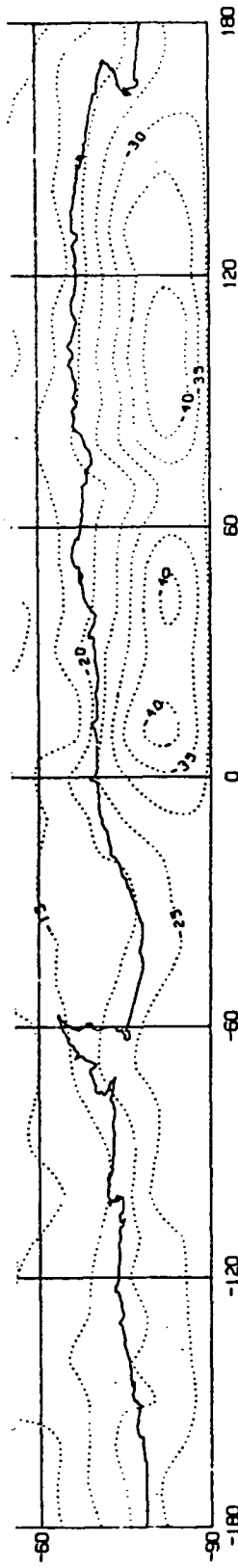
Sensitivity tests using the isotopic tracers can, however, examine the adequacy of certain tracer transport parameterizations. For example, a two month stable isotopes simulation was performed in which the usual slopes scheme for tracer advection (Section 2.3.1) was replaced by a simple upstream weighting scheme. That is, the tracer flux out of a grid box at any time step was set equal to the water flux out of the box multiplied by the average tracer/water ratio in the box. Thus, no subgrid

variation in tracer concentration was assumed. (This same change was imposed in Simulation T15 in Section 3.3 above.) The model conditions on a first of June during the three year stable isotopes simulation described above were used as the initial conditions for the model prognostic variables and the stable isotope concentrations.

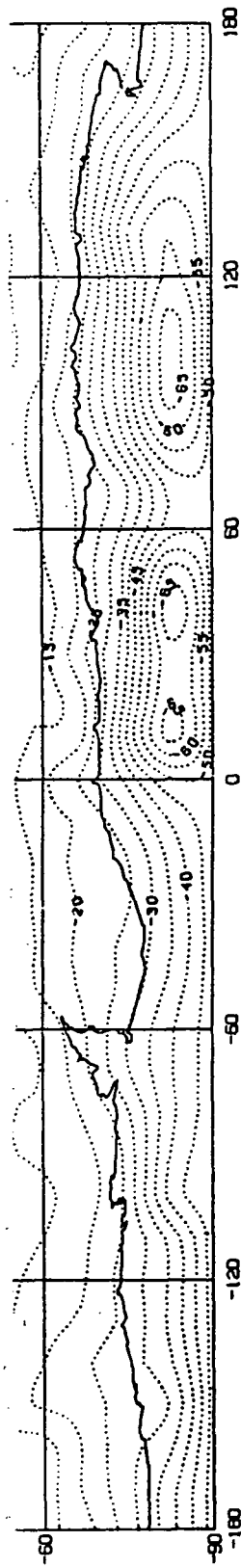
The spatial distribution of $\delta^{18}\text{O}$ in Antarctic precipitation during the second month is compared in Figure 3-27 to the corresponding distribution obtained using the slopes scheme and to the observed distribution for Antarctic winter (JJA). The $\delta^{18}\text{O}$ values produced with the slopes scheme are similar to the observed values, but the $\delta^{18}\text{O}$ values produced with the upstream weighting scheme are clearly too large. Larger values, remember, imply that the precipitation is relatively less depleted in H_2^{18}O .

This result reflects the added diffusivity inherent in the upstream weighting scheme. As water vapor and H_2^{18}O move toward the pole, isotopic fractionation and Rayleigh condensation act to deplete H_2^{18}O relative to water vapor. Implementing the more diffusive upstream weighting scheme increases the speed at which the H_2^{18}O travels toward the pole and thereby provides fractionation and Rayleigh condensation less time to act on it. Thus, more of the H_2^{18}O reaches the Antarctic continent. The comparison in Figure 3-27 suggests that in terms of not producing this excessive diffusivity, the slopes scheme for tracer advection is superior to the upstream weighting scheme.

a. Upstream weighting scheme



b. Slopes scheme



c. Observations

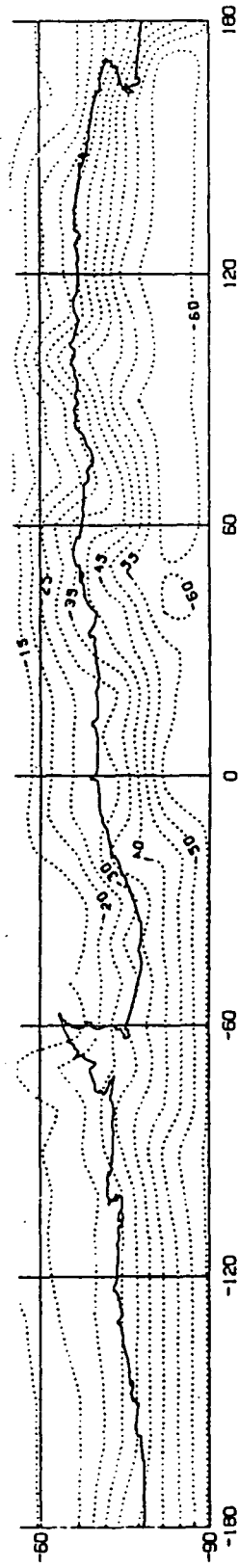


Figure 3-27 $\delta^{18}O$ in Antarctic precipitation.

Chapter 4

Examples of Model Applications and Comparisons with Other Models

The three sets of simulations described in this chapter demonstrate some further uses of the tracer water version of the GISS GCM. The first determines where evaporated water from specified source regions first returns to the earth's surface, and the second determines the evaporative sources of precipitation for several individual grid squares. The third determines how evaporative sources influence the isotope content of Antarctic precipitation. None of the hydrological information presented in this chapter can be measured in the real world. A small section at the end of the chapter examines how the tracer water model results compare with simple models of local water recycling found in the literature.

The tracer simulations described below have some basic similarities. Each simulation used aboveground tracers evaporating from tracer source regions on the earth's surface. (See Section 2.4.2.) Each simulation lasted two months, using (except where marked) a set of instantaneous model conditions obtained during the standard five-year GISS GCM simulation (Hansen et al, 1983) as initial conditions for the GCM's prognostic variables. Preliminary studies have shown that the typical atmospheric residence time of an aboveground tracer is on the order of days; a one month preconditioning period was therefore considered adequate to bring the tracers' atmospheric distributions to steady-state. The tracer precipitation fluxes were monitored starting at the beginning of the second simulation month.

4.1 Return of Evaporated Water to the Earth's Surface

The tracer water model simulations presented in the inter-annual variability study (Section 3.2) determined the characteristic distances and directions traveled by water evaporating from a Southeast Asia grid square. Due to the influence of local climate, water evaporating from a different source region would probably exhibit a different set of travel characteristics. To examine this, one of the simulations following Southeast Asia water also followed tracers from six other source regions, located in the Sudd region of Sudan, the African Sahel, the Amazon Basin, the Mississippi River Basin, Western Europe, and the European U.S.S.R.

The initial conditions for the simulation were the model conditions on June 1 of Year 3 of the standard GCM simulation. The thirty-day July tracer precipitations are shown in Figures 4-1 through 4-6; the source regions are indicated by the shaded squares or rectangles. As discussed in Section 3.2, tracer precipitation results are least likely to be accurate when integrated over small spatial scales; thus, the 10 mm/30-day contours in Figures 4-1 through 4-6 do not deserve as much attention as the 1 mm/30-day contours. The spotty pattern of the 1 mm/30-day contours produced by the European U.S.S.R. source region (Figure 4-6) is, in fact, only important in roughly indicating the lateral extent and direction of tracer movement.

The tracer transport characteristics do vary with source location. Tracers from the Sahelian and Sudd source regions in Africa (Figures 4-3

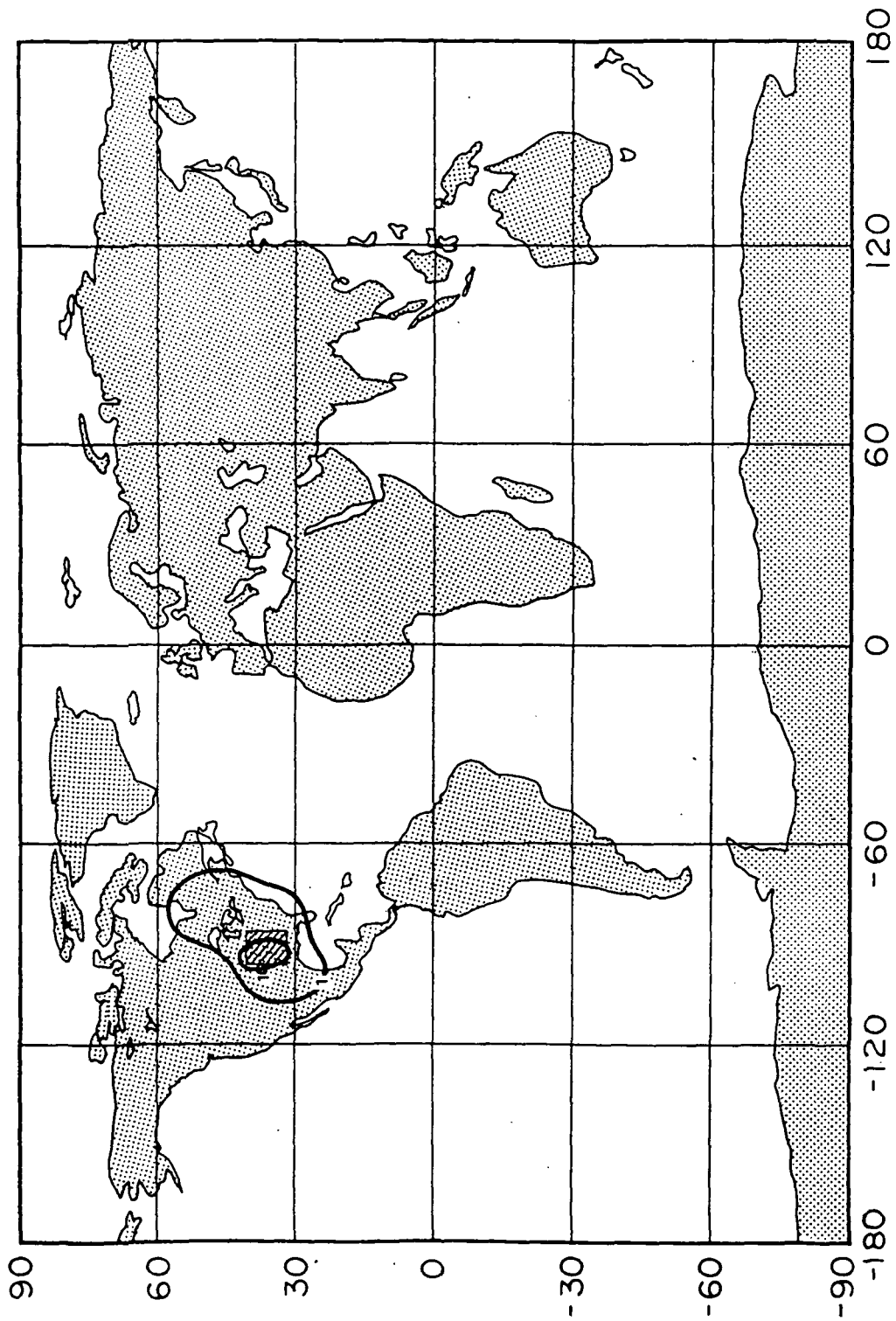


Figure 4-1 Thirty-day steady-state July tracer precipitation (mm). The tracer source region lies in the Mississippi Valley. During 30 July days, tracer precipitation = 2.7×10^{13} kg and tracer evaporation = 1.9×10^{13} kg.

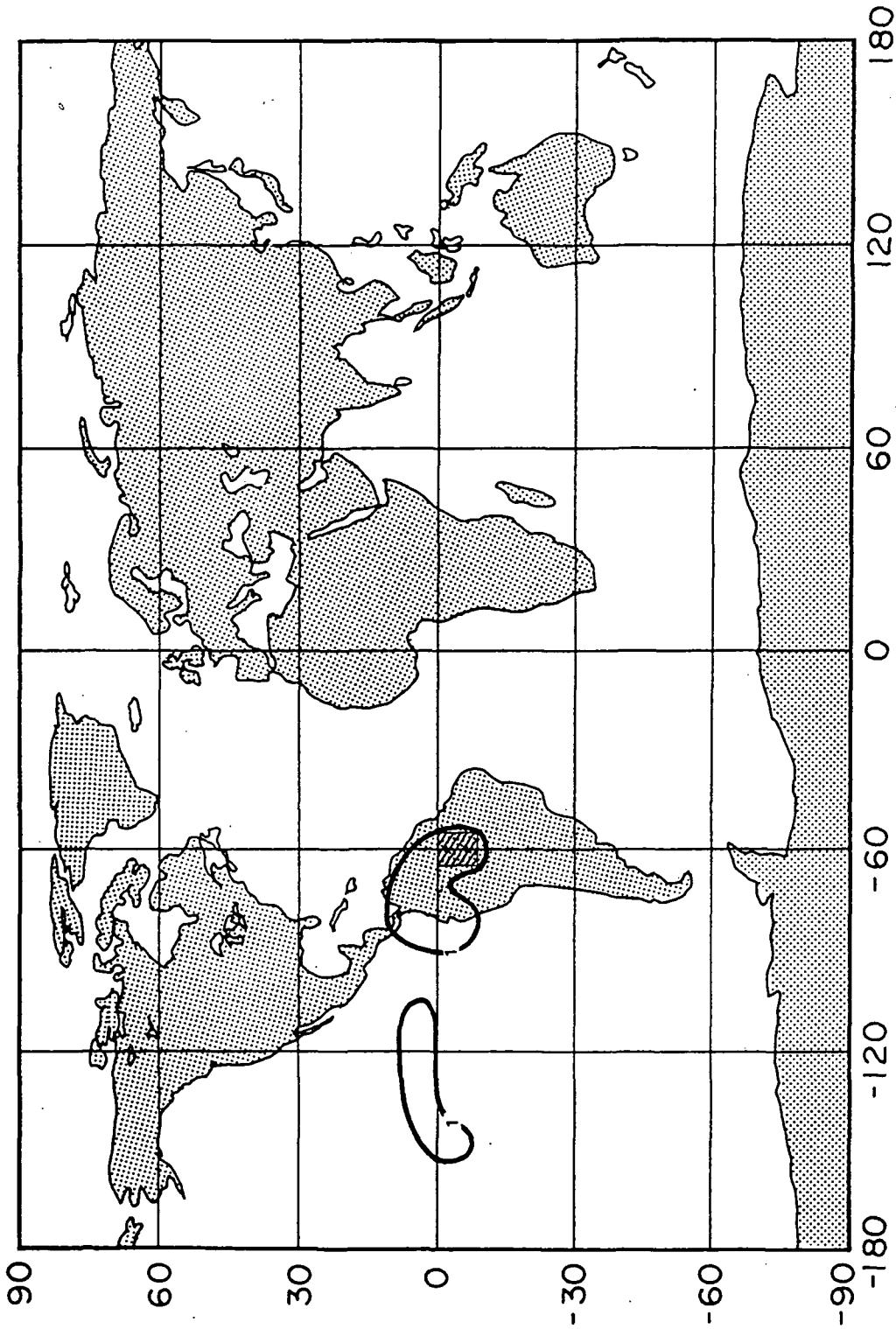


Figure 4-2 Thirty-day steady-state July tracer precipitation (mm). The tracer source region lies in the Amazon Basin. During 30 July days, tracer precipitation = 4.1×10^{13} kg and tracer evaporation = 8.9×10^{13} kg.

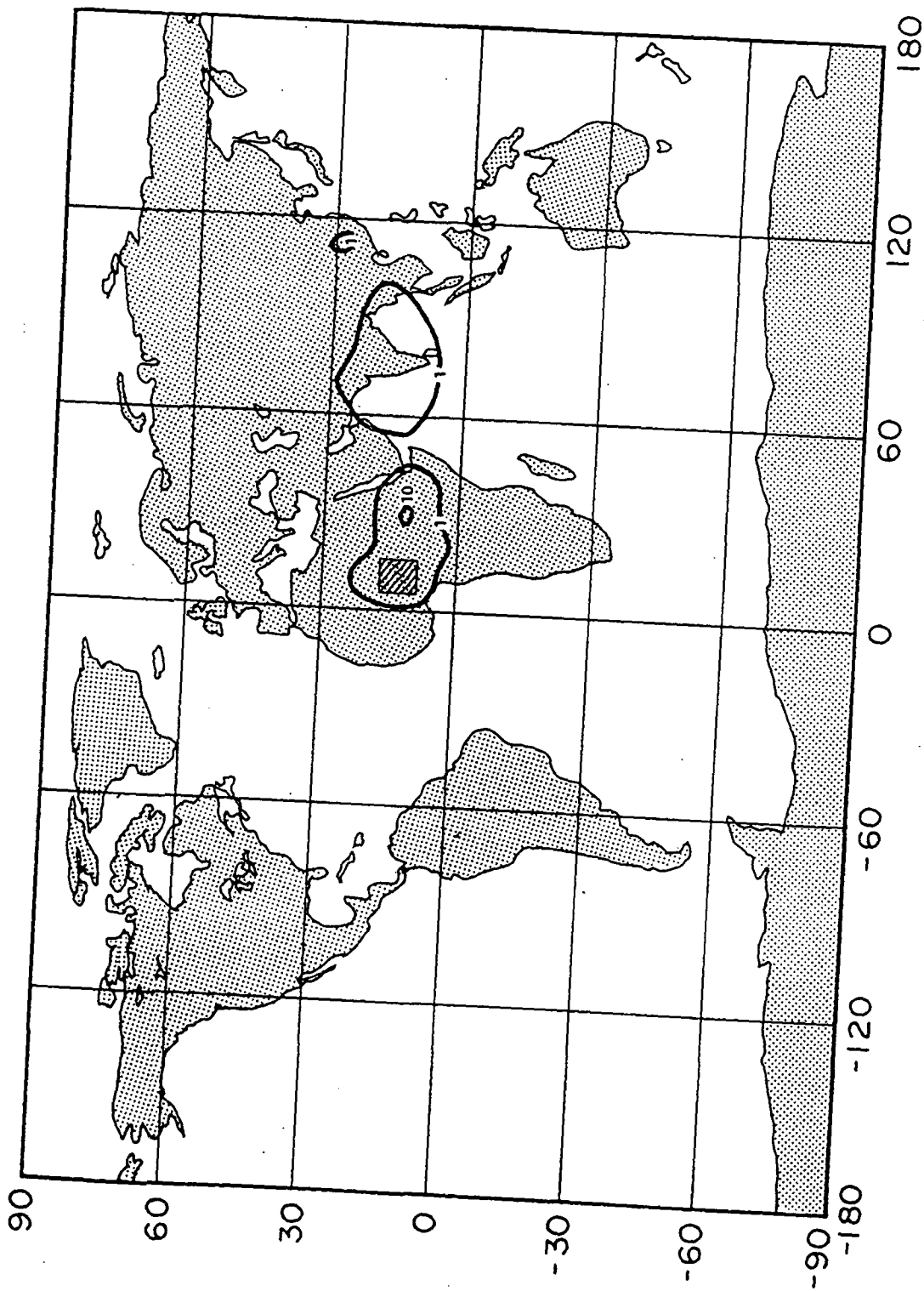


Figure 4-3 Thirty-day steady-state July tracer precipitation (mm). The tracer source region lies in the African Sahel. During 30 July days, tracer precipitation = 6.4×10^{13} kg and tracer evaporation = 9.3×10^{13} kg.

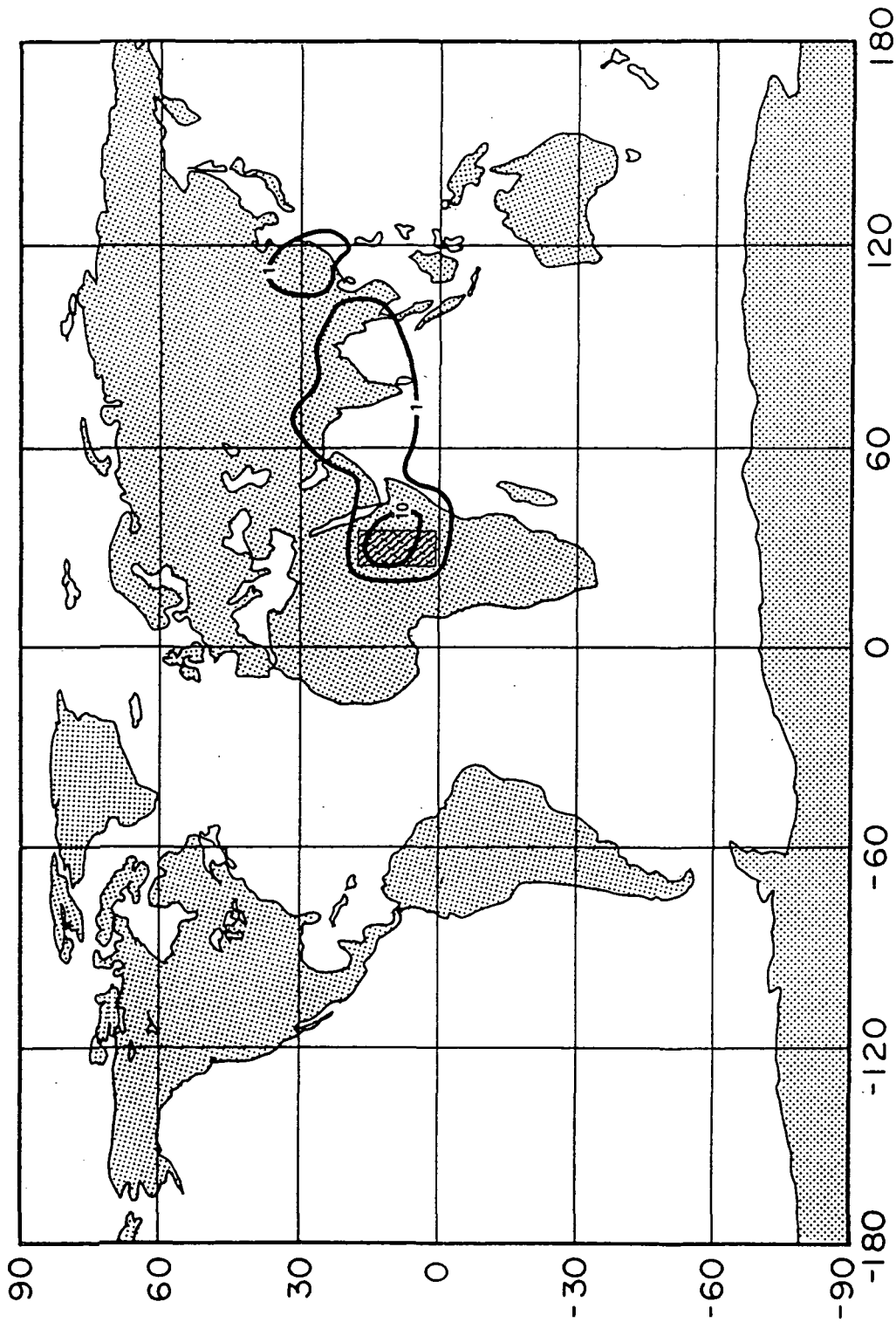


Figure 4-4 Thirty-day steady-state July tracer precipitation (mm). The tracer source region lies in the Sudd area of Sudan. During 30 July days, tracer precipitation = 1.1×10^{14} kg and tracer evaporation = 1.8×10^{14} kg.

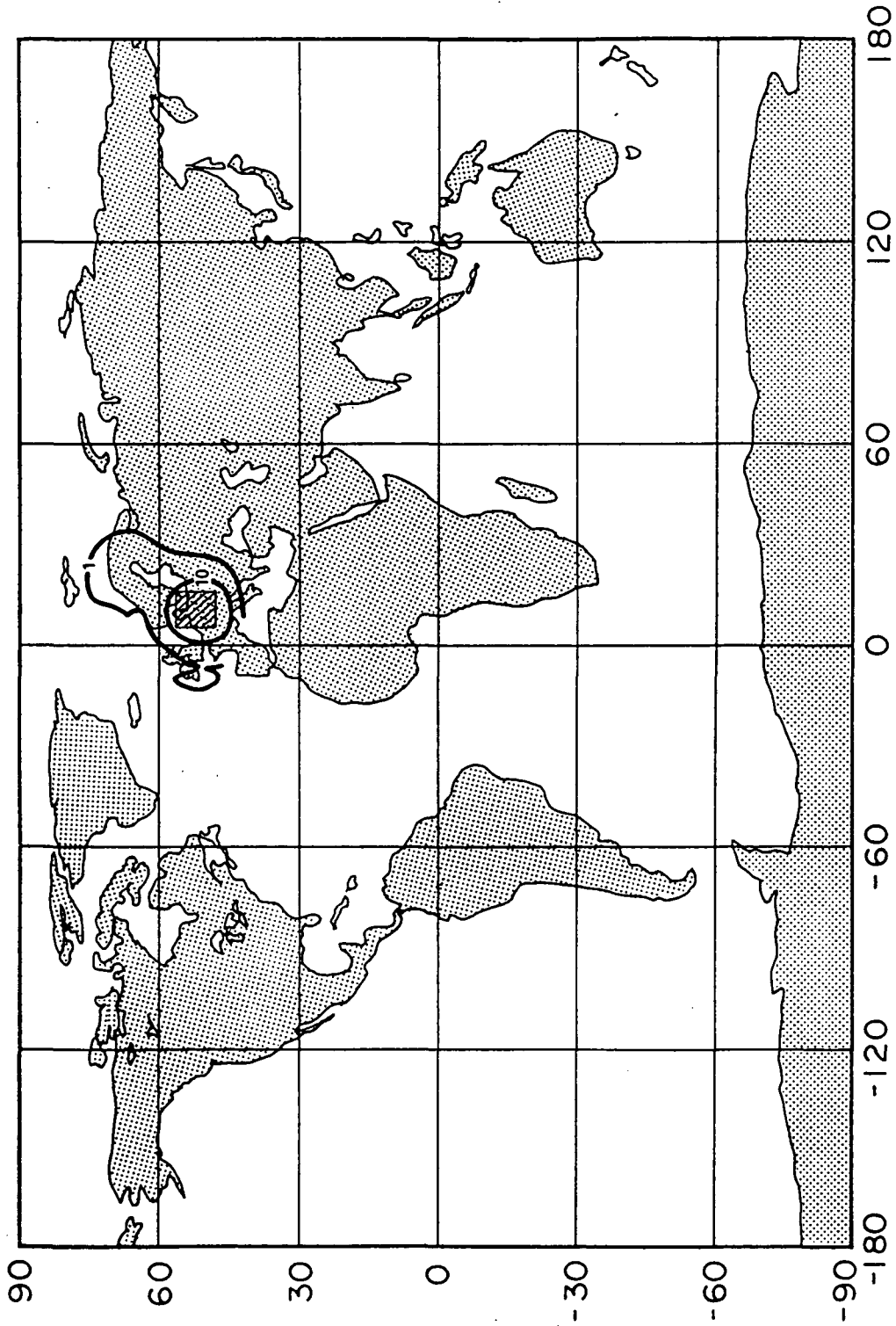


Figure 4-5 Thirty-day steady-state July tracer precipitation (mm). The tracer source region lies in Western Europe. During 30 July days, tracer precipitation = 6.8×10^{13} kg and tracer evaporation = 9.8×10^{13} kg.

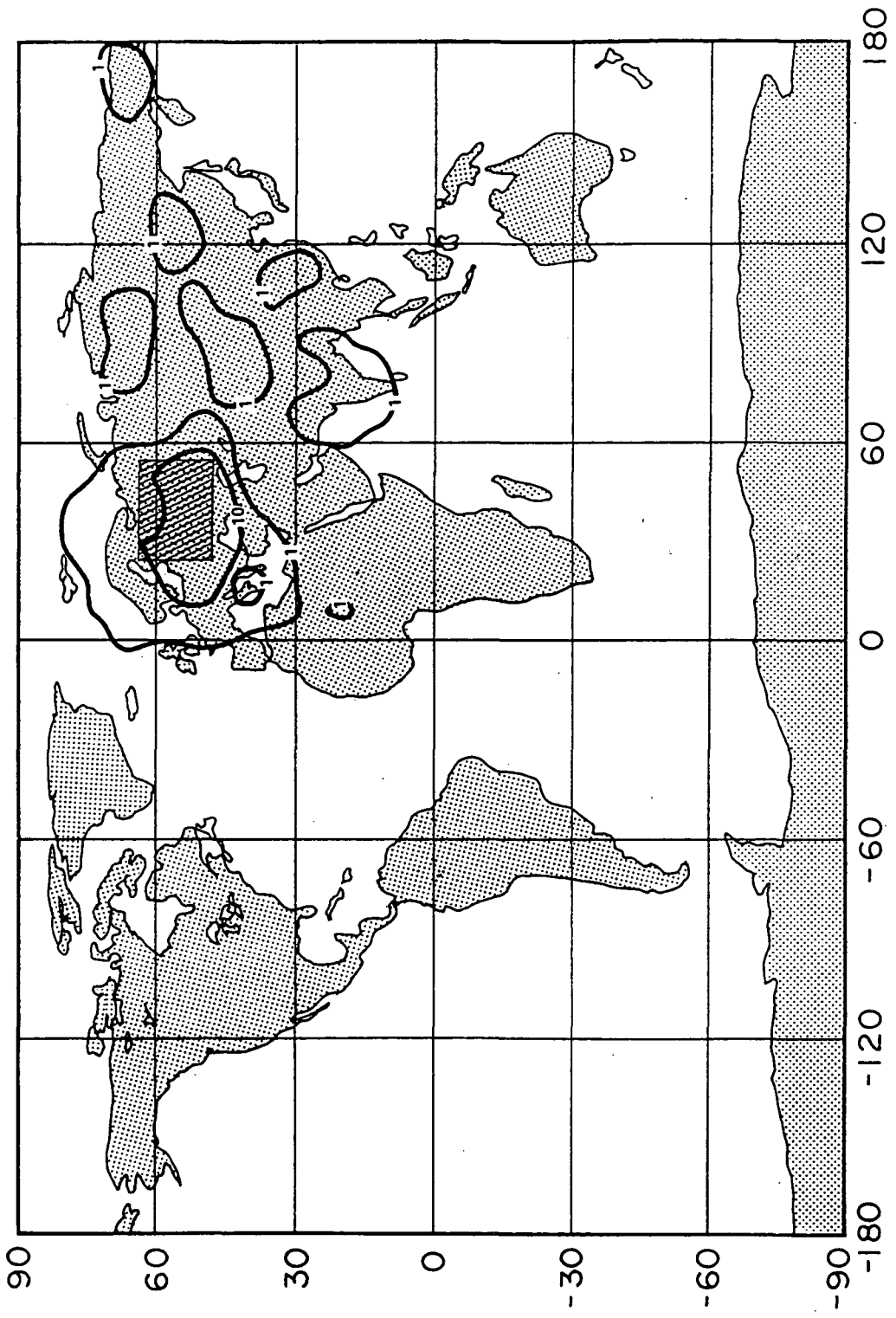


Figure 4-6 Thirty-day steady-state July tracer precipitation (mm). The tracer source region lies in the European U.S.S.R. During 30 July days, tracer precipitation = 2.4×10^{14} kg and tracer evaporation = 3.2×10^{14} kg.

and 4-4), for example, move eastward before precipitating, while tracer water from the Amazon source region, which also lies in the tropics (Figure 4-2), moves to the west. The transports of tracer water from the midlatitudinal Mississippi Valley and Western Europe source regions (Figures 4-1 and 4-5) and from the tropical Southeast Asia source region (Section 3.2) have a relatively larger meridional component. Also indicated on each figure is the total July tracer evaporation from its source region and the globally integrated July tracer precipitation. The precipitation can be greater than the evaporation because the former is partly composed of tracer evaporated during June. Notice that although the Western European and Sahelian tracers evaporate at roughly the same rate in July and have roughly the same thirty-day global precipitations, the Sahelian tracer exhibits a greater lateral influence. Notice also how India receives significant amounts of precipitation from the Sahelian, Sudd, and European U.S.S.R. source regions.

The water vapor flux maps provided in Section 3.1 can be used to evaluate the accuracy of the tracer precipitation contours. Consider, for example, the Sudd region of Africa. A comparison of Figures 3-3a and 3-3b indicates that if the observed summer zonal vapor fluxes over this region are accurate, then the GCM tends to move water vapor the wrong direction there. The tracer precipitation contours lying to the east of the Sudd source region in Figure 4-4 are thus suspect. The GCM's Sahelian tracer precipitation distribution may be incorrect for the same reason. Discrepancies between observed and modeled summer vapor flux distributions (both zonal and meridional) are not as obvious over the other source regions.

To illustrate the magnitude of tracer loss through oceanic vapor exchange, Figure 4-7 shows the two-dimensional distribution of downward tracer vapor flux onto the ocean surface for one of the Southeast Asia tracer simulations. A comparison with the magnitudes of tracer precipitation in Figure 3-18 indicates that precipitation is the more important mechanism for removing tracer from the atmosphere.

4.2 Origins of Local Precipitation

Every water molecule in the earth's atmosphere can be assigned a unique location on the earth's surface from which it most recently evaporated. Consequently, the precipitation forming from the water vapor above a given location (e.g., New England) is composed of evaporative water contributions from a complete set of earth divisions (e.g., North America, the North Atlantic, the Tropical Atlantic, and so on.) In the experiment described below, the tracer water model was used to determine the relative magnitudes of such evaporative contributions to certain local precipitations, at least for the inherent GCM climate. Determining the evaporative sources of a given region's precipitation is essentially the inverse of the problem studied in Section 4.1.

4.2.1 Description of Experiment

Figure 4-8 shows the Northern Hemisphere divided into nine sections, roughly representing nine climatic regions. For completeness, the entire Southern Hemisphere was taken to be a tenth section. Each section was defined to be a source region for a unique aboveground, non-isotopic

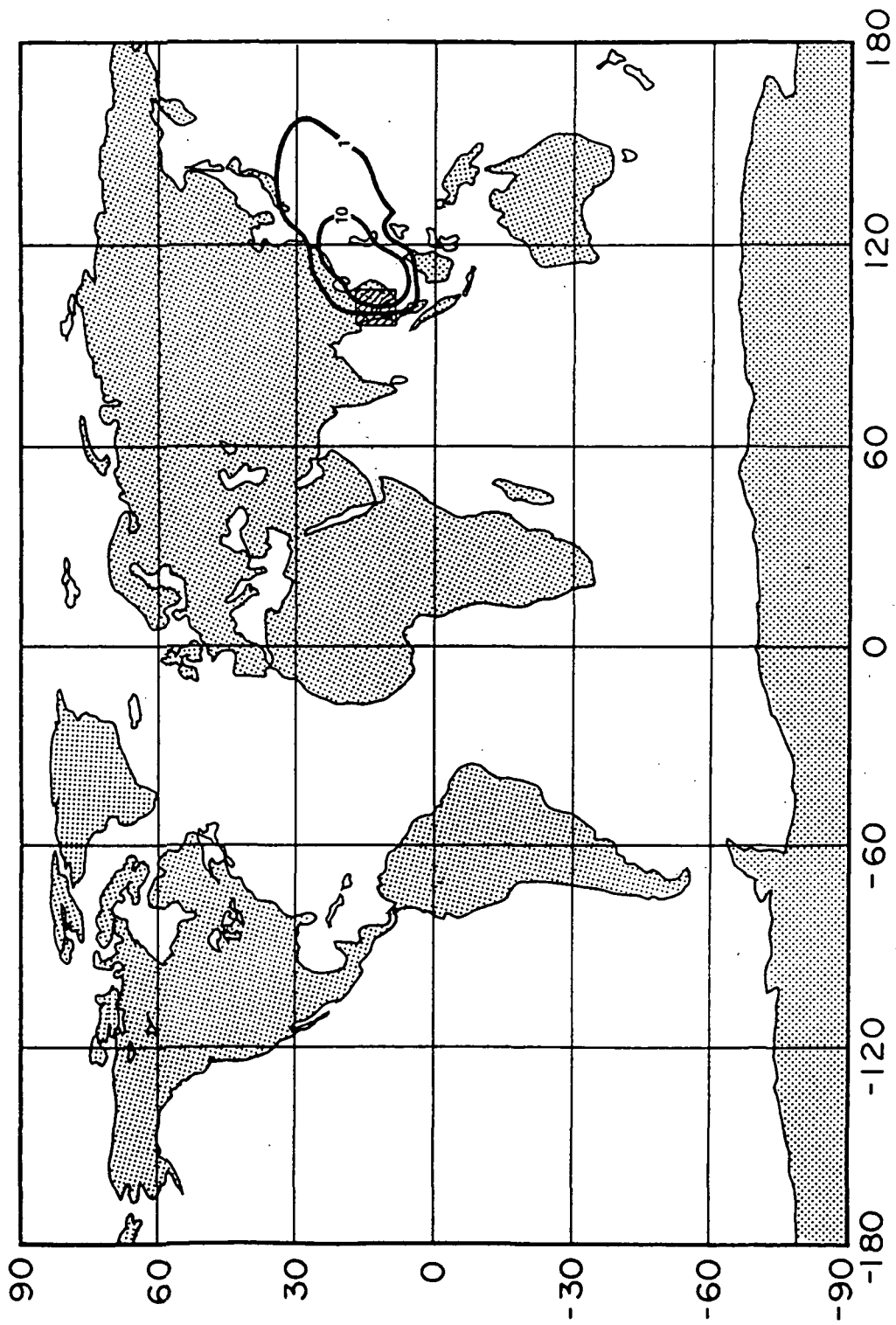


Figure 4-7 Thirty-day steady-state tracer vapor impact onto ocean surface in July (mm). The tracer source region lies in Southeast Asia.

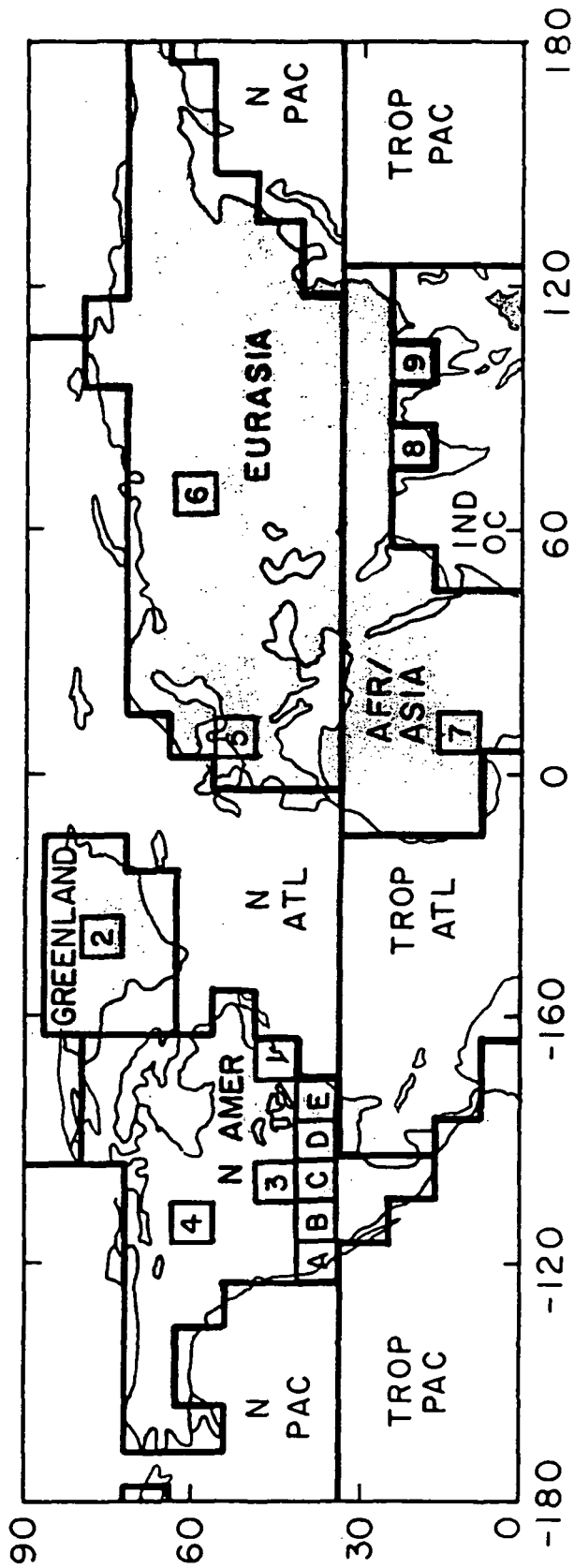


Figure 4-8 Source regions chosen for "origins of precipitation" experiment. Heavy lines separate the tracer source regions. The local precipitations analyzed occur in the small numbered or lettered squares.

tracer. Therefore, water evaporating from any location on the earth's surface during a simulation was effectively tagged as one of ten different tracers. After the initial atmospheric water had precipitated or condensed to the surface, the total precipitation onto any surface grid square was necessarily equal to the sum of the ten tracer precipitations. This allowed the calculation of the relative contribution of each source region to the precipitation over the square.

The tracer experiment consisted of four two-month simulations, the first month of each allowing for the removal of initial atmospheric vapor, and the second month providing a thirty-day averaging period for the tracer precipitations. The chosen initial conditions were the model conditions on December 1 of Year 2 and on March 1, June 1, and September 1 of Year 3 in the standard five-year Model II simulation. Some of the results presented below have previously been published (Koster et al, 1986).

4.2.2 Results

Figure 4-8 also displays, as numbered or lettered squares, the local regions analyzed in this experiment. The numbers correspond to the numbered sections of Table 4-1, which provides the relative contributions (in percent) of the source regions in Figure 4-8 to the local precipitations, for each season. (Contributions from regions providing, for each season, less than 5% of a local precipitation do not appear in the corresponding section.) Again, these results are for thirty-day periods in April, July, October, and January, respectively. The sum of the ten source region

Table 4-1

Percent contributions of the source regions to the local precipitations. Each numbered section corresponds to a like-numbered local area in Figure 4-8. The Southern Hemisphere is the tenth source region.

		N	Trop	Eur	Afr/	Ind	N	Trop	N	Green	Sum
		Atl	Atl	Asia	Asia	Oc	Pac	Pac	Amer	land	of 10
1. Northeast U.S.	Spring	43.3	22.4					4.3	27.8		99.9
	Summer	54.1	10.5					0.8	32.7		99.2
	Fall	63.5	4.5					3.6	25.1		99.7
	Winter	34.0	13.0					8.8	40.5		100.0
2. Central Greenland	Spring	40.0	5.3	2.9			6.6	7.1	10.5	24.9	99.4
	Summer	15.0	3.2	12.8			4.5	2.8	30.8	27.2	97.7
	Fall	52.2	3.8	2.1			9.3	4.8	8.3	17.2	98.7
	Winter	44.4	16.6	0.5			4.4	9.5	7.2	15.8	99.9
3. Midwest U.S.	Spring		4.7				3.0	18.1	67.4		99.5
	Summer		4.2				3.9	3.5	82.6		98.9
	Fall		4.5				20.3	20.7	49.0		98.9
	Winter		7.4				18.7	32.8	35.7		99.8
4. Northern Canada	Spring	1.4		1.8			15.5	12.6	64.9		99.6
	Summer	2.0		5.9			6.0	2.7	79.6		98.3
	Fall	1.9		2.1			43.3	14.4	34.7		98.6
	Winter	6.4		1.1			36.8	25.8	23.9		99.8
5. Germany	Spring	20.1	8.4	62.4	5.5						99.4
	Summer	9.9	1.0	86.1	0.2						98.9
	Fall	20.7	2.6	70.4	4.2						99.1
	Winter	44.7	10.4	40.1	1.0						99.9
6. Northern Asia	Spring	6.2	3.7	77.6	3.7						99.1
	Summer	9.5	0.6	80.1	0.4						96.6
	Fall	21.3	4.5	52.5	14.7						98.9
	Winter	16.7	9.8	56.8	10.6						99.7
7. Sahel	Spring		22.6	9.2	65.5	3.5					99.9
	Summer		59.8	3.9	30.0	0.0					99.3
	Fall		30.4	1.9	62.9	0.0					98.9
	Winter		2.7	2.2	67.4	26.9					99.5
8. India	Spring			0.6	35.2	63.1					99.9
	Summer			7.9	43.5	42.6					98.3
	Fall			0.2	50.0	47.8					98.8
	Winter			0.1	26.4	71.8					100.0
9. Southeast Asia	Spring			0.4	39.0	56.6					98.8
	Summer			6.1	33.7	56.9					98.6
	Fall			1.6	41.5	53.9					99.2
	Winter			1.1	30.6	65.5					100.0

contributions is listed in the right column of the table for each local region and season. The fact that the sums approximate 100% indicates that the one-month start-up time is indeed adequate.

Some of the trends inherent in the data are worth mentioning. For example, the data indicate that the percent contribution of an important continental source region to a midlatitude or high latitude precipitation is usually largest in the summer and smallest in the winter, in phase with the seasonal cycle of continental evaporation. This trend is lost in the subtropics and even reversed in the Sahel. Of the local areas studied, Southeast Asia and India are unique in that their precipitation essentially originates from only two source regions, in both cases being the Indian Ocean and Africa/Southern Asia. The seasonal variations of the two relative contributions for Southeast Asia precipitation are quite small. In contrast, five different source regions provide, at some time during the year, a significant portion (over 10%) of Central Greenland's precipitation, and the contributions of North America to the rainfall in Central Canada increases from 24% in the winter to 80% in the summer. The results for the other local areas lie between these extremes.

Table 4-2 displays, for the thirty-day January and July periods, the spatial variation of the source region contributions along a latitudinal strip spanning North America. The letters in the table refer to the lettered squares in Figure 4-8. As expected, the influence of the Pacific decreases and the influence of the Atlantic increases (though not so clearly in January) with eastward distance. Notice that the Pacific's

Table 4-2. Percent contributions of the source regions to the January and July precipitations in the lettered squares of Figure 4-8.

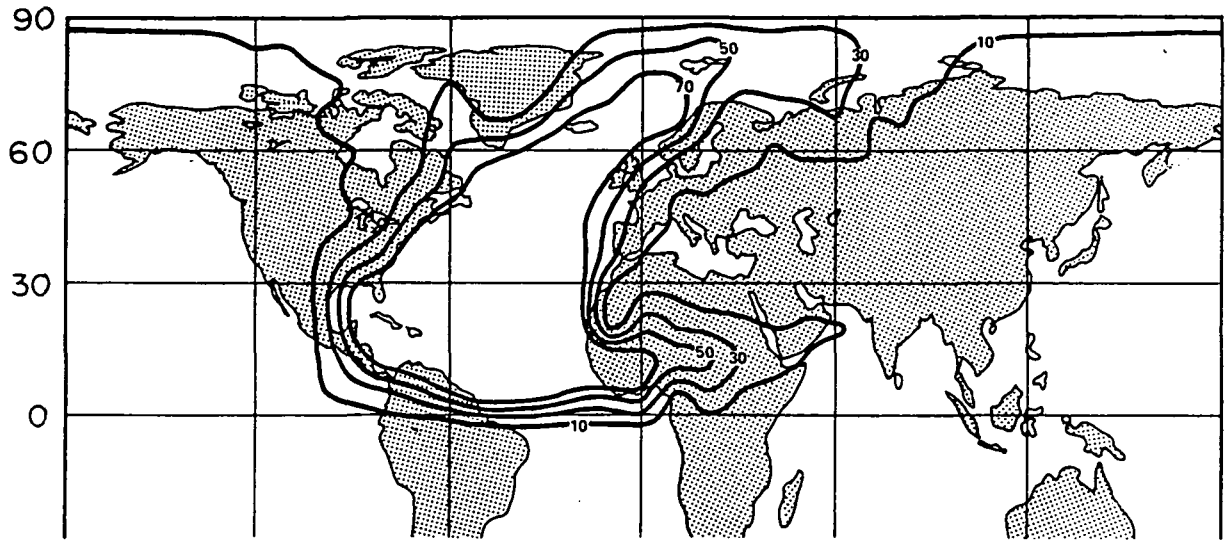
<u>Winter</u>	<u>N</u> <u>Atl</u>	<u>Trop</u> <u>Atl</u>	<u>N</u> <u>Pac</u>	<u>Trop</u> <u>Pac</u>	<u>N</u> <u>Amer</u>	<u>Sum</u> <u>of 10</u>
Square A	0.0	8.6	7.5	48.2	35.1	100.0
B	0.0	12.8	3.5	47.5	34.8	99.9
C	1.1	29.7	4.1	27.1	36.4	100.0
D	2.2	22.8	4.2	27.2	41.6	100.0
E	11.1	15.0	2.0	8.3	62.9	100.0
<u>Summer</u>	<u>N</u> <u>Atl</u>	<u>Trop</u> <u>Atl</u>	<u>N</u> <u>Pac</u>	<u>Trop</u> <u>Pac</u>	<u>N</u> <u>Amer</u>	<u>Sum</u> <u>of 10</u>
Square A	1.3	2.1	1.7	16.2	71.4	95.9
B	0.7	0.0	2.7	5.0	86.6	98.3
C	1.0	10.7	1.9	2.9	80.1	99.0
D	2.5	31.4	0.7	1.5	61.9	99.3
E	16.0	37.1	0.2	1.7	44.0	99.6

impact on western precipitation is larger in the winter, whereas the Atlantic's impact on eastern precipitation is larger in the summer.

Tables 4-1 and 4-2 indicate the important evaporative sources of precipitation for individual GCM grid squares. GCM results, however, are generally more realistic when integrated over larger spatial scales, and thus an alternative presentation of the simulation results is provided in Figures 4-9 through 4-12. Following the example of Joussaume et al (1986) (see below), the influence of a source region on continental precipitation is described by a set of percentage contours. Figure 4-9a indicates the portions of North American, European, and African summer precipitation that are made up of water from the combined North and Tropical Atlantic source regions; 1/10 of the precipitation onto a point on the 10% contour, for example, is composed of Atlantic water. Figures 4-10a and 4-11a provide the analogous summertime plots for Pacific (North Pacific plus Tropical Pacific) and Indian Ocean water, respectively. Figure 4-12a indicates how water from the North Africa/Southern Asia source region influences precipitation in Northern Asia.

Corresponding plots for the winter season are provided in Figures 4-9b through 4-12b. Again, notice how oceanic evaporative sources have a greater influence on continental precipitation during winter, when continental evaporation rates are low. The influence of the Africa/Southern Asia source region on precipitation in Northern Asia also clearly increases in winter; apparently the winter evaporation rates are more reduced in the north than in the south.

a. Summer



b. Winter

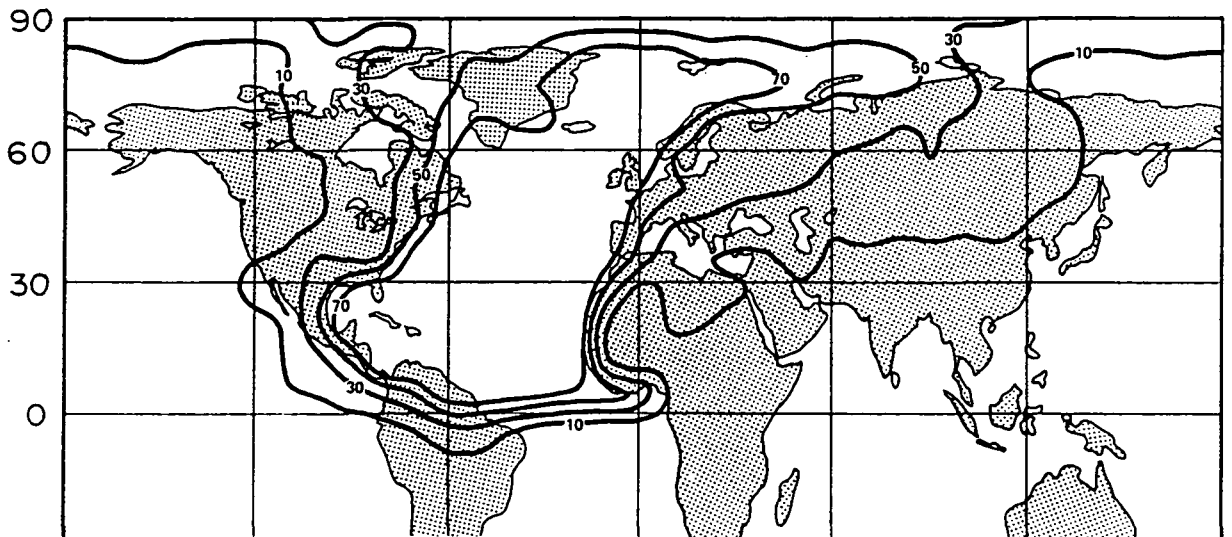
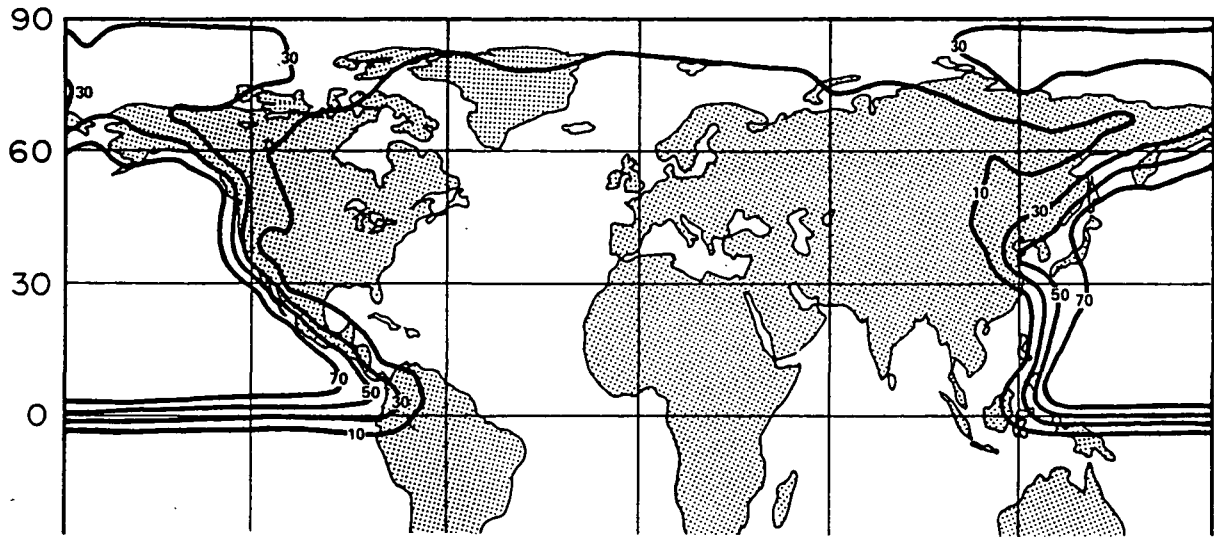


Figure 4-9 **Contours showing percentage of local precipitation derived from combined North Atlantic and Tropical Atlantic source regions. (a) Summer. (b) Winter.**

a. Summer



b. Winter

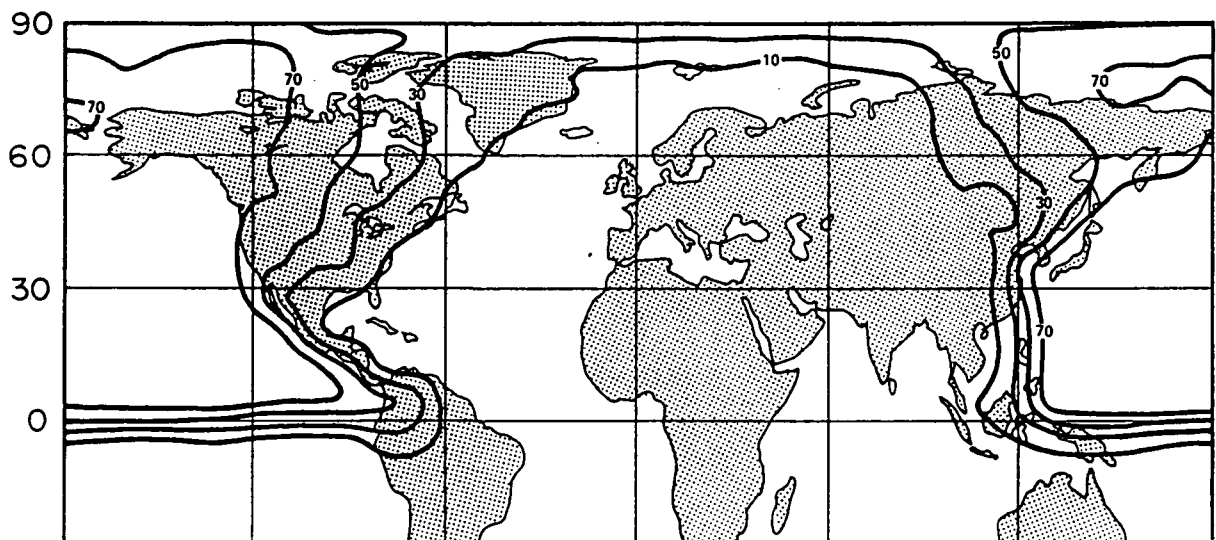
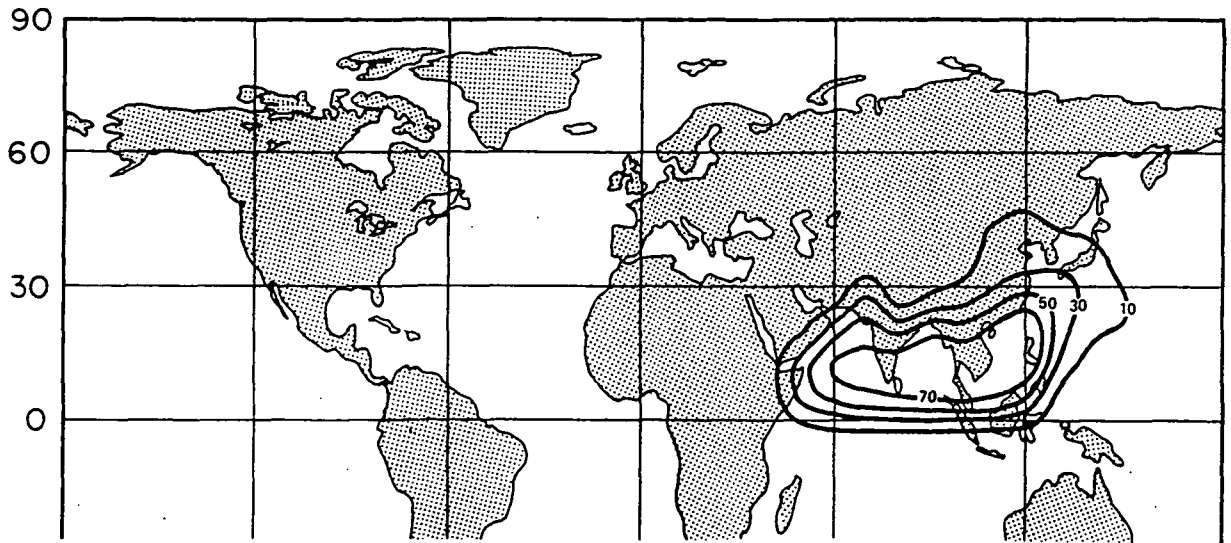


Figure 4-10 Contours showing percentage of local precipitation derived from combined North Pacific and Tropical Pacific source regions. (a) Summer. (b) Winter.

a. Summer



b. Winter

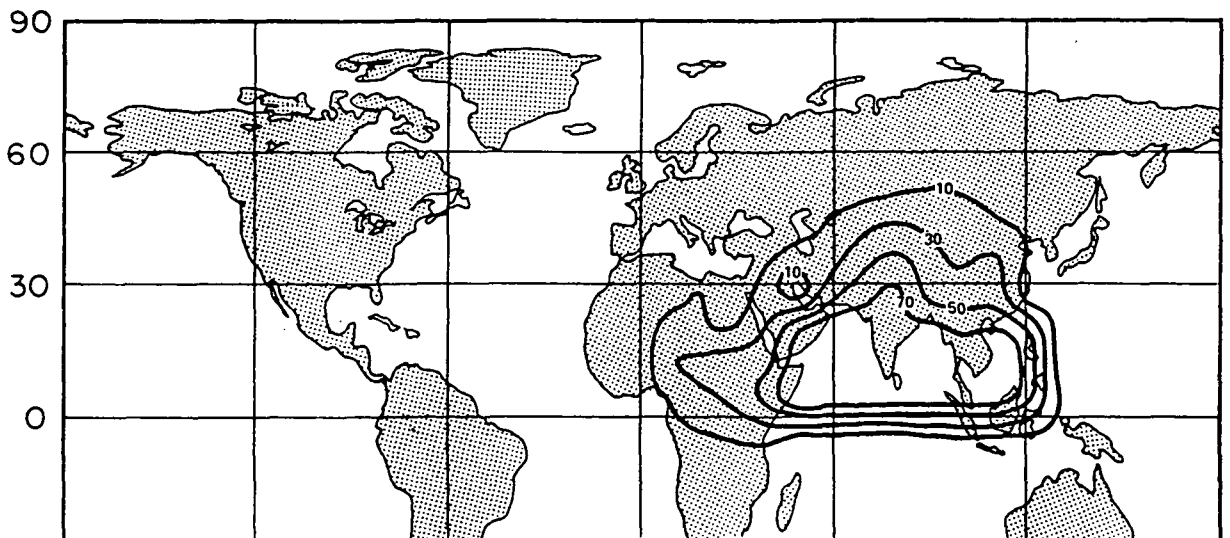
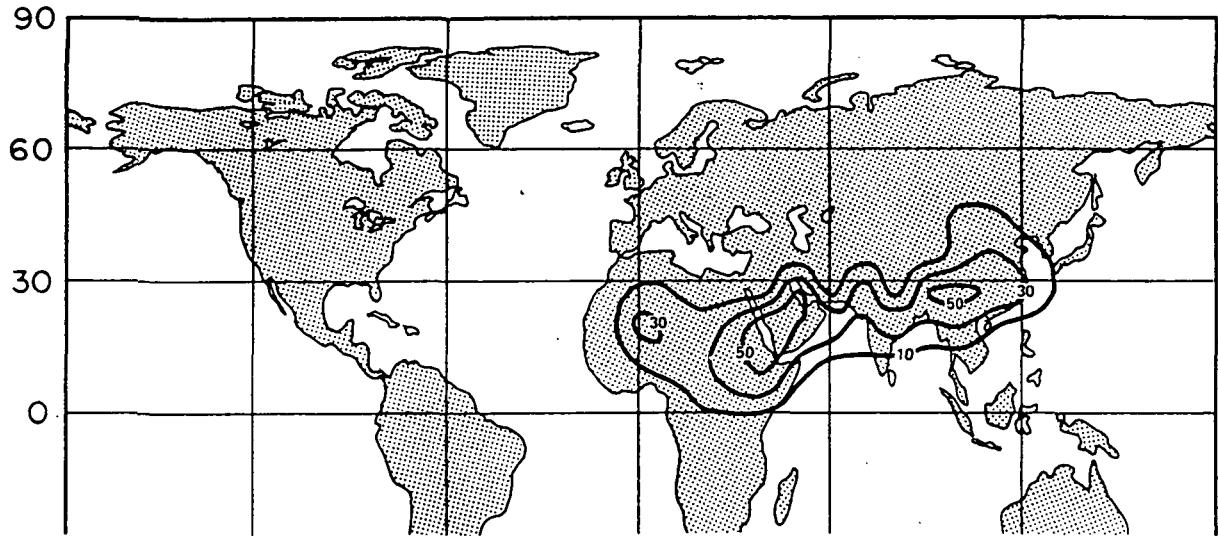


Figure 4-11 Contours showing percentage of local precipitation derived from Indian Ocean source region. (a) Summer. (b) Winter.

a. Summer



b. Winter

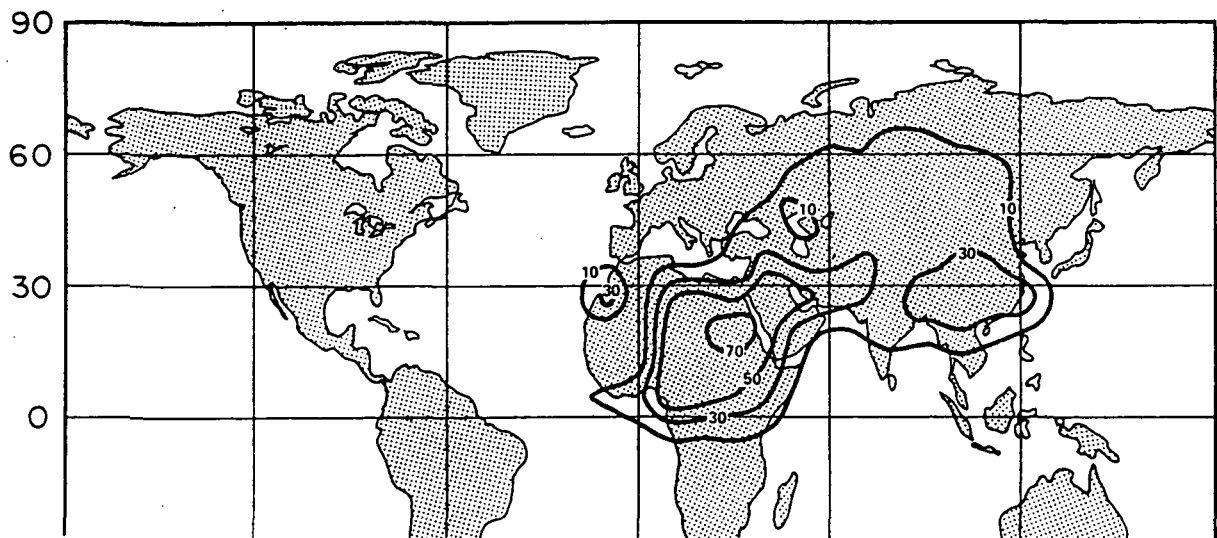


Figure 4-12 Contours showing percentage of local precipitation derived from North Africa/Southern Asia source region. (a) Summer. (b) Winter.

4.2.3 Comparison with Results from the LMD Tracer Water Model

A tracer water model similar to the one described in this report was developed concurrently by researchers using the LMD (Laboratoire de Meteorologie Dynamique) GCM in Paris, France. This model has been used to simulate the global distributions of stable isotopes in a January climate (Joussaume et al, 1984a, 1984b) and has more recently (Joussaume et al, 1986) been applied to the problem described in the present section, i.e. that of determining the origin of local precipitation. The two "origins of precipitation" experiments are similar enough to allow a comparison between the LMD and GISS tracer water models.

The GISS and LMD tracer water models are substantially different in many of their transport parameterizations. The LMD model uses, for example, an upstream weighting scheme (as examined in Section 3.4.3) to calculate tracer advection in the horizontal. This scheme is inherently more diffusive than the slopes scheme used in the GISS tracer water model. The LMD model also doesn't formulate tracer vapor exchange at the ocean surface; downward flux of tracer onto an ocean square occurs only when the net water evaporation from the square is negative. The LMD model employs a crude tracer mixing parameterization during moist convective events, since (unlike the GISS GCM's moist convection scheme) the LMD GCM's moist convection scheme does not permit the separate calculation of tracer fluxes during the rise of the plume, the subsidence of surrounding air, and the precipitation of condensate. In their favor, the LMD tracer water simulations employ a finer ($4^\circ \times 5^\circ$) horizontal resolution and a more detailed formulation of vertical turbulent tracer transport in the boundary layer.

The LMD "origins of precipitation" experiment was performed in essentially the same way as the corresponding GISS tracer water model experiment. The tracer source regions used in the LMD simulation are shown in Figure 4-13. The LMD simulation ran from June 11 through July 30, with the tracer precipitation fluxes stored during the final 30 days.

Notice that although the source regions shown in Figure 4-13 do not exactly match those used in the GISS tracer water model simulation (Figure 4-8), the oceanic source regions are sufficiently similar to allow a comparison of modeled oceanic influences on continental precipitation. Figures 4-14 and 4-15 show the influence regions of Atlantic and Pacific water, respectively, obtained from the LMD July simulation; contours show the percentage of continental precipitation that is composed of evaporated ocean water. The figures can therefore be directly compared with Figures 4-9a and 4-10a for the summer GISS tracer simulation. Only contours in midlatitudes should be compared, since the oceanic source regions are quite different in high latitudes and since contours in the tropics are affected by the Southern Hemisphere oceans in the LMD simulation but not in the GISS simulation. The small cross-equatorial vapor transport implied by Table 4-1 and Figures 4-9 through 4-12 suggest that the lack of a Southern Hemisphere ocean tracer in the GISS simulation should not greatly affect the contours generated in midlatitudes.

A major difference between the two sets of model results is the more extensive lateral influence of oceanic vapor in the LMD simulation. The 10% contour for Pacific Ocean water, for example, extends into the Mississippi Valley in the LMD simulation but only as far as the Rocky

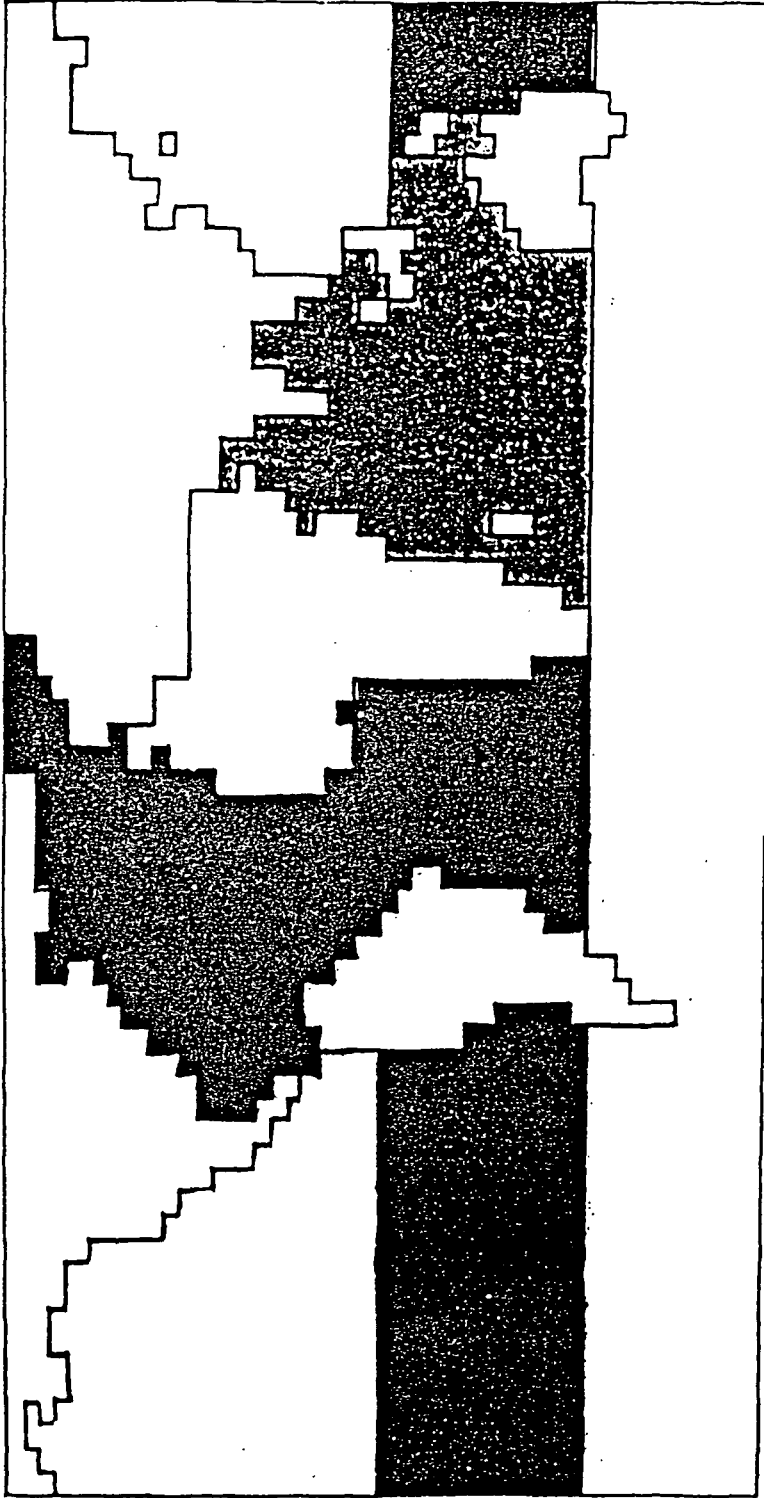


Figure 4-13 Source regions used in LMD GCM "origins of precipitation" experiment. (From Joussaume et al, 1986.)

ORIGINAL PAGE IS
OF POOR QUALITY

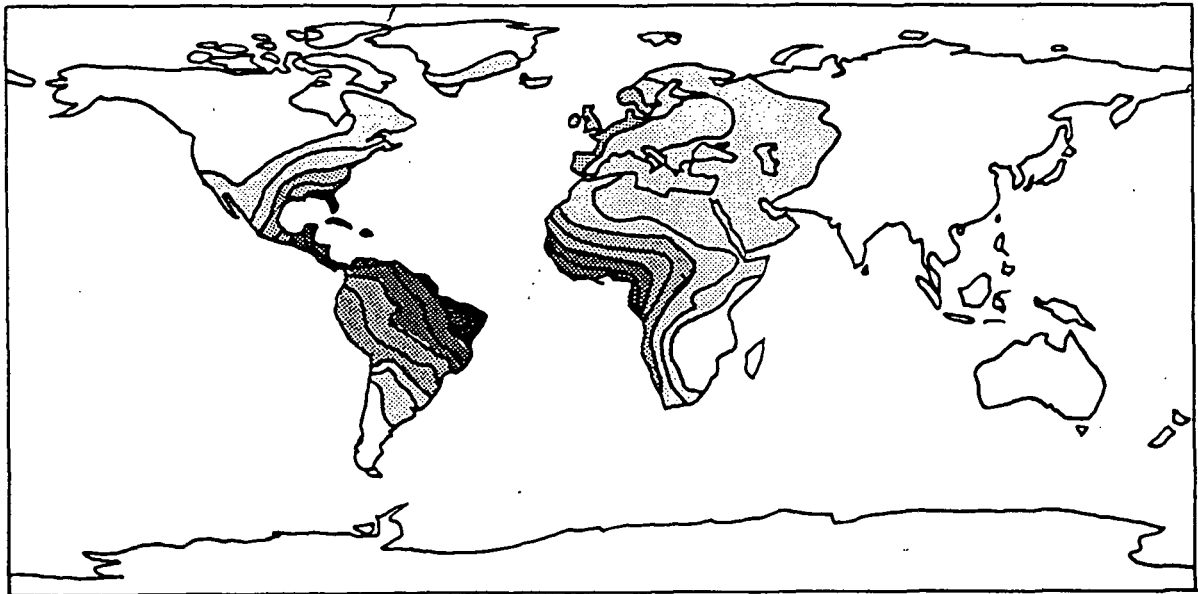


Figure 4-14 Contours showing percentage of local July precipitation derived from Atlantic source region in LMD GCM experiment. Isolines are drawn every 10%. Light shading: 10 to 30%; medium shading: 30 to 50%; heavy shading: 50 to 70%; black: more than 70%. (From Joussaume et al, 1986.)

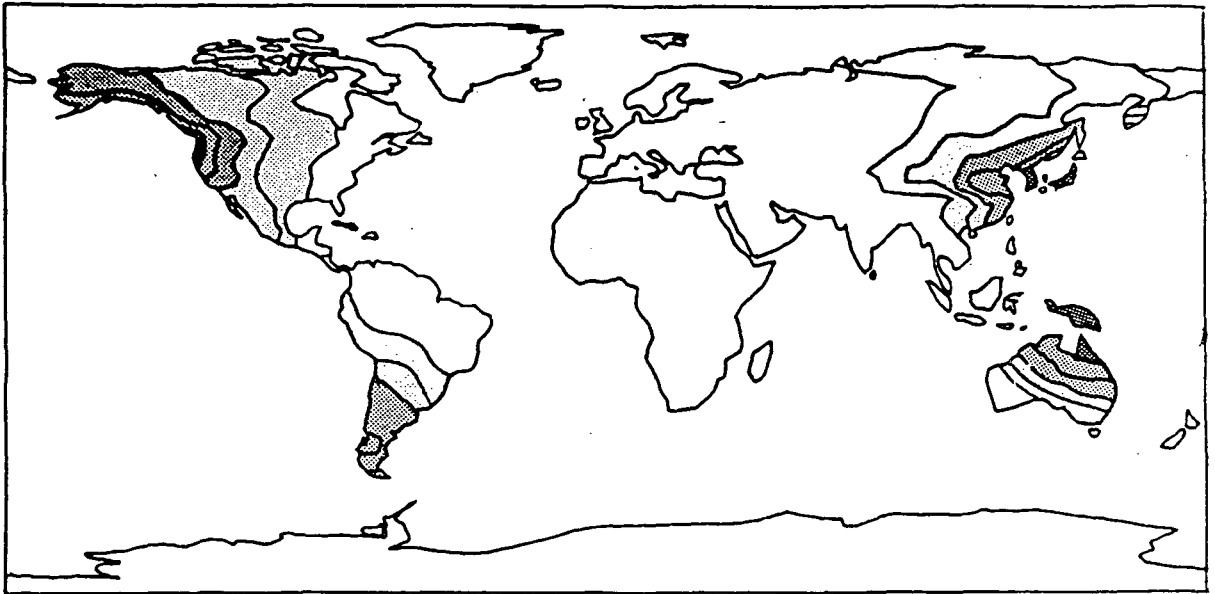


Figure 4-15 Contours showing percentage of local July precipitation derived from Pacific source region in LMD GCM experiment. Isolines are drawn every 10%. Light shading: 10 to 30%; medium shading: 30 to 50%; heavy shading: 50 to 70%; black, more than 70%. (From Joussaume et al, 1986.)

Mountains in the GISS simulation. This is perhaps due to differences in the windfields generated by the two GCMs or to the GISS GCM's excessive convection over midlatitude continents. It may also result from the LMD GCM's use of an upstream weighting scheme for tracer advection; the excess diffusivity of this scheme tends to overestimate the lateral transport of tracer, as was demonstrated in Section 3.4.3. Although the upstream weighting scheme produces a realistic water cycle in the LMD GCM (Joussaume et al, 1986), the high diffusivity must have a greater impact on tracer water transport, since the horizontal gradients of tracer water in the atmosphere are much larger.

4.3 Precipitation of Deuterium in Antarctica

4.3.1 Background

Recall from Section 3.4.2 that for surface temperatures T_g below 15°C , a linear relationship exists between T_g and the H_2^{18}O concentration in precipitation. A similar linear relationship has been observed for HDO concentrations in precipitation. Figure 4-16 was constructed with the same observational data base used to construct Figure 3-25b; the points in the plot were located according to the observed mean annual surface temperature and δD content in precipitation at various measurement sites. As explained in Section 3.4, the linear relationship is usually attributed to the effects of Rayleigh condensation.

It is reasonable to expect, however, that the isotope content in precipitation is also a function of the evaporative source of the water.

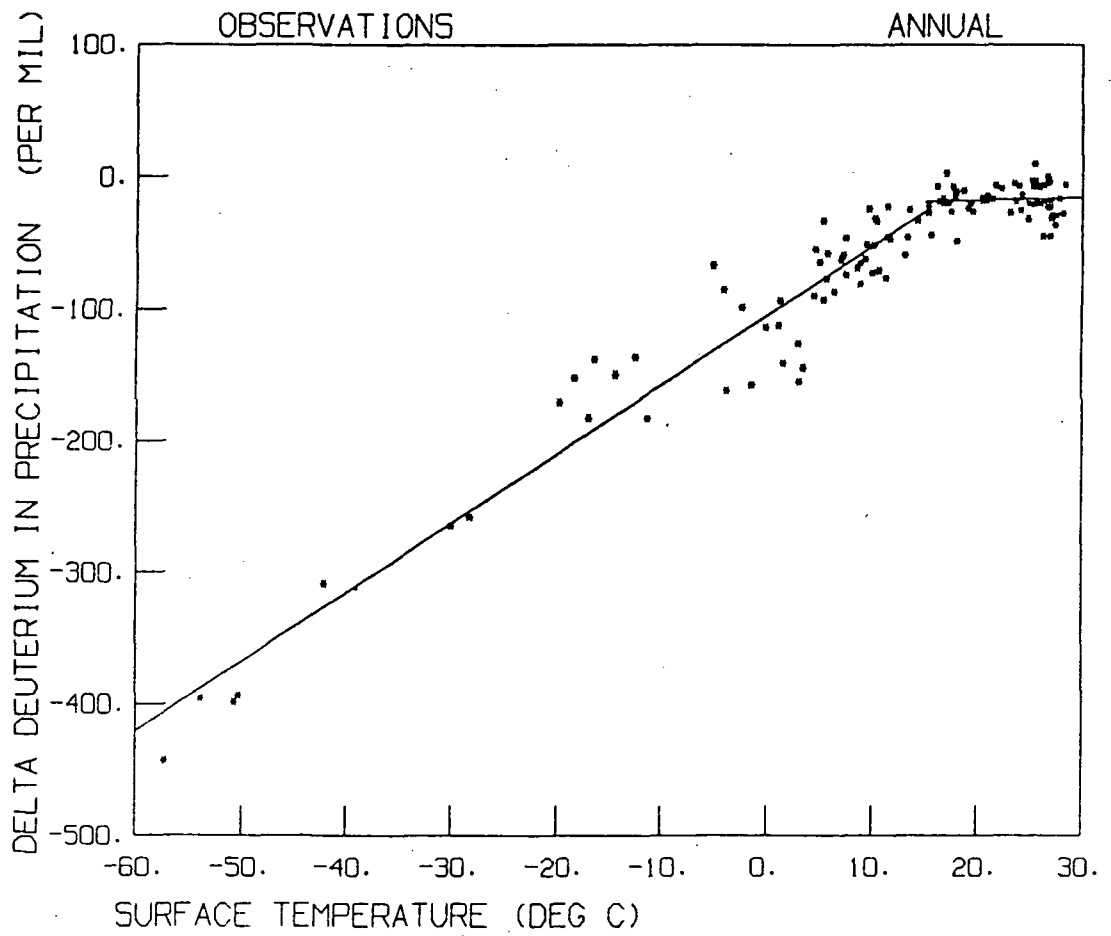


Figure 4-16 Mean annual δD in precipitation versus mean annual surface temperature at the precipitation site, from observations. Two lines are fitted to the data, one for temperatures below 15°C and the other for temperatures above 15°C.

An Antarctic site which gets its precipitation water mainly from warmer evaporative sources might feature lower precipitation isotope contents than an Antarctic site with the same mean surface temperature but with colder evaporative sources for its precipitation. This is because a water vapor mass above the former site had been subjected to a greater change in temperature and thus to a greater number of Rayleigh condensation events. The effect might be partly counterbalanced by the presence of the fractionation factor $\alpha_{l/v}$ in Equation 2-19; $\alpha_{l/v}$ decreases with increasing temperature (Equation 2-2), so vapor from a warmer region should initially contain a higher concentration of isotope. The present experiment tested the hypothesis that the observed deviations from complete linearity in Figure 4-16 are related to differences in evaporative sources.

4.3.2 Description of Experiment

In this experiment, the tracer water model evaporated water and HDO from special tracer source regions and determined the relative amounts that returned to earth in Antarctic precipitation. The source regions were not defined geographically, as they were in the previous experiment. Rather, the six source regions were defined by six surface temperature ranges:

Source Region A	$T < 5^{\circ}\text{C}$
B	$5^{\circ}\text{C} < T < 10^{\circ}\text{C}$
C	$10^{\circ}\text{C} < T < 15^{\circ}\text{C}$
D	$15^{\circ}\text{C} < T < 20^{\circ}\text{C}$
E	$20^{\circ}\text{C} < T < 25^{\circ}\text{C}$
F	$25^{\circ}\text{C} < T$

Every pure open ocean grid square in the Southern Hemisphere was assigned to be a member of one of the source regions according to its surface temperature on January 1. The ocean surface temperatures, remember, are determined from observed climatic means and are not interactive with the model. Figure 4-17 shows the geographical locations of the six source regions.

Two different aboveground tracers were assigned to each source region. One was a standard aboveground tracer; it had the properties of non-isotopic water and evaporated from the source region at the water evaporation rate. The other was given unique properties for this particular experiment. This tracer had the isotopic properties peculiar to HDO and evaporated from the source region at a reduced rate:

$$E_{T,HDO} = E_{T,H_2O} \cdot C_o \cdot C_s / \alpha_{l/v} \quad (4-1)$$

where E_{T,H_2O} represents the upward flux of the non-isotopic water tracer, C_o is the average weight fraction of HDO in seawater, and C_s is a correction factor for near-surface waters (see Equation 2-19). Thus, while the first tracer represented the water that evaporated from ocean grid squares having a certain temperature, the second represented the HDO that evaporated from these squares. In addition to the twelve aboveground tracers, a surface-conserved tracer representing global HDO was also defined (see Section 2.4.1).

The initial conditions used for this experiment were the model conditions on Dec. 1 of Year 2 of the standard five-year Model II GISS GCM simulation. Each atmospheric grid box and each surface reservoir was initialized with a reasonable temperature-dependent concentration for the surface-conserved HDO tracer. The model simulation lasted two months, with the Antarctic precipitation fluxes monitored throughout January.

4.3.3 Results

As discussed in Section 2.2.2, deuterium concentrations are usually described relative to a Standard Mean Ocean Water concentration:

$$\delta D = \frac{\frac{x_D}{x_H} - 155.76 \times 10^{-6}}{155.76 \times 10^{-6}} \times 1000\% \quad (4-2)$$

where x is the mole fraction of a given atom. For the purposes of the present experiment, the x_D/x_H ratio for a given HDO tracer is defined with respect to the corresponding water tracer. That is, if x_{HA} represents the mole fraction of hydrogen atoms from Source Region A that precipitates at a given Antarctic location, and if x_{DA} represents the mole fraction of deuterium atoms from Source Region A that also precipitates there, then δD for this particular HDO tracer at this location is defined as:

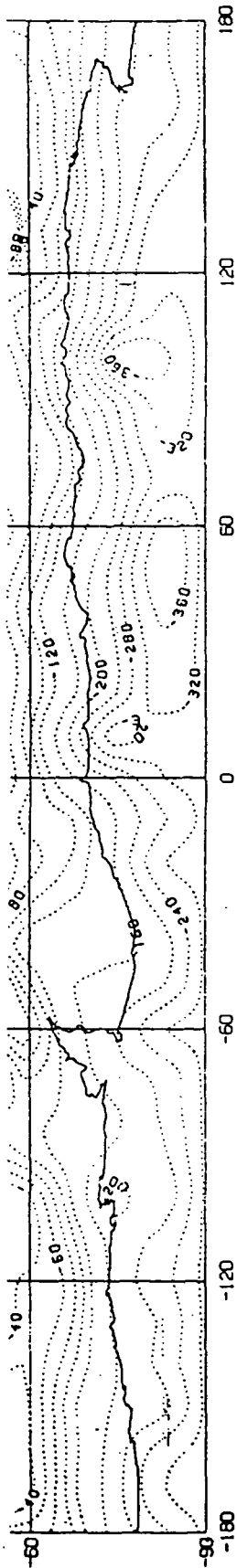
$$\delta D = \frac{\frac{x_{DA}}{x_{HA}} - 155.76 \times 10^{-6}}{155.76 \times 10^{-6}} \times 1000\% \quad (4-3)$$

Equation 4-3 thus computes the depletion of HDO relative to H₂O from the same source.

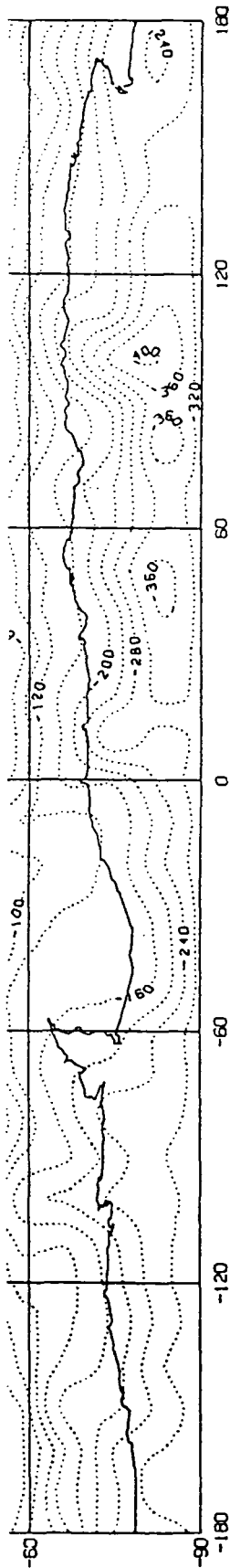
The simulation results presented in Figure 4-18 indicate that the HDO concentration in Antarctic precipitation is indeed a function of the evaporative source. Figure 4-18a shows a map of the δD values in precipitation produced by a cold ($T < 5^\circ\text{C}$) evaporative source, Figure 4-18b shows the values produced by a medium ($10^\circ\text{C} < T < 15^\circ\text{C}$) source, and Figure 4-18c shows the values produced by a warm ($25^\circ\text{C} < T$) source. The warmer the source, the lower the δD values in Antarctic precipitation and thus the greater the depletion of the isotope. This is the trend predicted by the Rayleigh condensation argument. The actual δD value measured at an Antarctic site would be related to the relative importance of each evaporative source. (Note that due to their proximity to the pole, the spatial extents of the contours in Figure 4-18 are greatly exaggerated.)

Table 4-3 provides an alternative presentation of these results. In the table, the zonal mean δD in Antarctic precipitation for each tracer is listed as a function of latitude. For each latitude, the decrease of zonal mean δD in precipitation with an increase in evaporative source temperature is readily apparent.

a. Source Region A (Source temperature less than 5C)



b. Source Region C (Source temperature between 10C and 15C)



c. Source Region F (Source temperature greater than 25C)

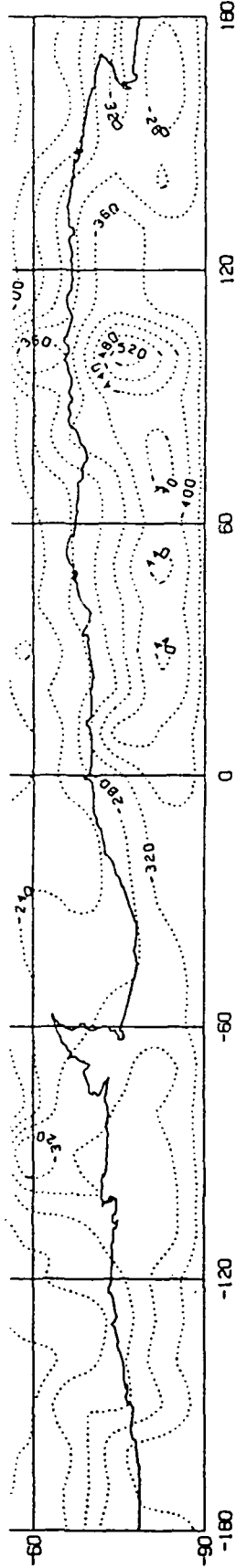


Figure 4-18 δD in Antarctic precipitation (in permil) for three different tracers. (a) Tracer from Source Region A. (b) Tracer from Source Region C. (c) Tracer from Source Region F.

Table 4-3 Zonal mean of δD in precipitation versus latitude for each tracer. All numbers are in units of permil.

Latitude	δD					
	Tracer A	Tracer B	Tracer C	Tracer D	Tracer E	Tracer F
51°S	-46.5	-64.8	-53.7	-76.7	-105.3	-161.5
59°S	-60.4	-102.1	-98.8	-125.3	-157.3	-218.7
67°S	-116.5	-149.8	-151.4	-166.8	-197.1	-258.1
74°S	-199.9	-204.8	-214.3	-232.0	-254.2	-316.5
82°S	-265.0	-236.8	-281.0	-307.3	-319.6	-339.0
90°S	-291.2	-233.6	-299.2	-332.8	-321.6	-340.6

Accounting for differences in evaporative sources, however, does not fully explain the scatter around the fitted line in Figure 4-16. First consider Figure 4-19, which shows a plot of time-averaged δD in Antarctic precipitation versus time-averaged precipitation site temperature for the surface-conserved HDO tracer. Figure 4-19 is thus equivalent to Figure 4-16, using model-generated data for global deuterium rather than observations. The correlation coefficient for the fitted line is 0.62.

If the scatter around the fitted line in Figure 4-19 is explained by the fact that precipitations at different Antarctic sites originate from different evaporative sources with different surface temperatures, then the corresponding plot for any one of the six aboveground HDO tracers should show less scatter. This is because a given aboveground tracer evaporates from a source region with a roughly uniform surface temperature. Above all Antarctic precipitation sites having a certain surface temperature, air parcels containing the tracer will have experienced roughly the same drop in temperature and thus roughly the same amount of Rayleigh condensation; the tracer concentrations in the air parcels should therefore be roughly the same. The enhanced one-to-one correspondence between precipitation site temperature and HDO concentration should reduce the scatter.

A reduction in scatter in the δD /temperature plot could be identified by an increased correlation coefficient for the fitted line relative to 0.62, the value found for the global HDO tracer. As an example, the plot for the HDO tracer evaporating from the $10^{\circ}\text{C} < T < 15^{\circ}\text{C}$ ocean grid squares is

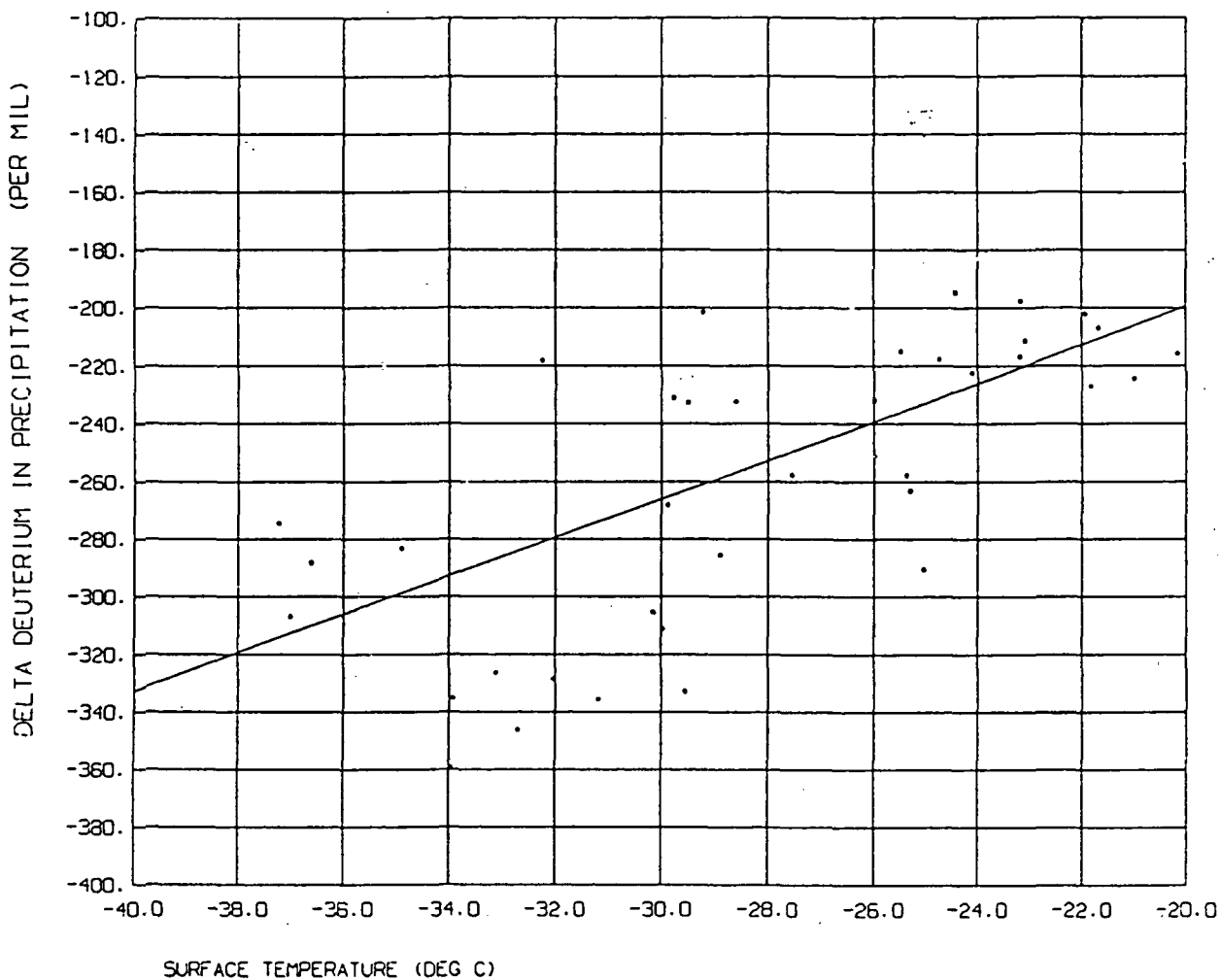


Figure 4-19 Time-averaged δD in precipitation versus time averaged surface temperature, as determined by the tracer water model. Only Antarctic sites with an average surface temperature below -20°C are considered.

shown in Figure 4-20. The correlation coefficient for this plot is 0.71, a slight improvement.

Plots similar to Figure 4-20 were constructed for the other HDO tracers, and the resulting correlation coefficients are listed in the first column of Table 4-4. Four of the six HDO tracers produced higher correlation coefficients than that produced by the global HDO tracer. The improvements do not, however, seem very significant.

Notice that the tracer from the $5^{\circ}\text{C} < T < 10^{\circ}\text{C}$ source region produces the lowest correlation coefficient. As shown in Figure 4-17, this tracer is also unique in that its source region includes very few grid squares in the southern Atlantic Ocean. The two features are perhaps related.

Plots comparing the time-averaged surface temperature at an Antarctic site with the corresponding time-averaged HDO content in moist convective precipitation, in non-convective precipitation, and in the vapor of the first layer grid box were constructed next. The resulting correlation coefficients are also presented in Table 4-4. Again, no clear decrease in scatter is apparent when the aboveground tracers are considered independently. Interestingly, though, the results do indicate that isotope contents in non-convective precipitation are more related to precipitation site temperature than are isotope contents in moist convective precipitation.

4.3.4 Comparison of Results with a Simple Isotope Model

Merlivat and Jouzel (1979) describe the isotope content of a moist air mass as a function of the extent of water vapor condensation in the

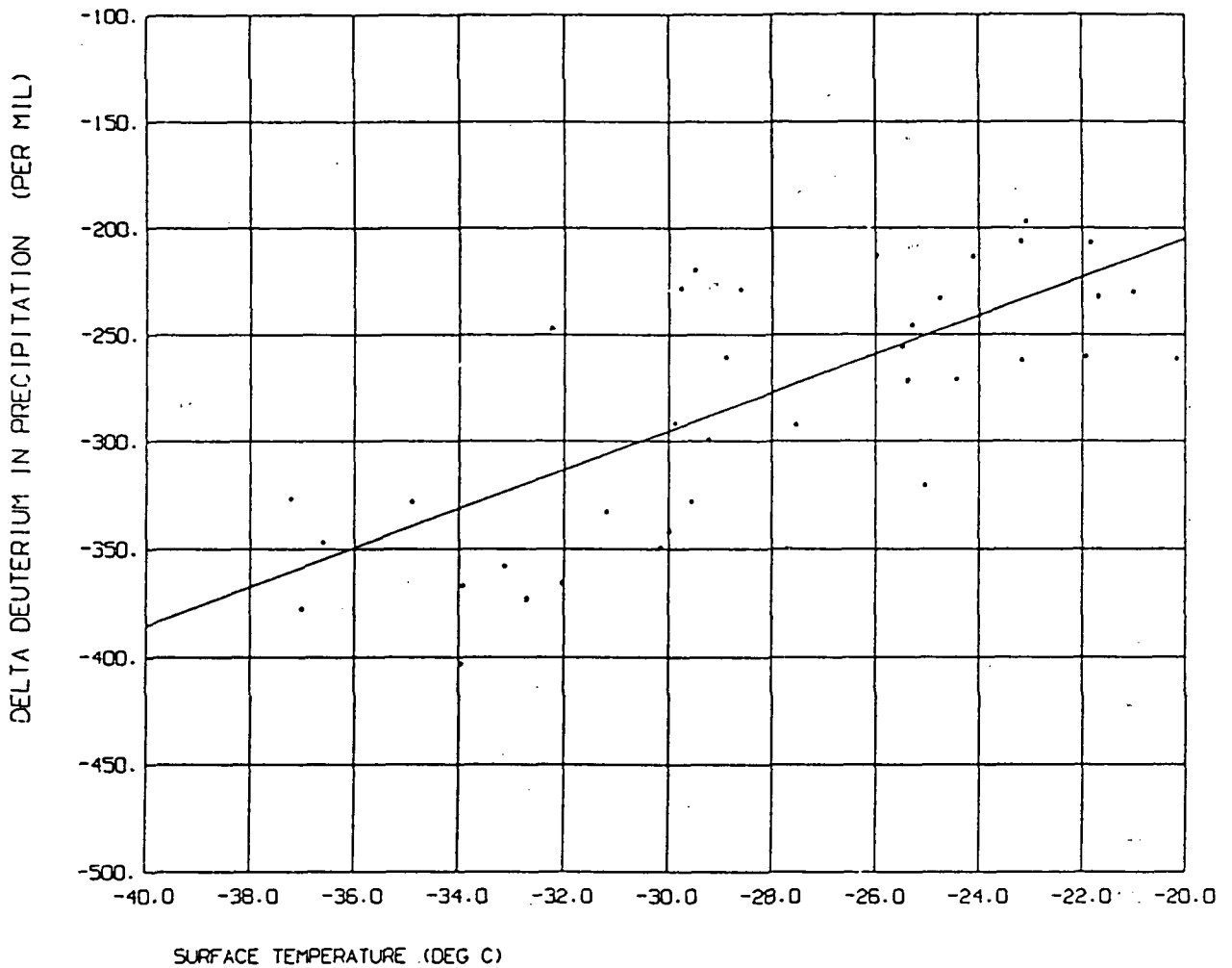


Figure 4-20 Time-averaged δD in precipitation versus time-averaged surface temperature for the HDO tracer evaporating from the $10^{\circ}\text{C} < T_G < 15^{\circ}\text{C}$ ocean grid squares. Only Antarctic sites with an average surface temperature below -20°C are considered.

Table 4-4. Correlation coefficients obtained when fitting a linear relationship between time-averaged surface temperature and time-averaged δD .

Source Region	δD determined in:			
	Total Precip.	Moist Convective Precip.	Non-Convective Precip.	First Layer Vapor
T < 5°C	0.71	0.52	0.74	0.60
5°C < T < 10°C	0.25	0.25	0.28	0.26
10°C < T < 15°C	0.71	0.58	0.72	0.70
15°C < T < 20°C	0.59	0.54	0.57	0.62
20°C < T < 25°C	0.68	0.53	0.69	0.70
25°C < T	0.65	0.50	0.67	0.69
Global HDO	0.62	0.44	0.66	0.70

air mass. Aristarain and Jouzel (1986) used an extended version of this simple model, incorporating kinetic fractionation during snow formation (Jouzel and Merlivat, 1984), to determine the following relationship between the evaporative source temperature T_E , the temperature at the precipitation site T_G , and the deuterium content δD in Antarctic precipitation:

$$\Delta\delta D = 8.5\Delta T_G - 4.2\Delta T_E \quad (4-4)$$

Thus, if T_G , T_E , and δD are known for one Antarctic site and T_G and T_E are known for another, the δD in precipitation at the second site can be estimated with Equation 4-4. The equation assumes a constant relative humidity of 0.8 over the ocean surface and a zero fraction of liquid or solid condensate traveling with the air mass (i.e., Rayleigh condensation); the authors, however, found the equation to be insensitive to changes in these two parameters.

The relationship between deuterium content and evaporative source temperature in Equation 4-4 may or may not be consistent with the results of the tracer water model simulation described above. Consistency can be tested by examining the deuterium contents in the tracer precipitations at a single Antarctic site. Since the precipitation temperature at a single site is the same for each tracer, Equation 4-4 reduces to

$$\Delta\delta D = -4.2\Delta T_E \quad (4-5)$$

Thus, for consistency, if the δD in precipitation at a given site for each of the six tracers (from Equation 4-3) is plotted against the tracer's average evaporative source temperature, the slope of the line fitted to the six points should be -4.2 permil/ $^{\circ}C$.

Such a slope was calculated for every grid square south of $63^{\circ}S$. The average of all the slopes was -4.3 permil/ $^{\circ}K$, in very good agreement with the simple model of Aristarain and Jouzel. The slopes did, however, exhibit a fair degree of variability; they ranged from -1.3 to -8.2 permil/ $^{\circ}K$, with a standard deviation of 1.5 permil/ $^{\circ}K$. The tracer water model results therefore suggest that the model of Aristarain and Jouzel is valid on the average but does not necessarily hold at an arbitrarily chosen point.

4.4 Comparison with Simple Models of Local Water Recycling

Various studies in the literature use simple models to provide estimates of local water recycling ratios, i.e. the fractions of precipitation water made up of locally evaporated water. Some of these estimates, namely those of Budyko (1974), Benton et al (1950), and Libby (1959), can be compared with results from the tracer water model simulations. The comparisons might be thought of as tests of the simple models, since the models are much less sophisticated than the tracer water model; the fact that the tracer water model results are themselves subject to question, however, works against this interpretation.

In Budyko's (1974, p.239-243) analysis, a uniform wind with velocity u flows over a land surface of length ℓ . Both the average evaporation rate E_{ave} from the land surface and the water vapor content w of the incoming air are known. To determine the local recycling ratio f_{local} , for this system being the fraction of precipitation along the length ℓ that is derived from water evaporating along the length ℓ , Budyko assumes that any water evaporating from a given point is immediately and completely mixed into the water vapor directly above the point. The complete vertical mixing assumption effectively allows the percentage of downwind precipitation derived from the evaporated water to be determined. The analysis leads to an approximate equation for f_{local} :

$$f_{local} = \frac{1}{1 + \frac{2wu}{E_{ave} \ell}} \quad (4-6)$$

Budyko uses Equation 4-6 to deduce that in July, the European territory of the U.S.S.R. derives only 14% of its precipitation water from local evaporation. The GISS GCM tracer water model produces a quite different result. One of the tracers discussed in Section 4.1 evaporated from a source region representing the European U.S.S.R. (See Figure 4-6). Tracer precipitation onto the source region represented 47% of the total

July precipitation onto the region, implying an f_{local} of 0.47. The much lower recycling ratio produced by Budyko's analysis is not surprising in light of Budyko's rather extreme vertical mixing assumption, which mixes evaporated water away from near-surface air. Perhaps precipitation in nature is usually formed from water vapor in near-surface air. This would particularly be true of moist convective precipitation.

In one of the earliest studies of its type, Benton et al (1950) analyze vapor flux data to estimate the various components of the hydrological cycle in the Mississippi Watershed. Part of the study involved combining a year long time series of precipitation at one Ohio Valley station with concurrent surface and upper air weather charts to deduce the fraction of precipitation derived from "continental air masses" and the fraction derived from "maritime air masses". The authors estimate that at least 86% of the annual precipitation in the Mississippi Watershed is derived from oceanic sources, implying a recycling ratio of 0.14.

Perhaps the reason this recycling ratio is so similar to that predicted by Budyko (1974) for the European U.S.S.R. is that Benton et al (1950) employ the same (probably faulty) assumption of complete vertical mixing. As maritime air masses move over the continents, Benton et al assume that evaporated continental water is mixed away from the earth's surface until it is uniformly distributed in the vertical. The contribution of re-evaporated precipitation to future precipitation over the continent is thus found to be insignificant. As might be expected, then, the GCM

"origins of precipitation" simulations, as described in Section 3.2, produced significantly higher recycling ratios in the Mississippi Watershed. According to the maps in Figures 4-9 and 4-10, the Pacific and Atlantic Oceans combined provide less than 70% of the winter precipitation water and less than 50% of the summer precipitation water in the watershed.

Libby (1959) infers a recycling ratio for North America from the tritium content in Chicago rain. The rain is assumed to be composed of evaporated ocean water, with a tritium content of 2.5 TU (see Section 2.2.2), and evaporated North American water, with an average tritium content of 39 TU. The tritium content in North American water is estimated from measurements in the Mississippi River and is corrected for the presence of cosmic ray tritium. The tritium content in Chicago precipitation, also corrected for cosmic ray tritium, is measured as 14 TU, implying that roughly one-third of the precipitation is derived from continental water.

The GCM "origins of precipitation" simulations described in Section 4.2, on the other hand, maintain that the percentage contribution of evaporated North American water to the precipitation falling on the grid square containing Chicago ranges from 47% in winter to 83% in summer. Again, the GCM produces a higher recycling ratio than the simple model. The discrepancy might be explained in part by oversimplifications in Libby's approach. Consider, for example, Figure 3-23, which shows that present-day tritium concentrations in rain vary greatly across the North

American continent. Assuming a similar relative variation in the 1950's, different sections of the North American continent at that time would evaporate water with different tritium concentrations. Libby perhaps oversimplifies the problem by assigning the tritium content in Mississippi River water to the entire continent. Libby also claims that the tritium concentration in Chicago precipitation is roughly constant during the time period under consideration. The time series plots he provides with his analysis, however, seem to show that during May through July of this time period, no measurements for Chicago precipitation were taken. The missing data might invalidate his claim. As seen in Figure 3-21, the seasonal cycle of T/H ratio in precipitation has a very strong peak during these months in the 1960's; perhaps the same seasonal cycle was in effect in the 1950s.

Chapter 5

Fractional Wetting of GCM Grid Squares.

Studies With a One-Dimensional Soil-Atmosphere Model

Two distinct topics are addressed in the present report, namely the development of a tracer water model and the problem of subgrid wetting of soil during precipitation events. Chapters 2, 3, and 4 have addressed the first topic. The present chapter addresses the second, using a one-dimensional soil-atmosphere model to simulate the workings of a GCM.

5.1 Fractional Wetting of GCM Grid Squares and Storm Statistics

As discussed in Section 1.4.1, the uniform wetting of a grid square during a GCM precipitation event is unrealistic and can potentially limit the accuracy of a GCM's inherent hydrological cycle. A proper formulation of surface runoff, for example, requires realistic precipitation depths, and these depths cannot be produced without accounting for the partial wetting of a grid square. The uniform wetting assumption also prevents any subgrid variability in soil moisture content or surface temperature, and such variations could have important effects on computed areally-averaged evaporation and sensible heat fluxes.

Runoffs generated with the GISS GCM under the uniform wetting assumption do not, in fact, show tremendous deviations from runoffs observed in nature. This is not due so much to a realistic runoff formulation, however, as it is to an arbitrary tuning of certain model parameters. A model "tuned" for one climate is limited in that it cannot

be expected to respond properly to an imposed change in climate. It is thus important to consider the possibility of parameterizing the subgrid wetting of GCM grid squares.

A heretofore unmentioned aspect of the uniform wetting assumption is its effect on GCM-generated storm statistics. The GISS GCM was not tuned to reproduce the storm statistics observed in nature. GCM-generated and observed storm statistics therefore differ markedly. Consider, for example, storms simulated by the Model II version of the GISS GCM in the $8^\circ \times 10^\circ$ grid square centered on New England. The probability distribution functions (pdf's) of storm duration and time between storms derived from hourly GCM precipitation data for the square are shown as histograms in Figures 5-1 and 5-2, respectively; the mean storm duration m_{tr} for the square was 2.9 hours, and the mean time between storms m_{tb} was 5.5 hours. Observational records, however, indicate that the values of m_{tr} and m_{tb} at Boston are 7.7 hours and 3 days, respectively (Eagleson, 1978).

The GCM underestimates these local storm properties, which are important to specify correctly in physically-based hydrological models (Eagleson, 1978). The Boston data, however, represent point observations and do not account for storms lying outside of Boston but still within the area defined by a grid square. The GCM, on the other hand, conceptually does model all storms within the grid square and thus should generate a higher storm frequency (i.e. a lower mean storm inter-arrival time, $m_{tr} + m_{tb}$). If the GCM was modified so that a simulated precipitation quantity was assigned to fall on an appropriate fraction of the grid square

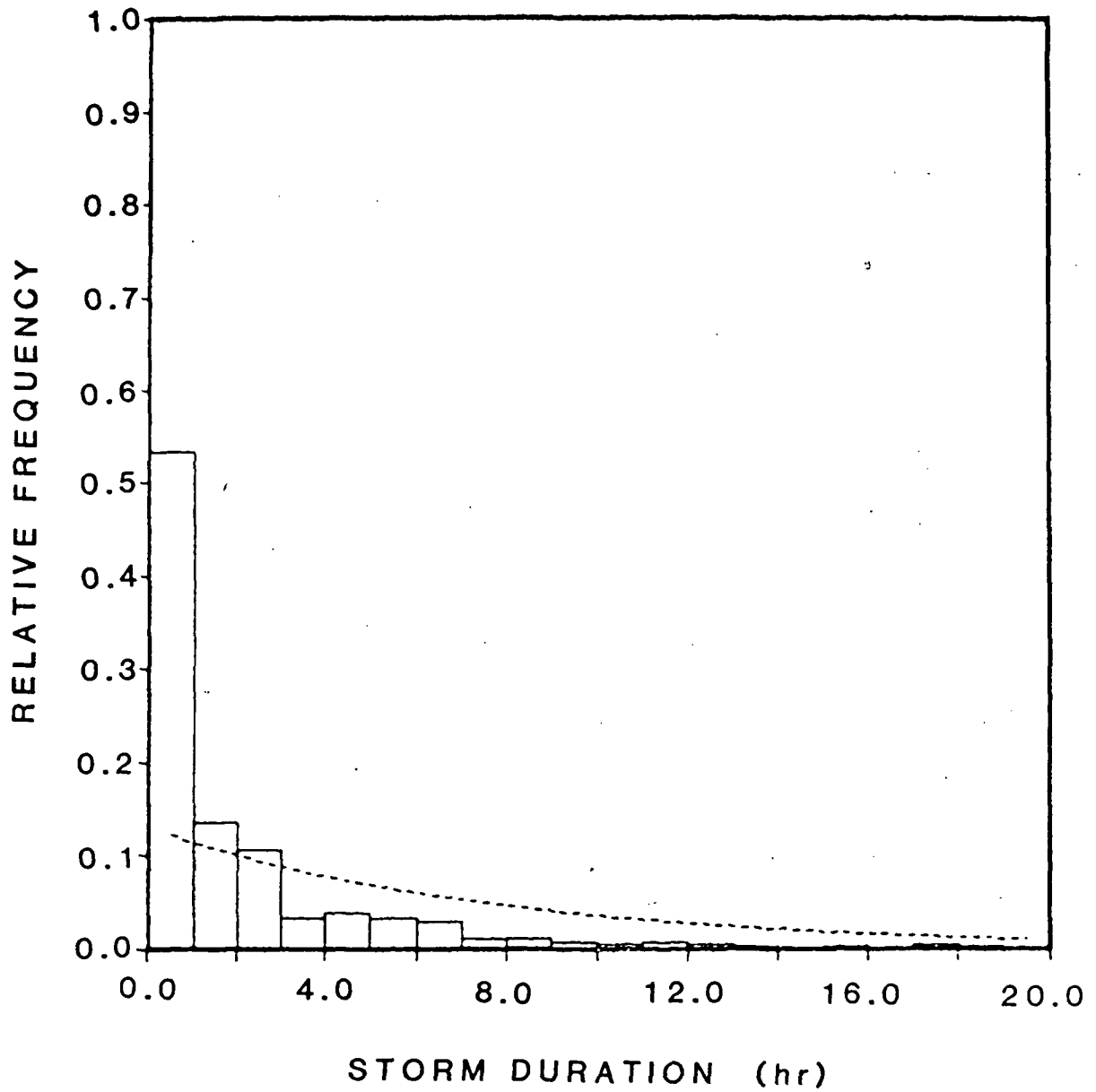


Figure 5-1 Probability density function of storm duration derived from precipitation data at New England grid square in GISS GCM. Dashed line represents an exponential fit to the observed distribution at Boston. (Mean observed storm duration = 7.7 hours.)

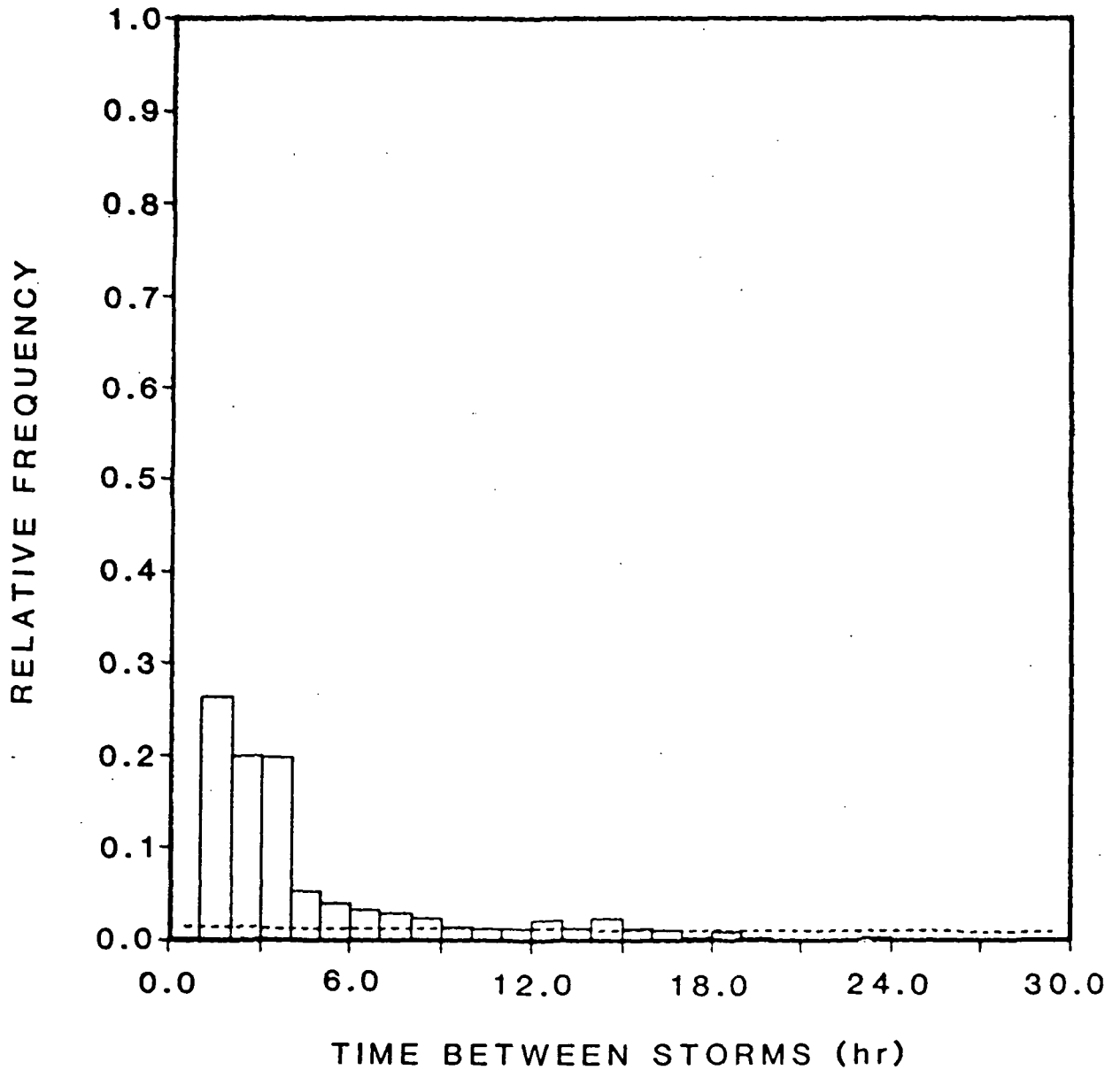


Figure 5-2 Probability density function of time between storms derived from precipitation data at New England grid square in GISS GCM. Dashed line represents an exponential fit to the observed distribution at Boston. (Mean observed time between storms = 3 days.)

rather than uniformly over the square, the storm statistics generated at a given fraction would more closely match those derived from point observations.

Mean storm depths generated by the GCM are similarly distorted. For the New England grid square, the average storm depth determined from the hourly precipitation data was 1.7 mm, whereas the observed mean storm depth at Boston was 8.6 mm. Note that if each storm was allowed to wet only 20% of the grid square, the mean storm depth would increase to the locally observed value. The simulated mean storm inter-arrival time would also increase, though it would still be too low.

The sensitivity of many aspects of the GCM's hydrological cycle to the fraction of a grid square wetted during a precipitation event is investigated quantitatively below.

5.2 A One-Dimensional Soil-Atmosphere Model

As discussed in Section 1.4.2, the effects of fractional wetting are analyzed with a one-dimensional model designed to simulate the workings of the three-dimensional GISS GCM. The model is computationally efficient, allowing a far greater number of sensitivity studies than could be performed with the GCM itself. It is also capable of simulating the feedbacks existing between soil moisture state and overlying atmospheric conditions. Most of the individual atmospheric and soil processes in the 1-D model employ the same formulations used in the GISS GCM.

5.2.1 Structure of the 1-D Model

The structure of the one-dimensional model (hereafter referred to as the 1-D model) is essentially that of the atmosphere/soil column at a single grid square in the GISS GCM. Nine atmospheric layers lie above a land surface, and two soil layers lie below it. Vertically-integrated heat and moisture convergences are assigned at each time step to the atmospheric column; an assumed vertical convergence distribution deposits this heat and moisture non-uniformly among the atmospheric layers. The convergences effectively account for both horizontal and vertical advective transports of heat and moisture. The thermodynamic conditions of the air column determine if moist convective or non-convective precipitation processes produce rainfall at the surface. Rain is either converted to runoff or added to the existing moisture in the upper soil layer; this soil moisture can in turn evaporate into the lowest atmospheric layer or diffuse into the lower soil layer. The atmospheric layers and the ground surface are heated by solar radiation and cooled by outgoing thermal radiation. The ground surface is also cooled by the outgoing fluxes of latent and sensible heat.

The various components of the model will now be discussed in detail. The complete computer code is provided in Appendix D.

a. Model Resolution. The pressure intervals and mean pressures assigned to the nine atmospheric layers in the 1-D model are similar to those typically utilized by the GISS GCM, as listed in Table 2-1. The same

sigma spacing is used, but the surface pressure is assigned to be 1000 mb at all times. As for the soil, the depth of the upper layer is 10 cm and that of the lower layer is 50 cm. With an assumed (drainable) soil porosity of 0.3, the corresponding water field capacities in the upper and lower soil layers are 30.0 kg/m² and 150.0 kg/m², respectively. The model is one-dimensional and thus the specified horizontal area spanned by the land surface does not affect the model computations.

b. Advection. The working assumption in the present modeling of advection is that changes in the parameterizations of surface hydrology cannot affect large-scale transports of heat and moisture, at least not in a way that the 1-D model can predict. Therefore, convergences of heat and moisture in each atmospheric layer of the 1-D model, corresponding to net advective transports into or out of the layer, are assigned at each time step rather than computed.

The vertically-integrated convergences of heat flux (H_{conv}) and moisture flux (Q_{conv}) assigned to the entire atmospheric column are taken to be

$$H_{conv} = H_{conv0} + H_{conva} \cos \left(\frac{2\pi t}{365 \times 24} \right) \quad (5-1)$$

$$Q_{conv} = Q_{conv0} + Q_{conva} \cos \left(\frac{2\pi t}{365 \times 24} \right) \quad (5-2)$$

where H_{convo} and Q_{convo} are the annual mean values, H_{conva} and Q_{conva} are the specified amplitudes of seasonal variation, and t is the time in hours since the winter solstice. The vertically-integrated flux convergences thus follow a sinusoidal seasonal cycle with extrema at the winter and summer solstices. Characteristic means and amplitudes can be obtained from observations.

Equations 5-1 and 5-2 provide the total amounts of heat and moisture added to (or subtracted from) the atmospheric column at any time step. To partition these convergences among the nine atmospheric layers, the 1-D model assumes that the vertical profiles of heat and moisture flux convergence always have the same well-defined shape. The following shape, roughly based on the shapes of vertical convergence profiles observed in nature, is used for both moisture and heat flux convergence in the present version of the 1-D model. Maximum convergence occurs at 900 mb. The heat or moisture added per unit air mass decreases exponentially above this level, reaching the fraction $1/e$ of the maximum value at 500 mb. Convergence is assumed to increase linearly between the surface and 900 mb, with zero convergence assumed at the surface.

This convergence profile is integrated between the pressures at the top and bottom of a given atmospheric layer in the 1-D model to determine the fraction of the total convergence assigned to the layer. Suppose $H_{\text{conv}}(\lambda)$ and $Q_{\text{conv}}(\lambda)$ represent the heat and moisture flux convergences, respectively, calculated for layer λ . The change in the temperature $T(\lambda)$ and total water content $Q(\lambda)$ of the layer during a time step Δt is calculated as

$$T(\lambda)_{\text{new}} = T(\lambda)_{\text{old}} + H_{\text{conv}}(\lambda) \cdot \Delta t / C(\lambda) \quad (5-3)$$

$$Q(\lambda)_{\text{new}} = Q(\lambda)_{\text{old}} + Q_{\text{conv}}(\lambda) \cdot \Delta t \quad (5-4)$$

where $C(\lambda)$ is the heat capacity of layer λ .

c. Moist Convection and Large-Scale Precipitation. The algorithms used to compute moist convective and nonconvective precipitation in the 1-D model are essentially the same as those used in the GISS GCM. These algorithms have already been outlined in Sections 2.3.2 and 2.3.3. Both precipitation processes are allowed to occur at every time step. They modify the heat and moisture contents of the atmosphere while producing rainfall at the earth's surface.

d. Surface Runoff. Runoff R in the 1-D model is calculated as it is in the Model II version of the GISS GCM:

$$R = A \cdot \text{Max}\left(\frac{1}{2} P \frac{W_1}{W_{fc1}}, P + W_1 - W_{fc1}\right) \quad (5-5)$$

where A is the area of the land surface, P is the precipitation at the earth's surface (in kg/m^2), W_1 is the water content of the upper soil layer (in kg/m^2), and W_{FC1} is the field capacity, or maximum water content, of the upper soil layer. Drier soils therefore produce less runoff. Precipitation water that doesn't run off the surface infiltrates into the upper soil layer; the second term in the maximization operator in Equation 5-5 insures that infiltration doesn't wet the soil beyond the field capacity. The coefficient of $1/2$ was found to produce realistic runoffs in the GISS GCM (Hansen et al, 1983).

e. Surface Evaporation and Sensible Heat Flux. As in the GISS GCM, evaporation from the earth's surface in the 1-D model is proportional to the specific humidity deficit $q_G - q_S$:

$$E = \beta \cdot \rho \cdot W_S \cdot C_Q \cdot (q_G - q_S) \quad (5-6)$$

where β is an efficiency factor, ρ is the density of air, W_S is the surface wind speed, C_Q is a vapor transfer coefficient, q_G is the saturated specific humidity at the surface temperature T_G , and q_S is the specific humidity at the top of the surface layer. The surface layer is a parameterized portion of the lowest atmospheric layer that lies just above the ground. Sensible heat transfer at the earth's surface is computed similarly:

$$H = c_p \cdot \rho \cdot W_S \cdot C_H \cdot (T_G - T_S) \quad (5-7)$$

where c_p is the specific heat of air, C_H is a heat transfer coefficient, and T_S is the temperature at the top of the surface layer. The parameters c_p , ρ , and W_s are assigned constant values.

To allow the calculation of C_Q , C_H , q_S , and T_S , the fluxes of moisture and heat from the ground into the surface layer are assumed to equal exactly the fluxes from the surface layer into the remainder of the lowest atmospheric box. The subgrid parameterization of the surface layer in the 1-D model is based on the equations outlined by Hansen et al (1983) for the GISS GCM. The parameterization varies according to whether the surface layer is stable ($T_1 > T_G$, where T_1 is the average temperature in the lowest atmospheric box) or unstable ($T_1 < T_G$). The surface boundary layer equations, not provided here, are coupled with the constant flux assumption to produce values of q_S and T_S that are effectively weighted averages of ground conditions and the conditions in the lowest atmospheric box:

$$q_S = \frac{C_H W_s q_G + \frac{K}{\Delta z} q_1}{C_H W_s + \frac{K}{\Delta z}} \quad (5-8)$$

$$T_S = \frac{C_H W_s T_G + \frac{K}{\Delta z} T_1}{C_H W_s + \frac{K}{\Delta z}} \quad (5-9)$$

where K is an eddy diffusion coefficient, Δz is the distance between the surface layer and the average height of the lowest atmospheric box, and

q_1 is the average specific humidity in the lowest atmospheric box. Equation 5-8 also assumes that C_H and C_q are equal. Since C_H and K are themselves functions of T_S , an iterative procedure is required to find consistent values of T_S and q_S .

Note that evaporation can be negative (corresponding to dew formation) if q_S is larger than q_G in Equation 5-6. Sensible heat flux can also be negative.

As in the GISS GCM, the efficiency factor β is set equal to the extent of saturation in the upper soil layer:

$$\beta = \frac{W_1}{W_{fc1}} \quad (5-10)$$

The presence of β in Equation 5-6 reflects the fact that the evaporation rate from a subsaturated soil lies below the potential rate due to soil resistance to water exfiltration.

f. Soil Hydrology. In analogy with the GISS Model II soil hydrology, groundwater runoff is not allowed in the 1-D model. Instead, the lower soil layer acts as a water reservoir that builds up water reserves in the winter and provides water to the upper soil layer during the growing season.

Downward diffusion of soil water in the 1-D model occurs whenever the saturation in the upper soil layer is greater than the saturation in the

lower layer. The downward water flux is reflected in the computed changes in soil saturation:

$$\Delta\left(\frac{W_1}{W_{fc1}}\right) = \frac{\Delta t}{\tau_D} \left(\frac{W_2}{W_{fc2}} - \frac{W_1}{W_{fc1}}\right) \quad (5-11)$$

$$\Delta\left(\frac{W_2}{W_{fc2}}\right) = \frac{\Delta t}{\tau_D} \cdot \frac{W_{fc1}}{W_{fc2}} \left(\frac{W_1}{W_{fc1}} - \frac{W_2}{W_{fc2}}\right) \quad (5-12)$$

where Δt is the time step, W_2 is the water content of the lower soil layer, W_{fc2} is the field capacity of the lower soil layer, and τ_D is the diffusion time constant, assumed to be 1 day. These changes in saturation conserve total water mass.

In further agreement with the GISS GCM Model II hydrology, upward diffusion of water is calculated quite differently. When the saturation in the lower soil layer is greater than that in the upper layer, the 1-D model checks to see if the current time step lies within the growing season, defined to be the period between April 21 and August 21, inclusive. (This growing season, in fact, slightly precedes the growing season assumed in the GISS GCM.) If it does, upward diffusion is immediate; i.e. just enough water is transported from the lower soil layer to the upper layer to make their saturations equal. This immediate diffusion is meant to reflect the ability of vegetation to extract water from deep in the soil. If the time step lies outside the growing season, no upward diffusion at all occurs.

g. Radiation. The model is driven in part by a solar radiation flux R_{sw} that is continuously applied at the top of the atmospheric column. The flux is a function of both the time of day and the season:

$$R_{sw} = \left\{ R_{swo} - R_{swa} \cos \frac{2\pi t}{365 \cdot 24} \right\} \quad (5-13)$$

$$\cdot \frac{\pi}{2d_\lambda} \text{Max} \left(0, \cos \left\{ \frac{(t_{day} - 12) \cdot 2\pi}{48d_\lambda} \right\} \right)$$

In the equation, R_{swo} is the annual mean incoming shortwave radiation flux (in Joules/m²-sec) at the top of the atmosphere, R_{swa} is the seasonal amplitude of the flux, d_λ is the fraction of daylight hours in the current day, t is the time in hours since the most recent winter solstice, and t_{day} is the time in hours since the most recent midnight.

Since R_{swa} is positive, the average daily solar radiation, as represented by the first factor in Equation 5-13, has a sinusoidal seasonal cycle with a minimum in winter and a maximum in summer. Values of R_{swo} as a function of latitude are provided by Held and Suarez (1974), and reasonable values of R_{swa} can be inferred from tables of solar radiation at the earth's surface (e.g., CRC, 1975). The remaining terms in Equation 5-13 distribute the solar radiation over the hours of the day, producing a peak flux at noon and zero incoming radiation at night. The fraction of daylight hours in a day is computed as

$$d_{\lambda} = 0.5 - d_{\lambda\text{amp}} \cos\left(\frac{2\pi t}{365 \cdot 24}\right) \quad (5-14)$$

where $d_{\lambda\text{amp}}$ is an assigned seasonal amplitude.

The incoming solar radiation energy from Equation 5-13 is distributed among the atmospheric layers and the soil surface using the algorithm of Held, Linder and Suarez (1981; see their Appendix A). An algorithm for determining the vertical distribution of longwave radiation heating and cooling is taken from the same source. (See also Held and Suarez, 1978.) To apply the algorithms to the 1-D model, several approximations had to be made; these are outlined in Appendix C of the present report.

The algorithms assume that the state of the atmosphere is completely defined (for the purposes of the radiation calculations) by the surface temperature and the temperatures at 250 mb and 750 mb. The 1-D model need not provide the computed changes in atmospheric water vapor content. This is because a constant relative humidity was assumed when the coefficients for the algorithms were computed, and thus the algorithms implicitly account for the increase in atmospheric water vapor content with temperature. Typical cloud cover values are also implicit in the algorithms' coefficients.

In addition to determining the net radiative heating or cooling of each atmospheric layer, the radiation algorithms produce downward fluxes of shortwave and longwave radiation at the earth's surface. The upward longwave radiation flux at the earth's surface is determined from the surface temperature T_G using the Stefan-Boltzmann law:

$$R_{\lambda w\text{-surface}} = \varepsilon \sigma T_G^4 \quad (5-15)$$

where ε is the surface emissivity and σ is the Stefan-Boltzmann constant (5.67×10^{-8} Joules/m²-sec-deg⁴). The energy balance of the upper soil layer uses the radiative fluxes in combination with latent and sensible heat fluxes to update the soil temperature.

5.2.2 Model Deficiencies

Most of the 1-D model parameterizations described above, such as those used for moist convective storms, nonconvective storms, surface evaporation, sensible heat flux, surface runoff, and soil moisture diffusion between ground layers, are consistent with the corresponding parameterizations used in the Model II version of the GISS GCM. In the 1-D model, however, it was found necessary to simplify the parameterizations of certain GCM processes. For example, the 1-D model uses the algorithms of Held, Linder and Suarez (1981) to compute radiative heating and cooling in the atmosphere, whereas the GISS GCM computes more exact values using the detailed radiation model of Lacis and Hansen (1974). As another (perhaps less important) example, near-surface wind speeds used in the subgrid parameterization of the surface boundary layer (Equations 5-7 and 5-8) vary with local weather conditions in the GISS GCM but are assumed constant in the 1-D model. These simplifications detract from the 1-D model's ability to mimic the GCM.

Furthermore, some of the processes modeled in the GISS GCM are completely absent from the 1-D model. For example, regardless of the temperature, ice formation is presently prohibited in the 1-D model both in the ground and during precipitation events. Heat conduction between the first and second soil layers is also not yet incorporated into the 1-D model.

The dimensionality of the 1-D model may be its greatest handicap. When, for example, a precipitation event occurs over a grid square in the three-dimensional GISS GCM, the change in the energy state of the air column can result in a subsequent change in the air mass (and associated changes in the heat and moisture) advected into the column, which in turn will affect the future weather there. The GCM can determine feedbacks in air mass advection because the GCM also monitors the states of the air columns over neighboring grid squares. The 1-D model, by its very nature, cannot do this. The 1-D model assigns rather than predicts heat and moisture convergences.

The sensitivity to a change in model parameterization might also be magnified in the GCM. Consider, for example, a coastal grid square receiving winds off the ocean. A change in, say, the parameterization of surface runoff might affect the local climate over the coastal square only slightly. The slight change, however, will modify slightly the characteristics of the air advected out of the grid square's air column and into the air column of a grid square farther inland. This inland square will therefore feel the effects of both the surface runoff parameterization change and the slight change in the state of its incoming wind. The 1-D model cannot account for this effect.

Future versions of the 1-D model will improve on several of the problems mentioned in this section. Thermal conduction between soil layers, for example, could be modeled straightforwardly, as could the formation of ice in precipitation and in the ground. Perhaps some of the three-dimensional feedbacks, such as those existing between column energy state and horizontal convergence, could be parameterized through a study of the feedbacks existing in the GISS GCM. For the present, though, it is necessary to keep the 1-D model's deficiencies in mind when analyzing the model results.

5.3 A Test of the 1-D Model

The 1-D model was designed to simulate the workings of the Model II version of the GISS GCM. A test of the 1-D model's effectiveness in this regard is presented below. In the test, the model sensitivity to the parameterization of surface runoff is seen to compare well with the sensitivity observed in the GISS GCM.

5.3.1 The GISS GCM Runoff Sensitivity Experiment

The two Model II GISS GCM simulations chosen for the sensitivity analysis differed only in their surface runoff formulations. The "control" run (Run #814 of a long line of simulations performed by GISS personnel) calculated the surface runoff produced during a precipitation event using Equation 5-5. The "experiment" run (Run #809 of the GISS GCM simulations) calculated runoff using almost the same equation, but with a coefficient of 1.0 rather than $1/2$:

$$R = A \cdot \text{Max}\left(1.0 \cdot P \frac{W_1}{W_{fc1}}, P + W_1 - W_{fc1}\right) \quad (5-16)$$

Thus, given the same precipitation rate and soil saturation at a grid square, the experiment run would typically produce twice as much surface runoff as would the control run. The experiment run was expected to produce greater runoff amounts in the spring and a drier soil in the summer.

The two GISS GCM simulations ran for twenty months. Generated time series of precipitation, evaporation, runoff, surface temperature, and soil saturation during the second year are presented in Section 5.3.3 for comparison with the 1-D model results.

5.3.2 The 1-D Model Runoff Sensitivity Experiment

The 1-D model sensitivity analysis was performed in much the same way. A two-year model simulation calculating runoff with Equation 5-5 was compared to a different two-year simulation calculating runoff with Equation 5-16. Time series of the water balance components during the second simulation year of each run are presented in Section 5.3.3.

The values chosen for the 1-D model constants are listed in Table 5-1. They agree, for the most part, with the values used in the GISS GCM. One exception is the near-surface wind speed, which is calculated explicitly in the GCM but assumed constant at 2 m/sec in the 1-D model. The 1-D model also assumed a constant near-surface air density of 1.2 kg/m³ and an effective surface roughness of 0.3 m, typical for continental plains. Ground albedo remained constant at 0.15.

Table 5-1

Values used for 1-D model parameters

i) Resolution parameters		
Surface pressure		1000 mb
Time step for surface flux calculation		6 min
Time step for all other processes		1 hr
ii) Radiation parameters		
R_{swo}		325 Joules/m ² -sec
R_{swa}		162 Joules/m ² -sec
Ground albedo		0.15
ϵ		1.0
d_l		2.8 hours
Teddy		20 days
iii) Convergence parameters		
H_{convo} (for 1 m ² area)		-34.0 Joules/sec
H_{conva} (for 1 m ² area)		39.8 Joules/sec
Q_{convo} (for 1 m ² area)		9.2×10^{-6} kg/sec
Q_{conva} (for 1 m ² area)		6.83×10^{-6} kg/sec
iv) Surface boundary layer parameters		
Surface layer height		30 m
Roughness height		0.3 m
w_s		2 m/sec
Height of lowest atmospheric layer		500 m
ρ		1.2 kg/m ³
v) Soil parameters		
Porosity		0.3
Heat capacity of dry earth	1.130×10^6	Joules/m ³ °K
w_{fc1}		30 kg/m ²
w_{fc2}		150 kg/m ²
τ_D		1 day

Parameters specific to the 1-D model are those that define the incoming solar radiation flux and the horizontal convergences of heat and moisture. These parameters effectively establish the climate generated by the 1-D model. For the runoff sensitivity experiment, the incoming solar radiation varied with season and time of day according to Equation 5-13, with the annual mean radiation flux R_{SWO} at the top of the atmosphere being $325 \text{ J/m}^2\text{-sec}$ and the seasonal amplitude R_{SWa} being $162 \text{ J/m}^2\text{-sec}$. This approximates the seasonal cycle of solar radiation received at 40°N (Held and Suarez, 1974; CRC, 1975).

A seasonal cycle for heat convergence was inferred from the monthly zonally-averaged meridional energy transports provided by Oort (1971). First, monthly total energy convergences were estimated by subtracting the northward total energy flow past 45°N from the flow past 40°N and then dividing by the area of the region in between. Next, monthly latent energy convergences between 40°N and 45°N were estimated in the same way. The difference between the total energy convergence and the latent energy convergence in a given month was interpreted as that month's heat convergence. The seasonal cycle fitted to the monthly heat convergences is defined by an H_{convo} value of -34.0 Joules/sec and an H_{conva} value of 39.8 Joules/sec in Equation 5-1 (for a ground surface area of 1 m^2). Thus, the assigned heat convergence is generally negative, with relatively small positive values in the winter.

The seasonal cycle for moisture convergence could not be determined in such a straightforward manner. Unlike heat convergence, moisture convergence over a continental region cannot be approximated by the zonal

mean convergence, since continentality plays a dominant role. Convergence over continents during summer, for example, is reduced due to increased soil evaporation rates. Another problem arises from possible inconsistencies between the data sets used to determine the inputs. Assigned seasonal cycles of radiation, heat convergence, and moisture convergence may seem reasonable when each is considered separately, but if they are inherently inconsistent, they do not necessarily produce a reasonable 1-D model climate. In early experiments, moisture convergences were inferred from the same data set used to construct the moisture flux divergence plots in Section 3.1.3. This resulted, however, in climates that were either too cold throughout the year or too wet in winter. It was desired to produce a warmer climate with a relatively wet summer for the comparison of climate sensitivities in the 1-D model and the GISS GCM.

Presumably, once the seasonal cycles of radiation and heat convergence over a typical continental region in the GCM are determined from a GCM simulation, a consistent seasonal cycle of moisture convergence there could be inferred from the plots in Section 3.1.3. For now, though, the seasonal cycle of moisture convergence is estimated as follows. A moisture balance in both the real world and the model requires that the annual means of moisture convergence and surface runoff be equal. Thus, the mean annual moisture convergence in the 1-D model is set equal to the mean annual global runoff in nature, estimated to be 29 cm/year, or 9.2×10^{-6} kg/m²-sec (Hansen et al., 1983, quoting L'vovich, 1980). Runoffs of this magnitude are known to exist between 40°N and 45°N (Baumgartner and Reichel, 1975). The assigned seasonal amplitude of 6.8×10^{-6} kg/m²-sec

is estimated from the GCM moisture flux divergence data (from Section 3.1.3) over certain pure land grid squares in North America.

Keep in mind that the 1-D model is designed not so much to simulate GCM climate as it is to simulate GCM climate response to changes in hydrological parameterization. During the course of the 1-D model's development, a wide range of heat and moisture convergences was assigned to the atmospheric column. The generated climate was seen to change with each set of imposed convergences. The model sensitivity to changes in hydrological parameterization, however, was found to be largely the same regardless of the convergences chosen. The response of the 1-D model under the convergences described above can be considered typical.

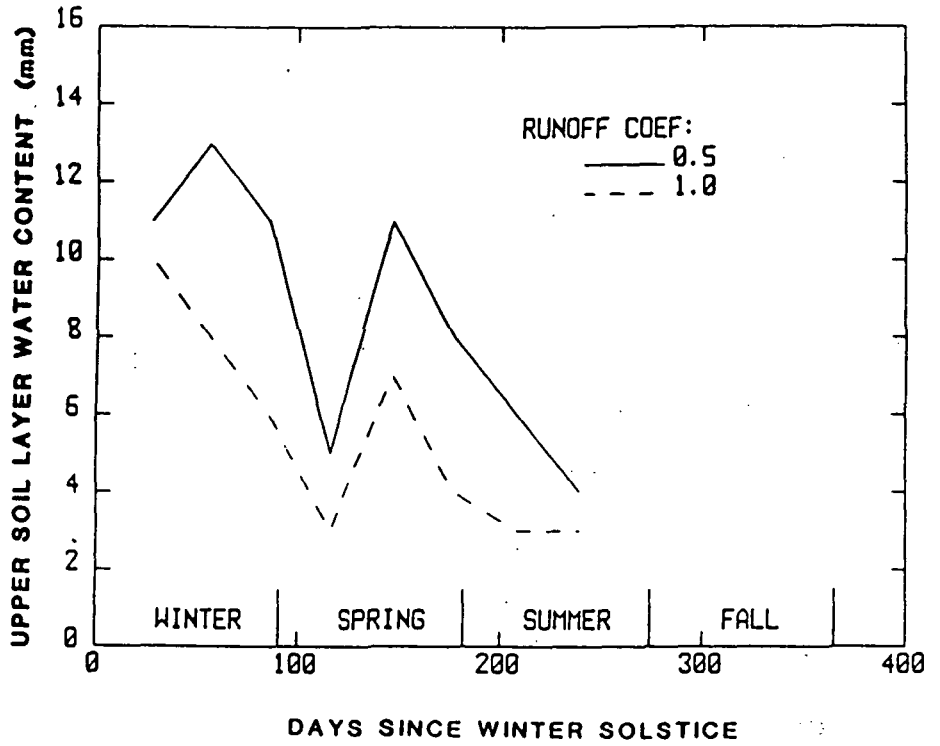
The 1-D model used a time step of 1 hour for all processes except surface evaporation, which employed a six minute time step for stability purposes.

5.3.3 Comparison of Sensitivities

The GCM data presented in Figures 5-3a through 5-7a represent monthly average conditions over land at 43°N. To produce the data, GCM variables were spatially averaged over the land portions of all grid squares at this latitude. Only eight months of GCM data were available during the second simulation year.

Figure 5-3a shows the soil water content W_1 in the upper soil layer (in kg/m^2) as a function of time for the GCM simulations. (Unavailable GCM data prevented a conversion of water content to soil saturation for the present discussion.) The solid line represents the control simulation

a. GISS GCM



b. 1-D Model

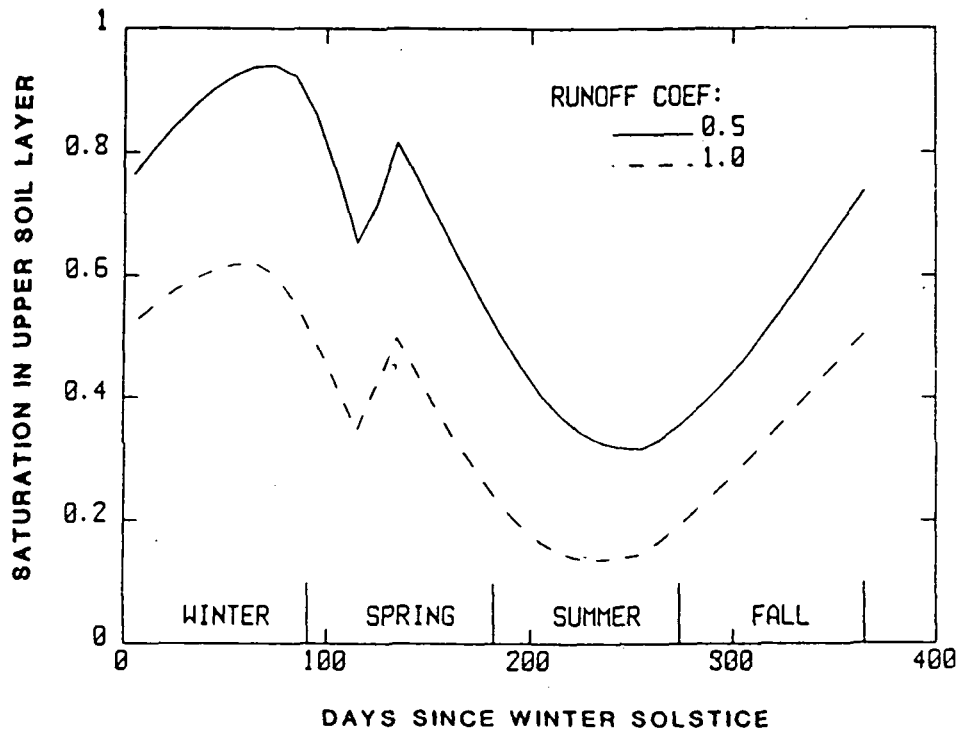


Figure 5-3

Sensitivity of upper soil layer moisture content to a change in the runoff coefficient. a) GISS GCM. b) 1-D model. Moisture contents are expressed in mm for the GISS GCM and as soil saturations for the 1-D model.

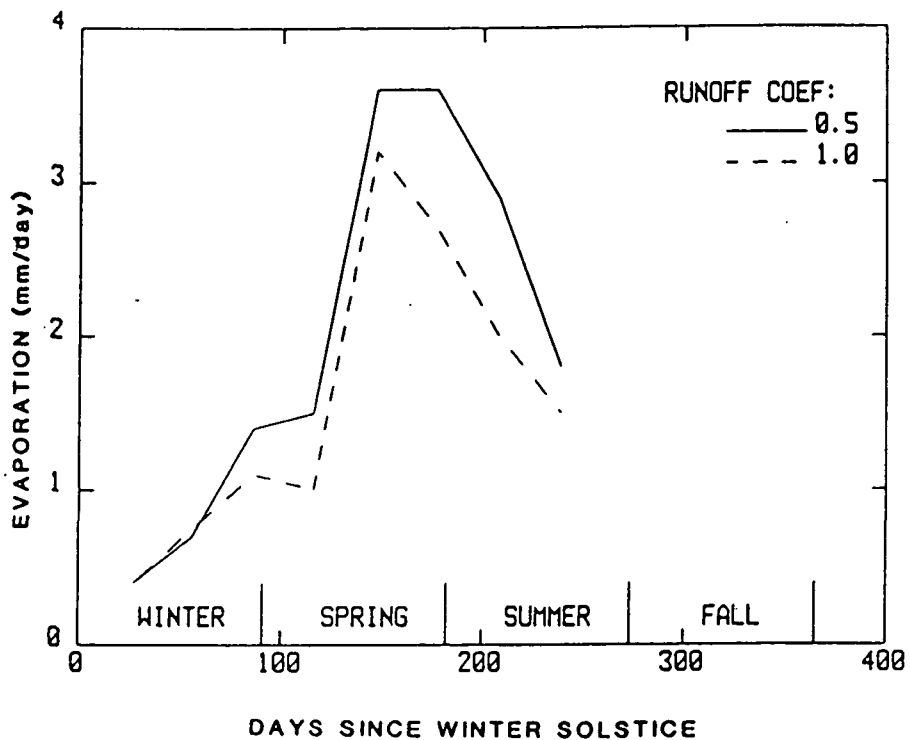
results, and the dashed line represents the experiment simulation results. In both simulations, the soil moisture content in late summer is lower than that in winter. Also, throughout the year, the use of Equation 5-17 to ease the production of surface runoff causes the experiment simulation to generate lower soil moisture contents than those observed in the control simulation.

Figure 5-3b compares the corresponding time series of upper level soil saturation from the two 1-D model simulations. Again, the solid line represents the control run results and the dashed line represents the experiment run results. In agreement with the GCM simulations, the arrival of summer is marked by a decrease in soil moisture, and the experiment run produces lower soil moisture contents throughout the year than does the control run.

Both the GCM and the 1-D model generate a local minimum (in time) of soil saturation in spring. The local minima certainly reflect the imposition of a growing season. Recall from Section 5.2.1f that diffusion of moisture from the lower soil layer to the upper soil layer is prevented in both models until a certain time in spring, when diffusion becomes immediate. (Unfortunately, this time is slightly different in the two models, being 132 days from the winter solstice in the GCM and 121 days in the 1-D model.) Thus, at the start of the growing season in either model, the upper soil layer suddenly has a rich new supply of moisture, and the soil saturation increases.

The sensitivity of the seasonal evaporation rates to the parameterization of surface runoff is shown in Figure 5-4a for the GCM and

a. GISS GCM



b. 1-D Model

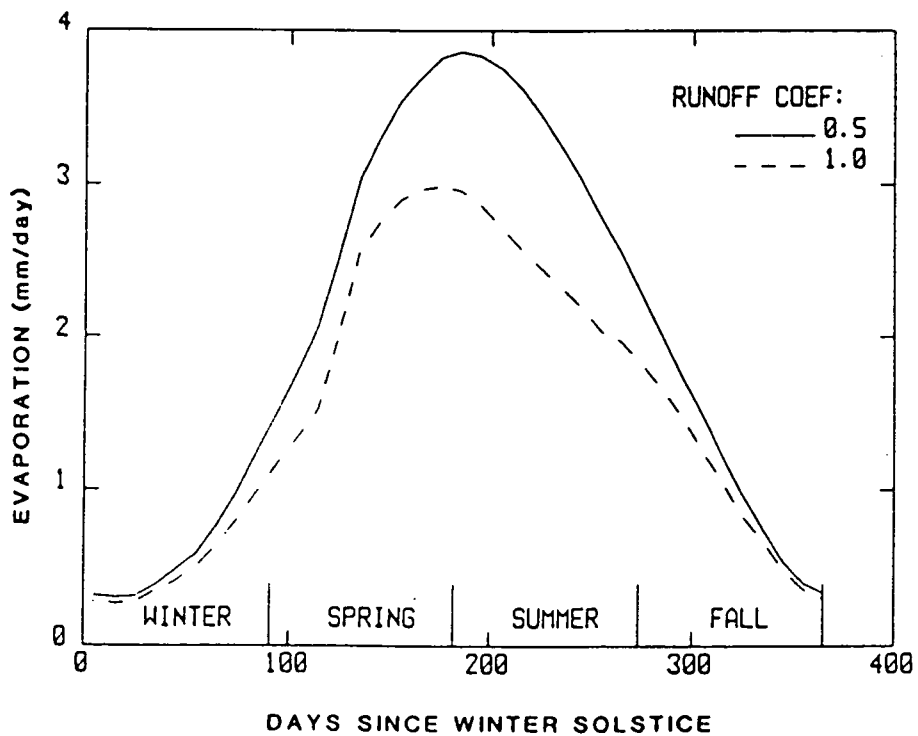


Figure 5-4

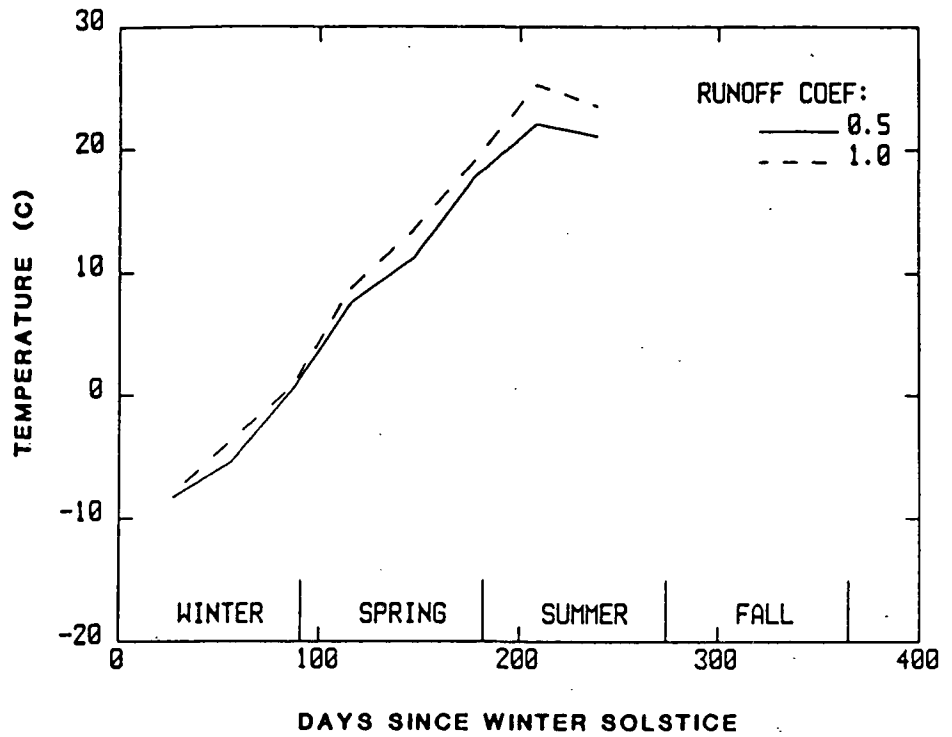
Sensitivity of evaporation (in mm/day) to a change in the runoff coefficient. a) GISS GCM. b) 1-D Model.

Figure 5-4b for the 1-D model. Notice that the same trends in evaporation reduction are indicated by both models. For both models, the evaporation rates in the experiment simulation are less than those in the control simulation during summer, apparently due to the lower soil moistures observed in Figures 5-3a and 5-3b. The greatest reduction occurs for both models after the summer evaporation maximum. Also for both models, winter evaporation rates are not affected much by the runoff parameterization. Notice that the magnitudes of the evaporation rates produced by the two models are similar.

Precipitation time series from the GCM simulations are shown in Figure 5-5a, and those from the 1-D model simulations are shown in Figure 5-5b. For both the GCM and the 1-D model, summer precipitation in the experiment run is less than that in the control run, probably due to the reduction in evaporation rates noted above. The lowered evaporation rates in each experiment run also result in higher temperatures at the earth's surface in summer, due to the reduction in evaporative cooling. This is demonstrated in Figure 5-6a for the GCM simulations and in Figure 5-6b for the 1-D model simulations. The 1-D model climate is slightly cooler than the GCM climate in summer, probably due to the summer heat and moisture convergences chosen.

Finally, the sensitivity of the surface runoff itself to the runoff parameterization is shown in Figure 5-7a for the GCM and Figure 5-7b for the 1-D model. (The jagged nature of the GCM runoff curves reflects the fact that the GCM runoff data was provided to only one significant figure.) For both the GCM and the 1-D model, the use of Equation 5-16 in

a. GISS GCM



b. 1-D Model

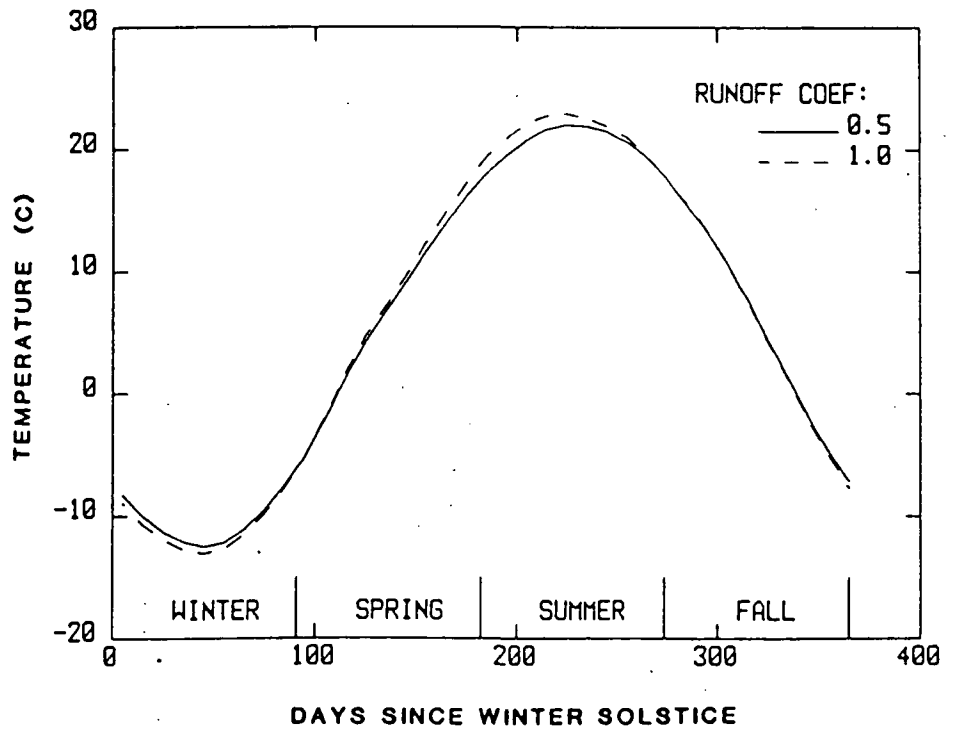
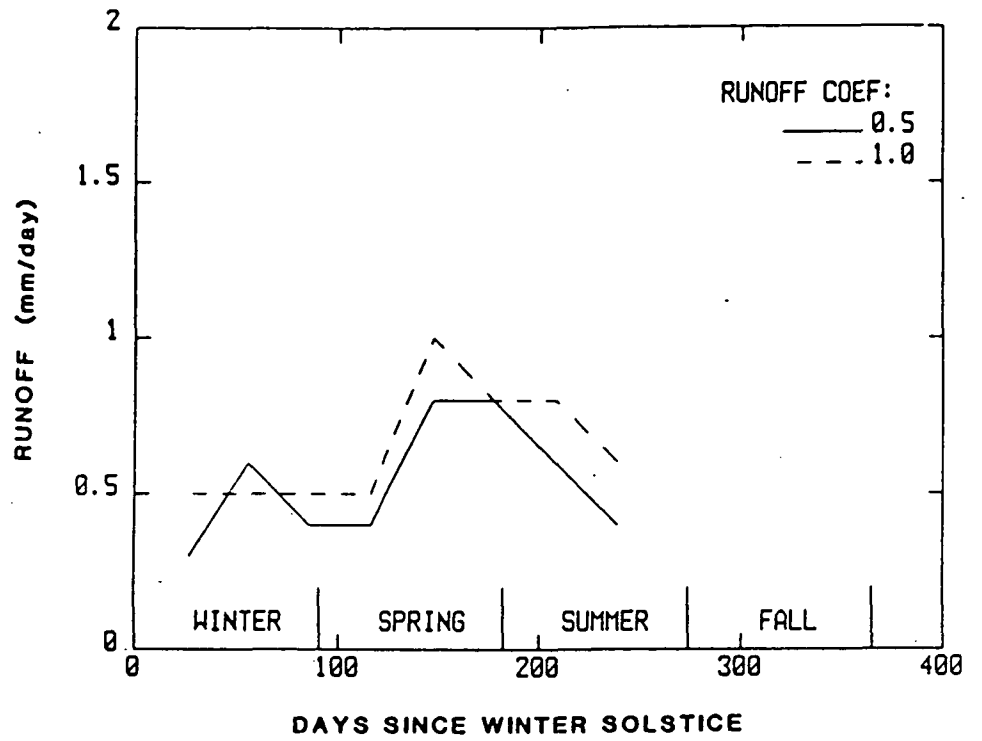


Figure 5-6 Sensitivity of surface temperature (in °C) to a change in the runoff coefficient. a) GISS GCM. b) 1-D model.

a. GISS GCM



b. 1-D Model

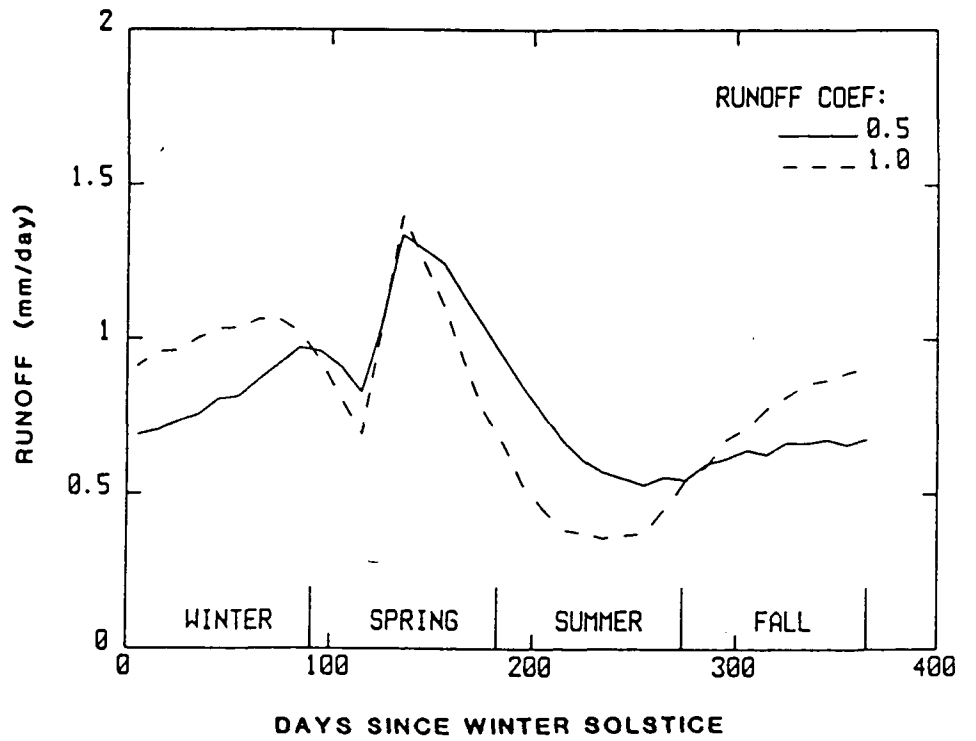


Figure 5-7

Sensitivity of surface runoff (in mm/day) to a change in the runoff coefficient. (a) GISS GCM. (b) 1-D model.

the experiment run to compute surface runoff results in higher runoffs in the winter and spring. Notice, however, that in the GCM, the experiment run produces higher runoffs than the control run in summer, while the reverse is true in the 1-D model. A similar discrepancy in late summer model behavior is seen in the precipitation time series shown in Figure 5-5. The discrepancies perhaps relate to the assignment of moisture convergences in the 1-D model, which constrains the annual runoff produced by the control and experiment runs to be the same. The GCM simulations are not subject to this constraint.

Aside from these discrepancies, though, the 1-D model quite successfully reproduces the inherent GCM sensitivities to runoff parameterization. Thus, in spite of its many simplified formulations, the 1-D model seems to capture the essential physics of GISS GCM hydrology. The test above helps justify the use of the 1-D model as a surrogate for the GCM in sensitivity studies examining various hydrological parameterizations, including that of fractional wetting of soil during precipitation events.

5.4 Fractional Wetting: Investigation with the 1-D Model

5.4.1 Parameterization of Fractional Wetting

Subgrid wetting of land during precipitation events is modeled by dividing the 1-D model land surface into sections of equal area and allowing precipitation formed in the atmospheric column to fall onto only one section, chosen randomly for each storm. The air column itself remains intact and effectively lies above all the land sections. Any number of land divisions may be specified by the user.

Surface runoff is calculated as in the original 1-D model, but since the precipitation is now assigned to fall onto a smaller area, the precipitation depth is correspondingly increased. Equation 5-5 thus becomes:

$$R = fA \cdot \text{Max}\left(\frac{1}{2} \frac{P}{f} \frac{W_{1\text{-local}}}{W_{fc1}}, \frac{P}{f} + W_{1\text{-local}} - W_{fc1}\right) \quad (5-17)$$

where f is the fraction of the total land area represented by a single section, P is the precipitation in kg/m^2 under the uniform wetting assumption, and $W_{1\text{-local}}$ is the water content in kg/m^2 of the section being wetted. With this formulation, a given land section experiences precipitation wetting that is more intense yet less frequent.

The soil moisture content of each land section is followed separately. The 1-D model soil hydrology and evaporation formulations described in Section 5.2 above are applied to each section individually, and the model continuously updates and stores each section's soil saturations and surface temperature. The different local surface temperatures also produce different sensible heat and outgoing longwave radiation fluxes. Horizontal transport of heat and moisture between neighboring land sections is prohibited.

The single atmospheric column above the land sections, on the other hand, is assumed to be well-mixed horizontally. All heat and moisture additions from the surface into the first atmospheric layer are spread evenly throughout the layer. Thus, the specific humidity q_1 and temperature T_1 in the lowest atmospheric layer are assumed to be the same over

each land section when calculating the local surface layer characteristics with Equations 5-8 and 5-9, even if evaporation and sensible heat fluxes in previous time steps varied greatly among the sections.

In some future version of the 1-D model, it might be sensible to adjust the radiation fluxes calculated above that land section receiving precipitation during a time step. The shortwave radiation incident on the land section, for example, should perhaps be reduced due to increased cloud albedo. At the present stage of model development, however, the outgoing longwave flux is the only radiative flux that varies among the sections.

The present parameterization of fractional wetting assumes that precipitation generated in consecutive time steps constitutes a single storm and that all rainfall from a given storm falls onto the same land section. Thus, the increase in soil saturation achieved by a section during the first hour of a storm directly affects the runoff produced during the second hour of the storm. The section to receive precipitation is randomly chosen at the beginning of each storm. While such a formulation would be unrealistic for a climate with infrequent dry periods, the average storm duration in a 1-D model simulation is generally less than three hours.

5.4.2 Sensitivity of 1-D Model to Fractional Wetting

Four 1-D model simulations were performed to produce the results presented below, one with a single land section, one with five sections, one with ten sections, and one with twenty sections. The simulations

employed the model parameter values outlined in Section 5.3.2 above. Model data were collected during the second year of each two-year simulation. The data for each simulation represent average conditions over all sections.

The seasonal cycle of average soil saturation in the upper soil layer is shown for each simulation in Figure 5-8. Except for a period in late spring and early summer, smaller wetted fractions lead to lower average soil saturations. The twenty-division simulation has lower soil saturations throughout the year.

An examination of the surface runoff formulation helps explain the behavior of the soil saturation curves in winter. Smaller wetted fractions are more likely to become saturated by precipitation events. Once a section is saturated, the runoffs generated over the section increase markedly. (Runoff from a saturated fraction is calculated with the second term in the maximization operator in Equation 5-17.) This effect is felt the most in winter, when soil saturations are already high. Figure 5-9 shows the seasonal cycles of surface runoff for the four simulations. Notice that in winter, a decrease in wetted fraction size results in an increase in surface runoff. The increase in runoff is apparently at the expense of average water infiltration into the soil, and thus winter soil saturations are lower for smaller wetted fractions.

In late summer, at approximately Day 240, the average soil saturations in the wetted fractions simulations drop suddenly, while that in the uniform wetting simulation does not. The drop corresponds to the end of the growing season. Recall that at this time, upward diffusion of

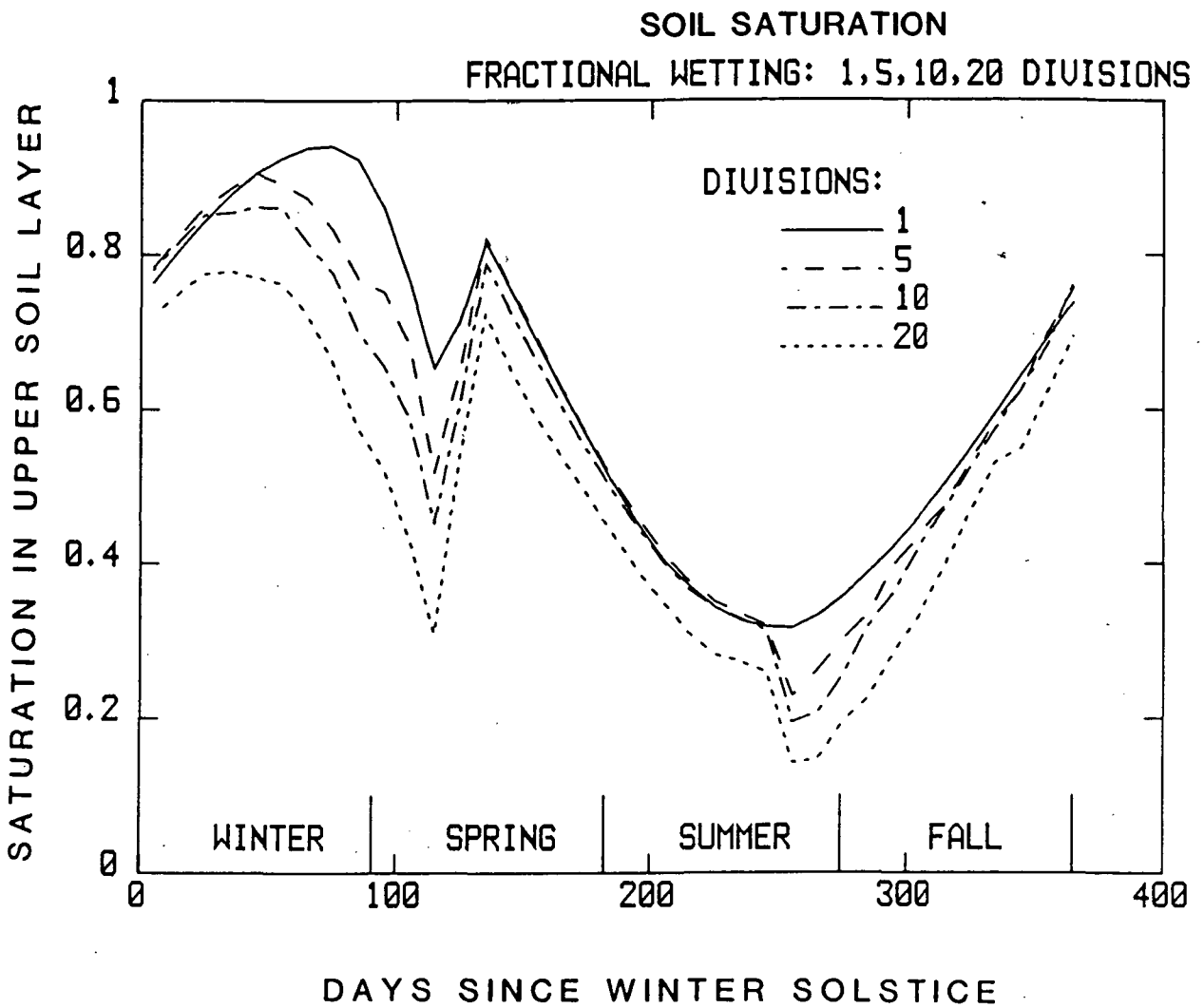


Figure 5-8 Seasonal cycle of average saturation in upper soil layer of the 1-D model for varying sizes of the wetted fraction.

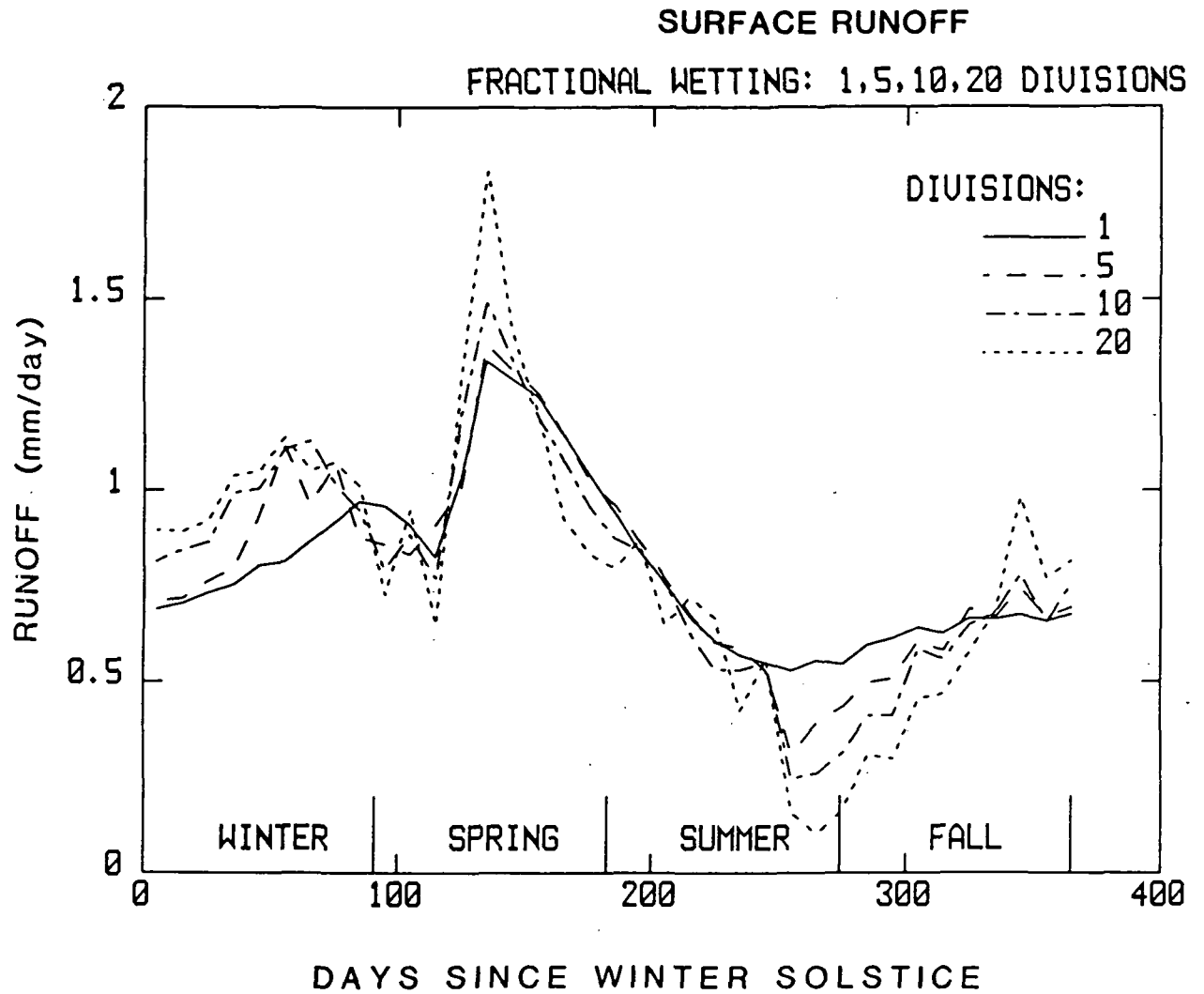


Figure 5-9 Seasonal cycle of surface runoff in the 1-D model for varying sizes of the wetted fraction. (Units: mm/day)

moisture from the lower to the upper soil layer is suddenly prohibited, while downward diffusion can continue as before; the upper soil layer thus loses a potential source of moisture then. This loss is felt the most in the wetted fractions simulations, perhaps due to their non-uniform spatial distributions of soil moisture. At the end of the growing season, high downward diffusion rates in certain soil sections are no longer offset by high upward diffusion rates in other sections. The greater the spatial variation in soil moisture is, the greater the bias will be toward larger downward diffusion rates.

Runoffs in late summer show a strong sensitivity to wetted fraction size, with smaller wetted fractions producing smaller runoffs. This is partly due to the fact that the soil is dryer in the summer, making it much more difficult for a precipitation event to completely saturate a land section. Thus, Equation 5-17 generally uses the first term in the maximization operator to calculate runoff, i.e., runoff is calculated as being proportional to soil saturation. Since soil saturation decreases with wetted fraction size in late summer, so does runoff.

Another reason for the late summer runoff sensitivity is the concurrent sensitivity observed in precipitation. Figure 5-10 shows the seasonal cycle of precipitation for each simulation. Notice the decrease of late summer precipitation with wetted fraction size. According to Equation 5-17, lower precipitations result in lower runoffs.

The late summer precipitation sensitivity, along with the one observed in early spring, corresponds to and probably results from the concurrent sensitivities observed in the evaporation cycle, shown in

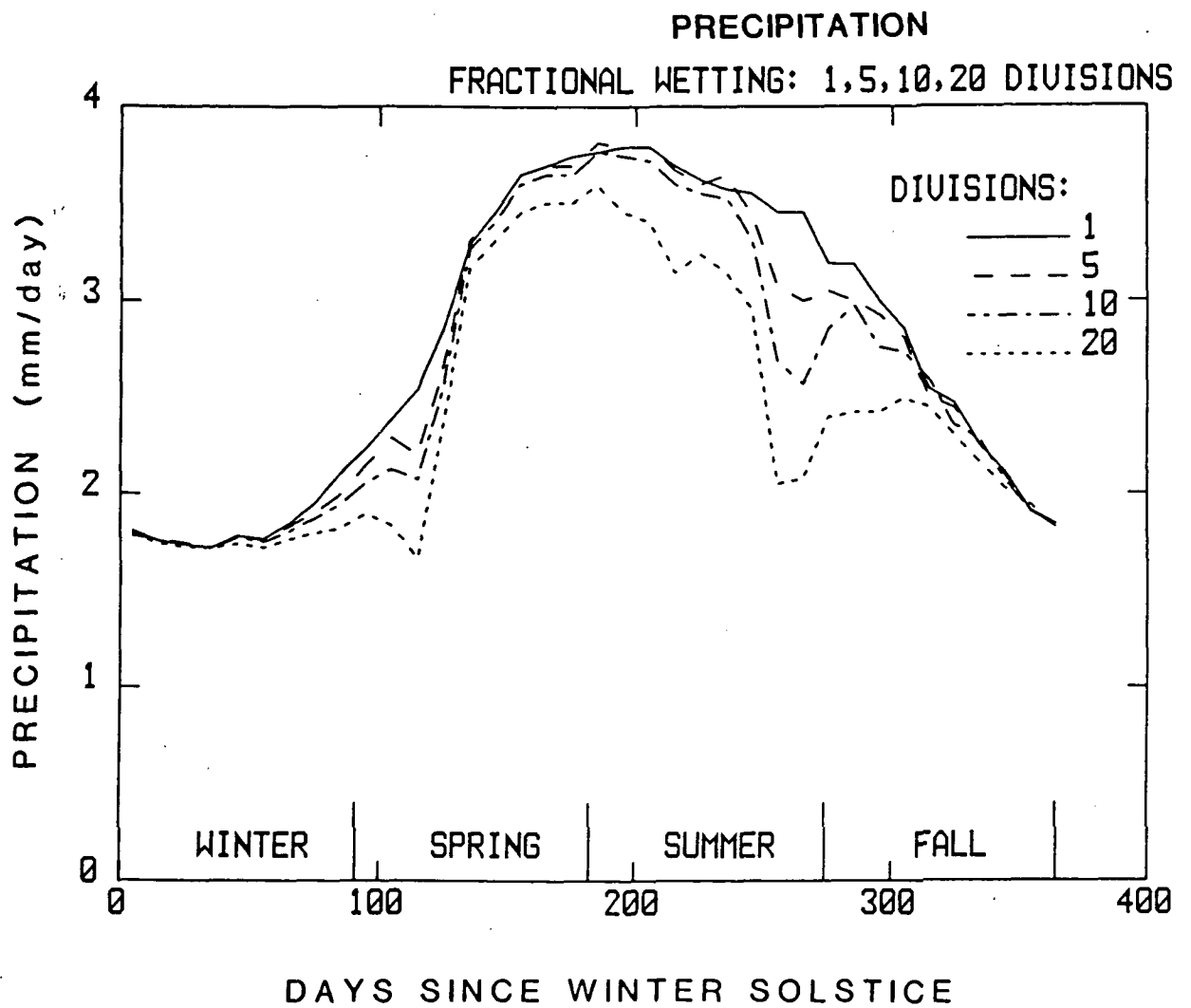


Figure 5-10 Seasonal cycle of precipitation in the 1-D model for varying sizes of the wetted fraction. (Units: mm/day)

Figure 5-11. For smaller wetted fractions, surface evaporation in late summer and early spring pumps less precipitable water into the air, resulting in reduced precipitation. The reduction of evaporation with wetted fraction size during these times in turn reflects the concurrently reduced soil saturations observed in Figure 5-8. As indicated by Equations 5-6 and 5-10, evaporation in the 1-D model is directly proportional to the soil saturation. Notice also that early summer evaporations are significantly reduced only for the twenty-division simulation, as are early summer soil saturations.

The seasonal cycle of average surface temperature is shown for each simulation in Figure 5-12. Fractional wetting seems to have little effect on surface temperature. The small variation observed among the simulations in summer probably reflects the observed variation in evaporation rates; for smaller wetted fractions, the lower evaporation rates result in reduced latent cooling of the surface and thus in higher temperatures.

In summary, the seasonal cycles of the climatic variables appear to be controlled by the seasonal cycle of soil saturation. Fractional wetting apparently modifies soil saturation in winter through its effect on runoff production and in summer through its effect on moisture diffusion between soil layers.

Table 5-2 lists the annual mean precipitations, evaporations, surface runoffs, and upper soil layer saturations for each simulation. The annual precipitation and evaporation values decrease with the fraction of land receiving precipitation. Notice that the precipitation and evaporation

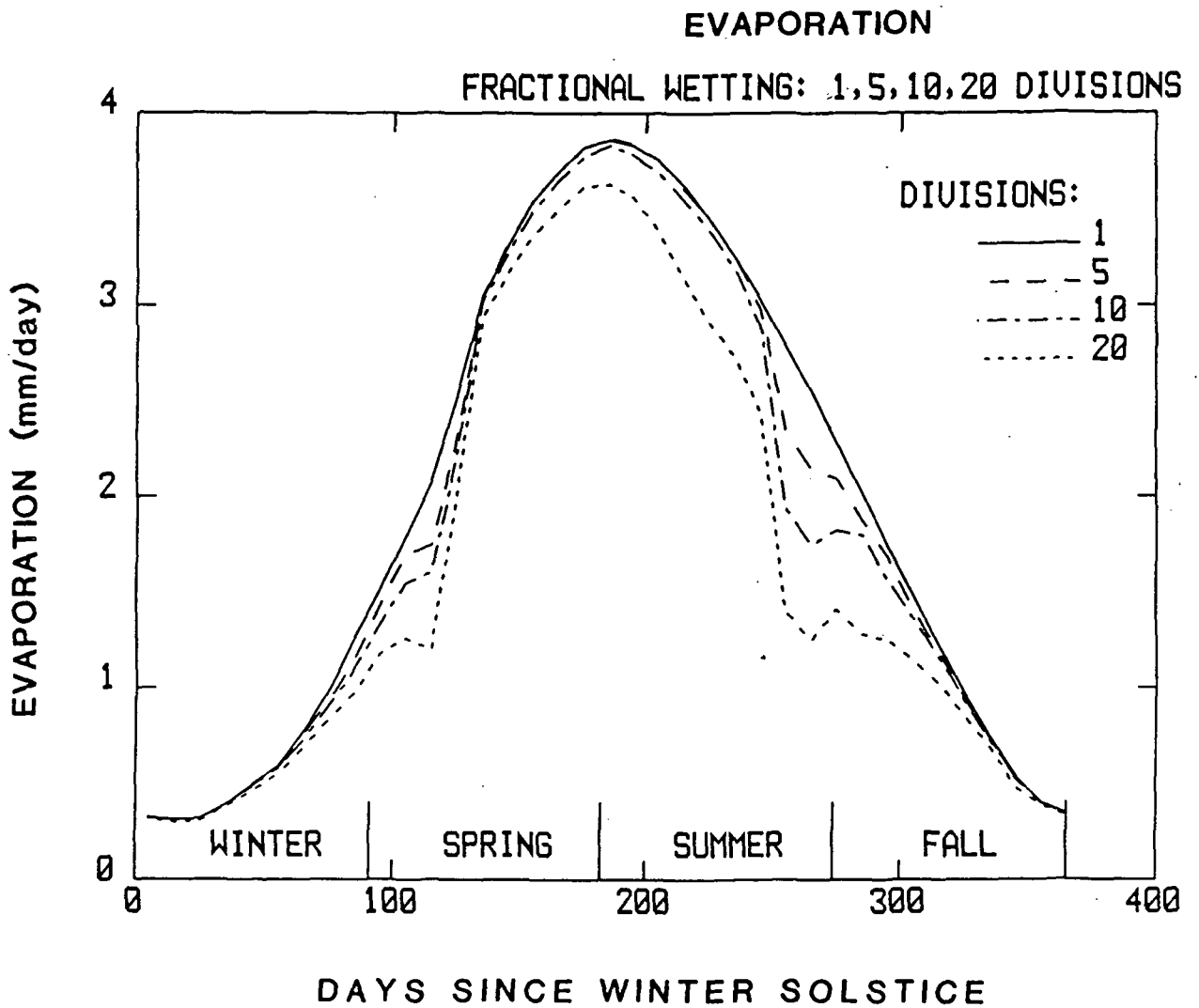


Figure 5-11 Seasonal cycle of evaporation in the 1-D model for varying sizes of the wetted fraction. (Units: mm/day).

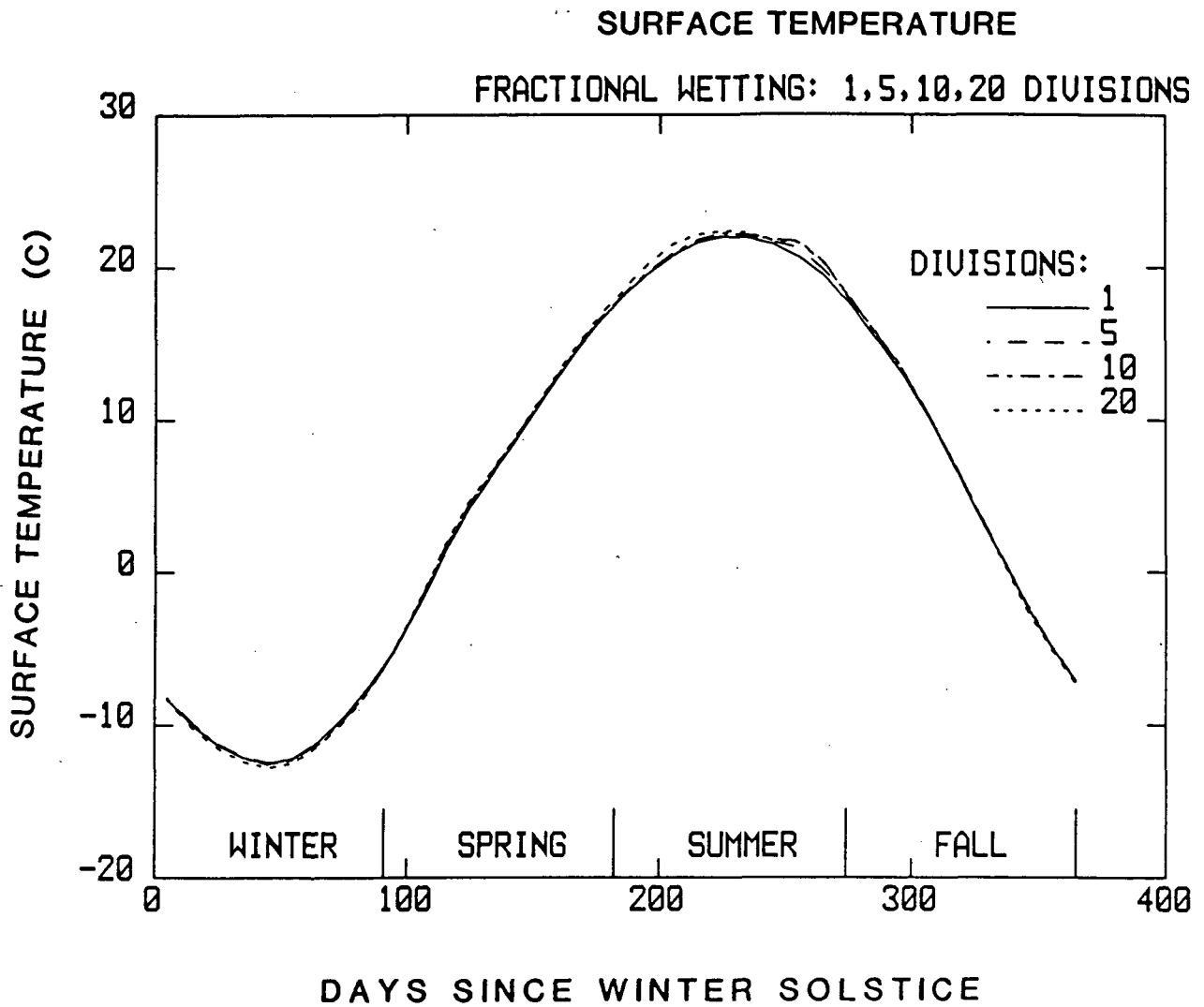


Figure 5-12 Seasonal cycle of surface temperature in the 1-D model for varying sizes of the wetted fraction. (Units: °C)

Table 5-2. Annual water balance quantities
for the wetted fractions simulations

	Number of Land Divisions			
	<u>1</u>	<u>5</u>	<u>10</u>	<u>20</u>
Precipitation (mm/year)	1015	991	965	892
Evaporation (mm/year)	725	701	675	601
Runoff (mm/year)	291	291	290	290
Saturation in Upper Soil Layer	0.62	0.59	0.57	0.49

decrease together so that the annual runoff is the same in all simulations, as is necessary from the assignment of atmospheric moisture convergences. As indicated in Figure 5-9, however, seasonal runoffs do vary with wetted fraction size. A small decrease in the annual mean soil saturation with wetted fraction size is also apparent.

5.4.3 A Simple Approximation to the Fractional Wetting Parameterization

The above simulation results indicate that the 1-D model climate is sensitive to the fraction of land surface wetted during a storm. The alternative fractional wetting parameterization presented below is found to generate some of the same model sensitivities. It is simpler in nature and potentially can be incorporated into a GCM.

In the alternative parameterization, which is based on a suggestion by GISS personnel, the 1-D model land surface is divided into only two sections, one larger than the other. All precipitation generated by the model falls onto the smaller section. Runoff is calculated with Equation 5-17, with f now being the fraction of the land surface represented by the smaller section; the runoff calculation thus accounts for the increase in precipitation depth associated with fractional wetting. As before, soil water diffusion and evaporation fluxes are calculated separately for each section, and the air above the land surface is assumed to be well mixed.

At the beginning of every storm, just before the first precipitation water reaches the land surface, the model redistributes the moisture in the upper soil layers of the two sections so that the two upper soil layers are at the same saturation state. This is the key simplification in

the alternative parameterization. The soil moisture in the lower layers and the heat contents of the upper layers are similarly mixed. Again, precipitation amounts generated in consecutive time steps constitute a single storm. The heat and moisture contents of the two sections are followed separately, with no horizontal transfers allowed during the period between the start of a storm and the start of the next storm.

Three 1-D model simulations were performed using this alternative, "wet-and-dry-fraction" fractional wetting parameterization. The smaller section constituted $1/5$ of the land surface in the first simulation, $1/10$ of the land surface in the second, and $1/20$ of the land surface in the third; the three simulations thus correspond to the five-division, ten-division, and twenty-division simulations described in Section 5.4.2 above. The simulations used the model parameters listed in Table 5-1. They ran for two years each, with model data being collected in the second year.

Time series of saturation in the upper soil layer for the three simulations are shown in Figure 5-13. The results from the 1-D model simulation with uniform precipitation wetting are also shown for comparison. Notice that the sensitivity of soil saturation to wetted fraction size is similar in winter and spring to that observed under the original parameterization (see Figure 5-8). The simplified parameterization is not successful, however, in reproducing the sensitivity inherent in the original method in late summer. This is seen more clearly in Figure 5-14, in which the seasonal cycles of soil saturation using the original and simplified methods for a wetted fraction of $1/20$ are directly compared.

SOIL SATURATION

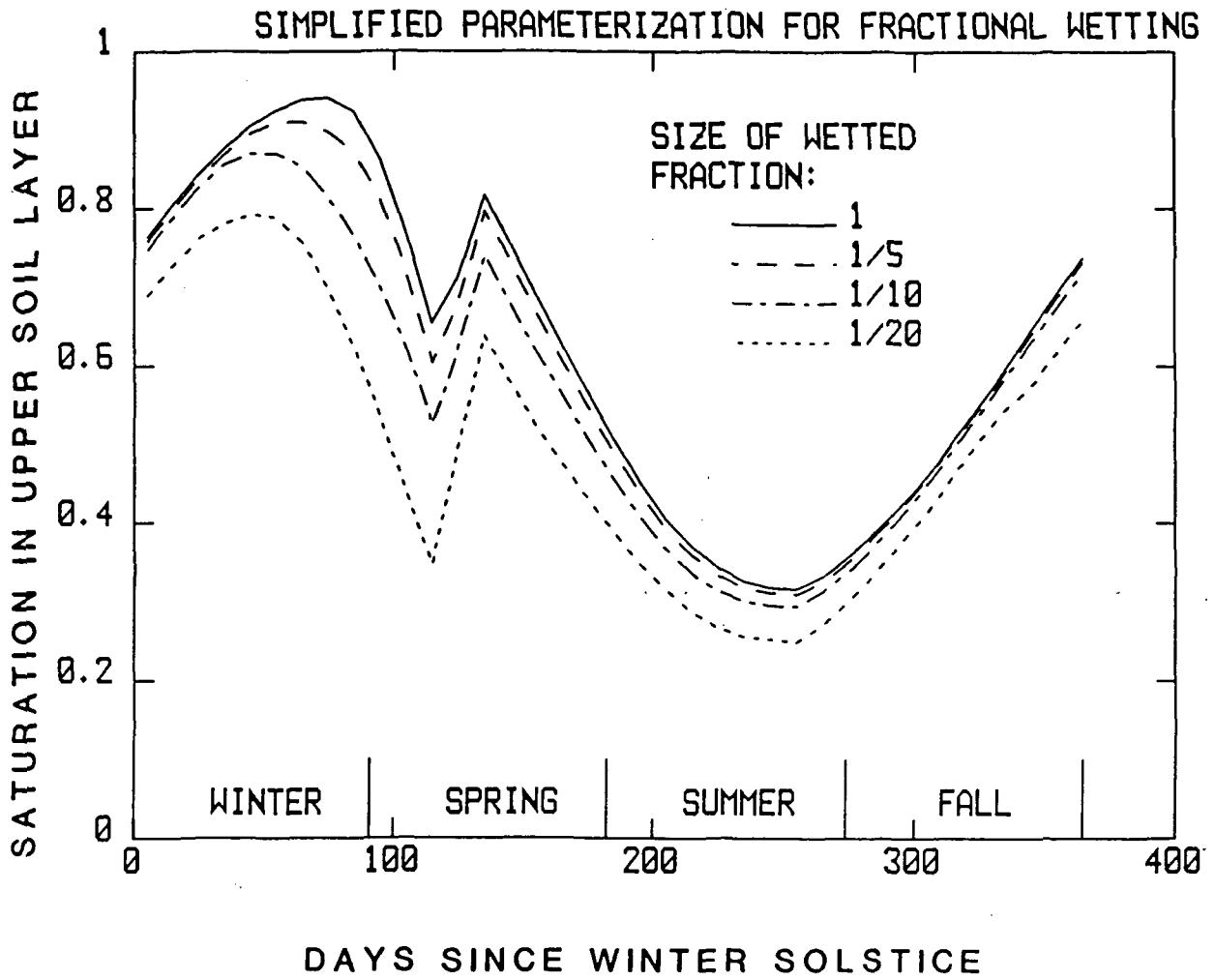


Figure 5-13 Seasonal cycle of average saturation in upper soil layer of the 1-D model for varying sizes of the wetted fraction, under simplified parameterization.

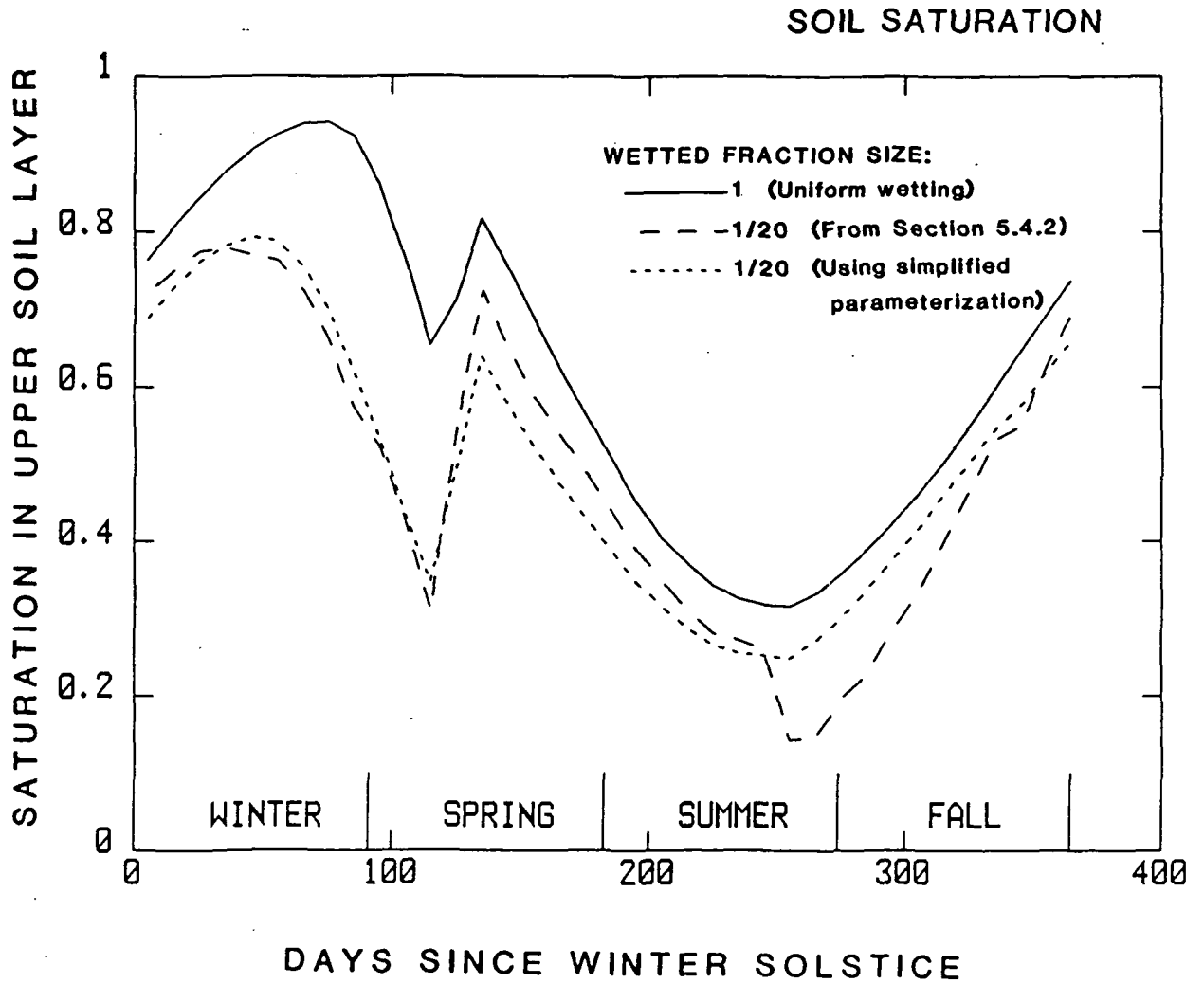


Figure 5-14 Seasonal cycle of average saturation in upper soil layer of 1-D model. Solid line shows cycle under uniform precipitation wetting, dashed line shows cycle derived in Section 5.4.2 for a wetted fraction of 1/20, and dotted line shows cycle derived under simpler parameterization for a wetted fraction of 1/20.

Figures 5-15 and 5-16 provide the corresponding plots for precipitation. Again, the simplified parameterization reproduces the original method's winter and spring sensitivities but fails to generate the original method's reduction in late summer precipitation. Corresponding plots for evaporation, runoff, and surface temperature (not shown here) reflect the same performance.

To explain the late summer deficiency in the simplified parameterization, recall from Section 5.4.2 that fractional wetting seemed to act in two different ways to reduce average soil saturations from their values under the uniform wetting assumption. In winter and spring, high average soil saturations allowed excess runoff to be produced from the increased precipitation depths allowed by fractional wetting. This resulted in decreased infiltration and thus in reduced saturations. In late summer, the end of the growing season prevented moisture in the lower soil level from diffusing into the upper level. This especially enhanced downward diffusion in the fractional wetting simulations, due to their spatially non-uniform distributions of soil saturation. The larger downward diffusion rates resulted in smaller upper level soil saturations.

Apparently, since the simplified fractional wetting parameterization does assign larger precipitation depths to a fractional area, it can account for the first mechanism. It thus performs well in winter and spring. The less severe non-uniformity in soil saturations, however, apparently cannot provide for the second mechanism, and the simplified parameterization performs poorly in late summer.

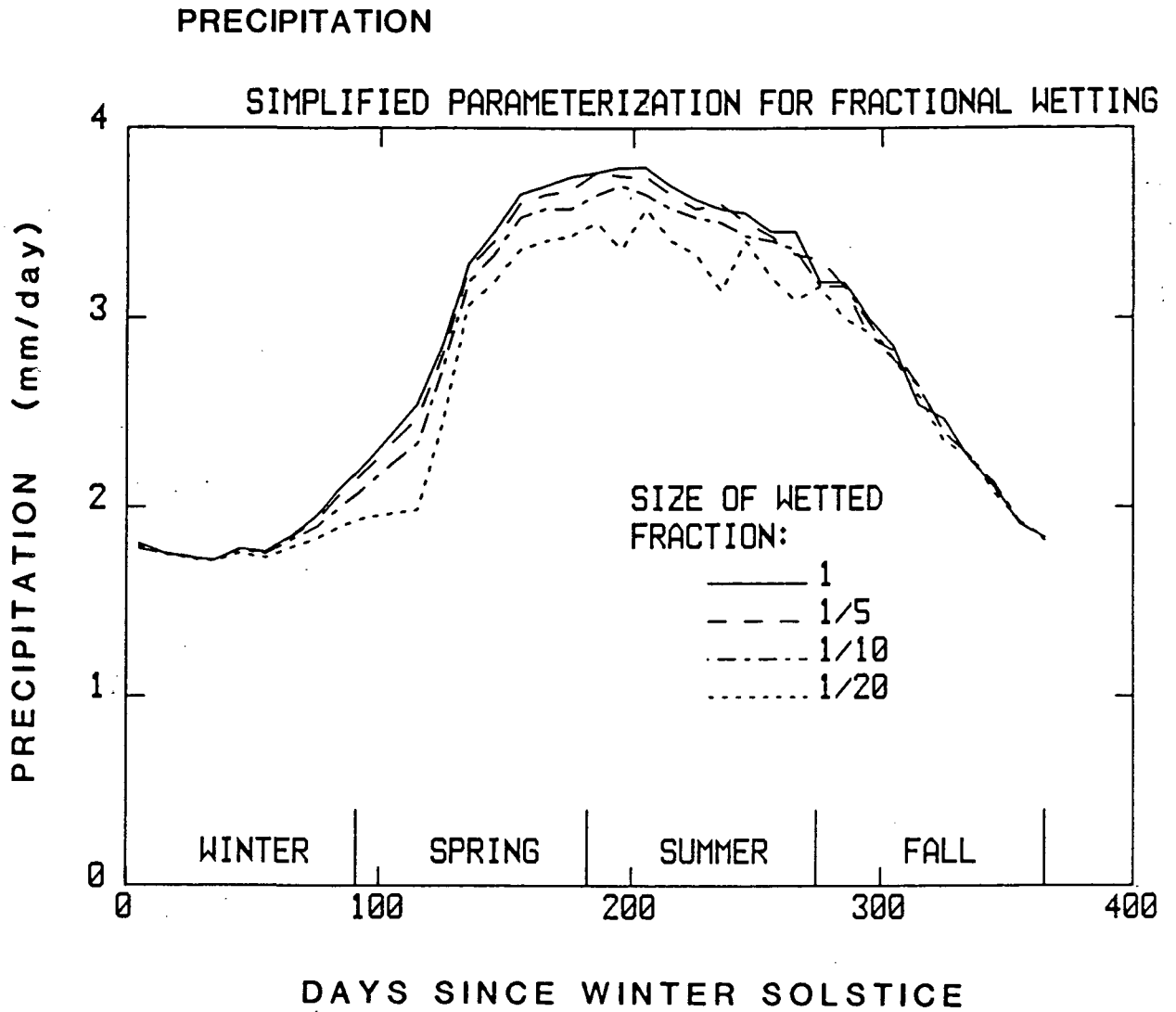


Figure 5-15 Seasonal cycle of precipitation in the 1-D model for varying sizes of the wetted fraction, under simplified parameterization. (Units: mm/day)

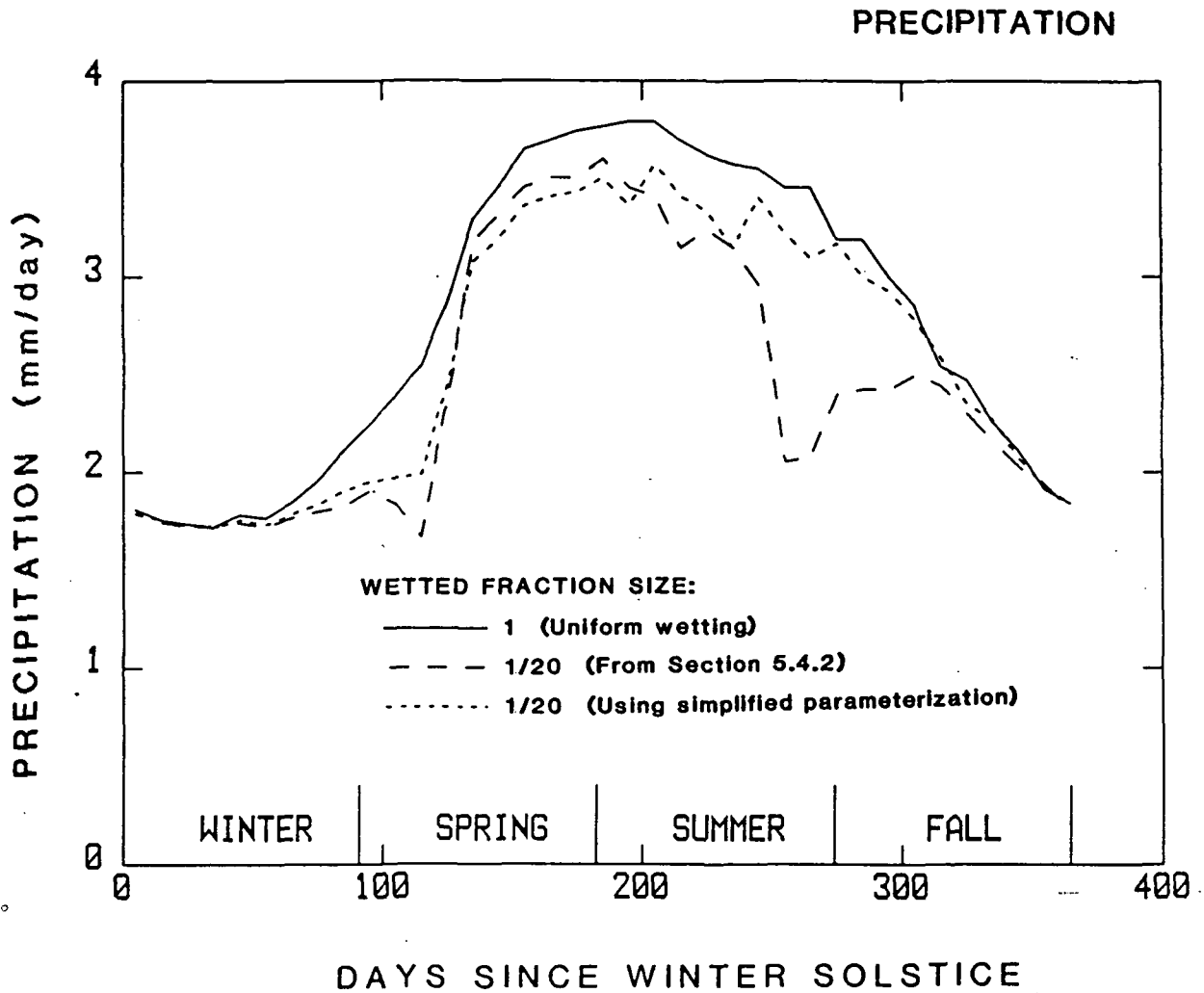


Figure 5-16 Seasonal cycle of precipitation in 1-D model. Units: mm/day. Solid line shows cycle under uniform precipitation wetting, dashed line shows cycle derived in Section 5.4.2 for a wetted fraction of 1/20, and dotted line shows cycle derived under simpler parameterization for a wetted fraction of 1/20.

5.5 Interpretation of Model Results

It is essential to keep the 1-D model in perspective. The model was designed to simulate the response of a three-dimensional GCM to changes in hydrological formulation. It is effectively, then, a "model of a model". The fractional wetting experiment described above, for example, does not examine the nature of spatially varying precipitation in real-world hydrological basins. It examines only potential GCM sensitivities to the incorporation of fractional wetting.

Furthermore, note that the GISS GCM's present formulation of surface runoff is tuned (e.g., through the parameter $1/2$ in Equation 5-5) to produce reasonable runoffs from a uniform precipitation wetting over a grid square. Assigning rainfall to a fraction of the surface is certainly more realistic, but it won't produce a more realistic hydrology under the present runoff parameterization. To produce a more realistic hydrology, the various model parameterizations would have to be retuned.

A more complete sensitivity study might proceed as follows. The land surface in the 1-D model would be divided into a certain number of sections. The relevant model parameterizations would be retuned (but not reformulated) to produce the most realistic climate possible. The land surface would then be divided into a different number of sections, and the model parameterizations would again be retuned. The true sensitivity of the 1-D model climate to the inclusion of fractional wetting would be indicated by the differences in these climates.

Regardless of whether these new climates indicate a sensitivity to wetted fraction size, however, accounting for fractional wetting can only

lead to model improvement. The more realistic a GCM formulation is, the more accurately the GCM can be used to predict climate changes. The added arbitrary tuning necessary to produce a reasonable soil hydrology under the inaccurate uniform wetting assumption may not be appropriate under a modified model climate.

Even though the fractional wetting simulations presented in Section 5.4 do not account for the necessary retuning of model parameterizations, their results are still suggestive. The GISS GCM hydrological formulations imposed in the 1-D model caused certain climatic variables, such as average soil saturation, to respond in well-defined ways to the size of the wetted fraction when the land surface was divided horizontally into a number of sections. At certain times of the year, essentially the same responses were observed under an alternative fractional wetting parameterization employing only two sections, as described in Section 5.4.3. This latter parameterization, which is less computationally demanding and which potentially could be incorporated into a GCM, perhaps can capture in part the important effects of fractional wetting.

Again, though, it is necessary to qualify this statement. Other GCMs, including the planned Model III version of the GISS GCM, use different soil hydrology formulations. If the 1-D model was fitted with a different set of formulations, the response of model climate to wetted fraction size might be markedly different, and it would be difficult to predict in advance the success of the simpler fractional wetting parameterization in reproducing this climate response. Furthermore, once the modeler was satisfied with a given parameterization's performance

under an appropriate version of the 1-D model, the parameterization would still have to be tested in the three-dimensional GCM. The 1-D model, remember, is necessarily limited in its ability to examine GCM behavior, being unable to simulate such features as horizontal convergence of air mass in the atmospheric column.

Furthermore, only model sensitivities to various wetted fraction sizes have been discussed above. This report has not attempted to determine the proper wetted fraction size to assign to a given precipitation event. Perhaps the fraction size could be assigned probabilistically, using a different probability distribution for moist convective and non-convective precipitation events. The distributions might be derived from studies such as that of Eagleson and Wang (1985) for non-convective events and Eagleson et al (1987) for convective events. Note that the fractional wetting parameterizations employed above can be modified easily to allow a time-varying wetted fraction size.

Although more work needs to be done, the 1-D model simulations presented above provide at least the start of a potentially useful fractional wetting analysis. Before concluding this section, it should be noted that a significant feature of the above analysis is the development of the 1-D model, which seems (from the test in Section 5.3) to capture the essential physics inherent in the GISS GCM's hydrological cycle. It is thus potentially useful for other GCM hydrology studies as well. Some of these potential uses are outlined in the following chapter.

Chapter 6

Summary, Conclusions, and Outlook

This chapter summarizes the basic findings of the present report and suggests possible courses for future research. The chapter is naturally divided into two parts, the first discussing the tracer water model, and the second discussing the fractional wetting analysis.

6. The GISS GCM Tracer Water Model

The tracer water version of the GISS GCM allows one to determine, for the inherent GCM climate, where a water mass evaporating from a specified region on the earth first returns to the earth's surface as precipitation, exchanged vapor (over the ocean), or dew. As discussed in Chapter 2, the model allows all important atmospheric processes to act on the three-dimensional tracer distribution. To the extent that the GCM climate is accurate, the model results can suggest lateral scales of hydrological transport in the real world.

6.1.1. Validity of the Tracer Water Model

The extent to which the tracer water model results are limited by the accuracy of the GISS GCM itself is indicated, in part, by a comparison of observed and modeled fields of vertically-integrated vapor flux. These comparisons, presented in Chapter 3, show that the GCM simulates the

large-scale features of the observed fields fairly well but fails to reproduce properly a great many features at smaller spatial scales. The global maps in Section 3.1 should be used when evaluating the results of the tracer water model simulations. Simulated tracer transport cannot be trusted in regions where the total vertically-integrated water vapor flux is poorly simulated.

The inter-annual variability inherent in the tracer water model was investigated in Section 3.2. Five July simulations, each using a different set of GCM initial conditions, produced roughly the same tracer precipitation contours for a Southeast Asia source region. The results speak for the adequacy of a one-month integration time in the determination of average tracer transport characteristics.

The tracer water model was then used to simulate tritium transport from the stratosphere to the ocean. The ratio of tritium input into the ocean via vapor exchange to that via precipitation was found to be strongly insensitive to changes in source location and to changes in the parameterizations of vapor exchange, precipitation, and advective transport. Furthermore, the ratio was significantly less (by a factor of two) than that deduced from observational data by Weiss and Roether (1980). Weiss and Roether, however, employed a number of questionable assumptions, and it is therefore difficult to evaluate the tracer water model's performance on the basis of their analysis. Chapter 3 also provided a brief overview of a tracer water model simulation of stable water isotope distributions, as performed by Jouzel et al (1987).

6.1.2 Hydrological Implications of Model Results

Chapter 4 presented some further applications of the tracer water model. One set of simulations, for example, determined the relative contributions of large-scale evaporative sources on the globe to the precipitation at each GCM grid square. As expected, midlatitude continental regions in the model were found to be a more important source of continental precipitation water during summer than during winter. In fact, the results indicate a fair degree of continental water recycling during summer in midlatitudes. In some tropical land regions of the Northern Hemisphere, on the other hand, continental moisture sources were more important in winter than in summer.

The strong water recycling indicated at times in both midlatitudes and the tropics is contrary to the conclusions of various studies in the literature that stress the dominance of oceanic evaporative sources for continental precipitation (e.g., Benton et al., 1950; Budyko, 1974; McDonald, 1962). These latter studies, remember, rely on simplifying assumptions of water vapor transport and precipitation formation, since water recycling in the real world cannot be measured directly. In some ways, the results of the tracer water model are more reliable, since the model is more complete. For example, only the tracer water model accounts explicitly for the formation of convective precipitation from recently evaporated, near-surface continental water vapor. On the other hand, the accuracy of the tracer water model results are necessarily constrained by the accuracy of the GCM climate itself and by the suitability of the GCM's internal parameterizations. The

parameterizations for moist convection and surface evaporation, for example, were (to an extent) tuned to produce reasonable total water transports and were not originally designed to transport specific tracer water masses.

The tracer water model constitutes one obvious way of using the GCM to examine the hydrological interconnections existing between land regions. The model results must be interpreted properly, though. Consider, for example, the simulation using the tracer source region situated in the Mississippi Valley. (See Section 4.1 and Figure 4-1.) The simulation results suggest that for the model climate, roughly 1 mm of the 30-day July precipitation in parts of New England is derived from evaporated Mississippi Valley water. Suppose now that to simulate a large-scale irrigation project in the Mississippi Valley, evaporation from the grid square was artificially increased by 10%. The simulation results do not imply that the contribution to the New England precipitation will increase to 1.1 mm/30-days. Changing the evaporation rate can change the model climate in unpredictable ways. This must be remembered when using the model to examine the effects of modifying an evaporative source region in the real world.

Again, although it is tempting to accept the model results as representative of nature, it must be remembered that they only reflect hydrological transport within the inherent model climate. The poor performance of the GISS GCM in reproducing realistic climate patterns at small spatial scales deserves special consideration; it would be wrong, for example, to infer more than a general direction and rough

characteristic travel distance from Figure 4-1 for water evaporating from the Mississippi Valley.

The fact that the computed hydrological transports are relevant to the GCM climate does, however, suggest that the tracer water model can serve potentially as a GCM diagnostic and thus can be used to improve the GCM. Consider, for example, the fact that the GISS GCM currently produces too much precipitation over Greenland. The "origins of precipitation" simulations discussed in Section 4.2 determined the evaporative sources of Central Greenland precipitation for each season. During the season in which simulated Greenland precipitation is especially excessive, the surface conditions in the important evaporative sources could be checked for accuracy and possibly corrected.

As the GISS GCM becomes further developed and improved, the tracer water model results will increasingly reflect the movement of specific evaporated water masses in the real world. Nevertheless, the tracer water model (and other models like it, such as that of Joussaume et al, 1986) at the present time constitutes the most comprehensive (and possibly most accurate) method available for quantifying the lateral scales of hydrological transport.

6.1.3 Future Research with the Tracer Water Model

Certain aspects of the tracer transport parameterizations could be improved. As discussed in Section 2.3.1, for example, the linear slopes scheme used in calculating tracer advection occasionally produces small negative tracer amounts. GISS personnel are currently developing a

"parabolic slopes scheme" that is inherently more accurate and prevents the formation of negative tracer. Other features that could be incorporated into the model include the rise of tracer condensate within moist convective plumes and a more appropriate interpretation of upward and downward tracer vapor flux at the ocean surface.

Sensitivity studies can be used to determine which features of the tracer water model are essential and which are probably unnecessary. One such study has already been performed. The tracer water model followed water evaporating from the Southeast Asia grid square under the assumption that during moist convective events, falling tracer condensate experiences complete equilibration with the tracer vapor in the surrounding air. As discussed in Section 2.3.2, the tracer water model standardly assumes that only half of the falling condensate equilibrates with the surrounding vapor. The tracer precipitation contours produced by the sensitivity simulation are essentially the same as those produced by the control simulation, suggesting that the modeling of such tracer equilibration may not be necessary.

The tracer water model simulation described in Section 4.3, which investigated the importance of evaporative source temperature on the deuterium content of Antarctic precipitation, demonstrates just one of the model's many possible applications in studies of water isotope geochemistry. Another water isotope study, currently being performed by Dr. Jean Jouzel (of CEN in Paris, France), Randal Koster, and GISS personnel, uses the tracer water model to evaluate various formulations for water isotope behavior present in the literature. A typical

sensitivity simulation might impose, for example, an alternative formulation for kinetic fractionation during moist convective events. If the formulation produces more realistic global fields of isotope concentration, it might be considered superior to the formulation that is standardly used. This not only would improve the structure of the tracer water model, but also it would improve understanding of the behavior of water isotopes in the real world. One of the sensitivity simulations was already described in Section 3.4.3. In this simulation, the slopes scheme for water isotope advection was replaced by an upstream weighting scheme, resulting in an excessive diffusion of isotopes to the poles.

6.2 Fractional Wetting of GCM Grid Squares

6.2.1 The 1-D Model Fractional Wetting Simulations

A one-dimensional model was constructed to study the response of the GCM climate to the imposition of a parameterization for fractional wetting during precipitation events. As discussed in Section 5.2, most of the formulations for the physical processes within the 1-D model were taken directly from the GISS GCM. The ability of the 1-D model to adequately predict GISS GCM sensitivities to changes in hydrological parameterization was confirmed in Section 5.3.

The 1-D model simulations discussed in Section 5.4.2 show that the imposition of fractional wetting causes large changes in seasonal precipitation, evaporation, and surface runoff rates. Changes in mean annual precipitation and evaporation are also seen. These changes are

related to changes in soil saturation, which is directly modified by fractional wetting in two different ways. First, increased precipitation depths cause increased surface runoff in winter, resulting in lower soil saturations. Second, increased spatial variations in soil moisture content seem to cause, under the GISS GCM formulation for soil moisture diffusion, increased downward diffusion rates in late summer.

The preliminary one-dimensional model simulations discussed in Section 5.4.3 tested a simple fractional wetting parameterization. In this parameterization, land surface conditions are homogenized at the beginning of every storm, and the land surface is then divided into only two sections, one of which is wetted. The simulation results, when compared to results of simulations using the more detailed parameterization, suggest that the simple parameterization may allow a GCM to more realistically account for the larger precipitation depths associated with subgrid wetting.

As discussed in Section 5.5, however, a complete analysis would require more work. It would be important to determine, for example, the sensitivity of the 1-D model climate to the imposition of fractional wetting when all model formulations are "retuned" to the fullest extent possible. Work should also be focused on improving the 1-D model's ability to simulate GCM behavior. For example, the 1-D model's present radiation scheme could be replaced by the scheme used in the GCM (see Lacis and Hansen, 1974). Also, it is sensible to choose a representative atmospheric column in the GISS GCM and to run a GCM simulation that stores, at every time step, the convergences of moisture and heat into

each layer of the column. These time series of moisture and heat convergences can then be applied to the 1-D model in place of the sinusoidal seasonal cycles of convergence calculated in Equations 5-1 and 5-2.

It would also be useful to study model response to fractional wetting under different boundary conditions. The imposed seasonal cycles of incoming solar radiation and of heat and moisture convergence in Section 5.4 were derived from cycles observed over continents at 43°N. Perhaps the model would respond differently if the imposed seasonal cycles represented a warmer and dryer climate, such as that typical over continents at 25°N.

One aspect of the 1-D model that will eventually require modification is the formulation of soil hydrology itself. The climate sensitivities to wetted fraction size presented in Section 5.4 are probably somewhat specific to the imposed GISS GCM soil hydrology. The GISS GCM, however, is presently evolving from the Model II version to a Model III version, which features a more complex soil hydrology. Model III will include, for example, a formulation for a vegetation canopy and a nonlinear relationship between soil saturation and evaporation. A 1-D model analysis that relates to the improved GCM will require an equivalent increase in the 1-D model's hydrological complexity.

Furthermore, the suggested "wet and dry fraction" parameterization for fractional wetting could be improved. As hinted in Section 5.5, it could be modified to allow the relative size of the fractions to vary with each storm. This is possible because the moisture and heat in the two sections are redistributed uniformly between them immediately before the storm

water falls. The assigned areal coverage of a storm might be based in part on the precipitation volume and in part on an assumed probability distribution; the distribution might employ different parameters for moist convective and nonconvective precipitation.

6.2.2 Other Potential Uses of the 1-D Model

Certainly a very important feature of the preliminary fractional wetting analysis presented in Chapter 5 is the development of the 1-D model. This report will close with some speculations on the 1-D model's further potential uses.

The 1-D model can perhaps play a unique role in developing the soil hydrology formulation scheduled for the Model III version of the GISS GCM. The 1-D model could initially be fitted, for example, with a proposed formulation, and in a series of sensitivity studies, individual components of the formulation could be removed, modified, or added. An insensitivity of model climate to an imposed change in a hydrological component may indicate the non-essential nature of that component.

When applied in this way, the 1-D model acts as a screening model. Presumably, components essential for the soil hydrology in the 1-D model will be essential for the hydrology in the GCM also. The approach allows the evaluation of various components of a proposed GCM soil hydrology without performing numerous costly GCM simulations.

The ability of the 1-D model to reproduce the GISS GCM climate sensitivity to runoff coefficient, as described in Section 5.3, suggests that perhaps the 1-D model can even be used to help "tune" the Model III

soil hydrology formulations. GCM simulations, however, would also be necessary in this phase of model development.

Potential uses of the 1-D model go beyond the study of GCM sensitivities. Since the 1-D model is designed to approximate the GISS GCM, and since the GISS GCM is designed to approximate the real world, it is perhaps possible to apply the 1-D model to real world hydrological problems. Irrigation development in the real world, for example, could perhaps be simulated by artificially increasing the soil saturation in the upper soil layer of the 1-D model during the growing season. The model would produce associated changes in evaporation and precipitation rates.

The 1-D model simulation results presented in Chapter 5 by themselves suggest sensitivities that might be inherent in real-world soil hydrology. Consider, for example, the fractional wetting simulation results presented in Figures 5-8 through 5-12. It would be difficult to infer much from the strong correlation between precipitation and evaporation sensitivities, since these are necessarily linked by the assignment of moisture convergence in the column. Notice, however, that a reduction in average soil saturation during the warmer part of the year is always associated with a reduction in evaporation rate, whereas near the winter solstice, differing soil saturations produce roughly the same evaporation rates. Perhaps soil moisture conditions can only affect climate during warm periods in the real world, also. The relatively minor sensitivity of surface temperature to changes in evaporation and precipitation rates is also significant; perhaps surface temperatures in the real world are essentially controlled only by the incoming radiation

and the convergences of moisture and heat in the overlying atmospheric column.

Assuredly, general circulation models are better equipped to study such real-world climate sensitivities. The 1-D model, however, does provide for quick and convenient preliminary studies.

REFERENCES

- Arakawa, A. and V. R. Lamb, Computational design of the basic dynamical processes of the UCLA general circulation model, in Methods in Computational Physics. Volume 17. General Circulation Models of the Atmosphere, edited by J. Chang, pp. 173-265, Academic Press, New York, N.Y., 1977.
- Aristarain, A., J. Jouzel and M. Pourchet, Past Antarctic Peninsula climate (1850-1980) deduced from an ice core isotope record, Climatic Change, 8, 69-89, 1986.
- Baumgartner, A., and E. Reichel, Die Weltwasserbilang, 179 pp., Oldenbourg Verlag, München, Germany, 1975.
- Benton, G. S., R. T. Blackburn, and V. O. Snead, The role of the atmosphere in the hydrologic cycle, Transactions, American Geophysical Union, 31, 61-73, 1950.
- Broecker, W. S., T.-H. Peng and G. Ostlund, The distribution of bomb tritium in the ocean, J. Geophys. Res., 91, 14331-14344, 1986.
- Budyko, M., Climate and Life, English translation edited by D. H. Miller, 508 pp., Academic Press, New York, 1974.
- Chang, J. (Ed.), Methods in Computational Physics. Volume 17. General Circulation Models of the Atmosphere, 337 pp., Academic Press, New York, 1977.
- Craig, H., Standard for reporting concentrations of deuterium and oxygen-18 in natural waters, Science, 133, 1833-1834, 1961.
- Craig, H., and L. I. Gordon, Deuterium and oxygen-18 variations in the ocean and the marine atmosphere, in Stable Isotopes in Oceanographic Studies and Paleotemperatures, Spoleto Conference Proceedings, E. Tongiorgi pp. 9-130, 1965.
- Craig and Lal, "The vapor pressure of HTO", unpublished (?) manuscript.
- CRC, Handbook of Chemistry and Physics, 56th Edition, CRC Press, Cleveland, Ohio, 1975.
- Dansgaard, W., Stable isotopes in precipitation, Tellus, 16, 436-468, 1964.
- Eagleson, P. S., Dynamic Hydrology, 462 pp., McGraw-Hill, Inc., New York, 1970.

- Eagleson, P. S., Climate, Soil, and the Water Balance: A Framework for Their Analytical Coupling. The Tenth John R. Freeman Memorial Lectures of the Boston Society of Civil Engineers, 1977.
- Eagleson, P. S., Climate, soil and vegetation, (7 parts), Water Resources Research, 14, 705-776, 1978.
- Eagleson, P. S., N. M. Fennessey, W. Qinliang and I. Rodriguez-Iturbe, Application of spatial Poisson models to air mass thunderstorm rainfall, J. Geophys Res., 92(D8), 9661-9678, 1987.
- Eagleson, P. S. and R. F. Larivière, The scale of oceanic influence on continental precipitation, IASH Proc. UNESCO Symposium on World Water Balance, 34-39, Reading, England, July 1970.
- Eagleson, P. S., and Q. Wang, Moments of Catchment Storm Area, Water Resources Research, 21, 1185-1194, 1985.
- Ehhalt, D. H., Vertical profiles and transport of HTO in the troposphere, J. Geophys. Res., 76, 7351-7367, 1971.
- Federer, B., N. Brichet, and J. Jouzel, Stable isotopes in hailstones. Part I. The isotopic cloud model, J. Atmos. Sci., 39(b), 1323-1335, 1982.
- Fowler, W. B., and J. D. Helvey, Effect of large-scale irrigation on climate in the Columbia Basin, Science, 184, 121-127, 1974.
- Fowler, W. B. and J. D. Helvey, (no title) Science, 188, 281, 1975.
- Hansen, J., A. Lacis, D. Rind, G. Russell, P. Stone, I. Fung, R. Ruedy, and J. Lerner, Climate sensitivity: Analysis of feedback mechanisms, in Geophysical Monographs 29, Maurice Ewing Symposium. Vol. 5, pp. 130-163, 1984.
- Hansen, J., G. Russell, D. Rind, P. Stone, A. Lacis, S. Lebedeff, R. Ruedy, and L. Travis, Efficient three-dimensional global models for climate studies: Models I and II, Monthly Weather Review, 111, pp. 609-662, 1983.
- Held, I. M., D. I. Linder, and M. J. Suarez, Albedo feedback, the meridional structure of the effective heat diffusivity, and climatic sensitivity: Results from dynamic and diffusive models, Journal of the Atmospheric Sciences, 38, 1911-1927, 1981.
- Held, I. M. and M. J. Suarez, A two-level primitive equation atmospheric model designed for climatic sensitivity experiments, Journal of the Atmospheric Sciences, 35, 206-229, 1978.

- Held, I. M. and M. J. Suarez, Simple albedo feedback models of the icecaps, Tellus, 26, pp. 613-628, 1974.
- Holzmann, B., Sources for moisture for precipitation in the U.S., U.S.D.A. Technical Bulletin 589, 1937.
- Horton, R. E., Hydrologic interrelations between lands and oceans, Trans. Amer. Geophys. Union, 24, 753-764, 1943.
- Houze, R. A., Jr., and A. K. Betts, Convection in GATE, Reviews of Geophysics and Space Physics, 19, 541-576, 1981.
- IAEA, Statistical treatment of environmental isotope data in precipitation, Technical Report Series, 206, 256 pp, 1981.
- Jacob, D., M. Prather, S. Wofsy, and M. McElroy, Atmospheric Distribution of ^{85}Kr simulated with a general circulation model. Submitted to Journal of Geophysical Research, 1987.
- Jaeger, L, Monatskarten des Niederschlags für die ganze Erde, Ber. Dt. Wetterd., 18 (139), 38 pp., 1976.
- Joussaume, S., J. Jouzel and R. Sadourny, Water isotope cycles in the atmosphere: first simulation using a general circulation model, Nature, 311, 24-29, 1984a.
- Joussaume, S., R. Sadourny, and J. Jouzel, Simulation of the HDO and H_2^{18}O cycles in an atmospheric general circulation model, Annals of Glaciology, 5, 208-210, 1984b.
- Joussaume, S., R. Sadourny and C. Vignal, Origin of precipitating water in a numerical simulation of the July climate, Ocean-Air Interactions, 1, 43-56, 1986.
- Jouzel, J. and L. Merlivat, Deuterium and Oxygen 18 in precipitation, Modeling of the isotopic effects during snow formation, Journal of Geophysical Research, 89, 11749-11757, 1984..
- Jouzel, J., G. Russell, R. Suozzo, R. Koster, J. W. C. White, and W. S. Broecker, Simulations of the HDO and H_2^{18}O atmospheric cycles using the NASA/GISS general circulation model: The seasonal cycle for present day conditions, J. Geophys. Res., 92, 14739-14760, 1987.
- Koster, R., J. Jouzel, R. Suozzo, G. Russell, W. Broecker, D. Rind, and P. S. Eagleson, Global sources of local precipitation as determined by the NASA/GISS GCM, Geophysical Research Letters, 13, 121-124, 1986.

- Koster, R., W. S. Broecker, J. Jouzel, R. Suozzo, G. Russell, D. Rind, and J. W. C. White, The global geochemistry of bomb-produced tritium; general circulation models compared to the real world, to be submitted to Journal of Geophysical Research.
- Lacis, A., and J. Hansen, A parameterization for the absorption of solar radiation in the earth's atmosphere, J. Atmos. Sci., 31, 118-133, 1974.
- Lettau, H., K. Lettau, and L. C. B. Molion, Amazonia's hydrologic cycle and the role of atmospheric recycling in assessing deforestation effects, Monthly Weather Review, 107, 227-238, 1979.
- Libby, W. F., Tritium in hydrology and meteorology, in Researches in Geochemistry, edited by P. H. Abelson, pp. 151-168, John Wiley and Sons, New York, 1959.
- Lorius, C., J. Jouzel, C. Ritz, L. Merlivat, N. I. Barkov, Y. S. Korotkevitch, and V. M. Kotlyakov, A 150,000 year climatic record from Antarctic ice, Nature, 316, 591-596, 1985.
- L'vovich, M., World Water Resources and Their Future, English translation, U. S. Depart. of Commerce, Washington, D.C., 414 pp., 1980.
- Majoube, M., Fractionnement en oxygène 18 et en deuterium entre l'eau et sa vapeur, J. Chim. Phys., 10, 1423-1436, 1971a.
- Majoube, M., Fractionnement en oxygène 18 et en deuterium entre la glace et la vapeur d'eau, J. Chim. Phys., 68, 625-636, 1971b.
- Mason, B. J., The physics of clouds, in Oxford Monographs of Meteorology, P. A. Sheppard, ed., Clarendon Press, 1971.
- McDonald, J., The evaporation-precipitation fallacy, Weather, 17, 168-177, 1962.
- Merlivat, L., Molecular diffusivities of $H_2^{16}O$, $HD^{16}O$, and $H_2^{18}O$ in gases, J. Chem. Phys., 69, 2864-2871, 1978.
- Merlivat, L., and J. Jouzel, Global climatic interpretation of the deuterium-oxygen 18 relationship for precipitation, Journal of Geophysical Research, 84, 5029-5033, 1979.
- Merlivat, L. and G. Nief, Fractionnement isotopique lors des changements d'état solide-vapeur et liquide-vapeur de l'eau à des températures inférieures à 0°C, Tellus, 19, 122-127, 1967.

- National Resources Board, Report of the Water Planning Committee, pp. 253-388, 1934.
- Oort, A. H., The observed annual cycle in the meridional transport of atmospheric energy, Journal of the Atmospheric Sciences, 28, 325-339, 1971.
- Oort, A. H., Global Atmospheric Circulation Statistics, 1958-1973, NOAA Professional Paper 14, Geophysical Fluid Dynamics Laboratory, Princeton, N.J., 1983.
- Peixoto, J. P. and A. H. Oort, The atmospheric branch of the hydrological cycle and climate, in Variations in the Global Water Budget, edited by Street-Perrott, Beran, and Ratcliffe, D. Reidel Publ. Co., Dordrecht, 1983.
- Prupaccher, H. R. and J. D. Klett, Microphysics of Clouds and Precipitation, Reidel Publ. Co., 1978.
- Ramanathan, V., The role of ocean-atmosphere interactions in the CO₂ climate problem, J. Atmos. Sci., 38, 918-930, 1981.
- Randall, D. A., Monthly and seasonal simulations with the GLAS Climate Model, Proceedings of the Workshop on Intercomparison of Large-Scale Models used for Extended Range Forecasts of the European Center for Medium Range Weather Forecasts, 107-166, Reading, England, 1982.
- Rasmusson, E. M., A study of the hydrology of Eastern North America using atmospheric vapor flux data, Monthly Weather Review, 99, 119-135, 1971.
- Rind, D., The influence of ground moisture conditions in North America on summer climate as modeled in the GISS GCM, Monthly Weather Review, 110, 1487-1494, 1982.
- Rind, D., The influence of vegetation on the hydrological cycle in a global climate model, in Geophysical Monograph, 29, Maurice Ewing Vol. 5, 73-91, 1984.
- Russell, G. L. and J. A. Lerner, A new finite-differencing scheme for the tracer transport equation, J. App. Met., 20, 1483-1498, 1981.
- Sadourny, R. and K. Laval, January and July performance of the LMD general circulation model, in New Perspectives in Climate Modeling, edited by A. Berger and C. Nicolis, Elsevier, pp. 173-197, 1984.
- Salati, E., A. Dall'Olio, E. Matsui, and J. R. Gat, Recycling of water in the Amazon Basin: An isotopic study, Water Resources Research, 15, 1250-1258, 1979.

- Salati, E. and P. B. Vose, Amazon Basin: A system in equilibrium, Science, 225, 129-138, 1984.
- Schickedanz, P. T. and W. C. Ackermann, Influence of irrigation on precipitation in semi-arid climates, in Arid Land Irrigation in Developing Countries: Environmental Problems and Effects, E. B. Worthington, ed., 185-196, Pergamon Press, Oxford, 1977.
- Sellers, P., Y. Mintz, Y. Sud, and A. Dalcher, A simple biosphere model (SiB) for use within general circulation models, J. Atmos. Sci., 43, 505-531, 1986.
- Shukla, J., and Y. Mintz, Influence of land-surface evapotranspiration on the earth's climate, Science, 215, 1498-1501, 1982.
- Stallard, R. F. and J. M. Edmond, Geochemistry of the Amazon. 1. Precipitation chemistry and the marine contribution to the dissolved load at the time of peak discharge, J. Geophys. Res., 86, 9844-9858, 1981.
- Stewart, M. K., Stable isotope fractionation due to evaporation and isotopic exchange of falling waterdrops: applications to atmospheric processes and evaporation of lakes, J. Geophys. Res., 80, 1133-1146, 1975.
- Stidd, C. K., Local moisture and precipitation, Preprint No. 45a, Desert Research Institute, University of Nevada, 34 pp., 1968.
- Stidd, C. K., Irrigation increases rainfall?, Science, 188, 279-280, 1975.
- Sud, Y. C. and M. J. Fennessy, Influence of evaporation in semi-arid regions on the July circulation: a numerical study, Journal of Climatology, 4, 383-398, 1984.
- Taylor, C. B., The vertical variations of isotopic concentrations of tropospheric water vapor over continental Europe, and their relationship to tropospheric structure, Rep. INS-R-107, Institute of Nuclear Sciences, Lower Hutt, New Zealand, 1972.
- von Loon, H. (ed.), World Survey of Climatology. Volume 15, Elsevier, Amsterdam, 1984.
- Walker, J. and P. R. Rowntree, The effect of soil moisture on circulation and rainfall in a tropical model, Quart. J. R. Met. Soc., 103, p. 29-46, 1977.
- Washington, W. M. and D. L. Williamson, A description of the NCAR global circulation models, in Methods in Computational Physics, Volume 17. General Circulation Models of the Atmosphere, edited by J. Chang, pp. 111-172, Academic Press, New York, 1977.

Weiss, W., R. Roether and E. Dreisigacker, Tritium in the North Atlantic Ocean: inventory, input and transfer into the deep water, in: The Behaviour of Tritium in the Environment, International Atomic Energy Agency, Vienna, pp. 315-336, 1979.

Weiss, W. and W. Roether, The rates of tritium input to the world oceans, Earth and Planetary Science Letters, 49, 435-446, 1980.

Yeh, T.-C., R. T. Wetherald, and S. Manabe, The effect of soil moisture on the short-term climate and hydrology change--a numerical experiment, Monthly Weather Review, 112, 474-490, 1984.

Appendix A

Processing the GISS GCM and GFDL Vapor Flux Data

Values of time-averaged vertically integrated vapor flux were determined during a two year GISS GCM simulation for each 8° X 10° grid square shown in Figure 2-1. A corresponding data set was derived from ten years of observations provided by the Geophysical Fluid Dynamic Laboratory (GFDL) of NOAA at Princeton University (Oort, 1983). The present section describes the processing required to bring the two data sets to a consistent form.

A.1 The GISS GCM Data

Figure A-1 will help describe the GCM water transport computations. In the figure, ΔP_{ijl} is the pressure difference between the top and the bottom of the grid box at column i , row j , and level l , q_{ijl} is the specific humidity there, and u_{ijl} and v_{ijl} represent the local zonal and meridional velocities, respectively. Notice that the pressure difference and the specific humidity are defined at the center of the box, whereas the velocities are defined at the southeast corner. The GCM produces values for these quantities at every time step and computes Q_λ and Q_ϕ as:

$$Q_{\lambda ij} = \frac{1}{n_o g} \sum_{v=1}^{n_o} \sum_l \left\{ \left(\frac{\Delta P_{ijl} + \Delta P_{i+1,j,l}}{2} \right) \cdot \right.$$

(A-1)

$$\left. \cdot \left(\frac{u_{ijl} + u_{i,j+1,l}}{2} \right) \cdot \left(\frac{q_{ijl} + q_{i+1,j,l}}{2} \right) \right\}$$

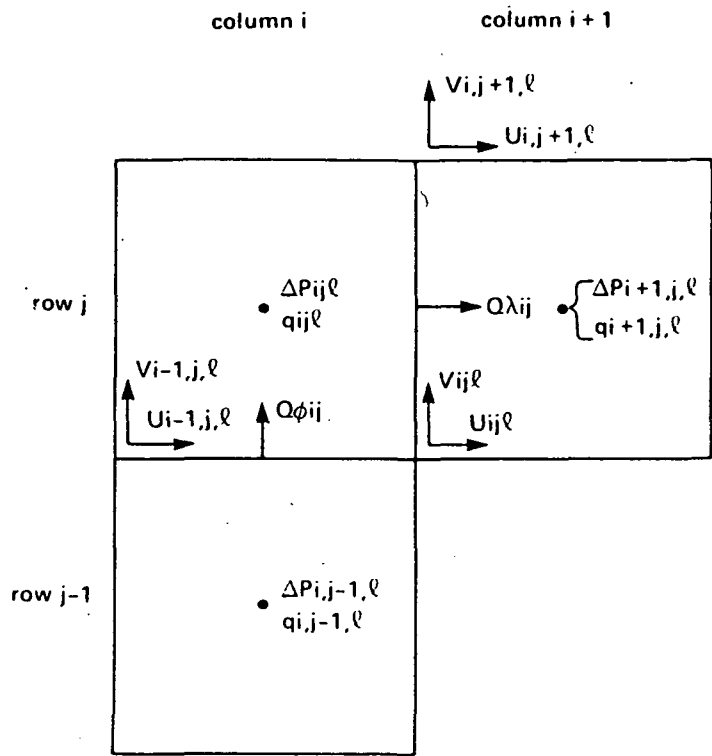


Figure A-1 GCM variables used in calculations of vertically-integrated horizontal water vapor transports.

$$Q_{\phi ij} = \frac{1}{ng_0} \sum_{n=1}^{n_0} \sum_{\ell} \left\{ \left(\frac{\Delta P_{i,j-1,\ell} + \Delta P_{ij\ell}}{2} \right) \cdot \left(\frac{v_{i-1,j,\ell} + v_{ij\ell}}{2} \right) \cdot \left(\frac{q_{i,j-1,\ell} + q_{ij\ell}}{2} \right) \right\}$$

(A-2)

Thus, $Q_{\lambda ij}$ is defined at the center of the eastern side of grid square i,j , with eastward flow being positive, and $Q_{\phi ij}$ is defined at the center of the southern side, with northward flow being positive. Accumulating the water transports n_0 times during the season and then dividing by n_0 produces the desired time average.

The GISS GCM vapor flux data was produced during the final two years of Model Run 882. A small error in the storage of the meridional vapor flux was corrected.

A.2 The GFDL Data

The observed data required a substantial amount of processing to be put into the same form as the GCM data. GFDL performed the first step; they transformed several years of wind and vapor measurements at irregularly-spaced stations into a convenient gridded form before offering the data for general use. Thus, the initial data consisted of \bar{q} , \bar{u} , \bar{v} , $\overline{q'u'}$, and $\overline{q'v'}$ values for eleven pressure levels at each node of a fine horizontal grid, with $\overline{q'u'}$ and $\overline{q'v'}$ being the transient horizontal eddy vapor fluxes in the zonal and meridional directions, respectively. The overbars indicate seasonal means.

The next step in processing the data involved transforming the values over GFDL's finer grid to values over the grid in Figure 2-1. This was

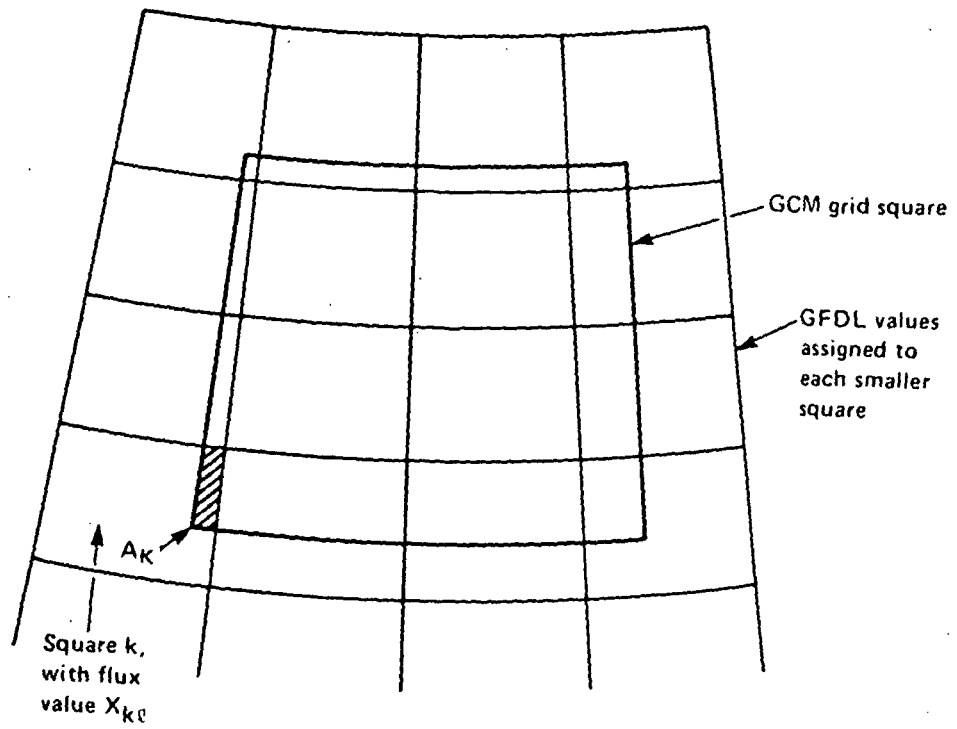
achieved through simple area-weighted averaging, as illustrated in Figure A-2. The larger square in the figure represents a GCM-size grid square, and GFDL vapor flux values are provided in each of the smaller squares. If A_k represents the area of intersection of the large square and the k th smaller square, and if $X_{k\ell}$ represents the observed value of quantity X (at some level ℓ) over the k th smaller square, then the assigned coarse grid value of X (at level ℓ) is calculated as

$$X_{\ell} = \frac{\sum_k X_{k\ell} A_k}{\sum_k A_k} \quad (\text{A-3})$$

The determination of the total water transport field naturally required vertical integration over the pressure levels. The gridded GFDL data set used in this study included values at such pressure levels as 1000 mb and 950 mb for all grid squares and thus contained spurious data for grid squares with low surface pressure. It was therefore deemed necessary, before integrating over pressure, to assign typical values of surface pressure to the lower limit of integration.

Typical values of surface pressure were obtained for each season from a GISS GCM simulation. Time-averaged equivalent sea level pressures P_{SL} were stored during Model Run 882; over continents, these are surface pressures P_S corrected for topographic height Z :

$$P_{SL} = P_S \left(1 + \frac{\beta Z}{T_G} \right)^{g/R\beta} \quad (\text{A-4})$$



$$X_{\ell} \text{ for GCM grid square} = \frac{\sum_k X_{k\ell} A_k}{\sum_k A_k}$$

Figure A-2 Area weighting used in processing GFDL data.

In the equation, T_G is the surface temperature, g is gravitational acceleration, R is the gas constant, and β is an assumed uniform vertical temperature gradient, assigned the value -0.0065 °K/m. The global distribution of surface pressure is thus obtained directly from the stored distribution of equivalent sea level pressure. Surface pressure contours constructed from the GCM data sets roughly follow the continental topography and do not show great seasonal variation.

The vertical integrals were estimated as follows:

$$Q_{\lambda ij} = \frac{1}{g} \sum_{\lambda=1}^{11} (\bar{q}_{ij\lambda} \bar{u}_{ij\lambda} + \overline{q'u'}_{ij\lambda}) \Delta P_{ij\lambda} \quad (A-5)$$

$$Q_{\phi ij} = \frac{1}{g} \sum_{\lambda=1}^{11} (\bar{q}_{ij\lambda} \bar{v}_{ij\lambda} + \overline{q'v'}_{ij\lambda}) \Delta P_{ij\lambda} \quad (A-6)$$

The ΔP 's are pressure intervals associated with measurement pressure levels; a measurement at 300 mb, for example, was assigned to all points between 350 mb and 250 mb, and ΔP for this level was thus 100 mb. (It should be kept in mind that the roughly exponential form of vertical specific humidity profiles in nature may limit the accuracy of assigning constant specific humidities throughout a pressure interval.) The grid square's surface pressure determined the magnitudes of ΔP for the lowest measurement levels.

The resulting values of Q_λ and Q_ϕ were defined in the centers of the $8^\circ \times 10^\circ$ grid squares. A slightly revised set of values was then created by simple interpolation between the values in adjacent grid squares; these new values are completely consistent with the corresponding GCM values, which are defined on the sides of squares.

Appendix B

Supplemental Flux Data From Tritium Simulations

Table 3-3 presented flux data for certain tritium sensitivity simulations. The corresponding data for the remainder of the tritium simulations is presented below. See Section 3.3.2(a) for an explanation of the table.

Median Lat. °N	Water Fluxes kg/m ²			Tritium/Hydrogen Ref to 51°N Ocean			Tritium Fluxes % of total		
	Cont. Precip.	Ocean Precip.	Ocean Vapor	Cont. Precip.	Ocean Precip.	Ocean Vapor	Cont. Precip.	Ocean Precip.	Ocean Vapor
	Simulation T4			Injection Over Continents 51°N					
74	41	38	110	2.23	1.26	0.21	7.22	1.25	0.62
66	69	56	119	1.59	1.16	0.18	13.48	2.25	0.75
59	68	55	138	1.28	1.42	0.23	10.78	6.43	2.66
51	80	59	114	1.01	1.00	0.27	11.63	6.17	3.21
43	87	55	151	0.79	0.54	0.18	9.59	4.44	4.11
35	68	86	273	0.33	0.14	0.09	3.09	2.28	4.33
27	68	115	231	0.23	0.03	0.02	2.22	0.60	1.27
20	106	112	258	0.08	0.00	0.01	1.01	0.08	0.52
TOTAL							59.02	23.51	17.47
	Simulation T5			Injection Over Oceans 51°N					
74	41	38	110	1.59	1.66	0.26	6.77	2.16	1.01
66	69	56	119	1.06	1.26	0.23	11.74	3.20	1.21
59	68	55	138	0.74	0.99	0.24	8.18	5.88	3.54
51	80	59	114	0.61	1.00	0.34	9.22	8.10	5.32
43	87	55	151	0.30	0.45	0.26	4.68	4.83	7.82
35	68	86	273	0.14	0.11	0.12	1.77	2.27	7.43
27	68	115	231	0.08	0.03	0.03	1.03	0.80	2.06
20	106	112	258	0.04	0.00	0.01	0.71	-0.02	0.28
TOTAL							44.10	27.22	28.68
	Simulation T7			Injection just above ocean 30°N					
74	41	38	110	0.18	0.31	0.15	0.53	0.29	0.41
66	69	56	119	0.15	0.52	0.21	1.18	0.93	0.80
59	68	55	138	0.13	0.58	0.21	0.98	2.45	2.18
51	80	59	114	0.12	1.00	0.50	1.29	5.71	5.48
43	87	55	151	0.11	0.99	0.61	1.23	7.58	12.68
35	68	86	273	0.05	1.01	0.72	0.46	14.87	33.86
27	68	115	231	0.01	0.07	0.12	0.06	1.58	5.14
20	106	112	258	0.01	0.00	0.01	0.07	0.00	0.25
TOTAL							5.80	33.41	60.79
	Simulation T15			Upstream weighting for tracer transport*					
74	40	44	108	1.57	1.34	0.23	4.29	1.34	0.56
66	65	57	144	1.28	1.26	0.17	8.79	2.15	0.71
59	65	57	137	1.10	1.09	0.18	7.56	4.41	1.78
51	91	49	102	0.92	1.00	0.26	10.43	4.40	2.38
43	93	64	149	0.69	0.69	0.24	7.65	5.73	4.67
35	75	79	249	0.42	0.36	0.15	3.75	4.58	6.12
27	69	105	224	0.32	0.19	0.10	2.70	3.55	4.22
20	98	120	239	0.19	0.10	0.07	1.86	2.64	3.71
TOTAL							47.04	28.80	24.16

Median Lat. °N	Water Fluxes kg/m ²			Tritium/Hydrogen Ref to 51°N Ocean			Tritium Fluxes % of total		
	Cont. Precip.	Ocean Precip.	Ocean Vapor	Cont. Precip.	Ocean Precip.	Ocean Vapor	Cont. Precip.	Ocean Precip.	Ocean Vapor
	Simulation T16			Tritium mixed in lowest 3 layers					
74	40	44	108	1.18	0.79	0.16	5.37	1.31	0.64
66	65	57	144	0.98	0.92	0.13	11.21	2.62	0.92
59	65	57	137	0.79	0.94	0.20	9.03	6.33	3.16
51	91	49	102	0.58	1.00	0.33	10.92	7.30	5.00
43	93	64	149	0.37	0.53	0.22	6.81	7.24	7.08
35	75	79	249	0.14	0.14	0.08	2.09	2.93	5.03
27	69	105	224	0.11	0.02	0.03	1.50	0.58	1.90
20	98	120	239	0.02	0.01	0.01	0.28	0.26	0.49
TOTAL							47.20	28.58	24.22
	Simulation T19			Tritium mixed into surface boundary layer					
74	41	38	110	1.61	1.12	0.33	5.63	1.20	1.04
66	69	56	119	1.13	0.92	0.36	10.26	1.92	1.60
59	68	55	138	0.93	1.12	0.45	8.38	5.50	5.57
51	80	59	114	0.73	1.00	0.47	9.09	6.65	6.01
43	87	55	151	0.55	0.60	0.33	7.12	5.29	8.06
35	68	86	273	0.29	0.15	0.12	2.89	2.63	6.41
27	68	115	231	0.16	0.04	0.03	1.63	0.92	1.47
20	106	112	258	0.05	0.00	0.00	0.62	0.10	0.01
TOTAL							45.62	24.20	30.18
	Simulation T20			Total equilibration in moist convection					
74	41	38	110	1.60	1.15	0.18	6.24	1.37	0.63
66	69	56	119	1.14	1.00	0.16	11.65	2.33	0.78
59	68	55	138	0.91	1.21	0.23	9.25	6.64	3.11
51	80	59	114	0.72	1.00	0.31	9.97	7.43	4.36
43	87	55	151	0.52	0.55	0.22	7.62	5.43	6.08
35	68	86	273	0.28	0.14	0.09	3.09	2.66	5.82
27	68	115	231	0.16	0.03	0.03	1.89	0.81	1.73
20	106	112	258	0.05	0.00	0.01	0.77	0.00	0.33
TOTAL							50.49	26.68	22.83
	Simulation T21			No equilibration in moist convection					
74	41	38	110	1.37	1.03	0.14	6.49	1.50	0.60
66	69	56	119	0.91	0.86	0.13	11.26	2.44	0.77
59	68	55	138	0.72	1.01	0.17	8.84	6.74	2.92
51	80	59	114	0.53	1.00	0.23	8.95	9.04	4.05
43	87	55	151	0.40	0.61	0.17	7.06	7.34	5.71
35	68	86	273	0.21	0.11	0.08	2.89	2.47	5.78
27	68	115	231	0.12	0.02	0.02	1.76	0.53	1.80
20	106	112	258	0.04	0.00	0.01	0.65	0.03	0.38
TOTAL							47.89	30.09	22.02
	Simulation T22			Down drafts in moist convection					
74	48	40	86	1.29	1.01	0.17	5.36	1.17	0.39
66	63	55	131	1.34	0.94	0.10	11.19	1.93	0.49
59	74	66	140	1.41	1.20	0.14	13.77	6.98	1.83
51	75	59	120	1.17	1.00	0.19	13.81	6.68	2.46
43	66	50	162	0.65	0.52	0.15	6.44	4.23	3.94
35	127	87	244	0.31	0.23	0.07	5.92	3.97	3.45
27	71	63	326	0.23	0.02	0.02	2.49	0.26	1.32
20	130	63	340	0.05	0.01	0.01	0.88	0.25	0.80
TOTAL							59.86	25.47	14.67

Median Lat. °N	Water Fluxes kg/m ²			Tritium/Hydrogen Ref to 51°N Ocean			Tritium Fluxes % of total		
	Cont. Precip.	Ocean Precip.	Ocean Vapor	Cont. Precip.	Ocean Precip.	Ocean Vapor	Cont. Precip.	Ocean Precip.	Ocean Vapor
	Simulation T23			Moist convective plume size reduced					
74	41	37	96	1.59	1.05	0.18	7.47	1.46	0.62
66	52	54	98	1.05	0.86	0.14	9.62	2.29	0.71
59	66	64	176	0.82	1.15	0.14	9.44	8.67	2.90
51	74	62	140	0.51	1.00	0.21	7.83	9.19	4.36
43	83	48	174	0.39	0.52	0.15	6.45	5.30	5.43
35	100	92	338	0.19	0.16	0.07	3.77	3.80	5.81
27	61	102	239	0.12	0.02	0.02	1.50	0.51	1.45
20	108	106	258	0.04	0.00	0.01	0.68	0.17	0.58
TOTAL							46.76	31.38	21.86
	Simulation T24			Spurious precip. formed above 600 mb removed					
74	40	44	108	1.02	0.73	0.14	4.61	1.22	0.58
66	65	57	144	0.94	0.85	0.12	10.74	2.40	0.85
59	65	57	137	0.77	0.87	0.18	8.77	5.83	2.96
51	91	49	102	0.62	1.00	0.33	11.61	7.30	4.93
43	93	64	149	0.37	0.64	0.21	6.86	8.81	6.70
35	75	79	249	0.16	0.18	0.08	2.35	3.85	5.45
27	69	105	224	0.10	0.02	0.02	1.36	0.59	1.33
20	98	120	239	0.02	0.00	0.01	0.29	0.19	0.44
TOTAL							46.58	30.18	23.24
	Simulation T25			Control run under winter conditions					
74	34	104	0	3.54	1.63	-	6.74	1.40	0.53
66	40	123	206	3.42	1.43	0.40	11.29	2.26	1.07
59	39	98	151	3.48	1.51	0.39	10.92	6.35	2.58
51	40	102	181	3.47	1.00	0.28	12.31	6.36	3.08
43	56	113	216	1.60	0.58	0.19	7.56	5.96	3.76
35	81	108	294	0.94	0.20	0.11	6.35	2.46	3.66
27	63	93	365	0.16	0.07	0.06	0.89	0.82	2.49
20	53	115	402	0.06	0.00	0.01	0.23	0.03	0.92
TOTAL							56.27	25.63	18.09

*The water fluxes in Simulations T15, T16, and T24 are slightly different from those in Simulation T1, even though the imposed changes in these simulations affected only tritium transport. The changes in the water fluxes are due to minor changes in the computer system between simulations and should not affect the inherent model climate or the resulting tritium input ratio.

Appendix C

Approximations Applied in the 1-D Model Radiation Algorithms

The 1-D model uses the algorithms provided by Held, Linder, and Suarez (1981) and Held and Suarez (1978) to compute the net radiative heating and cooling in each atmospheric layer. The use of the algorithms requires certain approximations, however, since they assume a simpler atmospheric structure than that produced by the 1-D model.

C.1 Form of the Vertical Temperature Profile

Both the shortwave and the longwave radiation algorithms assume a vertical temperature profile that is linear in $\log(P_s/P)$, where P_s is the surface pressure and P is the pressure at a given atmospheric level. For both algorithms, the profile must be specified by providing model-generated temperatures at 250 mb and 750 mb.

To make use of the radiation algorithms, then, the more complicated vertical temperature profile produced by the 1-D model is approximated by a linear profile. At each time step of a simulation, the 1-D model produces a temperature value at 206 mb (layer 7) and 329 mb (layer 6); a value at 250 mb is estimated by interpolating between these two temperatures, assuming a locally linear relationship between temperature and $\log(P_s/P)$. A 1-D model temperature at 750 mb is estimated in the same way. The estimated 250 mb and 750 mb temperatures are assumed to

define the approximate linear temperature profile in the 1-D model atmosphere. They are fed directly into the radiation algorithms.

C.2 Solar Radiation

As input, the solar radiation algorithm requires the 250 mb and 750 mb temperatures and the zenith angle. As output, the algorithm estimates the fraction of incoming solar radiation that is reflected to space by molecular scattering, the fraction that reaches the 500 mb level, the fraction reflected to space by clouds, and the fraction reaching the ground surface. The algorithm also computes the fraction of ground-reflected radiation that is absorbed in the lower atmosphere. Combining these terms allows one to calculate the net shortwave heating of the ground surface and of the atmosphere above and below 500 mb.

To distribute the shortwave heating of the atmosphere among the atmospheric layers, the layers are divided into three sets. The heat designated for the atmosphere below the 500 mb level is distributed among those layers with average pressures above 500 mb, under an assumed uniform heating per unit air mass. The heat designated for the atmosphere above the 500 mb level is distributed among those layers with average pressures between 200 mb and 500 mb, using a different uniform heating per unit air mass. Layers with average pressures below 200 mb do not receive solar heating.

For simplicity, the 1-D model always uses the algorithm coefficients provided for a zenith angle cosine of 0.4. This should cause no major problem; the coefficients provided for various zenith angle cosines show

only slight variation. For example, given a dry adiabatic lapse rate in the atmosphere and a surface temperature of 300°K, the fraction of solar radiation reaching the ground surface varies from .481 at a zenith angle cosine of 0.1 to .525 at a zenith angle cosine of 0.7.

C.3 Longwave Radiation

In addition to the temperatures at 250 mb and 750 mb, the longwave radiation algorithm requires the model-generated temperature at the earth's surface. As output, the algorithm produces the outgoing longwave radiation flux at the top of the atmosphere, the net upward longwave radiation flux at 500 mb, and the downward longwave radiation flux at the earth's surface. Coefficients for the algorithm are provided by both Held and Suarez (1978) and Held, Linder and Suarez (1981); the 1-D model employs those of the latter publication.

The downward longwave radiative flux at the earth's surface can be combined with the upward longwave radiative flux there (see Equation 5-15) to produce a net upward flux at the surface. Thus, with the longwave radiation algorithm, a net upward longwave radiation flux is computed at the earth's surface, at 500 mb, and at the top of the atmosphere. The net upward fluxes at the top and bottom of each atmospheric layer in the 1-D model are computed by interpolation on these values. The interpolation assumes that the net upward flux between the surface and 500 mb varies linearly with $\log (P_g/P)$, as does the net upward flux between 500 mb and 200 mb. Above 200 mb, the upward flux at each level is assumed to equal the flux out the top of the atmosphere.

Suppose $H_{\lambda w\text{-bot}}(\lambda)$ is the interpolated net upward longwave radiation flux at the lower boundary of layer λ , and suppose $H_{\lambda w\text{-top}}(\lambda)$ is the interpolated flux at the top boundary. The longwave heating of layer λ during a time step Δt is calculated as

$$T(\lambda)_{\text{new}} = T_{\text{old}} + (H_{\lambda w\text{-bot}}(\lambda) - H_{\lambda w\text{-top}}(\lambda))/C(\lambda) \quad (\text{C-1})$$

where $C(\lambda)$ is the heat capacity of the layer.

C.4 Adjustment of Eddy Temperatures

Naturally, the vertical temperature profiles generated by the 1-D model will not be as simple as the linear profiles assumed in the shortwave and longwave radiation algorithms. Suppose the temperature $T(\lambda)$ at level λ , for example, was higher than the temperature $T_{\text{prof}}(\lambda)$ estimated from the linear fit to the temperatures at 250 mb and 750 mb. One might expect that this level would radiate more and cool faster than predicted by the longwave radiation algorithm. To account for this, the difference between the actual and the linear profile temperature at level λ is considered to be an eddy temperature $T_{\text{eddy}}(\lambda)$, to be damped linearly at every time step according to

$$T(\lambda)_{\text{new}} = T(\lambda)_{\text{old}} - T_{\text{eddy}}(\lambda) \cdot \frac{\Delta t}{\tau_{\text{eddy}}} \quad (\text{C-2})$$

where

$$T_{\text{eddy}}(\lambda) = T(\lambda)_{\text{old}} - T_{\text{prof}}(\lambda) \quad (\text{C-3})$$

The parameter τ_{eddy} is a radiative decay time, normally chosen to be 20 days.

APPENDIX D

FORTRAN CODE FOR 1-D MODEL

The computer code for the 1-D model, as presented herein, is designed to run on a VAX/VMS computer operating system. Running the program on a different system should only require appropriate changes in file definitions and i/o statements.

Each simulation requires an input command file and an input data file. Samples of these files are presented after the body of the code. Appendix D concludes with a listing of the corresponding output file.

C***** LM NUMBER OF ATMOSPHERIC LAYERS
C***** LMM1 NUMBER OF ATMOSPHERIC LAYERS MINUS ONE
C***** LSTRAT LOWEST LAYER IN STRATOSPHERE
C***** MCCONT DIAGNOSTIC FOR RISE OF MOIST CONVECTIVE PLUME
C***** MPLUME MASS OF MOIST CONVECTIVE PLUME
C***** NDIV NUMBER OF LAND DIVISIONS
C***** NLMAX DIAGNOSTIC FOR RISE OF MOIST CONVECTIVE PLUME
C***** NONLIN PARAMETER SPECIFYING EVAPORATION FUNCTION
C***** P AVERAGE PRESSURE IN GRID BOX
C***** PPROB PROBABILITY THAT A GIVEN FRACTION GETS WETTED
C***** PRECIP PRECIPITATION
C***** PRPREV PRECIPITATION IN PREVIOUS TIME STEP
C***** PSURF SURFACE PRESSURE
C***** PTOP PRESSURE BELOW WHICH SIGMA COORDINATES ARE DEFINED
C***** P250W WEIGHTING FUNCTION FOR 250 MB TEMPERATURE
C***** P750W WEIGHTING FUNCTION FOR 750 MB TEMPERATURE
C***** QBIN INITIAL MOISTURE CONTENT IN GRID BOX
C***** QCONVA SEASONAL AMPLITUDE OF VERTICALLY-INTEGRATED
CONVERGENCE OF MOISTURE IN COLUMN
C***** QCONVM ANNUAL MEAN VERTICALLY-INTEGRATED CONVERGENCE OF
MOISTURE IN COLUMN
C***** QCONVO VERTICALLY-INTEGRATED CONVERGENCE OF MOISTURE IN COLUMN
C***** QINTOT VARIABLE USED IN VAPOR FLUX CONVERGENCE DIAGNOSTIC
C***** QM MOISTURE CONTENT IN GRID BOX
C***** QSW1W SHORTWAVE HEATING WEIGHTING FUNCTION
C***** QSW2W SHORTWAVE HEATING WEIGHTING FUNCTION
C***** RGAS GAS CONSTANT
C***** RCOEF RUNOFF COEFFICIENT
C***** RUNO SURFACE RUNOFF
C***** SAMP SEASONAL AMPLITUDE OF SOLAR RADIATION FLUX
C***** SDEPTH DEPTH OF UPPER SOIL LAYER
C***** SHA SPECIFIC HEAT OF AIR
C***** SHOUT SENSIBLE HEAT DIAGNOSTIC
C***** SHW SPECIFIC HEAT OF WATER
C***** SIG SIGMA COORDINATE FOR CENTER OF GRID BOX
C***** SIGE SIGMA COORDINATE FOR INTERFACE BETWEEN GRID BOXES
C***** SMEAN MEAN ANNUAL SOLAR RADIATION FLUX
C***** SRAD SOLAR RADIATION FLUX
C***** STATSO LOGICAL PARAMETER USED IN CALCULATING STORM STATISTICS
C***** STORM LOGICAL PARAMETER INDICATING OCCURRENCE OF STORM
C***** STRANS PARAMETER FOR USE IN TRANSIENT STUDIES
C***** T TEMPERATURE IN GRID BOX
C***** TB TIME BETWEEN STORMS DISTRIBUTION ARRAY
C***** TBIN INITIAL TEMPERATURE IN GRID BOX
C***** TG1 TEMPERATURE OF UPPER SOIL LAYER
C***** TNEIBR TEMPERATURE THAT CAN BE USED IN INITIALIZATIONS
C***** TR STORM DURATION DISTRIBUTION ARRAY
C***** TS TEMPERATURE AT TOP OF SURFACE LAYER
C***** WFC1 FIELD CAPACITY OF UPPER SOIL LAYER
C***** WFC2 FIELD CAPACITY OF LOWER SOIL LAYER
C***** WORIG TOTAL WATER ORIGINALLY IN SYSTEM
C***** WTR1 WATER CONTENT OF UPPER SOIL LAYER
C***** WTR2 WATER CONTENT OF LOWER SOIL LAYER
C*****
C*****

COMMON SIG(9), SIGE(10), AIRM(9), P(9), T(9), QM(9), TBIN(9), QBIN(9),
* AIJ(7), AIJAVE(2,9), AHEAT(4), DSIG(9), EVAP(20), PRECIP,
* LM, LMM1, LSTRAT, GRAV, LHE, RGAS, KAPA, MPLUME, SHA, SHW,
* PTOP, PSURF, AREA, TNEIBR, WORIG, STRANS, RCOEF,

```

* QINTOT, WFC1, SDEPTH, HC1DE, TG1 (20), PRPREV, RUNO,
* FPLUME, FREEVA, FREEVB, TR (50), TB (50), NLMAX, MCCONT,
* AXCONS, BXCONS, BYTF, LHX, DTSTEP, KRAND, KSEED, KWET, KGWRUN,
* NONLIN, FSECT, WTR1 (20), ASOIL (2, 20), PPROB (20), SAMP,
* WTR2 (20), WFC2, EVOUT, TS (20),
* P25OW (9), P75OW (9), AL1W (10), AL2W (10), AL3W (10), QSW1W (9), QSW2W (9),
* SRAD, SMEAN, HSWINT, HLWINT, HLWOTT, SHOUT,
* QCONVO, HCONVO, QCONVM, QCONVA, HCONVM, HCONVA, CONVW (9),
* IDACC (3), KTSTEP, KTZERO, KTTOT, NDIV, STORM, STATSO, GROW
REAL LHE, KAPA, LAT, LHX, LIQD, MPLUME, MLCLOUD, ML, MNEW
LOGICAL STORM, STATSO, GROW

```

C*****

C*****

```

CALL INPUT
CALL CHECKT (1)

```

C*****

```

DO 100 KTSTEP=1, KTTOT
CALL TRTIME
CALL DYNAM
CALL CHECKT (2)
CALL MSTONV
CALL CHECKT (3)
CALL CONDSE
CALL CHECKT (4)
CALL PSTATS
CALL RAIN
CALL CHECKT (5)
CALL SURFCE
CALL CHECKT (6)
CALL GROUND
CALL CHECKT (7)
CALL RADIA
CALL CHECKT (8)

```

100 CONTINUE

C*****

```

CALL OUTPUT
STOP
END

```

C*****

C*****

C*****

C*****

C*****

SUBROUTINE INPUT

C*****

C*****

C*****

```

THIS SUBROUTINE INITIALIZES THE SIMULATION VARIABLES
COMMON SIG (9), SIGE (10), AIRM (9), P (9), T (9), QM (9), TBIN (9), QBIN (9),
* AIJ (7), AIJAVE (2, 9), AHEAT (4), DSIG (9), EVAP (20), PRECIP,
* LM, LMM1, LSTRAT, GRAV, LHE, RGAS, KAPA, MPLUME, SHA, SHW,
* PTOP, PSURF, AREA, TNEIBR, WORIG, STRANS, RCOEF,
* QINTOT, WFC1, SDEPTH, HC1DE, TG1 (20), PRPREV, RUNO,
* FPLUME, FREEVA, FREEVB, TR (50), TB (50), NLMAX, MCCONT,
* AXCONS, BXCONS, BYTF, LHX, DTSTEP, KRAND, KSEED, KWET, KGWRUN,
* NONLIN, FSECT, WTR1 (20), ASOIL (2, 20), PPROB (20), SAMP,
* WTR2 (20), WFC2, EVOUT, TS (20),
* P25OW (9), P75OW (9), AL1W (10), AL2W (10), AL3W (10), QSW1W (9), QSW2W (9),
* SRAD, SMEAN, HSWINT, HLWINT, HLWOTT, SHOUT,
* QCONVO, HCONVO, QCONVM, QCONVA, HCONVM, HCONVA, CONVW (9),

```

```

* IDACC(3),KTSTEP,KTZERO,KTOT,NDIV,STORM,STATSO,GROW
REAL LHE,KAPA,LAT,LHX,LIQD,MPLUME,MCLOUD,ML,MNEW
DIMENSION RTDIFO(2),SIGO(9),SIGEO(10),CHI1(20)
LOGICAL STORM,STATSO,GROW
CHARACTER*80 TITLE,TJUNK,FILEIN,FILOUT
CHARACTER*20 TDATE,TTIME,TJ20
DATA SIGO/0.974264,.907372,.796957,.640124,.470418,.318899,
* .195759,.094938,.016897/
DATA SIGEO/ 1.,.948665,.866530,.728953,.554415,.390144,
* .251540,.143737,.061602,0./

```

```

C****
C****
C**** SET CONSTANTS
C****

```

```

LM=9
LMM1=LM-1
LSTRAT=8
GRAV=9.81
LHE=2500000.
LHX=LHE
RGAS=287.
KAPA=0.286
AXCONS=ALOG(6.1071)
BXCONS=0.622/RGAS
TF=273.16
BYTF=1./TF
PTOP=10.
PSURF=1000.
SHA=RGAS/KAPA
SHW=4185.
PORSTY=0.3
KSEED=1234567

```

```

C****

```

```

DO 30 L=1,LM
SIG(L)=SIGO(L)
SIGE(L)=SIGEO(L)
30 CONTINUE
SIGE(LM+1)=SIGEO(LM+1)

```

```

C****

```

```

AREA=1.E12
SAMP=162.
SMEAN=325.
TNEIBR=273.
SRAD=SMEAN-SAMP

```

```

C****

```

```

C**** INITIALIZATIONS

```

```

GROW=.TRUE.
STATSO=.FALSE.
STORM=.FALSE.
PRPREV=0.
PRECIP=0.

```

```

NLMAX=0
MCCONT=0

```

```

C****

```

```

DO 55 K=1,50
TR(K)=0.
TB(K)=0.

```

```

C****

```

```

DO 56 K=1,7

```

```

56      AIJ(K)=0.
        DO 57 K1=1,2
        DO 57 K2=1,9
57      AIJAVE(K1,K2)=0.
        DO 58 K1=1,2
        DO 58 K2=1,20
58      ASOIL(K1,K2)=0.
        DO 60 K=1,3
60      IDACC(K)=0
C*****
        DO 70 L=1,LM
        DSIG(L)=SIGE(L)-SIGE(L+1)
        AIRM(L)=100.*PSURF*AREA*DSIG(L)/GRAV
        P(L)=PSURF*SIG(L)+PTOP
70      CONTINUE
C*****
C***** -----
C***** WEIGHTING FUNCTIONS FOR HEAT AND MOISTURE CONVERGENCE.
C***** PSURF=SURFACE PRESSURE, PEXT=PRESSURE AT CONVERGENCE EXTREMUM,
C***** P1BYE=PRESSURE AT WHICH CONV. FALLS TO 1/e OF VALUE AT PEXT.
C*****
        PEXT=900.
        P1BYE=500.
C*****
        DUM1=EXP(-1.*PEXT/(PEXT-P1BYE))
        DUM2=(PEXT-P1BYE)*(1.-DUM1)
        DUM3=0.5*(PSURF-PEXT)
        CEXT=1./(DUM2+DUM3)
C*****
C***** INITIALIZE WEIGHTS:
        DO 72 L=1,LM
72      CONVW(L)=0.
C*****
C***** ASSIGN WEIGHTS ABOVE PEXT:
        DO 73 L=1,LM
        PUPPER=PSURF*SIGE(L+1)
        PLOWER=PSURF*SIGE(L)
        IF(PUPPER.GT.PEXT) GOTO 73
        IF(PLOWER.GT.PEXT) PLOWER=PEXT
        DUM1=EXP(-1.*PEXT/(PEXT-P1BYE))
        DUM2=EXP(PLOWER/(PEXT-P1BYE))
        DUM3=EXP(PUPPER/(PEXT-P1BYE))
        CNVADD=CEXT*DUM1*(PEXT-P1BYE)*(DUM2-DUM3)
        CONVW(L)=CONVW(L)+CNVADD
73      CONTINUE
C*****
C***** ASSIGN WEIGHTS BELOW PEXT:
        DO 74 L=1,LM
        PUPPER=PSURF*SIGE(L+1)
        PLOWER=PSURF*SIGE(L)
        IF(PLOWER.LT.PEXT) GOTO 74
        IF(PUPPER.LT.PEXT) PUPPER=PEXT
        DUM1=1./(PSURF-PEXT)
        DUM2=(PLOWER-PUPPER)*PSURF
        DUM3=0.5*(PLOWER*PLOWER-PUPPER*PUPPER)
        CNVADD=CEXT*DUM1*(DUM2-DUM3)
        CONVW(L)=CONVW(L)+CNVADD
74      CONTINUE
C*****

```

```

C**** -----
C**** COMPUTE WEIGHTING FUNCTION FOR 250 AND 750 MB HEIGHTS
C**** (FOR USE IN SUBROUT. RADIA)
C****
      DO 33 L=1,LM
      P250W(L)=0.
33    P750W(L)=0.
C****
      P250=LOG(PSURF/250.)
      DO 35 L=1,LMM1
      IF(250.LT.P(L+1).OR.250.GT.P(L)) GOTO 35
      PLNL=LOG(PSURF/P(L))
      PLNLP1=LOG(PSURF/P(L+1))
      P250W(L)=(PLNLP1-P250)/(PLNLP1-PLNL)
      P250W(L+1)=1.-P250W(L)
35    CONTINUE
C****
      P750=LOG(PSURF/750.)
      DO 36 L=1,LMM1
      IF(750.LT.P(L+1).OR.750.GT.P(L)) GOTO 36
      PLNL=LOG(PSURF/P(L))
      PLNLP1=LOG(PSURF/P(L+1))
      P750W(L)=(PLNLP1-P750)/(PLNLP1-PLNL)
      P750W(L+1)=1.-P750W(L)
36    CONTINUE
C****
C**** -----
C**** CALCULATE WEIGHTING FUNCTIONS FOR LONGWAVE COOLING RATES.
C**** (FOR USE IN SUBROUT. RADIA.)
C****
      LMP1=LM+1
      DO 38 L=1,LMP1
      AL1W(L)=0.
      AL2W(L)=0.
38    AL3W(L)=0.
      P200=LOG(PSURF/200.)
      P500=LOG(PSURF/500.)
C****
      DO 44 L=1,LM
      PL=LOG(PSURF/(SIGE(L)*PSURF))
      IF((SIGE(L)*PSURF).LT.500.) GOTO 40
C****
C**** LEVEL LIES BELOW 500 MB, SO INTERPOLATE BETWEEN L2 AND L3:
      AL2W(L)=PL/P500
      AL3W(L)=1.-AL2W(L)
      GOTO 44
C****
40    CONTINUE
C**** LEVEL LIES ABOVE 500 MB, SO INTERPOLATE BETWEEN L1 AND L2:
      AL2W(L)=(PL-P200)/(P500-P200)
      AL1W(L)=1.-AL2W(L)
      IF((SIGE(L)*PSURF).LT.200.) AL2W(L)=0.
      IF((SIGE(L)*PSURF).LT.200.) AL1W(L)=1.
44    CONTINUE
      AL2W(LMP1)=0.
      AL1W(LMP1)=1.
C****
C**** -----
C**** CALCULATE WEIGHTING FUNCTIONS FOR SHORTWAVE HEATING RATES:
C****

```

```

DO 46 L=1,LM
QSW1W(L)=0.
46 QSW2W(L)=0..
C*****
SUMAR1=0.
SUMAR2=0.
LTROP=LSTRAT-1
DO 48 L=1,LTROP
IF(P(L).LT.500) SUMAR1=SUMAR1+AIRM(L)
IF(P(L).GE.500) SUMAR2=SUMAR2+AIRM(L)
48 CONTINUE
C*****
DO 50 L=1,LTROP
IF(P(L).LT.500.) QSW1W(L)=AIRM(L)/SUMAR1
IF(P(L).GE.500.) QSW2W(L)=AIRM(L)/SUMAR2
50 CONTINUE
C*****
C***** -----
C***** OPEN INPUT AND OUTPUT FILES; WRITE DATE AND TIME
C***** WRITE INPUT FILE:
C PRINT *, 'ENTER NAME OF INPUT FILE:'
READ(5,2200) FILEIN
C PRINT *, 'ENTER NAME OF OUTPUT FILE:'
READ(5,2200) FILOUT
2200 FORMAT(A80)
OPEN(UNIT=90,FILE=FILEIN,READONLY,STATUS='OLD',RECL=80)
OPEN(UNIT=92,FILE=FILOUT,STATUS='NEW',RECL=80)
CALL DATE(TDATE)
CALL TIME(TTIME)
WRITE(92,2120) TDATE,TTIME
2120 FORMAT(/1X,2A20)
C*****
C***** WRITE INPUT FILE DIRECTLY INTO OUTPUT FILE
WRITE(92,2102)
75 READ(90,2100,END=80) TJUNK
WRITE(92,2101) TJUNK
GOTO 75
80 CONTINUE
C*****
WRITE(92,2103)
2100 FORMAT(A80)
2101 FORMAT(1X,A79)
2102 FORMAT(1X,18('===='),/1X,'INPUT FILE USED:',/1X)
2103 FORMAT(/1X,18('===='),/1X)
C*****
C***** READ VARIABLE PARAMETERS:
REWIND 90
READ(90,2001) TITLE
C*****
C***** INTEGER VARIABLES:
C***** READ TOTAL NUMBER OF TIME STEPS:
READ(90,2001) TJUNK
READ(90,2050) TJ20,KTTOT
C*****
C***** READ TIME STEP AT WHICH TRACER DIAGNOSTICS ARE ZEROED:
READ(90,2050) TJ20,KTZERO
C*****
C***** READ TYPE OF EVAPORATION FUNCTION USED
C***** (0=LINEAR IN SOIL MOISTURE, 1=NONLINEAR)

```

```

READ(90,2050) TJ20,NONLIN
C****
C**** READ NUMBER SPECIFYING USE (OR DISUSE) OF SUBROUT. GROUND:
C**** (0=DON'T USE 2ND SOIL LAYER, 1=USE 2ND SOIL LAYER)
READ(90,2050) TJ20,KGWRUN
C****
C**** READ NUMBER DESCRIBING WETTING ASSIGNMENT USED:
C**** (0=NON-RANDOM ASSIGNMENT, 1=RANDOM ASSIGNMENT)
READ(90,2050) TJ20,KRAND
2050 FORMAT(1X,A20,I10)
C****
C**** REAL VARIABLES (EMPTYO, EMPTY1, ETC. CURRENTLY NOT USED):
READ(90,2001) TJUNK
2001 FORMAT(A50)
READ(90,2002) FPLUME,FREEVA,FREEVB,QCONVM,QCONVA,HCONVM,HCONVA
2002 FORMAT(1X,7F10.3)
READ(90,2001) TJUNK
READ(90,2003) EMPTYO,DTSTEP,EMPTY1,SDEPTH,EMPTY2,STRANS,RCOEF
2003 FORMAT(1X,7F10.3)
C****
C**** READ INITIAL T(L), Q(L) AND WTR1(K),TG1(K):
READ(90,2001) TJUNK
DO 90 LPRIME=1,LM
L=LM+1-LPRIME
READ(90,2005) TBIN(L),QBIN(L)
2005 FORMAT(1X,2F13.5)
TBIN(L)=TNEIBR*((P(L)/P(1))**KAPA)
IF(L.GE.LSTRAT) TBIN(L)=TNEIBR*((P(LSTRAT-1)/P(1))**KAPA)
T(L)=TBIN(L)
C QBIN(L)=QBIN(L)*AIRM(L)*QSAT(TBIN(L),P(L))
C QBIN(L)=QBIN(L)*0.001*AIRM(L)
90 QM(L)=QBIN(L)*AIRM(L)*QSAT(TBIN(L),P(L))
C****
READ(90,2001) TJUNK
READ(90,2010) NDIV
2010 FORMAT(1X,I13)
ANDIV=NDIV
FSECT=1./ANDIV
C****
READ(90,2001) TJUNK
PRBTOT=0.
DO 93 K=1,20
READ(90,2015) KJUNK,TG1(K),CHI1(K),PPROB(K)
2015 FORMAT(1X,I13,3F13.5)
IF(CHI1(K).LT.0.) CHI1(K)=0.
IF(CHI1(K).GT.1.) CHI1(K)=1.
IF(K.GT.NDIV) CHI1(K)=0.
IF(K.LE.NDIV) PRBTOT=PRBTOT+PPROB(K)
93 CONTINUE
C****
C**** ESTABLISH SOIL WATER CONTENTS, SET FURTHER CONSTANTS
WFC1=SDEPTH*AREA*PORSTY*1000.
WFC2=5.*WFC1
HC1DE=SDEPTH*AREA*1129950.
DO 94 K=1,NDIV
WTR1(K)=CHI1(K)*WFC1*FSECT
94 WTR2(K)=CHI1(K)*WFC2*FSECT
C****
C**** NORMALIZE PROBABILITIES

```

```

DO 96 K=1,NDIV
96 PPROB(K)=PPROB(K)/PRBTOT
C*****
C***** ORIGINAL WATER CONTENT
WORIG=0.
DO 97 K=1,NDIV
97 WORIG=WORIG+WTR1(K)+WTR2(K)
DO 98 L=1,LM
98 WORIG=WORIG+QM(L)
C*****
WRITE(92,1000) TITLE
1000 FORMAT(///1X,10('/////'),/1X,A79,/1X,10('/////'),/1X)
C*****
C***** CHECK CONVERGENCE WEIGHTING:
SCONVW=0.
WRITE(92,7449)
7449 FORMAT(/1X,'WEIGHTINGS USED FOR HEAT AND MOISTURE CONVERGENCE:
* /1X)
DO 745 L=LM,1,-1
CONVWN=CONVW(L)*AREA/AIRM(L)
WRITE(92,7450) L,CONVW(L),CONVWN,P(L)
7450 FORMAT(1X,'L =',I3,' CONVW(L) =',F8.3,' (BY MASS: ',
* 1P,E13.5,') P =',OP,F10.2)
745 SCONVW=SCONVW+CONVW(L)
WRITE(92,7451) SCONVW
7451 FORMAT(/1X,'SUM OF WEIGHTS =',F10.3,/1X)
C*****
RETURN
END
C*****
C*****
C*****
C*****
SUBROUTINE TRTIME
C*****
C***** THIS SUBROUTINE RESETS SPECIFIED VARIABLES AT EACH TIME STEP AND ALSO
C***** RESETS DIAGNOSTIC QUANTITIES TO ZERO AT A SPECIFIED TIME.
C*****
COMMON SIG(9),SIGE(10),AIRM(9),P(9),T(9),QM(9),TBIN(9),QBIN(9),
* AIJ(7),AIJAVE(2,9),AHEAT(4),DSIG(9),EVAP(20),PRECIP,
* LM,LMM1,LSTRAT,GRAV,LHE,RGAS,KAPA,MPLUME,SHA,SHW,
* PTOP,PSURF,AREA,TNEIBR,WORIG,STRANS,RCOEF,
* QINTOT,WFC1,SDEPTH,HCIDE,TG1(20),PRPREV,RUNO,
* FPLUME,FREEVA,FREEVB,TR(50),TB(50),NLMAX,MCCONT,
* AXCONS,BXCONS,BYTF,LHX,DTSTEP,KRAND,KSEED,KWET,KGWRUN,
* NONLIN,FSECT,WTR1(20),ASOIL(2,20),PPROB(20),SAMP,
* WTR2(20),WFC2,EVOUT,TS(20),
* P25OW(9),P75OW(9),AL1W(10),AL2W(10),AL3W(10),QSW1W(9),QSW2W(9),
* SRAD,SMEAN,HSWINT,HLWINT,HLWOTT,SHOUT,
* QCONVO,HCONVO,QCONVM,QCONVA,HCONVM,HCONVA,CONVW(9),
* IDACC(3),KTSTEP,KTZERO,KTTOT,NDIV,STORM,STATSO,GROW
REAL LHE,KAPA,LAT,LHX,LIQD,MPLUME,MCLOUD,ML,MNEW
LOGICAL STORM,STATSO,GROW
DIMENSION QREL(9)
C*****
C***** DIURNAL AND SEASONAL CYCLES
THOUR=KTSTEP*DTSTEP/3600.
IHOURL=MOD(INT(THOUR+0.5),365*24)
JDAY=1+INT(IHOURL/24.)

```

```

FYEAR=IHOURL/(365.*24.)
COSFAC=COS(FYEAR*2.*3.14159)
C****
C**** COMPUTE SEASONAL CONVERGENCE OF HEAT AND MOISTURE:
QCONVO=QCONVM+QCONVA*COSFAC
HCONVO=HCONVM+HCONVA*COSFAC
C****
C**** LENGTH OF DAY, AS FRACTION OF UNITY
DAYMEN=0.5
DAYAMP=2.8/24.
DAYLEN=DAYMEN-DAYAMP*COSFAC
C****
C**** CORRECT SOLAR RADIATION FOR DIURNAL CYCLE
IDHOUR=MOD(IHOURL,24)
DAYFAC=(3.14159/(2.*DAYLEN))*
* COS((IDHOUR-12.)*2.*3.14159/(48.*DAYLEN))
IF(DAYFAC.LT.0.) DAYFAC=0.
SRAD=SMEAN-SAMP*COSFAC
SRAD=SRAD*DAYFAC
C****
C**** DETERMINE WHETHER TIME STEP LIES WITH GROWING SEASON
GROW=.FALSE.
IF(JDAY.GE.121.AND.JDAY.LE.243) GROW=.TRUE.
-----
C****
C**** ADD QUANTITIES INTO 'AVERAGE VALUE' DIAGNOSTIC ARRAYS
C****
20 CONTINUE
DO 50 L=1,LM
RELHUM=(QM(L)/AIRM(L))/QSAT(T(L),P(L))
AIJAVE(1,L)=AIJAVE(1,L)+RELHUM
50 AIJAVE(2,L)=AIJAVE(2,L)+T(L)
IDACC(1)=IDACC(1)+1
C****
DO 55 K=1,NDIV
ASOIL(1,K)=ASOIL(1,K)+WTR1(K)
55 ASOIL(2,K)=ASOIL(2,K)+TG1(K)
IDACC(2)=IDACC(2)+1
C****
-----
C****
C**** RESET VALUES AT KTZERO
IF(KTSTEP.NE.KTZERO) GOTO 400
C****
STATSO=.FALSE.
DO 80 K=1,50
TR(K)=0.
80 TB(K)=0.
C****
NLMAX=0
MCCONT=0
C****
DO 100 K=1,7
100 AIJ(K)=0.
C****
DO 150 K1=1,2
DO 150 K2=1,9
150 AIJAVE(K1,K2)=0.
DO 152 K1=1,2
DO 152 K2=1,20

```

```

152     ASOIL(K1,K2)=0.
        DO 155 K=1,4
155     AHEAT(K)=0
        DO 160 K=1,3
160     IDACC(K)=0
C****
      IF (STRANS.LT.0.) GOTO 300
C****
C****  -----
C****  RESET CONDITIONS FOR TRANSIENT EXPERIMENTS IF 0<STRANS
C****
      RCOEF=STRANS
      DO 170 K=1,20
      TG1(K)=TNEIBR
170    WTR1(K)=WFC1*FSECT
C****
C****  -----
300    CONTINUE
C****
      WORIG=0.
      DO 330 K=1,NDIV
330    WORIG=WORIG+WTR1(K)+WTR2(K)
      DO 340 L=1,LM
340    WORIG=WORIG+QM(L)
C****
      WRITE(92,1002)
      WRITE(92,1000)
      WRITE(92,1001) KTSTEP
      WRITE(92,1000)
      WRITE(92,1002)
C****
1000   FORMAT(1X,'*****')
1001   FORMAT(1X,'***** STEP =',I5,':  DIAGNOSTICS ZEROED *****')
1002   FORMAT(1X,' ')
C****
400    CONTINUE
      RETURN
      END
C****
C****  -----
C****  //////////////////////////////////////
C****  -----
C****
SUBROUTINE DYNAM
C****
C****  THIS SUBROUTINE ADJUSTS THE HEAT AND MOISTURE IN EACH ATMOSPHERIC
C****  LAYER ACCORDING TO THE ASSIGNED CONVERGENCES.
C****
COMMON SIG(9), SIGE(10), AIRM(9), P(9), T(9), QM(9), TBIN(9), QBIN(9),
*  AIJ(7), AIJAVE(2,9), AHEAT(4), DSIG(9), EVAP(20), PRECIP,
*  LM, LMM1, LSTRAT, GRAV, LHE, RGAS, KAPA, MPLUME, SHA, SHW,
*  PTOP, PSURF, AREA, TNEIBR, WORIG, STRANS, RCOEF,
*  QINTOT, WFC1, SDEPTH, HCLDE, TG1(20), PRPREV, RUNO,
*  FPLUME, FREEVA, FREEVB, TR(50), TB(50), NLMAX, MCCONT,
*  AXCONS, BXCONS, BYTF, LHX, DTSTEP, KRAND, KSEED, KWET, KGWRUN,
*  NONLIN, FSECT, WTR1(20), ASOIL(2,20), PPROB(20), SAMP,
*  WTR2(20), WFC2, EVOUT, TS(20),
*  P25OW(9), P75OW(9), AL1W(10), AL2W(10), AL3W(10), QSW1W(9), QSW2W(9),
*  SRAD, SMEAN, HSWINT, HLWINT, HLWOTT, SHOUT,
*  QCONVO, HCONVO, QCONVM, QCONVA, HCONVM, HCONVA, CONVW(9),
*  IDACC(3), KTSTEP, KTZERO, KTTOT, NDIV, STORM, STATSO, GROW

```

```

REAL LHE, KAPA, LAT, LHX, LIQD, MPLUME, MCLLOUD, ML, MNEW
LOGICAL STORM, STATSO, GROW
C****
      QINTOT=0.
C****
C**** COMPUTE CONVERGENCES OF MOISTURE AND HEAT:
C****
      DO 100 L=1, LM
      QCONV=QCONVO*CONVW(L)
      QM(L)=QM(L)+QCONV*AREA*DTSTEP
      QINTOT=QINTOT+QCONV*AREA*DTSTEP
      HCONV=HCONVO*CONVW(L)
      T(L)=T(L)+HCONV*AREA*DTSTEP/(SHA*AIRM(L))
100  CONTINUE
C****
      AIJ(5)=AIJ(5)+QINTOT
C****
      RETURN
      END
C****
C**** ////////////////////////////////////////////////////////////////////
C****
      SUBROUTINE MSTCNV
C****
C**** THIS SUBROUTINE COMPUTES PRECIPITATION CAUSED BY MOIST
C**** CONVECTION. IT HAS THE SAME BASIC STRUCTURE AS THE
C**** CORRESPONDING SUBROUTINE IN THE GISS GCM.
C****
      COMMON SIG(9), SIGE(10), AIRM(9), P(9), T(9), QM(9), TBIN(9), QBIN(9),
* AIJ(7), AIJAVE(2,9), AHEAT(4), DSIG(9), EVAP(20), PRECIP,
* LM, LMM1, LSTRAT, GRAV, LHE, RGAS, KAPA, MPLUME, SHA, SHW,
* PTOP, PSURF, AREA, TNEIBR, WORIG, STRANS, RCOEF,
* QINTOT, WFC1, SDEPTH, HC1DE, TG1(20), PRPREV, RUNO,
* FPLUME, FREEVA, FREEVB, TR(50), TB(50), NLMAX, MCCONT,
* AXCONS, BXCONS, BYTF, LHX, DTSTEP, KRAND, KSEED, KWET, KGWRUN,
* NONLIN, FSECT, WTR1(20), ASOIL(2,20), PPROB(20), SAMP,
* WTR2(20), WFC2, EVOUT, TS(20),
* P25OW(9), P75OW(9), AL1W(10), AL2W(10), AL3W(10), QSW1W(9), QSW2W(9),
* SRAD, SMEAN, HSWINT, HLWINT, HLWOTT, SHOUT,
* QCONVO, HCONVO, QCONVM, QCONVA, HCONVM, HCONVA, CONVW(9),
* IDACC(3), KTSTEP, KTZERO, KTTOT, NDIV, STORM, STATSO, GROW
      REAL LHE, KAPA, LAT, LHX, LIQD, MPLUME, MCLLOUD, ML, MNEW
      DIMENSION WATER(9), QMOLD(9), TOLD(9)
      CHARACTER*50 TITLE1, TITLE2, TXAXIS, TYAXIS
      LOGICAL STORM, STATSO, GROW
      DATA TF/273.16/, TI/233.16/, IFIRST/1/, TLS/248.16/, TFREEZ/263.16/
C****
C**** -----
C****
      DO 7 L=1, LM
      WATER(L)=0.
      QMOLD(L)=QM(L)
      7  TOLD(L)=T(L)
C****
      PRPREV=PRECIP
      PRECIP=0.
      PRCPMC=0.
C****
C**** -----
C**** START MOIST CONVECTION

```

```

C**** -----
      LMIN=0
C****
200  LMIN=LMIN+1
      IF (LMIN.EQ.LM) GOTO 900
C****
C****  CREATE A PLUME IN THE BOTTOM LAYER
      MPLUME=FPLUME*AIRM(LMIN)
      QMP=QM(LMIN)*FPLUME
      QM(LMIN)=QM(LMIN)-QMP
      TPLUME=T(LMIN)
C****
C**** -----
C****  START L LOOP
      DO 400 LMAX=LMIN,LMM1
      L=LMAX+1
C****
C****  TEST TO SEE IF CONVECTION PROCEEDS FOR ANOTHER LEVEL.
C****  FIRST HEAT PLUME DRY ADIABATICALLY, THEN HEAT BY CONDENSING
C****  MOISTURE, IF NECESSARY.
      LHX=LHE
      QNEW=QMP
      TNEW=TPLUME*(P(L)/P(LMAX))**KAPA
      QNEWS=QSAT(TNEW,P(L))*MPLUME
      IF(QNEW.LT.QNEWS) GO TO 250
C****
C****  (CONDENSE MOISTURE, USING ITERATION)
      CALL FINDT(TNEW,QNEW,MPLUME,L)
C****
250  IF(TNEW.LT.T(L)) GOTO 410
C****
C****  CONVECTION OCCURS
      WATER(L)=QMP-QNEW
      QMP=QNEW
      TPLUME=TNEW
C****
400  CONTINUE
      LMAX=LM
C****
C**** -----
C****  SUBSIDENCE AND MIXING
410  CONTINUE
C****
C****  RESTORE PLUME WATER TO ORIGINAL LEVEL IF NO CONVECTION
      IF(LMAX.GT.LMIN) GOTO 415
      QM(LMIN)=QM(LMIN)+QMP
      GOTO 200
C****
C****  MIXING IN LOWER LEVELS
415  CONTINUE
      IF(LMIN.EQ.1) NLMAX=NLMAX+LMAX
      IF(LMIN.EQ.1) MCCONT=MCCONT+1
C****
      LMAXM1=LMAX-1
      DO 420 L=LMIN,LMAXM1
      FNEW=MPLUME/AIRM(L)
      FORIG=1-FNEW
      TSBSID=T(L+1)*(P(L)/P(L+1))**KAPA
      T(L)=FORIG*T(L)+FNEW*TSBSID
      QABOVE=QM(L+1)*(MPLUME/AIRM(L+1))

```

```

QORIG=FORIG*QM(L)
IF(L.EQ.LMIN) QORIG=QM(L)
QM(L)=QORIG+QABOVE
420 CONTINUE
C*****
C***** MIX PLUME INTO TOP LAYER INVOLVED IN CONVECTION, LMAX
FNEW=MPLUME/AIRM(LMAX)
FORIG=1-FNEW
T(LMAX)=FORIG*T(LMAX)+FNEW*TPLUME
QM(LMAX)=FORIG*QM(LMAX)+QMP
C*****
C***** -----
C***** REEVAPORATION OF FALLING WATER
PRCP=WATER(LMAX)
C*****
C***** START L LOOP:
DO 700 LPRIME=1,LMAXM1
L=LMAX-LPRIME
FREEV=FREEVA
IF(L.LE.LMIN) FREEV=FREEVB
MCLLOUD=FREEV*AIRM(L)
C***** (EVAPORATE ALL WATER INTO SECTION OF BOX)
EVAPMC=PRCP
PRCP=0.
CLW=QMOLD(L)*FREEV+EVAPMC
C*****
HEAT=LHE*EVAPMC
TNEW=TOLD(L)-HEAT/(SHA*MCLLOUD)
WATER(L+1)=0.
QNEW=CLW
QNEWS=QSAT(TNEW,P(L))*MCLLOUD
C*****
IF(QNEWS.GT.CLW) GOTO 590
C***** SECTION BECOMES SATURATED:
CALL FINDT(TNEW,QNEW,MCLLOUD,L)
590 PRCP=CLW-QNEW
C*****
CONTINUE
T(L)=T(L)-(EVAPMC-PRCP)*LHE/(SHA*AIRM(L))
QM(L)=QM(L)+EVAPMC-PRCP
C*****
PRCP=PRCP+WATER(L)
700 CONTINUE
C*****
PRCPMC=PRCPMC+PRCP
WATER(1)=0.
C*****
DO 760 L=1,LM
TOLD(L)=T(L)
760 QMOLD(L)=QM(L)
C*****
GOTO 200
900 CONTINUE
C*****
PRECIP=PRECIP+PRCPMC
C*****
RETURN
END
C*****

```

```

C***** XXXXXXXXXXXXXXXXXXXXXXXXXXXXXXXXXXXXXXXXXXXXXXXXXXXXXXXXXXXXXXXXXXXXXXX
C*****
SUBROUTINE FINDT(TNEW,QNEW,ARMASS,L)
C*****
C***** THIS SUBROUTINE FINDS THE FINAL TEMPERATURE AND MOISTURE CONTENT
C***** OF A SUPERSATURATED AIR PARCEL.
C*****
COMMON SIG(9),SIGE(10),AIRM(9),P(9),T(9),QM(9),TBIN(9),QBIN(9),
* AIJ(7),AIJAVE(2,9),AHEAT(4),DSIG(9),EVAP(20),PRECIP,
* LM,LMM1,LSTRAT,GRAV,LHE,RGAS,KAPA,MPLUME,SHA,SHW,
* PTOP,PSURF,AREA,TNEIBR,WORIG,STRANS,RCOEF,
* QINTOT,WFC1,SDEPTH,HC1DE,TG1(20),PRPREV,RUNO,
* FPLUME,FREEVA,FREEVB,TR(50),TB(50),NLMAX,MCCONT,
* AXCONS,EXCONS,BYTF,LHX,DTSTEP,KRAND,KSEED,KWET,KGWRUN,
* NONLIN,FSECT,WTR1(20),ASOIL(2,20),PPROB(20),SAMP,
* WTR2(20),WFC2,EVOUT,TS(20),
* P25OW(9),P75OW(9),AL1W(10),AL2W(10),AL3W(10),QSW1W(9),QSW2W(9),
* SRAD,SMEAN,HSWINT,HLWINT,HLWOTT,SHOUT,
* QCONVO,HCONVO,QCONVM,QCONVA,HCONVM,HCONVA,CONVW(9),
* IDACC(3),KTSTEP,KTZERO,KTTOT,NDIV,STORM,STATSO,GROW
REAL LHE,KAPA,LAT,LHX,LIQD,MPLUME,MCLOUD,ML,MNEW
LOGICAL STORM,STATSO,GROW
C*****
C*****
ITER=0
QNEWS=QSAT(TNEW,P(L))*ARMASS
C*****
THETAQ=0.5
220 CONTINUE
ITER=ITER+1
IF(MOD(ITER,100).EQ.0) THETAQ=THETAQ/2.
IF(ITER.LT.1000) GOTO 230
C*****
-----
WRITE(92,1000) KTSTEP
1000 FORMAT(///1X,'PROGRAM TERMINATES:',/1X,
* '>1000 ITERATIONS IN FINDT AT KTSTEP =',I7)
STOP
C*****
-----
C***** ASSUME THAT AN AMOUNT THETAQ*(QNEW-QNEWS) IS CONDENSED.
230 HEAT=LHE*THETAQ*(QNEW-QNEWS)
TNEW=TNEW+HEAT/(SHA*ARMASS)
QNEW=QNEW-THETAQ*(QNEW-QNEWS)
QNEWS=QSAT(TNEW,P(L))*ARMASS
IF(ABS((QNEW-QNEWS)/QNEWS).GT..001) GOTO 220
C*****
RETURN
END
C*****
C***** XXXXXXXXXXXXXXXXXXXXXXXXXXXXXXXXXXXXXXXXXXXXXXXXXXXXXXXXXXXXXXXXXXXXXXX
C*****
FUNCTION QSAT(TM,PR)
C*****
C***** THIS FUNCTION RETURNS THE SATURATED SPECIFIC HUMIDITY AT
C***** TEMPERATURE TM AND PRESSURE PR.
C*****
COMMON SIG(9),SIGE(10),AIRM(9),P(9),T(9),QM(9),TBIN(9),QBIN(9),
* AIJ(7),AIJAVE(2,9),AHEAT(4),DSIG(9),EVAP(20),PRECIP,
* LM,LMM1,LSTRAT,GRAV,LHE,RGAS,KAPA,MPLUME,SHA,SHW,
* PTOP,PSURF,AREA,TNEIBR,WORIG,STRANS,RCOEF,

```

```

* QINTOT,WFC1,SDEPTH,HC1DE,TG1(20),PRPREV,RUNO,
* FPLUME,FREEVA,FREEVB,TR(50),TB(50),NLMAX,MCCONT,
* AXCONS,BXCONS,BYTF,LHX,DTSTEP,KRAND,KSEED,KWET,KGWRUN,
* NONLIN,FSECT,WTR1(20),ASOIL(2,20),PPROB(20),SAMP,
* WTR2(20),WFC2,EVOUT,TS(20),
* P25OW(9),P75OW(9),AL1W(10),AL2W(10),AL3W(10),QSW1W(9),QSW2W(9),
* SRAD,SMEAN,HSWINT,HLWINT,HLWOTT,SHOUT,
* QCONVO,HCONVO,QCONVM,QCONVA,HCONVM,HCONVA,CONVW(9),
* IDACC(3),KTSTEP,KTZERO,KTTOT,NDIV,STORM,STATSO,GROW
REAL LHE,KAPA,LAT,LHX,LIQD,MPLUME,MCLOUD,ML,MNEW
LOGICAL STORM,STATSO,GROW

C****
QSAT=0.622*EXP(AXCONS+LHX*BXCONS*(BYTF-1./TM))/PR
RETURN
END

C****
C**** XXXXXXXXXXXXXXXXXXXXXXXXXXXXXXXXXXXXXXXXXXXXXXXXXXXXXXXXXXXXXXXXXXXXXXX
C****
SUBROUTINE CONDSE

C****
C**** THIS IS A SIMPLIFIED VERSION OF SUBROUTINE CONDSE IN THE GISS GCM.
C**** IT COMPUTES THE PRECIPITATION FORMED DURING LARGE-SCALE,
C**** NON-CONVECTIVE STORMS.
C****
COMMON SIG(9),SIGE(10),AIRM(9),P(9),T(9),QM(9),TBIN(9),QBIN(9),
* AIJ(7),AIJAVE(2,9),AHEAT(4),DSIG(9),EVAP(20),PRECIP,
* LM,LM1,LSTRAT,GRAV,LHE,RGAS,KAPA,MPLUME,SHA,SHW,
* PTOP,PSURF,AREA,TNEIBR,WORIG,STRANS,RCOEF,
* QINTOT,WFC1,SDEPTH,HC1DE,TG1(20),PRPREV,RUNO,
* FPLUME,FREEVA,FREEVB,TR(50),TB(50),NLMAX,MCCONT,
* AXCONS,BXCONS,BYTF,LHX,DTSTEP,KRAND,KSEED,KWET,KGWRUN,
* NONLIN,FSECT,WTR1(20),ASOIL(2,20),PPROB(20),SAMP,
* WTR2(20),WFC2,EVOUT,TS(20),
* P25OW(9),P75OW(9),AL1W(10),AL2W(10),AL3W(10),QSW1W(9),QSW2W(9),
* SRAD,SMEAN,HSWINT,HLWINT,HLWOTT,SHOUT,
* QCONVO,HCONVO,QCONVM,QCONVA,HCONVM,HCONVA,CONVW(9),
* IDACC(3),KTSTEP,KTZERO,KTTOT,NDIV,STORM,STATSO,GROW
REAL LHE,KAPA,LAT,LHX,LIQD,MPLUME,MCLOUD,ML,MNEW
LOGICAL STORM,STATSO,GROW

C****
C**** LOOP FROM TOP TO BOTTOM
DO 500 LPRIME=1,LM
L=1+LM-LPRIME
PRCP=0.

C****
C**** CHECK FOR CONDENSABLE MOISTURE IN GRID BOX
QNEWS=QSAT(T(L),P(L))*AIRM(L)
IF(QNEWS.GT.QM(L)) GOTO 500

C****
QOLD=QM(L)
QNEW=QOLD
TNEW=T(L)
AMASS=AIRM(L)
CALL FINDT(TNEW,QNEW,AMASS,L)
PRCP=QOLD-QNEW
QM(L)=QNEW
T(L)=TNEW

C****
C**** ADD PRECIPITATION TO VAPOR IN NEXT LOWER GRID BOX

```



```

GOTO 900
C****
1000 FORMAT(1X,'STORM DURATION OF ',I5,' HOURS TOO LARGE')
C****
C**** DRY PERIOD ENDS
200 NHOOR=KTSTEP-KDRYST
IF(NHOOR.GT.50) WRITE(92,1001) NHOOR
IF(NHOOR.GT.50) NHOOR=50
TB(NHOOR)=TB(NHOOR)+1
KWETST=KTSTEP
STORM=.TRUE.
GOTO 900
1001 FORMAT(1X,'DRY DURATION OF ',I5,' HOURS TOO LARGE')
C****
C****
900 RETURN
END
C****
C**** XXXXXXXXXXXXXXXXXXXXXXXXXXXXXXXXXXXXXXXXXXXXXXXXXXXXXXXXXXXXXXXXXXXXXXXXXXXX
C****
SUBROUTINE RAIN
C**** THIS IS A VERY SIMPLIFIED VERSION OF SUBROUTINE PRECIP OF THE
C**** NASA/GISS GCM, WITH ADDITION OF WETTED FRACTION CALCULATIONS.
C**** IT COMPUTES SURFACE RUNOFF AND INFILTRATION DURING PRECIPITATION
C**** EVENTS.
C****
COMMON SIG(9),SIGE(10),AIRM(9),P(9),T(9),QM(9),TBIN(9),QBIN(9),
* AIJ(7),AIJAVE(2,9),AHEAT(4),DSIG(9),EVAP(20),PRECIP,
* LM,LMM1,LSTRAT,GRAV,LHE,RGAS,KAPA,MPLUME,SHA,SHW,
* PTOP,PSURF,AREA,TNEIBR,WORIG,STRANS,RCOEF,
* QINTOT,WFC1,SDEPTH,HC1DE,TG1(20),PRPREV,RUNO,
* FPLUME,FREEVA,FREEVB,TR(50),TB(50),NLMAX,MCCONT,
* AXCONS,BXCONS,BYTF,LHX,DTSTEP,KRAND,KSEED,KWET,KGWRUN,
* NONLIN,FSECT,WTR1(20),ASOIL(2,20),PPROB(20),SAMP,
* WTR2(20),WFC2,EVOUT,TS(20),
* P25OW(9),P75OW(9),AL1W(10),AL2W(10),AL3W(10),QSW1W(9),QSW2W(9),
* SRAD,SMEAN,HSWINT,HLWINT,HLWOTT,SHOUT,
* QCONVO,HCONVO,QCONVM,QCONVA,HCONVM,HCONVA,CONVW(9),
* IDACC(3),KTSTEP,KTZERO,KTTOT,NDIV,STORM,STATSO,GROW
REAL LHE,KAPA,LAT,LHX,LIQD,MPLUME,MCLOUD,ML,MNEW
DIMENSION CHI1(20)
LOGICAL STORM,STATSO,GROW
C****
RUNO=0.
KWET=0
IF(PRECIP.EQ.0.) GOTO 900
C****
C**** THE WAY RAIN IS ASSIGNED TO FRACTIONAL AREA DEPENDS ON VALUE
C**** OF KRAND
IF(KRAND.EQ.0) GOTO 50
IF(KRAND.EQ.1) GOTO 300
WRITE(92,1000) KRAND
1000 FORMAT(///1X,'KRAND ERROR. KRAND =',I10,/1X,
* 'STOPPING IN SUBROUTINE RAIN')
STOP
C****
C****
C**** -----
C**** MAKE SOIL CONDITIONS HOMOGENEOUS AT BEGINNING OF STORM
C****

```

```

50 CONTINUE
   IF (PRPREV.NE.O.) GOTO 100
C****
C**** SMEAR PREVIOUS GROUND MOISTURE AND HEAT OVER GRID SQUARE IF
C****   A NEW STORM HAS STARTED
      WTRTOT=0.
      AVETMP=0.
      DO 60 K=1,NDIV
      WTRTOT=WTRTOT+WTR1(K)
60   AVETMP=AVETMP+TG1(K)*FSECT
C****
      DO 70 K=1,NDIV
      WTR1(K)=WTRTOT/NDIV
70   TG1(K)=AVETMP
C****
C**** RUNOFF FORMS OVER WETTED SECTION (#1, ALWAYS)
100  KWET=1
      CHI1(1)=WTR1(1)/(WFC1+FSECT+1.E-30)
      RUNO=AMAX1(PRECIP*RCOEF*CHI1(1),PRECIP+WTR1(1)-(WFC1+FSECT))
      WTR1(1)=WTR1(1)+PRECIP-RUNO
      AIJ(3)=AIJ(3)+RUNO
      GOTO 900
C**** -----
C**** ASSIGN STORM LOCATION RANDOMLY
C****
300 CONTINUE
C****
C**** ASSURE THAT STORM OF DURATION > 1 HOUR FALLS ON SAME SECTION:
      IF (PRPREV.NE.O.) KSEED=KSEEDO
      KSEEDO=KSEED
      A=RAN(KSEED)
      IF ((A.LT.O.) .OR. (A.GT.1.)) WRITE(92,1001) A
1001  FORMAT(///1X,'RANDOM NUMBER GENERATOR ERROR. A =',1PE13.5)
      IF ((A.LT.O.) .OR. (A.GE.1.)) STOP
C****
C**** DETERMINE WHICH SECTION GETS WETTED:
      AHIGH=0.
      DO 320 K=1,NDIV
      ALOW=AHIGH
      AHIGH=AHIGH+PPROB(K)
      IF ((ALOW.LE.A) .AND. (A.LT.AHIGH)) KWET=K
320  CONTINUE
      IF ((AHIGH.LT.O.9999) .OR. (AHIGH.GT.1.0001)) WRITE(92,1002) AHIGH
1002  FORMAT(1X,'ERROR IN PRECIP PROBABILITY ASSIGNMENT: AHIGH =',
*       1PE13.5)
      IF ((AHIGH.LT.O.9999) .OR. (AHIGH.GT.1.0001)) STOP
C****
C**** CALCULATE RUNOFF:
      CHI1(KWET)=WTR1(KWET)/(WFC1+FSECT+1.E-30)
      RUNO=AMAX1(PRECIP*RCOEF*CHI1(KWET),
*       PRECIP+WTR1(KWET)-(WFC1+FSECT))
      WTR1(KWET)=WTR1(KWET)+PRECIP-RUNO
      AIJ(3)=AIJ(3)+RUNO
      GOTO 900
C**** -----
C****
900 RETURN
      END
C**** -----

```

```

C***** ////////////////////////////////////////////////////////////////////
C***** -----
SUBROUTINE SURFCE
C*****
C***** THIS SUBROUTINE IS A VERY SIMPLIFIED VERSION OF SUBROUTINE
C***** SURFCE IN THE NASA/GISS GCM. (SEE SECTION 2H OF GCM PAPER.)
C***** IT COMPUTES EVAPORATION AND SENSIBLE HEAT FLUX FROM THE
C***** EARTH'S SURFACE.
C*****
COMMON SIG(9), SIGE(10), AIRM(9), P(9), T(9), QM(9), TBIN(9), QBIN(9),
* AIJ(7), AIJAVE(2,9), AHEAT(4), DSIG(9), EVAP(20), PRECIP,
* LM, LMM1, LSTRAT, GRAV, LHE, RGAS, KAPA, MPLUME, SHA, SHW,
* PTOP, PSURF, AREA, TNEIBR, WORIG, STRANS, RCOEF,
* QINTOT, WFC1, SDEPTH, HC1DE, TG1(20), PRPREV, RUNO,
* FPLUME, FREEVA, FREEVB, TR(50), TB(50), NLMAX, MCCONT,
* AXCONS, BXCONS, BYTF, LHX, DTSTEP, KRAND, KSEED, KWET, KGWRUN,
* NONLIN, FSECT, WTR1(20), ASQIL(2,20), PPROB(20), SAMP,
* WTR2(20), WFC2, EVOUT, TS(20),
* P25OW(9), P75OW(9), AL1W(10), AL2W(10), AL3W(10), QSW1W(9), QSW2W(9),
* SRAD, SMEAN, HSWINT, HLWINT, HLWOTT, SHOUT,
* QCONVO, HCONVO, QCONVM, QCONVA, HCONVM, HCONVA, CONVW(9),
* IDACC(3), KTSTEP, KTZERO, KTTOT, NDIV, STORM, STATSO, GROW
REAL LHE, KAPA, LAT, LHX, LIQD, MPLUME, MLCLOUD, ML, MNEW
LOGICAL STORM, STATSO, GROW
DIMENSION QG(20), QS(20), CHI1(20), CH(20), BETA(20)
C*****
NSURF=10
DTSURF=DTSTEP/NSURF
SHOUT=0.
EVOUT=0.
C*****
C***** PERFORM CALCULATIONS NSURF TIMES
DO 900 NSTEP=1, NSURF
C*****
DO 10 K=1, NDIV
QG(K)=QSAT(TG1(K), PSURF)
10 CHI1(K)=WTR1(K)/(WFC1*FSECT)
C***** (CALCULATION OF BETA CAN BE LINEAR OR NONLINEAR)
DO 12 K=1, NDIV
12 BETA(K)=(1-NONLIN)*CHI1(K)+NONLIN*(CHI1(K)**.27)
C*****
C***** ASSUME ROUGHNESS LENGTH SO THAT LOG10(ZS/ZO)=2
ZS=30.
ZO=0.3
CDN=(0.35/LOG(ZS/ZO))**.2
VS=2.
Z1=500.
DELZ=Z1-ZS
DELU=2.
DELV=2.
C*****
C***** =====
C***** LOOP OVER GROUND DIVISIONS, FINDING CONSISTENT VALUES OF TS, QS
DO 500 K=1, NDIV
TS(K)=0.5*T(1)+0.5*TG1(K)
TSO=TS(K)
ITER=0
C*****
C***** SIMPLE TEST FOR STABILITY:

```

```

IF(T(1).LT.TG1(K)) GOTO 200
C****
C**** -----
C**** ATMOSPHERE IS STABLE WITH RESPECT TO THE GROUND.
C**** ITERATE UNTIL A PROPER VALUE OF TS IS FOUND.
C****
20 CONTINUE
TS(K)=0.5*(TSO+TS(K))
TSO=TS(K)
ITER=ITER+1
RIS=ZS*GRAV*(TS(K)-TG1(K))/(TG1(K)*(VS**2))
C****
DUMMY1=11.2+90.*RIS
DM=1./(1.+DUMMY1*RIS)
CD=DM*CDN
CHBYCD=1.35/(1.+1.93*RIS)
CH(K)=CHBYCD*CD
C****
DELT=T(1)-TS(K)
RI1=GRAV*DELT*DELZ/(T(1)*((DELU**2)+(DELV**2)))
AKEDC=60./(1.+50.*RI1)
C****
C**** OBTAIN NEW VALUE OF TS(K) (USING EQ. 54):
DUMMY1=CH(K)*VS
DUMMY2=AKEDC/(Z1-ZS)
TS(K)=(DUMMY1*TG1(K)+DUMMY2*T(1))/(DUMMY1+DUMMY2)
C****
C**** TEST FOR CONVERGENCE
IF(ABS(TSO-TS(K)).GT.0.001.AND.ITER.LT.100) GOTO 20
IF(ITER.GE.100) WRITE(92,1000) KTSTEP,TSO,TS(K)
1000 FORMAT(///1X,'PROGRAM STOPS IN SURFACE AFTER 100 ITERATIONS',
* /1X,'TIME STEP =',I10,' TSO,TS(K) =',2F10.2)
IF(ITER.GE.100) STOP
C****
IF(MOD(KTSTEP,2400).EQ.0.AND.NSTEP.EQ.1.AND.K.EQ.1)
* WRITE(92,8000) ITER,TS(K),TG1(K),T(1)
DUMMY1=CH(K)*VS
DUMMY2=AKEDC/(Z1-ZS)
Q1SPEC=QM(1)/AIRM(1)
QS(K)=(DUMMY1*QG(K)+DUMMY2*Q1SPEC)/(DUMMY1+DUMMY2)
C****
GOTO 500
C****
C**** -----
C**** ATMOSPHERE IS UNSTABLE WITH RESPECT TO GROUND
C**** ITERATE UNTIL A PROPER VALUE OF TS IS FOUND.
200 CONTINUE
C****
220 CONTINUE
TS(K)=0.5*(TSO+TS(K))
TSO=TS(K)
ITER=ITER+1
RIS=ZS*GRAV*(TS(K)-TG1(K))/(TG1(K)*(VS**2))
C****
DUMMY1=(1.-10.4*RIS)*(1.-0.845*RIS)
DUMMY2=1.-1.68*RIS
DM=(DUMMY1/DUMMY2)**0.5
CD=DM*CDN
DUMMY1=(1.-0.81*RIS)/(1.-0.14*RIS)

```

```

      CHBYCD=1.35*(DUMMY1**0.5)
      CH(K)=CD*CHBYCD
C****
      DELT=T(1)-TS(K)
      DTBYDZ=DELT/DELZ
      AKEDC=(60.-1.156E+07*DTBYDZ)/(1.-1.752E+04*DTBYDZ)
C****
C**** OBTAIN NEW VALUE OF TS(K) (USING EQ. 54):
      DUMMY1=CH(K)*VS
      DUMMY2=AKEDC/(Z1-ZS)
      TS(K)=(DUMMY1*TG1(K)+DUMMY2*T(1))/(DUMMY1+DUMMY2)
C****
C**** TEST FOR CONVERGENCE
      IF (ABS(TSO-TS(K)).GT.0.001.AND.ITER.LT.100) GOTO 220
      IF (ITER.GE.100) WRITE(92,1000) KTSTEP,TSO,TS(K)
      IF (ITER.GE.100) STOP
C****
      IF (MOD(KTSTEP,2400).EQ.0.AND.NSTEP.EQ.1.AND.K.EQ.1)
      * WRITE(92,8000) ITER,TS(K),TG1(K),T(1)
8000 FORMAT(1X,'ITERATION',I4,' TS(K),TG1(K),T(1) =',OP,3F10.2)
      DUMMY1=CH(K)*VS
      DUMMY2=AKEDC/(Z1-ZS)
      Q1SPEC=QM(1)/AIRM(1)
      QS(K)=(DUMMY1*QG(K)+DUMMY2*Q1SPEC)/(DUMMY1+DUMMY2)
C****
      500 CONTINUE
C**** =====
C****
      RHOA=1.20
      DO 540 K=1,NDIV
      EVAP(K)=BETA(K)*RHOA*CH(K)*VS*(QG(K)-QS(K))*DTSURF*FSECT*AREA
C      IF (EVAP(K).LT.0.) EVAP(K)=0.
      IF (EVAP(K).GT.WTR1(K)) EVAP(K)=WTR1(K)
      WTR1(K)=WTR1(K)-EVAP(K)
      540 CONTINUE
C****
      EVPTOT=0.
      DO 560 K=1,NDIV
      560 EVPTOT=EVPTOT+EVAP(K)
C****
      QM(1)=QM(1)+EVPTOT
      AIJ(4)=AIJ(4)+EVPTOT
      EVOUT=EVOUT+EVPTOT
C****
C**** SENSIBLE HEAT FLUX
      DO 700 K=1,NDIV
      SHF=SHA*RHOA*CH(K)*VS*(TG1(K)-TS(K))*DTSURF*AREA*FSECT
      SHOUT=SHOUT+SHF
      AHEAT(3)=AHEAT(3)+EVAP(K)*LHE
      AHEAT(4)=AHEAT(4)+SHF
      HC1=HC1DE*FSECT+WTR1(K)*SHW
      TG1(K)=TG1(K)-(SHF+EVAP(K)*LHE)/HC1
      T(1)=T(1)+SHF/(SHA*AIRM(1))
      700 CONTINUE
C****
      900 CONTINUE
      RETURN
      END
C**** -----

```

```

C**** ///////////////////////////////////////////////////////////////////
C**** -----
C**** SUBROUTINE GROUND
C****
C**** THIS SUBROUTINE IS A SIMPLIFIED VERSION OF SUBROUTINE GROUND IN
C**** THE NASA/GISS GCM. IT COMPUTES MOISTURE DIFFUSION BETWEEN SOIL LAYERS.
C****
COMMON SIG(9), SIGE(10), AIRM(9), P(9), T(9), QM(9), TBIN(9), QBIN(9),
* AIJ(7), AIJAVE(2,9), AHEAT(4), DSIG(9), EVAP(20), PRECIP,
* LM, LMM1, LSTRAT, GRAV, LHE, RGAS, KAPA, MPLUME, SHA, SHW,
* PTOP, PSURF, AREA, TNEIBR, WORIG, STRANS, RCOEF,
* QINTOT, WFC1, SDEPTH, HC1DE, TG1(20), PRPREV, RUNO,
* FPLUME, FREEVA, FREEVB, TR(50), TB(50), NLMAX, MCCONT,
* AXCONS, BXCONS, BYTF, LHX, DTSTEP, KRAND, KSEED, KWET, KGWRUN,
* NONLIN, FSECT, WTR1(20), ASOIL(2,20), PPROB(20), SAMP,
* WTR2(20), WFC2, EVOUT, TS(20),
* P25OW(9), P75OW(9), AL1W(10), AL2W(10), AL3W(10), QSW1W(9), QSW2W(9),
* SRAD, SMEAN, HSWINT, HLWINT, HLWOTT, SHOUT,
* QCONVO, HCONVO, QCONVM, QCONVA, HCONVM, HCONVA, CONVW(9),
* IDACC(3), KTSTEP, KTZERO, KTTOT, NDIV, STORM, STATSO, GROW
REAL LHE, KAPA, LAT, LHX, LIQD, MPLUME, MLOUD, ML, MNEW
LOGICAL STORM, STATSO, GROW

C**** IF(KGWRUN.EQ.0) GOTO 500
C**** -----
C**** COMPUTE FLUXES BETWEEN FIRST AND SECOND LAYERS
C**** (EQUATIONS 33,34 FROM MODEL PAPER)
F1BYF2=WFC1/WFC2
DO 480 K=1,NDIV
CHI1=WTR1(K)/(WFC1*FSECT)
CHI2=WTR2(K)/(WFC2*FSECT)

C****
C**** CHECK TO SEE IF DIFFUSION IS UPWARD OR DOWNWARD:
IF(CHI2.GT.CHI1) GOTO 300
C**** -----
C**** DOWNWARD DIFFUSION
TAUD12=24.*3600.
FLUX12=DTSTEP*(CHI2-CHI1)/TAUD12
C**** TEST THAT FLUX IS NOT EXCESSIVE
TEST=CHI1+FLUX12
IF(TEST.GT.1.) FLUX12=1.-CHI1
IF(TEST.LT.0.) FLUX12=-1.*CHI1
TEST=CHI2-FLUX12*F1BYF2
IF(TEST.GT.1.) FLUX12=-1.*(1.-CHI2)/F1BYF2
IF(TEST.LT.0.) FLUX12=CHI2/F1BYF2

C****
CHI1=CHI1+FLUX12
CHI2=CHI2-FLUX12*F1BYF2
WTR1(K)=CHI1*(WFC1*FSECT)
WTR2(K)=CHI2*(WFC2*FSECT)
GOTO 480
C**** -----
C**** UPWARD DIFFUSION
C**** FIRST CHECK TO SEE IF KTSTEP LIES IN GROWING SEASON
300 CONTINUE
IF(.NOT.GROW) GOTO 480
C****
C**** UPWARD DIFFUSION IS IMMEDIATE:

```

```

WTR12=WTR1(K)+WTR2(K)
WFC12=WFC1+WFC2
WTR1(K)=WTR12*(WFC1/WFC12)
WTR2(K)=WTR12*(WFC2/WFC12)
C****
480 CONTINUE
C**** -----
500 CONTINUE
RETURN
END
C**** -----
C**** //////////////////////////////////////
C**** -----
SUBROUTINE RADIA
C****
C**** THIS SUBROUTINE COMPUTES THE HEATING OR COOLING OF ATMOSPHERIC LAYERS
C**** BY SHORTWAVE AND LONGWAVE RADIATION. IT ALSO ALLOWS SHORTWAVE
C**** AND LONGWAVE RADIATION FLUXES TO ADJUST THE GROUND TEMPERATURE.
C****
COMMON SIG(9), SIGE(10), AIRM(9), P(9), T(9), QM(9), TBIN(9), QBIN(9),
* AIJ(7), AIJAVE(2,9), AHEAT(4), DSIG(9), EVAP(20), PRECIP,
* LM, LMM1, LSTRAT, GRAV, LHE, RGAS, KAPA, MPLUME, SHA, SHW,
* PTOP, PSURF, AREA, TNEIBR, WORIG, STRANS, RCOEF,
* QINTOT, WFC1, SDEPTH, HC1DE, TG1(20), PRPREV, RUNO,
* FPLUME, FREEVA, FREEVB, TR(50), TB(50), NLMAX, MCCONT,
* AXCONS, BXCONS, BYTF, LHX, DTSTEP, KRAND, KSEED, KWET, KGWRUN,
* NONLIN, FSECT, WTR1(20), ASOIL(2,20), PPROB(20), SAMP,
* WTR2(20), WFC2, EVOUT, TS(20),
* P25OW(9), P75OW(9), AL1W(10), AL2W(10), AL3W(10), QSW1W(9), QSW2W(9),
* SRAD, SMEAN, HSWINT, HLWINT, HLWOTT, SHOUT,
* QCONVO, HCONVO, QCONVM, QCONVA, HCONVM, HCONVA, CONVW(9),
* IDACC(3), KTSTEP, KTZERO, KTTOT, NDIV, STORM, STATSO, GROW
REAL LHE, KAPA, LAT, LHX, LIQD, MPLUME, MCLCUD, ML, MNEW
LOGICAL STORM, STATSO, GROW
DIMENSION QFRAC(9), ALWNET(10)
DATA D2, D3, D4, D5 / 0.847, 0.189, 0.513, 0.502 /
DATA E2, E3, E4, E5 / -.0008, -.00039, -.00149, -.00154 /
DATA F2, F3, F4, F5 / .00005, .00015, .00104, .00124 /
C****
SIGMA=5.67E-08
ALBDOG=0.15
C**** -----
C**** COMPUTE LONGWAVE COOLING OF ATMOSPHERE.
C**** (SEE HELD, LINDER, AND SUAREZ, 1981)
C****
C**** CALCULATE TEMPS AT 250 AND 750 MB:
T250=0.
T750=0.
DO 200 L=1, LM
T250=T250+P25OW(L)*T(L)
T750=T750+P75OW(L)*T(L)
200 CONTINUE
C****
C**** POTENTIAL TEMPERATURES AT 250 AND 750 MB:
TH750=T750*(PSURF/750)**KAPA
TH250=T250*(PSURF/250)**KAPA
C**** -----
C**** CALCULATE ATMOSPHERIC TEMP. AT SURFACE AND SLOPE OF PROFILE:

```

```

C****
P250=LOG(PSURF/250.)
P750=LOG(PSURF/750.)
PRATIO=P250/P750
TATMSU=(T750*PRATIO-T250)/(PRATIO-1.)
SLOPE=(T750-T250)/(P750-P250)
-----
C****
C**** CALCULATE THETA-BAR, THETA-HAT, AND DELTA T:
THBAR=0.5*(TH250+TH750)
THHAT=0.5*(TH250-TH750)
TG1AVE=0.
DO 205 K=1,NDIV
205 TG1AVE=TG1AVE+TG1(K)*FSECT
TDELTA=TG1AVE-TATMSU
-----
C****
C**** CALCULATE THE VALUES OF L1, L2, AND L3:
CALL LWFLUX(THBAR,THHAT,TDELTA,AL1,AL2,AL3)
-----
C****
C**** DISTRIBUTE RADIATIVE COOLING:
RAD1UP=SIGMA*(TG1AVE**4.)
AL3UP=RAD1UP-AL3
LMP1=LM+1
DO 210 L=1,LMP1
210 ALWNET(L)=AL1W(L)*AL1+AL2W(L)*AL2+AL3W(L)*AL3UP
-----
C****
C**** FIRST DAMP EDDY TEMPERATURES (USE 20-DAY TIME SCALE):
TAURAD=3600.*24.*20.
DO 250 L=1,LM
TCURVE=TATMSU+SLOPE*LOG(PSURF/P(L))
IF(L.GE.LSTRAT) TCURVE=TATMSU+SLOPE*LOG(PSURF/200.)
TEDDY=T(L)-TCURVE
250 T(L)=T(L)-(TEDDY/TAURAD)*DTSTEP
-----
C****
C****
LSM1=LSTRAT-1
DO 280 L=1,LSM1
280 T(L)=T(L)+(ALWNET(L)-ALWNET(L+1))*AREA*DTSTEP/(AIRM(L)*SHA)
-----
C****
C**** SHORTWAVE HEATING OF ATMOSPHERE. (SEE P. 1925-1926 OF HELD
C**** AND SUAREZ, 1981.)
C****
S2=D2+(THBAR-300)*E2+THHAT*F2
S3=D3+(THBAR-300)*E3+THHAT*F3
S4=D4+(THBAR-300)*E4+THHAT*F4
S5=D5+(THBAR-300)*E5+THHAT*F5
-----
C****
QSW1=SRAD*(0.9-S2)*DTSTEP*AREA
QSW2=SRAD*(S2-S3-S4*(1.-ALBDOG)-S5*ALBDOG)*DTSTEP*AREA
DO 300 L=1,LM
HEAT=QSW1*QSW1W(L)+QSW2*QSW2W(L)
T(L)=T(L)+HEAT/(AIRM(L)*SHA)
300 CONTINUE
-----
C****
C**** HEAT SOIL. GROUND ALBEDO IS SET TO 0.15.
C****
HSWINT=0.

```

```

HLWINT=0.
HLWOTT=0.
DO 100 K=1,NDIV
HSWIN=SRAD*S4*(1.-ALBDOG)*DTSTEP*AREA*FSECT
HLWIN=AL3*DTSTEP*AREA*FSECT
HLWOT=SIGMA*(TG1(K)**4)*DTSTEP*AREA*FSECT
HSWINT=HSWINT+HSWIN
HLWINT=HLWINT+HLWIN
HLWOTT=HLWOTT+HLWOT
AHEAT(1)=AHEAT(1)+HSWIN+HLWIN
AHEAT(2)=AHEAT(2)+HLWOT
HC1=HC1DE*FSECT+WTR1(K)*SHW
100 TG1(K)=TG1(K)+(HSWIN+HLWIN-HLWOT)/HC1
IDACC(3)=IDACC(3)+1

```

```

C*****
RETURN
END

```

```

C*****
C*****
C*****

```

SUBROUTINE LWFLUX(THBAR,THAT,TDELTA,AL1,AL2,AL3)

```

C*****
C***** THIS SUBROUTINE CALCULATES VALUES OF RADIATION CONSTANTS USING
C***** THE TABLE PROVIDED BY HELD, LINDER AND SUAREZ, JOURNAL OF THE
C***** ATMOSPHERIC SCIENCES, 38, P.1911-1927, 1981. (SEE PAGE 1925.)
C*****

```

```

DIMENSION THTAB(21)
DIMENSION A1(21),B1(21),C1(21),A2(21),B2(21),C2(21),A3(21),B3(21)

```

```

C*****
DATA THTAB/ -30., -25., -20., -15., -10., -5.,
*           0., 5., 10., 15., 20., 25.,
*           30., 35., 40., 45., 50., 55.,
*           60., 65., 70./
DATA A1/ 109.0, 118.0, 127.4, 136.9, 146.8, 156.8,
*        167.2, 177.6, 188.3, 199.2, 210.0, 221.0,
*        232.1, 243.2, 254.2, 265.0, 275.6, 286.1,
*        296.2, 306.0, 315.6/
DATA B1/ -1.10, -1.16, -1.22, -1.26, -1.30, -1.34,
*        -1.37, -1.40, -1.42, -1.43, -1.44, -1.44,
*        -1.43, -1.41, -1.39, -1.35, -1.30, -1.24,
*        -1.16, -1.08, -0.98/
DATA C1/ 1.00, 1.01, 1.01, 1.01, 1.01, 1.01,
*        1.01, 1.01, 0.99, 0.97, 0.95, 0.92,
*        0.88, 0.83, 0.77, 0.68, 0.59, 0.48,
*        0.39, 0.30, 0.24/
DATA A2/ 121.3, 131.0, 140.8, 150.6, 160.0, 168.3,
*        176.4, 183.7, 190.6, 197.0, 202.8, 208.1,
*        213.1, 217.6, 221.7, 225.0, 227.8, 230.2,
*        231.9, 233.0, 233.6/
DATA B2/ -2.18, -2.29, -2.38, -2.47, -2.52, -2.55,
*        -2.60, -2.64, -2.68, -2.72, -2.74, -2.75,
*        -2.76, -2.75, -2.73, -2.69, -2.65, -2.60,
*        -2.53, -2.45, -2.36/
DATA C2/ 1.26, 1.25, 1.25, 1.25, 1.26, 1.26,
*        1.26, 1.25, 1.24, 1.21, 1.18, 1.15,
*        1.10, 1.04, 0.96, 0.85, 0.74, 0.61,
*        0.48, 0.37, 0.29/
DATA A3/ 104.3, 119.1, 134.7, 150.9, 167.8, 185.7,
*        204.9, 225.7, 248.1, 271.9, 297.1, 323.6,

```



```

1010 FORMAT(///1X,20('---'),/1X,
* 'CONDITIONS AFTER ',I6,' TIME STEPS')
WRITE(92,1015)
1015 FORMAT(13X,'T',8X,'Q REL')
DO 60 LPRIME=1,LM
L=LM+1-LPRIME
QREL(L)=QM(L)/(AIRM(L)*QSAT(T(L),P(L)))
60 WRITE(92,1017) T(L),QREL(L)
1017 FORMAT(1X,2F13.5)
WRITE(92,1018)
1018 FORMAT(1X,' NDIV')
WRITE(92,1019) NDIV
1019 FORMAT(1X,I13)
WRITE(92,1020)
1020 FORMAT(13X,'K',7X,'TG1(K)',6X,'CHI1(K)',6X,'CHI2(K)')
DO 62 K=1,20
SAT=WTR1(K)/(WFC1*FSECT)
SAT2=WTR2(K)/(WFC2*FSECT)
62 WRITE(92,1021) K,TG1(K),SAT,SAT2
1021 FORMAT(1X,I13,3F13.5)
C****
C**** -----
C****
SCALE=100./AIJ(5)
SECS=(KTTOT-KTZERO)*DTSTEP
YRSEC=365.*24.*3600.
ADVMM=((AIJ(5)/AREA)/SECS)*YRSEC
WRITE(92,1022) AIJ(5),ADVMM
1022 FORMAT(/1X,'TOTAL WATER ADVECTED IN =' ,1PE13.5,
* ' (' ,OPF9.2,' mm/yr)')
C****
PRSCAL=AIJ(1)*SCALE
PRMM=(AIJ(1)/AREA)*(YRSEC/SECS)
WRITE(92,1023) PRSCAL,PRMM
1023 FORMAT(1X,'SCALED TOTAL PRECIP =' ,F7.2,' (' ,F9.2,' mm/yr)')
C****
EVSCL=AIJ(4)*SCALE
EVMM=(AIJ(4)/AREA)*(YRSEC/SECS)
WRITE(92,1035) EVSCL,EVMM
1035 FORMAT(1X,'SCALED TOTAL EVAP =' ,F7.2,' (' ,F9.2,' mm/yr)')
C****
QFLXIN=AIJ(5)*SCALE
QFINMM=(AIJ(5)/AREA)*(YRSEC/SECS)
QFLXOT=AIJ(2)*SCALE
QFOTMM=(AIJ(2)/AREA)*(YRSEC/SECS)
RUNFLX=AIJ(3)*SCALE
RUNMM=(AIJ(3)/AREA)*(YRSEC/SECS)
WRITE(92,1040) QFLXIN,QFINMM,QFLXOT,QFOTMM,RUNFLX,RUNMM
1040 FORMAT(/1X,'Q ADVECTED IN (SCALED) =' ,F7.2,' (' ,F9.2,
* ' mm/yr) ',/1X,'Q ADVECTED OUT (SCALED) =' ,F7.2,' (' ,
* F9.2,' mm/yr) ',/1X,' RUNOFF (SCALED) =' ,F7.2,' (' ,
* F9.2,' mm/yr)')
C****
RELHUM=AIJAVE(1,1)/IDACC(1)
WRITE(92,1052) RELHUM
1052 FORMAT(/1X,'AVERAGE RELATIVE HUMIDITY IN BOTTOM LAYER =' ,F8.4)
RATIO=AIJ(3)/(AIJ(1)+1.E-30)
WRITE(92,1053) RATIO
1053 FORMAT(1X,'RUNOFF/PRECIP RATIO =' ,F7.4)

```

```

C*****
WRITE(92,1055)
1055 FORMAT(/1X,'AVERAGE SOIL CONDITIONS:')
DO 65 K=1,NDIV
TAVE=ASOIL(2,K)/IDACC(2)
SAT=(ASOIL(1,K)/IDACC(2))/(WFC1+FSECT)
65 WRITE(92,1057) K,TAVE,SAT
1057 FORMAT(1X,'K =',I4,' GROUND TEMP =',F8.2,' SAT =',F8.4)
C*****
IF(AHEAT(3).EQ.0.) GOTO 68
RATIO=AHEAT(4)/AHEAT(3)
WRITE(92,1060) RATIO
1060 FORMAT(/1X,'SENSIBLE-TO-LATENT HEAT TRANSFER RATIO =',1PE10.2)
RATLW=AHEAT(2)*100./AHEAT(1)
RATLH=AHEAT(3)*100./AHEAT(1)
RATSH=AHEAT(4)*100./AHEAT(1)
WRITE(92,1065) RATLW,RATLH,RATSH
1065 FORMAT(1X,'% OF HEAT OUT: LW =',F8.3,
* ' LH =',F8.3,' SH =',F8.3)
C*****
68 QTOT=0.
DO 69 K=1,NDIV
69 QTOT=QTOT+WTR1(K)+WTR2(K)
DO 70 L=1,LM
70 QTOT=QTOT+QM(L)
DIFQ=(QTOT-WORIG)*SCALE
WRITE(92,1070) DIFQ
1070 FORMAT(/1X,'SCALED CHANGE IN WATER STORAGE (SINCE BEGINNING) =',
* F7.2)
DIFQP=(AIJ(5)-AIJ(2)-AIJ(3))*SCALE
WRITE(92,1080) DIFQP
1080 FORMAT(1X,'CHANGE PREDICTED FROM WATER BALANCE:
* F7.2)
C*****
C***** COMPUTE MEANS FROM TR, TB PDF'S:
NWET=0
NDRY=0
DO 80 K=1,50
NWET=NWET+TR(K)
80 NDRY=NDRY+TB(K)
C*****
TRMEAN=0.
TBMEAN=0.
DO 90 K=1,50
TRMEAN=TRMEAN+K*TR(K)/(NWET+1.E-20)
90 TBMEAN=TBMEAN+K*TB(K)/(NDRY+1.E-20)
C*****
WRITE(92,1090) NWET,TRMEAN,NDRY,TBMEAN
1090 FORMAT(/1X,I5,' WET PERIODS: MEAN LENGTH =',F6.2,' TIME STEPS',
* /1X,I5,' DRY PERIODS: MEAN LENGTH =',F6.2,' TIME STEPS')
C*****
DUM=MCCONT
ALMAX=NLMAX/(DUM+1.E-20)
WRITE(92,1092) ALMAX
1092 FORMAT(/1X,'MC CHARACTERISTICS: AVE. LMAX =',F6.2,
* /1X,' WHEN LMIN = 1')
C*****
RETURN
END

```

```

C**** -----
C**** //////////////////////////////////////
C**** -----
SUBROUTINE CHECKT(NCHK)
C****
C**** THIS SUBROUTINE IS CALLED AFTER EACH OTHER SUBROUTINE AND HAS BEEN
C**** USED IN THE PAST TO DEBUG THE MODEL. PRESENTLY IT IS BEING USED TO
C**** INTEGRATE MODEL VARIABLES OVER TIME.
C****
COMMON SIG(9),SIGE(10),AIRM(9),P(9),T(9),QM(9),TBIN(9),QBIN(9),
* AIJ(7),AIJAVE(2,9),AHEAT(4),DSIG(9),EVAP(20),PRECIP,
* LM,LMM1,LSTRAT,GRAV,LHE,RGAS,KAPA,MPLUME,SHA,SHW,
* PTOP,PSURF,AREA,TNEIBR,WORIG,STRANS,RCOEF,
* QINTOT,WFC1,SDEPTH,HC1DE,TG1(20),PRPREV,RUNO,
* FPLUME,FREEVA,FREEVB,TR(50),TB(50),NLMAX,MCCONT,
* AXCONS,BXCONS,BYTF,LHX,DTSTEP,KRAND,KSEED,KWET,KGWRUN,
* NONLIN,FSECT,WTR1(20),ASOIL(2,20),PPROB(20),SAMP,
* WTR2(20),WFC2,EVOU,TS(20),
* P25OW(9),P75OW(9),AL1W(10),AL2W(10),AL3W(10),QSW1W(9),QSW2W(9),
* SRAD,SMEAN,HSWINT,HLWINT,HLWOTT,SHOUT,
* QCONVO,HCONVO,QCONVM,QCONVA,HCONVM,HCONVA,CONVW(9),
* IDACC(3),KTSTEP,KTZERO,KTOT,NDIV,STORM,STATSO,GROW
REAL LHE,KAPA,LAT,LHX,LIQD,MPLUME,MCLOUD,ML,MNEW
LOGICAL STORM,STATSO,GROW
DIMENSION QREL(9)
C****
IF(NCHK.NE.8) RETURN
C****
C**** INITIALIZE SUMS IN FIRST TIME STEP:
C**** IF(KTSTEP.NE.1) GOTO 50
CHISUM=0.
CH2SUM=0.
TMPSUM=0.
EVPSUM=0.
RUNSUM=0.
PRCSUM=0.
SHSUM=0.
QSUM=0.
Q1SUM=0.
QGSUM=0.
DEFSUM=0.
Q1SSUM=0.
T1SUM=0.
SENSUM=0.
HSWSUM=0.
HLWSUM=0.
C****
50 CONTINUE
C**** -----
C**** NOW ADD TO SUMS AT EACH TIME STEP
WTOT=0.
W2TOT=0.
AVETMP=0.
DO 170 K=1,NDIV
WTOT=WTOT+WTR1(K)
W2TOT=W2TOT+WTR2(K)
170 AVETMP=AVETMP+TG1(K)*FSECT
CHIAVE=WTOT/WFC1
CH2AVE=W2TOT/WFC2

```

```

C****
  SHTOT=0.
  QTOT=0.
  DO 180 L=1,LM
  SHTOT=SHTOT+T(L)*AIRM(L)*SHA
180 QTOT=QTOT+QM(L)
C****
C**** (CALCULATE TEMP OF LAYER 1 PARCEL WHEN RAISED TO LEVEL 2)
  T1TO2=T(1)*(P(2)/P(1))**KAPA
C****
  CHISUM=CHISUM+CH1AVE
  CH2SUM=CH2SUM+CH2AVE
  TMPSUM=TMPSUM+AVETMP
  EVPSUM=EVPSUM+EVOUT
  RUNSUM=RUNSUM+RUNO
  PRCSUM=PRCSUM+PRECIP
  SHSUM=SHSUM+SHTOT
  QSUM=QSUM+QTOT
  Q1SUM=Q1SUM+QM(1)
C
  Q1SUM=Q1SUM+QM(1)/AIRM(1)
  QGSUM=QGSUM+QSAT(AVETMP,PSURF)
  DEFSUM=DEFSUM+(QSAT(AVETMP,PSURF)-(QM(1)/AIRM(1)))
  Q1SSUM=Q1SSUM+QSAT(T1TO2,P(2))*AIRM(1)
  T1SUM=T1SUM+T(1)
  SENSUM=SENSUM+SHOUT
  HSWSUM=HSWSUM+HSWINT
  HLWSUM=HLWSUM+HLWINT-HLWOTT
C****
C****
  KFLAG=0
  IWRITE=240
  IF(KTSTEP.GT.4800.AND.KTSTEP.LE.5040) IWRITE=1
  IF(MOD(KTSTEP,IWRITE).EQ.0) KFLAG=1
  TINT=IWRITE
C****
  IF(KFLAG.EQ.0) RETURN
C****
C**** SPECIAL DIAGNOSTICS
C****
  CHISUM=CHISUM/TINT
  CH2SUM=CH2SUM/TINT
  TMPSUM=TMPSUM/TINT
  EVPSUM=EVPSUM/TINT
  RUNSUM=RUNSUM/TINT
  PRCSUM=PRCSUM/TINT
  SHSUM=SHSUM/TINT
  QSUM=QSUM/TINT
  Q1SUM=Q1SUM/TINT
  QGSUM=QGSUM/TINT
  DEFSUM=DEFSUM/TINT
  Q1SSUM=Q1SSUM/TINT
  T1SUM=T1SUM/TINT
  SENSUM=SENSUM/TINT
  HSWSUM=HSWSUM/TINT
  HLWSUM=HLWSUM/TINT
  HEVSUM=EVPSUM*LHE
C****
  KWRITE=IWRITE*10
  IF(MOD(KTSTEP,KWRITE).EQ.0) WRITE(92,1200)

```

```

1200 FORMAT(/1X,' STEP SAT1 SAT2 TEMP LAT HEAT',
* ' PRECIP SEN HEAT SW HEAT RUNOFF',
* '/1X,' OUT IN ' OUT',
* WRITE(92,1201) KTSTEP,CHISUM,CH2SUM,TMPSUM,HEVSUM,
* PRCSUM,SENSUM,HSWSUM,RUNSUM
1201 FORMAT(1X,'*',I6,F6.3,F6.3,F10.2,1P,5E10.2)
C 1200 FORMAT(/1X,' STEP SAT TEMP EVAP RUNOFF',
C * ' PRECIP Q1SSUM Q1SUM T1SUM')
C WRITE(92,1201) KTSTEP,CHISUM,CH2SUM,HEVSUM,RUNSUM,
C * PRCSUM,Q1SSUM,Q1SUM,T1SUM
C 1201 FORMAT(1X,I6,F6.3,F7.2,1P5E10.2,OP1F10.3)
C 1200 FORMAT(/1X,' STEP SAT TEMP EVAP RUNOFF',
C * ' PRECIP DEFSUM QGSUM Q1SUM')
C WRITE(92,1201) KTSTEP,CHISUM,CH2SUM,HEVSUM,RUNSUM,
C * PRCSUM,DEFSUM,QGSUM,Q1SUM
C 1200 FORMAT(/1X,' STEP SAT TEMP EVAP RUNOFF',
C * ' PRECIP SHTOT QSUM Q1SUM')
C WRITE(92,1201) KTSTEP,CHISUM,CH2SUM,HEVSUM,RUNSUM,
C * PRCSUM,SHSUM,QSUM,Q1SUM
C 1201 FORMAT(1X,I6,F6.3,F7.2,1P6E10.2)
CHISUM=0.
CH2SUM=0.
TMPSUM=0.
EVPSUM=0.
RUNSUM=0.
PRCSUM=0.
DEFSUM=0.
QGSUM=0.
Q1SUM=0.
SHSUM=0.
QSUM=0.
Q1SSUM=0.
T1SUM=0.
SENSUM=0.
HSWSUM=0.
HLWSUM=0.
HEVSUM=0.
C****
C**** STORE TIME STEP IN TEMPORARY FILE
C OPEN(UNIT=93,FILE=' [KOSTER] TSTEP.DAT',STATUS='NEW',RECL=80)
C WRITE(93,3000) KTSTEP
C 3000 FORMAT(/1X,'PROGRAM TMJ: CURRENT TIME STEP IS',I10)
C CLOSE(UNIT=93)
C****
RETURN
C**** -----
C****
END

```

INPUT COMMAND FILE

The command file is specific to the VAX/VMS computer operating system. The program reads from the command file the names of the input and output files, in this case being [KOSTER.TMJ]TQ_TMJ9.DAT AND [KOSTER.TMJ]OUT_TMJ9.DAT, respectively. The command file need not be used when running the program on some other computer system, as long as the data file names are specified in some other way.

```
$ SD [KOSTER.TMJ]
$ SET VERIFY
$ SET NOON
$ RUN TMJ9
[KOSTER.TMJ]TQ_TMJ9.DAT
[KOSTER.TMJ]OUT_TMJ9.DAT
$ EXIT
```

SAMPLE INPUT FILE

The first line of the input file provides the title for the simulation. The next five lines describe how the simulation will be run, specifying respectively the total number of time steps, the time step at which diagnostics are zeroed, the evaporation function used, the use or disuse of the lower soil layer, and the method used to assign storm water to a specific land section. The "EVAP FUNCTION" is 0 if evaporation is to be linearly related to soil saturation and 1 if a nonlinear relationship is to be used. Under "2ND SOIL LAYER", a value of 1 indicates that the simulation employs the lower soil layer, while a value of 0 allows only one layer to represent the soil. A "FRAC WETTING" value of 1 specifies the use of the Section 5.4.1 fractional wetting parameterization, while a value of 0 specifies the simpler parameterization described in Section 5.4.3.

Various model parameters are set on the following four lines. Their definitions can be found at the beginning of the program listing. EMPTY0, EMPTY1, and EMPTY2 are currently not used by the program. STRANS, a transient studies parameter, is used only when it is given a positive value. RCOEF corresponds to the coefficient $1/2$ in Equation 5-5.

The columns of numbers below the headings T and Q REL indicate initial values for the temperatures and relative humidities in the atmospheric column, ordered so that the first row listed represents the top layer. Presumably, these values can be quite arbitrary, since the model climate will lose all memory of its initial conditions. As the program currently stands, the initial temperature values are reassigned anyway, so that the temperatures in the input file are not used at all.

After specifying the number of sections into which the land surface is divided (or, for the simplified fractional wetting parameterization, the reciprocal [an integer] of the wetted fraction size), the input file assigns the initial temperatures and soil saturations of each section. Twenty sections are listed even if only one is assumed. The probabilities listed on the far right are relative; they are normalized within the program.

SAMPLE RUN

TIME STEPS: 17520
 ZERDING: 8760
 EVAP FUNCTION: 0
 2ND SOIL LAYER: 1
 FRAC WETTING: 1
 FPLUME FREEVA FREEVB QCONVM QCONVA HCONVM HCONVA
 0.500 0.250 0.500 9.20E-6 6.83E-6 -34.0 39.8
 EMPTYO DTSTEP EMPTY1 SDEPTH EMPTY2 STRANS RCOEF
 0.000 3600.000 0.000 0.100 0.000 -0.500 0.500

T Q REL
 218.46000 0.70000
 238.83000 0.70000
 254.13000 0.80000
 265.24000 0.80000
 280.70000 0.80000
 289.91000 0.90000
 293.24000 0.90000
 296.64000 0.95000
 297.92000 0.95000

NDIV

1

	TG1 (K)	SAT (K)	PPROB (K)
1	293.00000	1.00000	1.00000
2	293.00000	1.00000	1.00000
3	293.00000	1.00000	1.00000
4	293.00000	1.00000	1.00000
5	293.00000	1.00000	1.00000
6	293.00000	1.00000	1.00000
7	293.00000	1.00000	1.00000
8	293.00000	1.00000	1.00000
9	293.00000	1.00000	1.00000
10	293.00000	1.00000	1.00000
11	293.00000	1.00000	1.00000
12	293.00000	1.00000	1.00000
13	293.00000	1.00000	1.00000
14	293.00000	1.00000	1.00000
15	293.00000	1.00000	1.00000
16	293.00000	1.00000	1.00000
17	293.00000	1.00000	1.00000
18	293.00000	1.00000	1.00000
19	293.00000	1.00000	1.00000
20	293.00000	1.00000	1.00000

SAMPLE OUTPUT FILE

The sample output file first lists the date and time of the run and then shows the input file used, in its entirety. The assumed heat and moisture convergence profile is presented.

Time series of simulation data then begin. The file lists time-integrated values of soil saturation (for both the upper and the lower soil layers), upper soil layer temperature (in degrees K), latent heat released from the surface, precipitation, sensible heat released from the surface, incoming shortwave radiation, and surface runoff. These values are average hourly values for a land surface area of 10^{12} square meters. The time integration normally proceeds over 10 days; for a certain ten-day period in the first simulation year, however, values are listed for each simulation hour.

This particular data file corresponds to the uniform wetting simulation that was compared to the fractional wetting simulations in Section 5.4. Diagnostics were zeroed after one year. Annual mean values of the climate variables computed during the second year are presented at the end of the data file. Water fluxes are expressed in mm/year and also relative to the net water convergence in the atmospheric column.

INPUT FILE USED:

SAMPLE RUN

TIME STEPS:	17520					
ZEROING:	8760					
EVAP FUNCTION:	0					
2ND SOIL LAYER:	1					
FRAC WETTING:	1					
FPLUME	FREEVA	FREEVB	QCONVM	QCONVA	HCONVM	HCONVA
0.500	0.250	0.500	9.20E-6	6.83E-6	-34.0	39.8
EMPTYO	DTSTEP	EMPTY1	SDEPTH	EMPTY2	STRANS	RCOEF
0.000	3600.000	0.000	0.100	0.000	-0.500	0.500

	T	Q REL
218.46000		0.70000
238.83000		0.70000
254.13000		0.80000
265.24000		0.80000
280.70000		0.80000
289.91000		0.90000
293.24000		0.90000
296.64000		0.95000
297.92000		0.95000

NDIV

1

	TG1 (K)	SAT (K)	PPROB (K)
1	293.00000	1.00000	1.00000
2	293.00000	1.00000	1.00000
3	293.00000	1.00000	1.00000
4	293.00000	1.00000	1.00000
5	293.00000	1.00000	1.00000
6	293.00000	1.00000	1.00000
7	293.00000	1.00000	1.00000
8	293.00000	1.00000	1.00000
9	293.00000	1.00000	1.00000
10	293.00000	1.00000	1.00000
11	293.00000	1.00000	1.00000
12	293.00000	1.00000	1.00000
13	293.00000	1.00000	1.00000
14	293.00000	1.00000	1.00000
15	293.00000	1.00000	1.00000
16	293.00000	1.00000	1.00000
17	293.00000	1.00000	1.00000
18	293.00000	1.00000	1.00000
19	293.00000	1.00000	1.00000
20	293.00000	1.00000	1.00000

```

////////////////////////////////////
SAMPLE RUN
////////////////////////////////////

```

WEIGHTINGS USED FOR HEAT AND MOISTURE CONVERGENCE:

L = 9	CONVW(L) =	0.017	(BY MASS:	2.74086E-05)	P =	26.90
L = 8	CONVW(L) =	0.027	(BY MASS:	3.28285E-05)	P =	104.94
L = 7	CONVW(L) =	0.046	(BY MASS:	4.16786E-05)	P =	205.76
L = 6	CONVW(L) =	0.080	(BY MASS:	5.68246E-05)	P =	328.90
L = 5	CONVW(L) =	0.139	(BY MASS:	8.31448E-05)	P =	480.42
L = 4	CONVW(L) =	0.226	(BY MASS:	1.27103E-04)	P =	650.12
L = 3	CONVW(L) =	0.263	(BY MASS:	1.87194E-04)	P =	806.96
L = 2	CONVW(L) =	0.169	(BY MASS:	2.01868E-04)	P =	917.37
L = 1	CONVW(L) =	0.032	(BY MASS:	6.17398E-05)	P =	984.26

SUM OF WEIGHTS = 1.000

*	240	0.998	1.000	262.35	4.24E+16	8.44E+10	3.47E+16	2.78E+17	6.75E+10
*	480	0.999	1.000	260.20	2.95E+16	7.00E+10	2.95E+16	2.87E+17	5.84E+10
*	720	0.999	1.000	259.20	3.29E+16	7.01E+10	3.76E+16	3.03E+17	5.70E+10
*	960	0.999	1.000	258.71	4.02E+16	7.07E+10	4.82E+16	3.26E+17	5.44E+10
*	1200	0.999	1.000	258.79	4.73E+16	6.99E+10	6.47E+16	3.54E+17	5.10E+10
*	1440	0.999	1.000	259.67	6.46E+16	7.28E+10	7.79E+16	3.92E+17	4.71E+10
*	1680	0.997	1.000	261.19	8.54E+16	7.67E+10	9.34E+16	4.33E+17	4.29E+10
*	1920	0.990	1.000	263.18	1.10E+17	8.20E+10	1.08E+17	4.75E+17	4.06E+10
*	2160	0.944	1.000	265.53	1.39E+17	8.82E+10	1.22E+17	5.16E+17	4.15E+10
ITERATION 15				TS(K),TG1(K),T(1) =	272.63	265.98	272.63		

	STEP	SAT1	SAT2	TEMP	LAT HEAT OUT	PRECIP	SEN HEAT OUT	SW HEAT IN	RUNOFF
*	2400	0.855	1.000	268.30	1.69E+17	9.46E+10	1.36E+17	5.59E+17	4.03E+10
*	2640	0.738	1.000	271.70	1.99E+17	1.02E+11	1.51E+17	6.02E+17	3.74E+10
*	2880	0.613	1.000	275.20	2.26E+17	1.06E+11	1.69E+17	6.41E+17	3.24E+10
*	3120	0.896	0.893	278.07	3.03E+17	1.33E+11	1.26E+17	6.74E+17	5.96E+10
*	3360	0.831	0.828	280.67	3.33E+17	1.42E+11	1.30E+17	7.01E+17	5.86E+10
*	3600	0.762	0.759	283.15	3.61E+17	1.49E+11	1.34E+17	7.26E+17	5.64E+10
*	3840	0.694	0.690	285.71	3.81E+17	1.54E+11	1.38E+17	7.44E+17	5.31E+10
*	4080	0.627	0.621	288.02	3.95E+17	1.57E+11	1.43E+17	7.56E+17	4.86E+10
*	4320	0.561	0.556	290.08	4.05E+17	1.57E+11	1.46E+17	7.59E+17	4.36E+10
*	4560	0.501	0.496	291.77	4.05E+17	1.58E+11	1.51E+17	7.56E+17	3.93E+10
ITERATION 16				TS(K),TG1(K),T(1) =	293.38	288.22	293.38		

	STEP	SAT1	SAT2	TEMP	LAT HEAT OUT	PRECIP	SEN HEAT OUT	SW HEAT IN	RUNOFF
*	4800	0.451	0.444	293.19	3.99E+17	1.59E+11	1.53E+17	7.46E+17	3.52E+10
*	4801	0.420	0.420	286.58	-1.02E+14	0.00E+00	-4.53E+14	0.00E+00	0.00E+00
*	4802	0.420	0.420	285.87	-1.06E+14	0.00E+00	-3.74E+14	0.00E+00	0.00E+00
*	4803	0.420	0.420	285.22	-1.03E+14	0.00E+00	-3.19E+14	0.00E+00	0.00E+00
*	4804	0.444	0.420	284.71	-5.30E+13	9.67E+11	-3.64E+14	0.00E+00	2.03E+11
*	4805	0.443	0.420	285.05	-5.97E+13	0.00E+00	-3.27E+14	1.36E+17	0.00E+00
*	4806	0.442	0.420	287.70	-5.89E+13	0.00E+00	-3.64E+14	5.35E+17	0.00E+00
*	4807	0.441	0.420	292.26	1.65E+14	0.00E+00	-8.67E+14	9.10E+17	0.00E+00
*	4808	0.438	0.421	297.36	1.65E+17	0.00E+00	5.45E+15	1.24E+18	0.00E+00
*	4809	0.429	0.421	299.60	6.72E+17	0.00E+00	2.50E+17	1.52E+18	0.00E+00

	STEP	SAT1	SAT2	TEMP	LAT HEAT OUT	PRECIP	SEN HEAT OUT	SW HEAT IN	RUNOFF
*	4810	0.420	0.420	301.52	8.18E+17	0.00E+00	3.48E+17	1.73E+18	0.00E+00
*	4811	0.418	0.418	303.05	9.23E+17	0.00E+00	4.13E+17	1.85E+18	0.00E+00
*	4812	0.430	0.418	302.77	1.19E+18	1.08E+12	5.27E+17	1.89E+18	2.26E+11

*	4813	0.418	0.418	303.41	1.05E+18	0.00E+00	4.48E+17	1.85E+18	0.00E+00
*	4814	0.424	0.418	302.08	1.20E+18	8.49E+11	5.25E+17	1.72E+18	1.78E+11
*	4815	0.417	0.417	301.58	9.62E+17	0.00E+00	3.90E+17	1.51E+18	0.00E+00
*	4816	0.415	0.415	300.48	8.41E+17	0.00E+00	3.17E+17	1.24E+18	0.00E+00
*	4817	0.426	0.415	297.37	8.78E+17	8.91E+11	3.26E+17	9.05E+17	1.85E+11
*	4818	0.419	0.415	295.34	5.11E+17	0.00E+00	1.31E+17	5.32E+17	0.00E+00
*	4819	0.416	0.415	292.92	2.71E+17	0.00E+00	3.22E+16	1.34E+17	0.00E+00

	STEP	SAT1	SAT2	TEMP	LAT HEAT OUT	PRECIP	SEN HEAT OUT	SW HEAT IN	RUNOFF
*	4820	0.416	0.415	291.51	1.84E+16	0.00E+00	-5.58E+15	0.00E+00	0.00E+00
*	4821	0.416	0.415	290.32	1.68E+15	0.00E+00	-2.03E+15	0.00E+00	0.00E+00
*	4822	0.415	0.415	289.27	2.93E+14	0.00E+00	-1.15E+15	0.00E+00	0.00E+00
*	4823	0.415	0.415	288.32	1.11E+12	0.00E+00	-7.75E+14	0.00E+00	0.00E+00
*	4824	0.415	0.415	287.46	-7.86E+13	0.00E+00	-5.75E+14	0.00E+00	0.00E+00
*	4825	0.415	0.415	286.68	-1.01E+14	0.00E+00	-4.54E+14	0.00E+00	0.00E+00
*	4826	0.415	0.415	285.97	-1.05E+14	0.00E+00	-3.75E+14	0.00E+00	0.00E+00
*	4827	0.415	0.415	285.33	-1.02E+14	0.00E+00	-3.20E+14	0.00E+00	0.00E+00
*	4828	0.415	0.415	284.73	-9.75E+13	0.00E+00	-2.81E+14	0.00E+00	0.00E+00
*	4829	0.441	0.415	285.07	-5.91E+13	1.01E+12	-3.20E+14	1.33E+17	2.10E+11

	STEP	SAT1	SAT2	TEMP	LAT HEAT OUT	PRECIP	SEN HEAT OUT	SW HEAT IN	RUNOFF
*	4830	0.440	0.416	287.72	-5.85E+13	0.00E+00	-3.56E+14	5.32E+17	0.00E+00
*	4831	0.439	0.416	292.29	1.49E+14	0.00E+00	-8.39E+14	9.07E+17	0.00E+00
*	4832	0.436	0.416	297.46	1.56E+17	0.00E+00	3.52E+15	1.24E+18	0.00E+00
*	4833	0.427	0.416	299.70	6.72E+17	0.00E+00	2.48E+17	1.52E+18	0.00E+00
*	4834	0.416	0.416	301.64	8.18E+17	0.00E+00	3.47E+17	1.72E+18	0.00E+00
*	4835	0.414	0.414	303.17	9.22E+17	0.00E+00	4.13E+17	1.85E+18	0.00E+00
*	4836	0.426	0.414	302.90	1.18E+18	1.07E+12	5.28E+17	1.89E+18	2.20E+11
*	4837	0.414	0.414	303.54	1.05E+18	0.00E+00	4.48E+17	1.85E+18	0.00E+00
*	4838	0.420	0.414	302.21	1.19E+18	8.38E+11	5.25E+17	1.72E+18	1.73E+11
*	4839	0.413	0.413	301.70	9.60E+17	0.00E+00	3.90E+17	1.51E+18	0.00E+00

	STEP	SAT1	SAT2	TEMP	LAT HEAT OUT	PRECIP	SEN HEAT OUT	SW HEAT IN	RUNOFF
*	4840	0.411	0.411	300.59	8.39E+17	0.00E+00	3.17E+17	1.24E+18	0.00E+00
*	4841	0.422	0.411	297.48	8.75E+17	8.82E+11	3.26E+17	9.02E+17	1.81E+11
*	4842	0.415	0.411	295.43	5.09E+17	0.00E+00	1.30E+17	5.28E+17	0.00E+00
*	4843	0.411	0.411	293.00	2.69E+17	0.00E+00	3.19E+16	1.31E+17	0.00E+00
*	4844	0.411	0.411	291.60	1.81E+16	0.00E+00	-5.58E+15	0.00E+00	0.00E+00
*	4845	0.411	0.411	290.42	1.67E+15	0.00E+00	-2.02E+15	0.00E+00	0.00E+00
*	4846	0.411	0.411	289.36	2.98E+14	0.00E+00	-1.15E+15	0.00E+00	0.00E+00
*	4847	0.411	0.411	288.42	5.27E+12	0.00E+00	-7.76E+14	0.00E+00	0.00E+00
*	4848	0.411	0.411	287.56	-7.55E+13	0.00E+00	-5.76E+14	0.00E+00	0.00E+00
*	4849	0.411	0.411	286.79	-9.85E+13	0.00E+00	-4.55E+14	0.00E+00	0.00E+00

	STEP	SAT1	SAT2	TEMP	LAT HEAT OUT	PRECIP	SEN HEAT OUT	SW HEAT IN	RUNOFF
*	4850	0.411	0.411	286.09	-1.03E+14	0.00E+00	-3.77E+14	0.00E+00	0.00E+00
*	4851	0.411	0.411	285.44	-1.01E+14	0.00E+00	-3.22E+14	0.00E+00	0.00E+00
*	4852	0.411	0.411	284.85	-9.65E+13	0.00E+00	-2.82E+14	0.00E+00	0.00E+00
*	4853	0.437	0.411	285.18	-5.83E+13	1.01E+12	-3.22E+14	1.30E+17	2.07E+11
*	4854	0.436	0.411	287.82	-5.77E+13	0.00E+00	-3.57E+14	5.29E+17	0.00E+00
*	4855	0.435	0.412	292.39	1.51E+14	0.00E+00	-8.40E+14	9.04E+17	0.00E+00
*	4856	0.432	0.412	297.57	1.56E+17	0.00E+00	3.63E+15	1.24E+18	0.00E+00
*	4857	0.422	0.412	299.82	6.70E+17	0.00E+00	2.48E+17	1.51E+18	0.00E+00
*	4858	0.412	0.412	301.76	8.17E+17	0.00E+00	3.47E+17	1.72E+18	0.00E+00
*	4859	0.410	0.410	303.29	9.21E+17	0.00E+00	4.14E+17	1.85E+18	0.00E+00

STEP	SAT1	SAT2	TEMP	LAT HEAT OUT	PRECIP	SEN HEAT OUT	SW HEAT IN	RUNOFF
* 4860	0.422	0.410	303.03	1.18E+18	1.06E+12	5.28E+17	1.89E+18	2.18E+11
* 4861	0.409	0.409	303.66	1.05E+18	0.00E+00	4.48E+17	1.85E+18	0.00E+00
* 4862	0.415	0.410	302.32	1.19E+18	8.35E+11	5.26E+17	1.72E+18	1.71E+11
* 4863	0.408	0.408	301.81	9.58E+17	0.00E+00	3.91E+17	1.51E+18	0.00E+00
* 4864	0.407	0.407	300.70	8.38E+17	0.00E+00	3.17E+17	1.23E+18	0.00E+00
* 4865	0.418	0.407	297.57	8.73E+17	8.79E+11	3.26E+17	8.99E+17	1.79E+11
* 4866	0.411	0.407	295.52	5.08E+17	0.00E+00	1.30E+17	5.25E+17	0.00E+00
* 4867	0.407	0.407	293.08	2.67E+17	0.00E+00	3.15E+16	1.28E+17	0.00E+00
* 4868	0.407	0.407	291.68	1.77E+16	0.00E+00	-5.58E+15	0.00E+00	0.00E+00
* 4869	0.407	0.407	290.51	1.65E+15	0.00E+00	-2.01E+15	0.00E+00	0.00E+00

STEP	SAT1	SAT2	TEMP	LAT HEAT OUT	PRECIP	SEN HEAT OUT	SW HEAT IN	RUNOFF
* 4870	0.407	0.407	289.46	2.99E+14	0.00E+00	-1.15E+15	0.00E+00	0.00E+00
* 4871	0.407	0.407	288.51	8.30E+12	0.00E+00	-7.75E+14	0.00E+00	0.00E+00
* 4872	0.407	0.407	287.66	-7.29E+13	0.00E+00	-5.76E+14	0.00E+00	0.00E+00
* 4873	0.407	0.407	286.89	-9.65E+13	0.00E+00	-4.56E+14	0.00E+00	0.00E+00
* 4874	0.407	0.407	286.19	-1.01E+14	0.00E+00	-3.78E+14	0.00E+00	0.00E+00
* 4875	0.407	0.407	285.55	-9.95E+13	0.00E+00	-3.23E+14	0.00E+00	0.00E+00
* 4876	0.407	0.407	284.97	-9.56E+13	0.00E+00	-2.83E+14	0.00E+00	0.00E+00
* 4877	0.407	0.407	285.20	-9.11E+13	0.00E+00	-2.53E+14	1.27E+17	0.00E+00
* 4878	0.434	0.407	287.85	-5.73E+13	1.05E+12	-3.50E+14	5.25E+17	2.13E+11
* 4879	0.432	0.407	292.42	1.37E+14	0.00E+00	-8.14E+14	9.00E+17	0.00E+00

STEP	SAT1	SAT2	TEMP	LAT HEAT OUT	PRECIP	SEN HEAT OUT	SW HEAT IN	RUNOFF
* 4880	0.429	0.407	297.66	1.47E+17	0.00E+00	1.90E+15	1.23E+18	0.00E+00
* 4881	0.420	0.407	299.91	6.70E+17	0.00E+00	2.47E+17	1.51E+18	0.00E+00
* 4882	0.409	0.407	301.86	8.17E+17	0.00E+00	3.46E+17	1.72E+18	0.00E+00
* 4883	0.406	0.406	303.40	9.21E+17	0.00E+00	4.13E+17	1.85E+18	0.00E+00
* 4884	0.417	0.406	303.15	1.18E+18	1.05E+12	5.28E+17	1.89E+18	2.13E+11
* 4885	0.405	0.405	303.78	1.04E+18	0.00E+00	4.49E+17	1.84E+18	0.00E+00
* 4886	0.403	0.403	303.78	1.01E+18	0.00E+00	4.28E+17	1.71E+18	0.00E+00
* 4887	0.415	0.403	301.51	1.16E+18	1.03E+12	4.95E+17	1.51E+18	2.07E+11
* 4888	0.403	0.403	300.45	8.43E+17	0.00E+00	3.16E+17	1.23E+18	0.00E+00
* 4889	0.402	0.402	298.81	6.78E+17	0.00E+00	2.27E+17	8.96E+17	0.00E+00

STEP	SAT1	SAT2	TEMP	LAT HEAT OUT	PRECIP	SEN HEAT OUT	SW HEAT IN	RUNOFF
* 4890	0.417	0.402	295.23	6.81E+17	9.34E+11	2.17E+17	5.22E+17	1.88E+11
* 4891	0.413	0.402	292.80	2.75E+17	0.00E+00	3.17E+16	1.24E+17	0.00E+00
* 4892	0.412	0.402	291.45	1.93E+16	0.00E+00	-5.58E+15	0.00E+00	0.00E+00
* 4893	0.412	0.402	290.32	2.02E+15	0.00E+00	-2.09E+15	0.00E+00	0.00E+00
* 4894	0.411	0.402	289.31	4.34E+14	0.00E+00	-1.21E+15	0.00E+00	0.00E+00
* 4895	0.411	0.402	288.40	7.18E+13	0.00E+00	-8.21E+14	0.00E+00	0.00E+00
* 4896	0.410	0.402	287.58	-3.86E+13	0.00E+00	-6.13E+14	0.00E+00	0.00E+00
* 4897	0.410	0.402	286.84	-7.61E+13	0.00E+00	-4.86E+14	0.00E+00	0.00E+00
* 4898	0.410	0.402	286.16	-8.84E+13	0.00E+00	-4.03E+14	0.00E+00	0.00E+00
* 4899	0.410	0.403	285.54	-9.11E+13	0.00E+00	-3.45E+14	0.00E+00	0.00E+00

STEP	SAT1	SAT2	TEMP	LAT HEAT OUT	PRECIP	SEN HEAT OUT	SW HEAT IN	RUNOFF
* 4900	0.409	0.403	284.97	-8.98E+13	0.00E+00	-3.03E+14	0.00E+00	0.00E+00
* 4901	0.409	0.403	285.20	-8.71E+13	0.00E+00	-2.71E+14	1.23E+17	0.00E+00
* 4902	0.409	0.403	287.81	-9.23E+13	0.00E+00	-2.91E+14	5.23E+17	0.00E+00
* 4903	0.408	0.403	292.38	-9.11E+13	0.00E+00	-6.13E+14	8.98E+17	0.00E+00
* 4904	0.408	0.403	298.27	3.61E+16	0.00E+00	-5.45E+15	1.23E+18	0.00E+00

*	4905	0.402	0.402	300.67	6.15E+17	0.00E+00	2.50E+17	1.51E+18	0.00E+00
*	4906	0.418	0.402	301.52	9.43E+17	1.11E+12	4.09E+17	1.72E+18	2.23E+11
*	4907	0.406	0.402	303.11	9.35E+17	0.00E+00	4.06E+17	1.84E+18	0.00E+00
*	4908	0.401	0.401	304.20	9.97E+17	0.00E+00	4.43E+17	1.89E+18	0.00E+00
*	4909	0.413	0.401	303.23	1.22E+18	1.08E+12	5.50E+17	1.84E+18	2.15E+11

	STEP	SAT1	SAT2	TEMP	LAT HEAT OUT	PRECIP	SEN HEAT OUT	SW HEAT IN	RUNOFF
*	4910	0.401	0.401	303.31	1.02E+18	0.00E+00	4.30E+17	1.71E+18	0.00E+00
*	4911	0.408	0.401	301.33	1.12E+18	8.47E+11	4.87E+17	1.50E+18	1.70E+11
*	4912	0.400	0.400	300.25	8.40E+17	0.00E+00	3.23E+17	1.23E+18	0.00E+00
*	4913	0.398	0.398	298.61	6.79E+17	0.00E+00	2.30E+17	8.93E+17	0.00E+00
*	4914	0.411	0.399	295.16	6.64E+17	8.27E+11	2.11E+17	5.18E+17	1.65E+11
*	4915	0.407	0.399	292.72	2.75E+17	0.00E+00	3.25E+16	1.20E+17	0.00E+00
*	4916	0.407	0.399	291.39	1.95E+16	0.00E+00	-5.57E+15	0.00E+00	0.00E+00
*	4917	0.406	0.399	290.28	2.13E+15	0.00E+00	-2.13E+15	0.00E+00	0.00E+00
*	4918	0.406	0.399	289.29	4.82E+14	0.00E+00	-1.24E+15	0.00E+00	0.00E+00
*	4919	0.406	0.399	288.40	9.66E+13	0.00E+00	-8.45E+14	0.00E+00	0.00E+00

	STEP	SAT1	SAT2	TEMP	LAT HEAT OUT	PRECIP	SEN HEAT OUT	SW HEAT IN	RUNOFF
*	4920	0.405	0.399	287.60	-2.43E+13	0.00E+00	-8.32E+14	0.00E+00	0.00E+00
*	4921	0.405	0.399	286.87	-6.73E+13	0.00E+00	-5.02E+14	0.00E+00	0.00E+00
*	4922	0.405	0.399	286.21	-8.27E+13	0.00E+00	-4.17E+14	0.00E+00	0.00E+00
*	4923	0.405	0.399	285.60	-8.72E+13	0.00E+00	-3.57E+14	0.00E+00	0.00E+00
*	4924	0.404	0.399	285.04	-8.72E+13	0.00E+00	-3.14E+14	0.00E+00	0.00E+00
*	4925	0.404	0.399	285.26	-8.53E+13	0.00E+00	-2.81E+14	1.19E+17	0.00E+00
*	4926	0.404	0.399	287.87	-9.01E+13	0.00E+00	-3.01E+14	5.19E+17	0.00E+00
*	4927	0.404	0.399	292.45	-7.61E+13	0.00E+00	-6.44E+14	8.95E+17	0.00E+00
*	4928	0.403	0.399	298.27	5.02E+16	0.00E+00	-5.34E+15	1.23E+18	0.00E+00
*	4929	0.399	0.399	300.63	6.19E+17	0.00E+00	2.56E+17	1.51E+18	0.00E+00

	STEP	SAT1	SAT2	TEMP	LAT HEAT OUT	PRECIP	SEN HEAT OUT	SW HEAT IN	RUNOFF
*	4930	0.414	0.399	301.55	9.33E+17	1.06E+12	4.06E+17	1.71E+18	2.12E+11
*	4931	0.401	0.399	303.15	9.33E+17	0.00E+00	4.09E+17	1.84E+18	0.00E+00
*	4932	0.397	0.397	304.25	9.95E+17	0.00E+00	4.46E+17	1.88E+18	0.00E+00
*	4933	0.408	0.397	303.31	1.22E+18	1.04E+12	5.50E+17	1.84E+18	2.07E+11
*	4934	0.397	0.397	303.38	1.02E+18	0.00E+00	4.32E+17	1.71E+18	0.00E+00
*	4935	0.403	0.397	301.42	1.12E+18	8.25E+11	4.87E+17	1.50E+18	1.64E+11
*	4936	0.396	0.396	300.34	8.39E+17	0.00E+00	3.24E+17	1.22E+18	0.00E+00
*	4937	0.394	0.394	298.69	6.77E+17	0.00E+00	2.30E+17	8.89E+17	0.00E+00
*	4938	0.407	0.395	295.24	6.61E+17	8.12E+11	2.11E+17	5.14E+17	1.60E+11
*	4939	0.403	0.395	292.79	2.74E+17	0.00E+00	3.23E+16	1.17E+17	0.00E+00

	STEP	SAT1	SAT2	TEMP	LAT HEAT OUT	PRECIP	SEN HEAT OUT	SW HEAT IN	RUNOFF
*	4940	0.402	0.395	291.47	1.91E+16	0.00E+00	-5.58E+15	0.00E+00	0.00E+00
*	4941	0.402	0.395	290.37	2.13E+15	0.00E+00	-2.13E+15	0.00E+00	0.00E+00
*	4942	0.402	0.395	289.39	4.92E+14	0.00E+00	-1.24E+15	0.00E+00	0.00E+00
*	4943	0.401	0.395	288.51	1.03E+14	0.00E+00	-8.50E+14	0.00E+00	0.00E+00
*	4944	0.401	0.395	287.71	-1.98E+13	0.00E+00	-6.37E+14	0.00E+00	0.00E+00
*	4945	0.401	0.395	286.99	-6.43E+13	0.00E+00	-5.07E+14	0.00E+00	0.00E+00
*	4946	0.401	0.395	286.33	-8.07E+13	0.00E+00	-4.21E+14	0.00E+00	0.00E+00
*	4947	0.400	0.395	285.73	-8.58E+13	0.00E+00	-3.61E+14	0.00E+00	0.00E+00
*	4948	0.400	0.395	285.17	-8.62E+13	0.00E+00	-3.17E+14	0.00E+00	0.00E+00
*	4949	0.400	0.395	285.37	-8.47E+13	0.00E+00	-2.84E+14	1.16E+17	0.00E+00

	STEP	SAT1	SAT2	TEMP	LAT HEAT	PRECIP	SEN HEAT	SW HEAT	RUNOFF
--	------	------	------	------	----------	--------	----------	---------	--------

				OUT		OUT		IN	
*	4950	0.400	0.395	287.98	-8.93E+13	0.00E+00	-3.04E+14	5.15E+17	0.00E+00
*	4951	0.399	0.395	292.56	-7.16E+13	0.00E+00	-8.51E+14	8.91E+17	0.00E+00
*	4952	0.399	0.395	298.37	5.37E+16	0.00E+00	-5.29E+15	1.23E+18	0.00E+00
*	4953	0.394	0.394	300.72	6.18E+17	0.00E+00	2.57E+17	1.50E+18	0.00E+00
*	4954	0.393	0.393	302.65	7.75E+17	0.00E+00	3.60E+17	1.71E+18	0.00E+00
*	4955	0.412	0.393	302.88	1.08E+18	1.30E+12	4.87E+17	1.84E+18	2.55E+11
*	4956	0.399	0.393	304.04	1.01E+18	0.00E+00	4.40E+17	1.88E+18	0.00E+00
*	4957	0.407	0.393	303.24	1.20E+18	9.32E+11	5.44E+17	1.83E+18	1.86E+11
*	4958	0.393	0.393	303.33	1.02E+18	0.00E+00	4.34E+17	1.71E+18	0.00E+00
*	4959	0.391	0.391	302.75	9.36E+17	0.00E+00	3.87E+17	1.50E+18	0.00E+00

STEP	SAT1	SAT2	TEMP	LAT	HEAT	PRECIP	SEN HEAT	SW HEAT	RUNOFF
					OUT		OUT	IN	
*	4960	0.402	0.391	299.99	1.02E+18	9.53E+11	4.26E+17	1.22E+18	1.86E+11
*	4961	0.393	0.391	298.37	6.84E+17	0.00E+00	2.30E+17	8.86E+17	0.00E+00
*	4962	0.390	0.390	296.26	4.84E+17	0.00E+00	1.27E+17	5.11E+17	0.00E+00
*	4963	0.390	0.390	293.77	2.45E+17	0.00E+00	2.66E+16	1.13E+17	0.00E+00
*	4964	0.390	0.390	292.30	1.36E+16	0.00E+00	-5.61E+15	0.00E+00	0.00E+00
*	4965	0.414	0.390	291.07	1.95E+16	9.59E+11	-5.58E+15	0.00E+00	1.87E+11
*	4966	0.413	0.390	290.03	2.52E+15	0.00E+00	-2.12E+15	0.00E+00	0.00E+00
*	4967	0.412	0.390	289.11	6.99E+14	0.00E+00	-1.28E+15	0.00E+00	0.00E+00
*	4968	0.411	0.391	288.27	2.19E+14	0.00E+00	-8.90E+14	0.00E+00	0.00E+00
*	4969	0.410	0.391	287.52	5.03E+13	0.00E+00	-6.74E+14	0.00E+00	0.00E+00

STEP	SAT1	SAT2	TEMP	LAT	HEAT	PRECIP	SEN HEAT	SW HEAT	RUNOFF
					OUT		OUT	IN	
*	4970	0.410	0.391	286.83	-1.85E+13	0.00E+00	-5.40E+14	0.00E+00	0.00E+00
*	4971	0.409	0.391	286.21	-4.89E+13	0.00E+00	-4.51E+14	0.00E+00	0.00E+00
*	4972	0.408	0.391	285.63	-6.28E+13	0.00E+00	-3.88E+14	0.00E+00	0.00E+00
*	4973	0.407	0.391	285.78	-6.90E+13	0.00E+00	-3.41E+14	1.12E+17	0.00E+00
*	4974	0.407	0.392	288.33	-7.08E+13	0.00E+00	-3.63E+14	5.11E+17	0.00E+00
*	4975	0.406	0.392	292.85	7.60E+13	0.00E+00	-8.25E+14	8.87E+17	0.00E+00
*	4976	0.404	0.392	298.13	1.36E+17	0.00E+00	1.79E+15	1.22E+18	0.00E+00
*	4977	0.395	0.392	300.43	6.40E+17	0.00E+00	2.54E+17	1.50E+18	0.00E+00
*	4978	0.391	0.391	302.38	7.87E+17	0.00E+00	3.55E+17	1.71E+18	0.00E+00
*	4979	0.389	0.389	303.92	8.97E+17	0.00E+00	4.18E+17	1.84E+18	0.00E+00

STEP	SAT1	SAT2	TEMP	LAT	HEAT	PRECIP	SEN HEAT	SW HEAT	RUNOFF
					OUT		OUT	IN	
*	4980	0.406	0.389	303.49	1.18E+18	1.24E+12	5.42E+17	1.88E+18	2.41E+11
*	4981	0.392	0.389	304.14	1.03E+18	0.00E+00	4.51E+17	1.83E+18	0.00E+00
*	4982	0.401	0.389	302.71	1.18E+18	9.37E+11	5.34E+17	1.70E+18	1.83E+11
*	4983	0.389	0.389	302.20	9.43E+17	0.00E+00	3.92E+17	1.49E+18	0.00E+00
*	4984	0.387	0.387	301.06	8.20E+17	0.00E+00	3.19E+17	1.22E+18	0.00E+00
*	4985	0.400	0.387	297.85	8.58E+17	9.21E+11	3.30E+17	8.81E+17	1.78E+11
*	4986	0.393	0.387	295.76	4.94E+17	0.00E+00	1.29E+17	5.07E+17	0.00E+00
*	4987	0.389	0.387	293.27	2.54E+17	0.00E+00	2.88E+16	1.09E+17	0.00E+00
*	4988	0.389	0.387	291.89	1.51E+16	0.00E+00	-5.60E+15	0.00E+00	0.00E+00
*	4989	0.389	0.387	290.71	1.40E+15	0.00E+00	-1.89E+15	0.00E+00	0.00E+00

STEP	SAT1	SAT2	TEMP	LAT	HEAT	PRECIP	SEN HEAT	SW HEAT	RUNOFF
					OUT		OUT	IN	
*	4990	0.389	0.387	289.67	2.50E+14	0.00E+00	-1.10E+15	0.00E+00	0.00E+00
*	4991	0.389	0.387	288.73	-1.85E+12	0.00E+00	-7.49E+14	0.00E+00	0.00E+00
*	4992	0.389	0.387	287.88	-7.29E+13	0.00E+00	-5.60E+14	0.00E+00	0.00E+00
*	4993	0.389	0.387	287.12	-9.35E+13	0.00E+00	-4.46E+14	0.00E+00	0.00E+00
*	4994	0.389	0.387	286.43	-9.74E+13	0.00E+00	-3.71E+14	0.00E+00	0.00E+00
*	4995	0.389	0.387	285.80	-9.55E+13	0.00E+00	-3.18E+14	0.00E+00	0.00E+00

*	4996	0.388	0.387	285.22	-9.17E+13	0.00E+00	-2.80E+14	0.00E+00	0.00E+00
*	4997	0.388	0.387	285.35	-8.75E+13	0.00E+00	-2.51E+14	1.08E+17	0.00E+00
*	4998	0.416	0.387	287.96	-5.85E+13	1.07E+12	-3.38E+14	5.07E+17	2.08E+11
*	4999	0.415	0.388	292.52	9.14E+13	0.00E+00	-7.61E+14	8.83E+17	0.00E+00

	STEP	SAT1	SAT2	TEMP	LAT	HEAT OUT	PRECIP	SEN HEAT OUT	SW HEAT IN	RUNOFF
*	5000	0.412	0.388	297.94	1.20E+17	0.00E+00	-1.59E+15	1.22E+18	0.00E+00	
*	5001	0.403	0.388	300.23	6.55E+17	0.00E+00	2.47E+17	1.50E+18	0.00E+00	
*	5002	0.392	0.388	302.20	8.03E+17	0.00E+00	3.49E+17	1.70E+18	0.00E+00	
*	5003	0.387	0.387	303.78	9.07E+17	0.00E+00	4.16E+17	1.83E+18	0.00E+00	
*	5004	0.399	0.387	303.53	1.16E+18	1.04E+12	5.34E+17	1.87E+18	2.02E+11	
*	5005	0.386	0.386	304.17	1.03E+18	0.00E+00	4.55E+17	1.83E+18	0.00E+00	
*	5006	0.384	0.384	304.15	9.98E+17	0.00E+00	4.32E+17	1.70E+18	0.00E+00	
*	5007	0.396	0.384	301.85	1.14E+18	1.01E+12	5.01E+17	1.49E+18	1.93E+11	
*	5008	0.385	0.384	300.76	8.30E+17	0.00E+00	3.19E+17	1.21E+18	0.00E+00	
*	5009	0.383	0.383	299.08	6.66E+17	0.00E+00	2.27E+17	8.78E+17	0.00E+00	

	STEP	SAT1	SAT2	TEMP	LAT	HEAT OUT	PRECIP	SEN HEAT OUT	SW HEAT IN	RUNOFF
*	5010	0.398	0.383	295.48	6.64E+17	9.08E+11	2.15E+17	5.03E+17	1.74E+11	
*	5011	0.394	0.383	293.00	2.63E+17	0.00E+00	2.96E+16	1.05E+17	0.00E+00	
*	5012	0.393	0.383	291.68	1.69E+16	0.00E+00	-5.59E+15	0.00E+00	0.00E+00	
*	5013	0.393	0.383	290.57	1.83E+15	0.00E+00	-2.01E+15	0.00E+00	0.00E+00	
*	5014	0.392	0.383	289.58	4.14E+14	0.00E+00	-1.19E+15	0.00E+00	0.00E+00	
*	5015	0.392	0.383	288.69	7.51E+13	0.00E+00	-8.14E+14	0.00E+00	0.00E+00	
*	5016	0.392	0.384	287.89	-3.16E+13	0.00E+00	-6.12E+14	0.00E+00	0.00E+00	
*	5017	0.391	0.384	287.16	-6.93E+13	0.00E+00	-4.88E+14	0.00E+00	0.00E+00	
*	5018	0.391	0.384	286.50	-8.25E+13	0.00E+00	-4.07E+14	0.00E+00	0.00E+00	
*	5019	0.391	0.384	285.89	-8.61E+13	0.00E+00	-3.49E+14	0.00E+00	0.00E+00	

	STEP	SAT1	SAT2	TEMP	LAT	HEAT OUT	PRECIP	SEN HEAT OUT	SW HEAT IN	RUNOFF
*	5020	0.390	0.384	285.34	-8.57E+13	0.00E+00	-3.07E+14	0.00E+00	0.00E+00	
*	5021	0.390	0.384	285.46	-8.36E+13	0.00E+00	-2.76E+14	1.03E+17	0.00E+00	
*	5022	0.390	0.384	288.03	-8.75E+13	0.00E+00	-2.90E+14	5.03E+17	0.00E+00	
*	5023	0.390	0.384	292.59	-8.50E+13	0.00E+00	-5.99E+14	8.80E+17	0.00E+00	
*	5024	0.389	0.384	298.53	3.02E+16	0.00E+00	-5.49E+15	1.22E+18	0.00E+00	
*	5025	0.384	0.384	301.00	6.00E+17	0.00E+00	2.48E+17	1.49E+18	0.00E+00	
*	5026	0.400	0.384	301.89	9.25E+17	1.09E+12	4.11E+17	1.70E+18	2.08E+11	
*	5027	0.387	0.384	303.51	9.22E+17	0.00E+00	4.10E+17	1.83E+18	0.00E+00	
*	5028	0.382	0.382	304.61	9.84E+17	0.00E+00	4.48E+17	1.87E+18	0.00E+00	
*	5029	0.394	0.382	303.63	1.20E+18	1.05E+12	5.57E+17	1.83E+18	2.00E+11	

	STEP	SAT1	SAT2	TEMP	LAT	HEAT OUT	PRECIP	SEN HEAT OUT	SW HEAT IN	RUNOFF
*	5030	0.382	0.382	303.70	1.01E+18	0.00E+00	4.36E+17	1.70E+18	0.00E+00	
*	5031	0.389	0.382	301.71	1.10E+18	8.21E+11	4.91E+17	1.49E+18	1.57E+11	
*	5032	0.381	0.381	300.60	8.28E+17	0.00E+00	3.25E+17	1.21E+18	0.00E+00	
*	5033	0.380	0.380	298.92	6.67E+17	0.00E+00	2.30E+17	8.74E+17	0.00E+00	
*	5034	0.379	0.379	296.76	4.72E+17	0.00E+00	1.22E+17	4.99E+17	0.00E+00	
*	5035	0.397	0.379	292.89	4.32E+17	9.34E+11	9.35E+16	1.00E+17	1.77E+11	
*	5036	0.396	0.379	291.61	1.90E+16	0.00E+00	-5.58E+15	0.00E+00	0.00E+00	
*	5037	0.396	0.379	290.54	2.27E+15	0.00E+00	-2.12E+15	0.00E+00	0.00E+00	
*	5038	0.395	0.379	289.58	5.78E+14	0.00E+00	-1.26E+15	0.00E+00	0.00E+00	
*	5039	0.394	0.380	288.73	1.54E+14	0.00E+00	-8.66E+14	0.00E+00	0.00E+00	

	STEP	SAT1	SAT2	TEMP	LAT	HEAT OUT	PRECIP	SEN HEAT OUT	SW HEAT IN	RUNOFF
--	------	------	------	------	-----	-------------	--------	-----------------	---------------	--------

*	5040	0.394	0.380	287.95	1.18E+13	0.00E+00	-6.53E+14	0.00E+00	0.00E+00
*	5280	0.372	0.364	294.80	3.72E+17	1.55E+11	1.55E+17	7.07E+17	2.82E+10
*	5520	0.348	0.340	294.93	3.52E+17	1.52E+11	1.52E+17	6.78E+17	2.58E+10
*	5760	0.334	0.326	294.71	3.30E+17	1.48E+11	1.46E+17	6.48E+17	2.42E+10
*	6000	0.327	0.323	294.15	3.05E+17	1.48E+11	1.39E+17	6.15E+17	2.33E+10
*	6240	0.333	0.329	293.12	2.81E+17	1.44E+11	1.28E+17	5.78E+17	2.31E+10
*	6480	0.352	0.344	291.67	2.53E+17	1.38E+11	1.15E+17	5.38E+17	2.33E+10
*	6720	0.379	0.367	289.63	2.25E+17	1.38E+11	1.01E+17	4.96E+17	2.52E+10
*	6960	0.411	0.396	287.49	1.97E+17	1.29E+11	8.86E+16	4.59E+17	2.55E+10
ITERATION 15				TS(K),TG1(K),T(1) =	286.93	280.32	286.94		

STEP	SAT1	SAT2	TEMP	LAT HEAT OUT	PRECIP	SEN HEAT OUT	SW HEAT IN	RUNOFF	
*	7200	0.447	0.430	285.07	1.69E+17	1.21E+11	7.61E+16	4.21E+17	2.63E+10
*	7440	0.487	0.468	282.30	1.42E+17	1.11E+11	6.42E+16	3.84E+17	2.64E+10
*	7680	0.529	0.509	279.20	1.13E+17	1.05E+11	5.38E+16	3.49E+17	2.72E+10
*	7920	0.575	0.554	275.93	8.89E+16	9.82E+10	4.45E+16	3.21E+17	2.78E+10
*	8160	0.624	0.601	272.67	6.67E+16	9.08E+10	3.82E+16	3.00E+17	2.80E+10
*	8400	0.673	0.649	269.66	4.82E+16	8.45E+10	3.53E+16	2.84E+17	2.82E+10
*	8640	0.720	0.697	267.09	3.78E+16	7.70E+10	3.20E+16	2.75E+17	2.75E+10

 ***** STEP = 8760: DIAGNOSTICS ZEROED *****

*	8880	0.764	0.743	264.89	3.38E+16	7.54E+10	2.86E+16	2.73E+17	2.87E+10
*	9120	0.806	0.786	263.12	3.23E+16	7.31E+10	3.01E+16	2.78E+17	2.94E+10
*	9360	0.844	0.826	261.84	3.30E+16	7.24E+10	3.55E+16	2.91E+17	3.05E+10
ITERATION 15				TS(K),TG1(K),T(1) =	266.75	258.83	266.75		

STEP	SAT1	SAT2	TEMP	LAT HEAT OUT	PRECIP	SEN HEAT OUT	SW HEAT IN	RUNOFF	
*	9600	0.877	0.861	261.03	4.05E+16	7.17E+10	4.16E+16	3.11E+17	3.14E+10
*	9840	0.904	0.891	260.65	5.10E+16	7.42E+10	5.13E+16	3.36E+17	3.35E+10
*	10080	0.925	0.915	260.97	6.14E+16	7.35E+10	6.75E+16	3.70E+17	3.39E+10
*	10320	0.938	0.932	262.04	8.01E+16	7.70E+10	8.18E+16	4.10E+17	3.61E+10
*	10560	0.941	0.940	263.63	1.03E+17	8.14E+10	9.66E+16	4.52E+17	3.83E+10
*	10800	0.924	0.941	265.64	1.31E+17	8.79E+10	1.10E+17	4.94E+17	4.05E+10
*	11040	0.862	0.941	268.00	1.58E+17	9.32E+10	1.26E+17	5.35E+17	4.00E+10
*	11280	0.766	0.941	271.03	1.87E+17	9.95E+10	1.41E+17	5.79E+17	3.79E+10
*	11520	0.653	0.941	274.34	2.16E+17	1.06E+11	1.59E+17	6.21E+17	3.44E+10
*	11760	0.713	0.900	277.36	2.63E+17	1.19E+11	1.50E+17	6.56E+17	4.32E+10
ITERATION 15				TS(K),TG1(K),T(1) =	281.99	276.53	281.99		

STEP	SAT1	SAT2	TEMP	LAT HEAT OUT	PRECIP	SEN HEAT OUT	SW HEAT IN	RUNOFF	
*	12000	0.817	0.814	279.93	3.17E+17	1.37E+11	1.31E+17	6.87E+17	5.58E+10
*	12240	0.754	0.752	282.29	3.45E+17	1.44E+11	1.36E+17	7.13E+17	5.39E+10
*	12480	0.690	0.687	284.82	3.69E+17	1.52E+11	1.40E+17	7.35E+17	5.20E+10
*	12720	0.627	0.622	287.19	3.85E+17	1.54E+11	1.45E+17	7.50E+17	4.77E+10
*	12960	0.564	0.558	289.39	3.98E+17	1.56E+11	1.49E+17	7.58E+17	4.34E+10
*	13200	0.505	0.499	291.18	4.02E+17	1.57E+11	1.54E+17	7.58E+17	3.92E+10
*	13440	0.452	0.446	292.68	3.99E+17	1.58E+11	1.57E+17	7.52E+17	3.52E+10
*	13680	0.405	0.400	293.91	3.91E+17	1.58E+11	1.60E+17	7.38E+17	3.16E+10
*	13920	0.370	0.363	294.77	3.77E+17	1.54E+11	1.59E+17	7.19E+17	2.78E+10
*	14160	0.343	0.335	295.14	3.59E+17	1.51E+11	1.58E+17	6.93E+17	2.53E+10
ITERATION 15				TS(K),TG1(K),T(1) =	294.77	289.29	294.78		

STEP	SAT1	SAT2	TEMP	LAT HEAT	PRECIP	SEN HEAT	SW HEAT	RUNOFF
------	------	------	------	----------	--------	----------	---------	--------

				OUT		OUT		IN	
*	14400	0.326	0.317	295.07	3.38E+17	1.49E+11	1.53E+17	6.63E+17	2.37E+10
*	14640	0.318	0.310	294.66	3.16E+17	1.48E+11	1.45E+17	6.32E+17	2.29E+10
*	14880	0.316	0.314	293.81	2.90E+17	1.44E+11	1.37E+17	5.97E+17	2.20E+10
*	15120	0.332	0.326	292.59	2.66E+17	1.44E+11	1.24E+17	5.58E+17	2.31E+10
*	15360	0.357	0.346	290.81	2.38E+17	1.33E+11	1.09E+17	5.16E+17	2.27E+10
*	15600	0.388	0.373	288.67	2.10E+17	1.33E+11	9.56E+16	4.77E+17	2.48E+10
*	15840	0.422	0.405	286.42	1.81E+17	1.25E+11	8.29E+16	4.40E+17	2.55E+10
*	16080	0.460	0.442	283.78	1.55E+17	1.19E+11	7.09E+16	4.02E+17	2.67E+10
*	16320	0.502	0.482	280.88	1.27E+17	1.06E+11	5.91E+16	3.66E+17	2.61E+10
*	16560	0.547	0.525	277.58	1.01E+17	1.03E+11	4.89E+16	3.34E+17	2.77E+10
ITERATION 15				TS(K), TG1(K), T(1) =	278.70	270.39	278.70		

	STEP	SAT1	SAT2	TEMP	LAT HEAT	PRECIP	SEN HEAT	SW HEAT	RUNOFF
					OUT		OUT	IN	
*	16800	0.595	0.572	274.42	7.75E+16	9.42E+10	4.14E+16	3.10E+17	2.76E+10
*	17040	0.644	0.620	271.15	5.66E+16	8.81E+10	3.68E+16	2.92E+17	2.81E+10
*	17280	0.692	0.669	268.36	4.23E+16	7.97E+10	3.35E+16	2.79E+17	2.74E+10
*	17520	0.738	0.717	265.97	3.57E+16	7.68E+10	2.96E+16	2.73E+17	2.82E+10

 CONDITIONS AFTER 17520 TIME STEPS

T	Q REL
193.17999	1.00167
193.50723	1.00172
191.42116	1.00272
213.50026	1.00286
227.61467	1.00447
245.25359	1.00787
258.70245	0.86423
266.92749	0.74010
271.48877	0.79227

NDIV

K	TG1(K)	CHI1(K)	CHI2(K)
1	262.25720	0.75825	0.73930
2	293.00000	0.00000	0.00000
3	293.00000	0.00000	0.00000
4	293.00000	0.00000	0.00000
5	293.00000	0.00000	0.00000
6	293.00000	0.00000	0.00000
7	293.00000	0.00000	0.00000
8	293.00000	0.00000	0.00000
9	293.00000	0.00000	0.00000
10	293.00000	0.00000	0.00000
11	293.00000	0.00000	0.00000
12	293.00000	0.00000	0.00000
13	293.00000	0.00000	0.00000
14	293.00000	0.00000	0.00000
15	293.00000	0.00000	0.00000
16	293.00000	0.00000	0.00000
17	293.00000	0.00000	0.00000
18	293.00000	0.00000	0.00000
19	293.00000	0.00000	0.00000
20	293.00000	0.00000	0.00000

TOTAL WATER ADVECTED IN = 2.90189E+14 (290.19 mm/yr)
SCALED TOTAL PRECIP = 349.76 (1014.98 mm/yr)
SCALED TOTAL EVAP = 249.81 (724.93 mm/yr)

Q ADVECTED IN (SCALED) = 100.00 (290.19 mm/yr)
Q ADVECTED OUT (SCALED) = 0.00 (0.00 mm/yr)
RUNOFF (SCALED) = 100.22 (290.81 mm/yr)

AVERAGE RELATIVE HUMIDITY IN BOTTOM LAYER = 0.7749
RUNOFF/PRECIP RATIO = 0.2865

AVERAGE SOIL CONDITIONS:

K = 1 GROUND TEMP = 278.83 SAT = 0.6221

SENSIBLE-TO-LATENT HEAT TRANSFER RATIO = 4.98E-01
% OF HEAT OUT: LW = 79.727 LH = 13.551 SH = 6.751

SCALED CHANGE IN WATER STORAGE (SINCE BEGINNING) = -0.21
CHANGE PREDICTED FROM WATER BALANCE: -0.22

1137 WET PERIODS: MEAN LENGTH = 1.66 TIME STEPS
1137 DRY PERIODS: MEAN LENGTH = 6.03 TIME STEPS

MC CHARACTERISTICS: AVE. LMAX = 5.30
WHEN LMIN = 1